Search for supersymmetry in events with two same-sign leptons or three leptons with the ATLAS detector at $\sqrt{s} = 13$ TeV

Dissertation

zur Erlangung des Doktorgrades der
Fakultät für Mathematik und Physik der

Albert Ludwigs Universität Freiburg

vorgelegt von Fabio Cardillo

Betreuer: Prof. Dr. Gregor Herten

Fakultät für Mathematik und Physik

Albert Ludwigs Universität Freiburg

Fabio Cardillo: *Search for supersymmetry in events with two same-sign leptons or three leptons with the ATLAS detector at $\sqrt{s}$ = 13 TeV*

Datum der mündlichen Prüfung: June 5, 2018

DEKAN:	Prof. Dr. Gregor Herten
BETREUER DER ARBEIT:	Prof. Dr. Gregor Herten
KOREFERENT:	Dr. Christian Weiser
PRÜFER:	Prof. Dr. Markus Schumacher
	Prof. Dr. Gregor Herten
	Prof. Dr. Harald Ita

Abstract

Supersymmetry is one of the possible extensions of the Standard Model of particle physics and has already been extensively studied during the recent years. In many supersymmetric models, the lightest supersymmetric particle, which is typically the lightest neutralino $\widetilde{\chi}_1^0$, is stable. Thus, it can be a promising candidate for dark matter.

This thesis presents a search for supersymmetric phenomena in final states with either two leptons of the same electric charge or three leptons, together with jets and missing transverse energy. While this event signature is present in various supersymmetric scenarios, Standard Model processes leading to such event signatures have typically very low production rates. Therefore, this analysis benefits from a small Standard Model background in the signal regions leading to a good sensitivity, in particular for scenarios with compressed mass spectra of the supersymmetric parameter space.

The search was performed with the full dataset collected at $\sqrt{s} = 13$ TeV with the ATLAS detector during the years 2015 and 2016, corresponding to a total integrated luminosity of 36.1 fb^{-1}. No significant excess above the Standard Model prediction has been observed. Accordingly, the results were used to set either model-independent upper limits on new physics signals or interpreting them in the context of a large variety of supersymmetric benchmark processes. The model-dependent interpretations allowed to set exclusion limits on the superpartner masses in new supersymmetric scenarios as well as improving existing limits obtained from previous searches.

ZUSAMMENFASSUNG

Supersymmetrie ist eine der Theorien zur Erweiterung des Standardmodells der Teilchenphysik und wurde in den vergangen Jahren bereits ausführlich untersucht. In vielen supersymmetrischen Modellen ist das leichteste supersymmetrische Teilchen, das Neutralino $\widetilde{\chi}_1^0$, stabil, womit es einen aussichtsreichen Kandidaten für dunkle Materie darstellen könnte.
Diese Dissertation behandelt eine Suche nach supersymmetrischen Phänomenen in Ereignissen mit zwei Leptonen gleicher elektrischer Ladung oder drei Leptonen, zusammen mit Jets und fehlender transversaler Energie. Solch eine Ereignissignatur ist in zahlreichen supersymmetrischen Modellen gegeben. Prozesse innerhalb des Standardmodells die zu solch einer Signatur führen haben jedoch typischerweise sehr kleine Produktionsraten. Daher profitiert diese Analyse von einem geringen Untergrund in den Signalregionen, was zu einer großen Sensitivität, besonders in komprimierten Massenbereichen des supersymmetrischen Parameterraumes, führt.
Die Analyse wurde mit dem kompletten ATLAS Datensatz, der in den Jahren 2015 und 2016 bei $\sqrt{s}$ = 13 TeV aufgenommen wurde, durchgeführt. Es konnten keine signifikanten Abweichungen von der Vorhersage des Standardmodells gefunden werden. Daher wurden die Resultate benutzt um modellunabhängige obere Grenzen für neue Physik zu bestimmen oder sie im Rahmen zahlreicher supersymmetischer Referenzmodelle zu interpretieren. Die modellabhängigen Interpretationen erlaubten Ausschlussgrenzen bezüglich der Teilchenmassen für neue supersymmetrische Szenarien zu setzen, sowie die Grenzen für bereits untersuchte Modelle zu verbessern.

Contents

INTRODUCTION

The Standard Model of particle physics is one of the most successful theories of the last century, describing nearly all known particle physics phenomena with a high level of precision. It also predicted the existence of several new particles which were subsequently discovered by experiments. Nevertheless, the Standard Model is considered to be an incomplete theory due to several unaddressed questions and various phenomena which cannot be fully explained.

The commissioning of the Large Hadron Collider in 2008 [1] provided many new opportunities to explore physical phenomena at the TeV scale. The data recorded at general-purpose particle detectors such as ATLAS and CMS [2, 3] allow us to study many theories that predict new physics in this energy range. Analyses on this new data are conducted targeting specific detector signatures which are predicted by these new physics scenarios. The intention of such a study is to reveal discrepancies between the observed data and the Standard Model prediction. There are multiple theoretical scenarios and Standard Model extensions that can be investigated, such as supersymmetric models, Technicolor, extra dimensions, and many others. In most of these models, the current Standard Model is assumed to be only an effective theory and new physics phenomena are expected to occur at high-energy particle interactions. In the last years, many of these models have been excluded by dedicated analyses using the ATLAS data from Run I (2009–2012). However, no evidence for the existence of new physics beyond the Standard Model has been found among these searches. The ongoing Run II started in 2015 and is operated with an increased center-of-mass energy and higher instantaneous luminosities. Therefore, the opportunities for new physics searches are significantly bigger than for all previous high-energy experiments in the past.

The search for supersymmetric phenomena takes an important place in the physics program of the ATLAS experiment and inspired numerous physics analyses. Supersymmetry is a hypothetical spacetime symmetry and an extension of the Standard Model that relates fermions and bosons by postulating the existence of an associated boson to each fermion and a fermion to each boson. These particles are also called superpartners. The concept of supersymmetry is strongly motivated by theoretical arguments and provides a multifarious phenomenology, making it a convenient benchmark for many experimental searches. Furthermore, some of these scenarios presume the lightest supersymmetric particle to be stable, neutral and only weakly interacting with ordinary matter. Thus, it could be a suitable candidate for dark matter, whose identity is one of the most profound questions in modern cosmology.

The topic of this thesis is a search for supersymmetric phenomena in final states with two leptons (electrons or muons) with the same electric charge (also referred to as same-sign leptons) or at least three leptons, jets and missing transverse energy. While the same-sign signature is present in many different supersymmetric scenarios, production of same-sign lepton pairs or three leptons is only induced by rare Standard Model processes with very low production rates. Accordingly, this search benefits from a small background contamination in the signal regions and has, therefore, good exclusion potential for various supersymmetric scenarios. Especially for the models with small mass differences between the superpartners, denoted as compressed scenarios, this analysis is particularly sensitive. The analysis presented is a resumption of an earlier search performed by the ATLAS experiment during Run I [4]. This search was conducted using the full $\sqrt{s} = 8$ TeV proton-proton collision data collected in 2012, corresponding to an integrated luminosity of 20.3 fb^{-1} and set important limits on a big variety of supersymmetric and other new physics scenarios. An improved sensitivity at a higher center-of-mass energy of $\sqrt{s} = 13$ TeV is expected due to the larger cross-sections predicted for the production of supersymmetric particles with larger masses [5]. Furthermore, improved techniques of the object reconstruction and background estimation compared to the Run I

analysis can significantly enhance the scope of the search with respect to the results obtained in the past. The sensitivity to a wide range of simulated new physics models is illustrated by the interpretation of the analysis results in the context of various simulated supersymmetric benchmark processes that can lead to same-sign or three-lepton signatures.

Chapter I is dedicated to the Standard Model of particle physics and summarizes the theoretical framework used to describe all known elementary particles as well as the electromagnetic, the weak, and the strong interactions. Chapter II gives an overview of the most important theories beyond the Standard Model. Although the main focus of this chapter is on supersymmetry, other models and theoretical approaches are briefly discussed. In Chapter III, details about the phenomenology of proton-proton collisions, description of collider conditions and Monte Carlo simulations are given. Chapter IV is dedicated to the Large Hadron Collider at the CERN research facility and the technical design of the ATLAS experiment. An overview of the techniques for object reconstruction and particle identification, as they are currently used in ATLAS is given in Chapter V. A brief review of previous searches for supersymmetry at ATLAS is presented in Chapter VI, with particular emphasis on the Run I results of the same-sign search.

The actual analysis is addressed in Chapter VII and VIII, presenting the search as it was firstly conducted in 2015 with 3.2 fb^{-1} of data [6], as well as the updates and improvements of the analysis during the year 2016. Therefore, new benchmark models are considered, the signal regions are revisited, and new signal regions are introduced in order to facilitate possible interpretations and to cover additional event topologies. Besides this, new methods are developed to provide a more reliable background estimation and to mitigate the contamination of reducible background sources in the signal regions. An intermediate update of the analysis using an integrated luminosity of 13.2 fb^{-1} was performed in the middle of 2016 to benefit from the additional data collected at the early 2016 operation [7]. The most recent results include the full dataset collected during the years 2015 and 2016, corresponding to a total integrated luminosity of 36.1 fb^{-1} [8]. In the absence of any significant deviation from the Standard Model prediction, model-independent, as well as model-dependent limits on different supersymmetric benchmark models have been placed. Chapter IX is dedicated to potential improvements and prospects of the search for the end of Run II. A conclusion regarding the results of the search and the achievements of the analysis within the recent years is drawn in Chapter X. Auxiliary material related to several topics discussed in the main part of the thesis is provided in Appendix A–H. A brief summary of the publications and details about the personal contributions from the author of this thesis can be found in the list of publications.

I. The Standard Model of Particle Physics

The Standard Model of elementary particle physics (SM) is the fundamental theoretical framework, which describes all known elementary particles and their interactions (with the exception of gravitational forces). It also provides the foundation for many research topics in high-energy physics. This theory has been validated with a high degree of precision during the previous decades. The Standard Model was also able to predict the existence of new particles and physics phenomena which have been subsequently discovered by experiments.

This chapter briefly introduces the theoretical structure of the Standard Model. Section I.1 summarizes the content of elementary particles in the SM. The fundamental interactions described by the SM, the electromagnetic force, the concept of electroweak unification, and the strong interaction are discussed in the Sections I.2, I.3, and I.4. In Section I.5, the effect of the running coupling constants in electromagnetic and strong interactions is explained. The electroweak symmetry breaking mechanism (also known as the Higgs mechanism) which is essential to explain particle masses [9, 10], is described in Section I.6. Section I.7 is dedicated to the open questions and limitations of the SM.

I.1. Particle Content of the Standard Model

The particles of the Standard Model are classified into twelve fermions which have half-integer spin quantum numbers, twelve bosons with integer-valued spins, and the scalar Higgs particle[1]. The fermions are further categorized into leptons, interacting via the electromagnetic and the weak force and quarks, which can also participate in strong interactions. The leptons and quarks are sorted into three different "generations", which contain particles with identical quantum numbers but distinct masses. Each of these generations consists of an up-type quark with electric charge $Q = {}^{2}/_{3}\, e$[2], a down-type quark ($Q = -{}^{1}/_{3}\, e$), a charged lepton ($Q = -e$) and an uncharged neutrino associated with the lepton. The leptons are the electrons $e^{\pm}$, muons $\mu^{\pm}$, and taus $\tau^{\pm}$, as well as their corresponding neutrinos. The quarks are called down, up, strange, charm, bottom, and top quark.

The neutrinos are only weakly interacting particles with very small masses with respect to the other SM particles. However, experimental results are indicating that they are not completely massless [12]. The quarks have also a property called color charge, which can be considered as an equivalent to the electric charge in the strong interaction. Due to *color confinement* [13], they are never directly observed as isolated particles and can only occur as colorless bound states, called hadrons. For each of the fermions, there is also a respective antiparticle with conjugated charge quantum number but identical other quantum numbers and the same mass.

The gauge bosons are vector bosons (spin $S = 1$) mediating the fundamental interactions in the Standard Model. The massless photon γ is associated with the electromagnetic interaction. The massive $W^{\pm}$ and Z^{0} bosons are related to the weak interactions. In fact, the electromagnetic force is described together with the weak interaction in a unified electroweak theory (see Section I.3). There are eight types of massless gluons g, mediating the strong force. A particle compatible with the SM Higgs boson was observed for the first time by the ATLAS and CMS experiments in July 2012 [14, 15]. A central role in the LHC physics program is occupied by the measurement of the nature of this particle and none of the recent measurements showed yet a significant contradiction to the properties expected by a SM Higgs boson with a mass of around 125 GeV [16].

[1] Particles with spin $S = 0$ are denoted as scalar particles.

[2] With the elementary electric charge $e = 1.602 \cdot 10^{-19}$ C [11].

A summary of the elementary particles of the SM and their most important properties is presented in Figure I.1. The fundamental interactions described by the SM are listed in Table I.1. The total range of the elementary particle masses goes from <2 eV for the electron neutrino [11] up to ≈ 172 GeV for the top quark [17]. Most of the ordinary matter in the universe consists of the lightest fermions from the first generation, as the heavier particles can decay into them. With the elementary SM particles, it is also possible to predict properties like mass, spin, and charge of non-elementary particles, which has been confirmed by various experiments in the past.

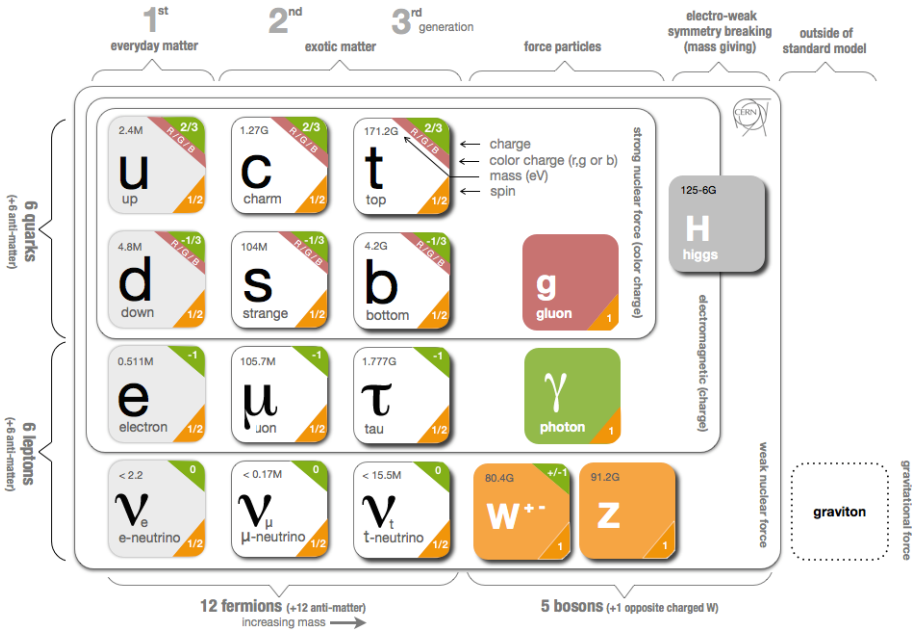

Figure I.1.: Elementary particles of the Standard Model [18].

Interaction	Mediator	Mass [GeV]	Associated charge	Particles affected
Electromagnetism	photons γ	0	electric charge Q	leptons, quarks
Weak force	Z^0, $W^\pm$ bosons	$m_Z = 91.2$, $m_W = 80.4$	weak isospin I_3	leptons, quarks
Strong force	gluons g	0	color charge	quarks

Table I.1.: Fundamental particle interactions described by the Standard Model and their corresponding mediators. The masses of the heavy gauge bosons are provided by the Particle Data Group [11].

I.2. QUANTUM ELECTRODYNAMICS

The theoretical framework of the Standard Model is a quantum field theory (QFT). This formalism uses relativistic quantum fields to represent the observed particles that are known from experiments. Quantum electrodynamics (QED) was developed in the 1940s and is a generalization of Maxwells theory of electromagnetism with a consistent quantum mechanical and relativistic description of charged particles and their interactions with photons.
Equivalent to the formulation in classical mechanics, where the equation of motion can be derived using

the Lagrange function L, the particles follow an equation of motion determined by the Lagrange density $\mathscr{L}$ of a system and the *Euler-Lagrange equation* for fields:

$$L = \int \mathscr{L}\, d^4x, \qquad \frac{\partial \mathscr{L}}{\partial \phi} - \partial_\mu \frac{\partial \mathscr{L}}{\partial(\partial_\mu \phi)} = 0, \tag{I.1}$$

where $\partial_\mu = \frac{\partial}{\partial x^\mu}$ denotes the partial derivatives with respect to the four-vector x^μ and ϕ is a quantum field representing a fermion or boson. The Lagrange density $\mathscr{L}_0$ and the equation of motion for a freely propagating fermion field ψ with spin-1/2 is given by the *Dirac equation*. In natural units ($c = \hbar = 1$[3]) they can be written as follows:

$$\mathscr{L}_0 = \overline{\psi}\,(i\,\gamma^\mu\,\partial_\mu - m)\,\psi, \qquad (i\,\gamma^\mu\,\partial_\mu - m)\,\psi = 0. \tag{I.2}$$

The parameter m denotes the mass term of the particle, ψ is the *Dirac spinor* describing the quantum field of the particle, and γ^μ, $\mu \in [0,3]$ are the gamma matrices which build a set of orthogonal basis vectors for contravariant vectors in a Minkowski space.
The Maxwell equations describing the classical electromagnetism are invariant under transformations of the gauge fields. The Lagrange density shown above is invariant under a global gauge transformation (corresponding to a transformation in the $U(1)$ group). However, performing a local gauge transformation in the context of a spacetime dependent gauge parameter $\varepsilon(x)$, the Lagrange density looses its invariance:

$$\psi(x) \longmapsto \psi(x)\,e^{iq\varepsilon(x)}, \qquad \overline{\psi}(x) \longmapsto \overline{\psi}(x)\,e^{-iq\varepsilon(x)}, \qquad \mathscr{L}_0 \longmapsto \mathscr{L}_0 - \partial_\mu \varepsilon(x)\,(\overline{\psi}\,\gamma^\mu\,\psi). \tag{I.3}$$

Considering this, a modification of $\mathscr{L}(\psi)$ is needed to maintain a gauge invariant description of particle dynamics. Introducing an interaction field between particles is, therefore, a direct consequence of demanding local gauge invariance. If an interaction term with a new vector field A_μ is added to the Lagrange density, one gets:

$$\mathscr{L}(\psi) = \mathscr{L}_0(\psi) - q\,(\overline{\psi}\,\gamma^\mu\,\psi)A_\mu, \tag{I.4}$$

where $\mathscr{L}_0(\psi)$ is the original Lagrange density and q states a coupling constant determining the strength of the interaction. The Lagrange density must also include a kinetic term for the field A_μ, the massless *Proca field*. Its Lagrange density is given by the expression $\mathscr{L}_A$:

$$\mathscr{L}_A = -\frac{1}{4} F^{\mu\nu} F_{\mu\nu}, \qquad F^{\mu\nu} = \partial^\mu A^\nu - \partial^\nu A^\mu. \tag{I.5}$$

The term $F^{\mu\nu}$ is the electromagnetic field tensor of the field A_μ. For massive particles, an additional term $m_A^2 A_\mu A^\mu$ has to be added. Since this term would violate the gauge invariance, m_A has to be set to zero. This requires an interaction term without associated mass parameter. The modified Lagrange density is now locally gauge invariant:

$$\mathscr{L}(\psi) = \overline{\psi}\,\left[\,i\,\gamma^\mu(\partial_\mu - i\,q\,A_\mu) - m\right]\,\psi - \frac{1}{4} F^{\mu\nu} F_{\mu\nu}. \tag{I.6}$$

Thus, a local $U(1)$ gauge invariance implies the existence of interaction particles (mediators). Quantum electrodynamics can be formalized in terms of a $U(1)$ group symmetry and describes the interactions

[3] The parametrization in natural units will be used throughout the rest of this thesis. In SI units, the values are $\hbar = 1.055 \cdot 10^{-34}$ Js and $c = 2.998 \cdot 10^8$ m/s [11].

between charged particles and photons at an elementary level. The interaction term can be accommodated in the definition of the partial derivative to build the covariant derivative $D_\mu = \partial_\mu - iqA_\mu$. Also direct interactions between charged particles are explained by the exchange of virtual photons. QED gives a good description of all electromagnetic phenomena and provides a more generalized characterization of the classical electromagnetism.

I.3. ELECTROWEAK UNIFICATION

The weak interaction was firstly proposed to explain the radioactive $\beta^\pm$ decay as a four-fermion[4] interaction with a coupling strength given by the Fermi constant G_f [19]. Besides phenomena related to radioactivity, this model was also able to explain the muon decay to an electron, a muon neutrino, and an electron antineutrino. Unlike the strong and electromagnetic interactions, the weak interaction violates the parity conservation, as it was confirmed by experiments from Lee, Yang [20] and Wu [21]. Only left-handed[5] particles (and right-handed antiparticles) are sensitive to it. The left- and right-handed chiral states of a fermion field ψ can be computed with the chirality-projection matrix γ^5:

$$\psi_{R,L} = \frac{1}{2}\left(1 \pm \gamma^5\right)\psi, \qquad \gamma^5 = i\sum_{\mu=0}^{3}\gamma^\mu. \tag{I.7}$$

This implies that a more complex coupling structure is required to fully explain the phenomenology of weak interactions.

In the *Yang-Mills theory* [22], the formalism described in Section I.2 is generalized to non-abelian groups. With this prescription it is possible to describe also other gauge theories than the abelian $U(1)$ group for quantum electrodynamics. A transformation under a non-abelian Lie-Group G is performed as: $\psi \longmapsto U\psi$ with $U \in G$. The transformation operator can be expressed as $U = \exp\{ig\,\theta_a T^a\}$, where the terms T^a denote the group generators of U.

As local gauge invariance of the system has to be maintained, a covariant derivative including additional gauge fields is required. The gauge fields are determined by the group generators. For a N-dimensional Lie-Group, the gauge fields and the covariant derivatives can be written as:

$$A_\mu = \sum_{a=1}^{N^2-1} A_\mu^a T^a, \qquad D_\mu = \partial_\mu - ig\sum_{a=1}^{N^2-1} nA_\mu^a, \tag{I.8}$$

with the coupling constant g. The global and local gauge invariant Yang-Mills Lagrange density $\mathscr{L}_{\mathrm{YM}}$ has the form:

$$\mathscr{L}_{\mathrm{YM}}(\psi) = \overline{\psi}\left(i\gamma^\mu D_\mu - m\right)\psi - \frac{1}{4}\,\mathrm{tr}\left\{F^{\mu\nu}F_{\mu\nu}\right\}. \tag{I.9}$$

Accordingly, one obtains a certain number of extra massless gauge fields depending on the number of group generators. The interaction between these extra gauge fields and the Dirac fields is given by the terms $\overline{\psi} D_\mu \psi$. To provide a common description of electromagnetic and weak interactions in this formalism which is compatible with the observation of distinct properties for left- and right-handed fields, a specific structure of the symmetry group is needed.

[4] Also referred to as *Four-Fermi interaction*.

[5] Chirality (handedness) is a symmetry property of particles. A chiral state is a property not identical to its mirror image. For massless particles it is equivalent to the helicity (projection of spin to the direction of momentum).

In the *Glashow-Salam-Weinberg model* (GWS model) [23–25], the observed weak and electromagnetic interactions are described in terms of a single underlying gauge group. This provides a common description of these two forces which were formerly treated as independent phenomena. Two new quantum numbers are assigned to the particles of the SM: the weak isospin $\vec{I}$ (whereby the electroweak coupling depends only on its third component I_3) and the weak hypercharge Y. The left-handed chiral states of quarks and leptons are composed of isospin doublets χ_L with $I_3 = \pm 1/2$, whereas the right-handed chiral states build isospin singlets χ_R with $I_3 = 0$. The gauge group G of the electroweak interaction has the structure:

$$G = SU(2)_L \otimes U(1)_Y, \tag{I.10}$$

with $SU(2)$ representing the special unitary group in two dimensions and $U(1)$ denoting the one-dimensional unitary group. The subscript L refers to the coupling to left-handed fields and Y denotes the hypercharge. The third component of the isospin, the hypercharge, and the electric charge are connected via the *Gell-Mann-Nishijima relation* [26]:

$$Q = I_3 + \frac{1}{2} Y. \tag{I.11}$$

The fermion doublets and singlets in this representation, as well as their corresponding quantum numbers, are summarized in Table I.2. The lepton doublets consist of the left-handed leptons and their associated neutrinos for each generation. The quark doublets consist of the up-like (u, c, t) and the down-like quarks (d', s', b'), with the label $'$ of the down-like quarks indicating that they are not in their mass eigenstates in this representation.

The transformation between the system of mass eigenstates and the eigenstates of the electroweak interaction for up- and down-like quark types can be expressed by the unitary 3×3 matrices U_u and U_d. The transition from the mass eigenstates of the down-like quarks to the doublet partners of the up-type quarks in the electroweak representation is given by their unitary product V_{CKM}, referred to as *Cabibbo-Kobayashi-Maskawa matrix* (CKM matrix) [27, 28]:

$$V_{\mathrm{CKM}} = U_u^\dagger U_d, \qquad \begin{pmatrix} u' \\ c' \\ t' \end{pmatrix} = U_u \begin{pmatrix} u \\ c \\ t \end{pmatrix}, \qquad \begin{pmatrix} d' \\ s' \\ b' \end{pmatrix} = U_d \begin{pmatrix} d \\ s \\ b \end{pmatrix}, \tag{I.12}$$

with its elements describing the mixing of the quark flavors in electroweak interactions. The CKM matrix can be fully defined by four independent observable parameters: three mixing angles and one complex phase. Experimental measurements of these parameters show that the mixing between different flavor types is relatively weak and the diagonal elements of V_{CKM} are between 0.974 and 0.999 [11].

A gauge transformation in the $SU(2)_L \otimes U(1)_Y$ group is given by its generators τ_n and ϕ. The transformation on the isospin singlets and doublets can be written as:

$$\chi_L \longmapsto e^{i\alpha^n \tau_n} e^{i\beta\phi} \chi_L, \qquad \alpha, \beta \in \mathbb{R}, \;\; n \in \{1,2,3\}, \tag{I.13}$$

$$\chi_R \longmapsto e^{i\beta\phi} \chi_R. \tag{I.14}$$

Accordingly, an introduction of four additional vector fields is essential to assure local gauge invariance of the electroweak Lagrange density. The three weak isospin currents couple to a weak isotriplet of vector bosons W_μ^n, $n \in \{1,2,3\}$, whereas the weak hypercharge current couples to an isosinglet B_μ. The fields W_μ^1 and W_μ^2 are electrically charged, while W_μ^3 and B_μ are neutral fields. Since B_μ couples symmetrically

to left- and right-handed particles, a right-handed component in the weak neutral current is expected. The full electroweak Lagrange density $\mathscr{L}_{\mathrm{EW}}$ is given by:

$$\mathscr{L}_{\mathrm{EW}} = \sum_j i\,\overline{\chi}_L^j\,\gamma^\mu\,D_\mu\,\chi_L^j + \sum_k i\,\overline{\chi}_R^k\,\gamma^\mu\,D_\mu\,\chi_R^k - \frac{1}{4}\,W_{\mu\nu}^n W_n^{\mu\nu} - \frac{1}{4}\,B_{\mu\nu}B^{\mu\nu}, \tag{I.15}$$

$$D_\mu = \partial_\mu + i\,\frac{g}{2}\,W_\mu^n\,\tau_n + \frac{g'}{2}\,B_\mu\,\phi, \tag{I.16}$$

with the indices j,k iterating on all left-handed doublets and right-handed singlets of the leptons and quarks in the SM. The parameters g and g' denote the coupling strengths to the weak isotriplet W_μ^n and the isosinglet B_μ, respectively. Their corresponding field strength tensors are given by $B^{\mu\nu}$ and $W_n^{\mu\nu}$. Similar to the situation described in Section I.2, the mass terms of the fields have to be set to zero to ensure local gauge invariance of the system.

Particle type	Doublets/singlets			Q,	I_3,	Y
Leptons	$\begin{pmatrix}\nu_e\\ e\end{pmatrix}_L$	$\begin{pmatrix}\nu_\mu\\ \mu\end{pmatrix}_L$	$\begin{pmatrix}\nu_\tau\\ \tau\end{pmatrix}_L$	± 0,	$+1/2$,	-1
				-1,	$-1/2$,	-1
	e_R	μ_R	τ_R	-1,	0,	-2
Quarks	$\begin{pmatrix}u\\ d'\end{pmatrix}_L$	$\begin{pmatrix}c\\ s'\end{pmatrix}_L$	$\begin{pmatrix}t\\ b'\end{pmatrix}_L$	$+2/3$,	$+1/2$,	$+1/3$
				$-1/3$,	$-1/2$,	$+1/3$
	u_R	c_R	t_R	$+2/3$,	0,	$+4/3$
	d_R	s_R	b_R	$-1/3$,	0,	$-2/3$

Table I.2.: Overview of the singlets and doublets in the SM and their relevant properties for the electroweak interaction: electric charge Q, weak hypercharge Y, and the third component of the weak isospin I_3.

The physical fields corresponding to the observed particles $W^\pm$, Z^0 and γ are given by linear combinations of the original gauge fields specified by the weak mixing angle θ_W, referred to as *Weinberg angle*. The two charged gauge fields are combined to the quantum fields describing the $W^\pm$ bosons, whereas the two neutral fields are combined to a massless field corresponding to the photon and a massive combination corresponding to the Z^0 boson[6]. While the $W^\pm$ bosons can only interact with χ_L (so left-handed particles) the Z^0 bosons and the photons can interact with both left- and right-handed particles:

$$\begin{pmatrix} Z_\mu \\ A_\mu \end{pmatrix} = \begin{pmatrix} \cos\theta_W & -\sin\theta_W \\ \sin\theta_W & \cos\theta_W \end{pmatrix} \times \begin{pmatrix} W_\mu^3 \\ B_\mu \end{pmatrix}, \tag{I.17}$$

$$W_\mu^\pm = \frac{1}{\sqrt{2}}\left(W_\mu^1 \mp i W_\mu^2\right). \tag{I.18}$$

I.4. QUANTUM CHROMODYNAMICS

The description of strong interactions happens in the theoretical framework of quantum chromodynamics (QCD). From deep inelastic scattering experiments, like electron-proton scattering, it is known that the proton is a composite particle of spin-$1/2$ constituents, so-called partons. Also, spectroscopy experiments

[6]The mass terms of the $W^\pm$, Z^0 bosons are included only after the spontaneous symmetry breaking described in Section I.6.

with baryons and mesons led to the hypothesis of a color charge similar to the electric charges but expressed in three dimensions (red, blue, green). According to their color charges, quarks can exist in three different color states.
As the electroweak theory in the GWS model, QCD is a local gauge invariant theory based on the Yang-Mills formalism. The underlying gauge group is the three-dimensional special unitary group $SU(3)$ to take into account the three different color states of particles participating in strong interactions. Therefore, quantum fields representing quarks in the QCD framework ψ_q can be written as color triplets:

$$\psi_q = \begin{pmatrix} \psi_{\text{red}} \\ \psi_{\text{blue}} \\ \psi_{\text{green}} \end{pmatrix}, \qquad \overline{\psi}_q = \left(\overline{\psi}_{\text{red}}, \overline{\psi}_{\text{blue}}, \overline{\psi}_{\text{green}}\right). \tag{I.19}$$

Under a local gauge transformation, a free quark field transforms as:

$$\psi_q \longmapsto e^{i\,\alpha^n\,\lambda_n}\,\psi_q, \qquad \alpha \in \mathbb{R},\ \ n \in \{1,\dots 8\}, \tag{I.20}$$

where λ_n denote the $SU(3)$ group generators, the *Gell-Mann matrices* [29] and α^n reflect local phases. As it is done in QED, a covariant derivative and gauge fields G_μ associated with the group generators can be introduced:

$$D_\mu = \partial_\mu - i\,g_s\,\frac{1}{2}\,\lambda_n\,G^n_\mu. \tag{I.21}$$

The parameter g_s refers to the strong coupling constant. One obtains eight different gauge fields for the $SU(3)$ generators, corresponding to the gauge bosons of the strong interaction, the gluons. Unlike the photons in the electromagnetic interaction, gluons themselves carry the color charge of the strong interaction. Due to the non-abelian group structure of $SU(3)$, the gluon fields have also self-interaction vertices. The complete Lagrange density for quantum chromodynamics including the free quarks fields, the interaction terms, and the gluon fields is:

$$\mathscr{L}_{\text{QCD}} = \sum_q \overline{\psi}_q\,(i\,\gamma^\mu\,D_\mu - m_q)\,\psi_q - \frac{1}{4}\,G^n_{\mu\nu}G^{\mu\nu}_n \tag{I.22}$$

$$= \sum_q \overline{\psi}_q\,(i\,\gamma^\mu\,\partial_\mu - m_q)\,\psi_q - \frac{1}{2}\,g_s\,(\overline{\psi}_q\,\gamma^\mu\,\lambda_n\,\psi_q)\,G^n_\mu - \frac{1}{4}\,G^n_{\mu\nu}G^{\mu\nu}_n. \tag{I.23}$$

The index q iterates on all six quark flavors. The gluon field strength tensors $G^n_{\mu\nu}$ are given by:

$$G^n_{\mu\nu} = \partial_\mu G^n_\nu - \partial_\nu G^n_\mu + g_s\,f^{nkl}\,G^k_\mu G^l_\nu, \tag{I.24}$$

where f^{nkl} denote the so-called structure constants determined by the commutator relations[7] of the Gell-Mann matrices $[\lambda_n, \lambda_k] = i\,f^{nkl}\lambda_l$.
As a consequence of the self-interaction properties of gluons, QCD has a completely different energy-scaling behavior than quantum electrodynamics. In QED, the electromagnetic coupling decreases for lower energies of the scattering process, as the electron charge is screened by vacuum polarization effects (see Section I.5). When two quarks are separated, a "cloud" of gluons is created by the exchange of virtual gluons. The effect of this is an increase of the effective coupling strength between color-charged

[7] The tensor f^{nkl} is completely antisymmetric in its three indices. Each set of matrices fulfilling these commutator relations can be used as generators of the $SU(3)$.

particles at lower energy scales (higher distances)[8]. This has the further consequence that particles with color charge do never occur isolated and appear only in colorless bound states of quarks and gluons, as already mentioned previously (color confinement). Also the opposite effect, referred to as *asymptotic freedom* [30,31] is possible. It describes a decreasing of the strong coupling strength at large energy scales (short distances).

I.5. RUNNING COUPLING CONSTANTS IN QED AND QCD

A common feature of QED and QCD is that the bare coupling constants describe the interaction strength between the particle and the gauge fields only at leading order. The observable interaction strength in an experiment is actually an effective coupling that includes the contribution of an infinite number of virtual loop diagrams.
An example for this phenomenon in QED are vacuum polarization effects (i.e. creation of polarized e^+e^- pairs) modifying the effective electron charge, as it is depicted in Figure I.2. This process is typically denoted as *screening*, as a field of virtual charged particles leads to a variation of the measurable charge of the particle. At short distances (high energies), the vacuum polarization is reduced and the effective charge increases.

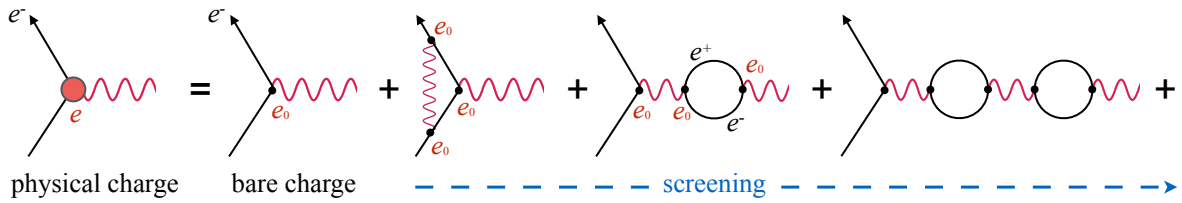

Figure I.2.: The vacuum polarization effect via virtual lepton pairs (screening) which is responsible for the energy dependence of the QED coupling parameter.

A full calculation of all those diagrams via an integration over all possible combinations of energy and momentum causes divergences (appearance of infinities in the calculations) at high-energy scales, denoted as *ultraviolet divergences* [30]. These divergences are typically removed by so-called renormalization methods, referring to several techniques to treat infinities arising in QFT calculations. It can be shown that local gauge invariance and renormalizability of a theory are connected [32]. Divergences can also occur at very small energy values, denoted as *infrared divergences*. Unlike the ultraviolet divergences, they can be removed without requiring the renormalization of a parameter in the theory.
In the case presented here, the bare coupling strength in natural units is given by $\alpha_0 = e_0^2/4\pi$. The effective coupling strength can only be measured at a specific reference energy:

$$\alpha(Q^2) = \frac{\alpha(\mu^2)}{1 - \frac{\alpha(\mu^2)}{3\pi} \ln\left(\frac{Q^2}{\mu^2}\right)}, \tag{I.25}$$

where Q is the transferred momentum, α the coupling constant, and μ^2 is the reference energy for which α is derived, denoted as "renormalization scale". With this prescription, the divergences arising in the calculations are absorbed by the effective coupling parameter. However, a consequence is that the coupling constant depends on the choice of the renormalization scale. This feature is commonly referred to as

[8] Spatial expansion (given by the wavelength λ) and energy (momentum p) of a particle in quantum mechanics are connected by the *de Broglie relation* $\lambda = \hbar/p$.

"running coupling constant". At very low energy scales, it converges to $\alpha(\mu = 0) \approx 1/137$. At the scale of the Z^0 mass ($\approx$91 GeV) it is $\alpha(m_Z) \approx 1/128$ [11].

The energy-scaling behavior of the interaction strength in QCD was mentioned already in Section I.4. Due to the self-interaction properties of gluons, the effective coupling between color-charged particles increases at lower energies. Since this is the opposite effect with respect to QED, it is accordingly called *antiscreening*. The energy dependence of the strong coupling parameter α_s can be written as:

$$\alpha_s(Q^2) = \frac{\alpha_s(\mu^2)}{1 + b_0\, \alpha_s(\mu^2) \ln\left(\frac{Q^2}{\mu^2}\right)}, \qquad b_0 = -\frac{n_f}{6\pi} + \frac{33}{12\pi}. \tag{I.26}$$

The parameter b_0 contains the number of active quark flavors n_f which can participate in the interaction[9]. Consequently, also α_s has to be quoted in terms of a reference energy. A commonly referred benchmark is $\alpha_s(m_Z) \approx 0.1185$ [11]. An additional feature of this energy-scaling behavior is that the hadronization process cannot fully be addressed with the methods of perturbation theory, since it looses its validity at low energies.
A similar behavior as for the strong interaction can be observed also in the weak coupling via $W^\pm$ and Z^0 bosons since they have self-interaction vertices as well.

I.6. THE HIGGS MECHANISM

As it was mentioned already in Section I.2 and I.3, the local gauge invariance of the electroweak Lagrange density can only be maintained if the gauge fields are massless. Unlike the photons and the gluons, the $W^\pm$ and Z^0 bosons are found to be massive. The mechanism used to incorporate massive gauge bosons in the electroweak model while retaining the overall gauge structure of the interaction is called *Brout-Englert-Higgs mechanism*[10] and was firstly proposed in 1964 [9, 10]. It is based on the general idea of spontaneous symmetry breaking, meaning that for a system the ground state is not equivalent to a fully symmetric state. Thus, the system can evolve into a ground state which is not invariant under its full symmetry group. The mechanism introduced in the GWS model to achieve a spontaneous breaking of the $SU(2)_L \otimes U(1)_Y$ group while preserving the gauge invariance of the Lagrange density, is referred to as electroweak symmetry breaking.
The Brout-Englert-Higgs mechanism postulates the existence of an additional weak isospin doublet Φ of complex scalar field with hypercharge $Y = 1$:

$$\Phi = \begin{pmatrix} \phi^+ \\ \phi^0 \end{pmatrix}, \qquad \phi^+, \phi^0 \in \mathbb{C}. \tag{I.27}$$

The Lagrange density $\mathscr{L}_H$ of this field is composed of a kinetic term and a potential V:

$$\mathscr{L}_H = (D_\mu \Phi)^\dagger (D_\mu \Phi) - V(\Phi), \qquad V(\Phi) = -\mu^2 (\Phi^\dagger \Phi) + \frac{1}{4} \lambda (\Phi^\dagger \Phi)^2. \tag{I.28}$$

The potential depends on $(\Phi^\dagger \Phi)$ and the parameters μ and λ . While $\lambda > 0$ is required for vacuum

[9] This is only the case for quarks with $m_q < Q$.
[10] Although developed by Brout, Englert, and Higgs independently, the concept is simply called "Higgs mechanism" in most references.

stability, the choice of μ^2 allows two different scenarios. If $\mu^2 > 0$ the potential has a global minimum for $(\Phi^\dagger \Phi) = 0$. On the other hand, if $\mu^2 < 0$, the ground state of the potential is finite and given by a field configuration of $(\Phi^\dagger \Phi) = 2\mu^2/\lambda$. Thus, the gauge symmetry is broken in the vacuum state. In this scenario, the ground state Φ_0 can be written as:

$$\Phi_0 = \frac{1}{\sqrt{2}} \begin{pmatrix} 0 \\ v \end{pmatrix}, \qquad v = 2\sqrt{\frac{\mu^2}{\lambda}}. \tag{I.29}$$

A schematic view of $V(\Phi)$ in a two-dimensional complex plane and a one-dimensional projection for the case $\lambda > 0$ and $\mu^2 < 0$ is given in Figure I.3. The parameter v is called "vacuum expectation value" and defines the circle with the minimum of the potential.

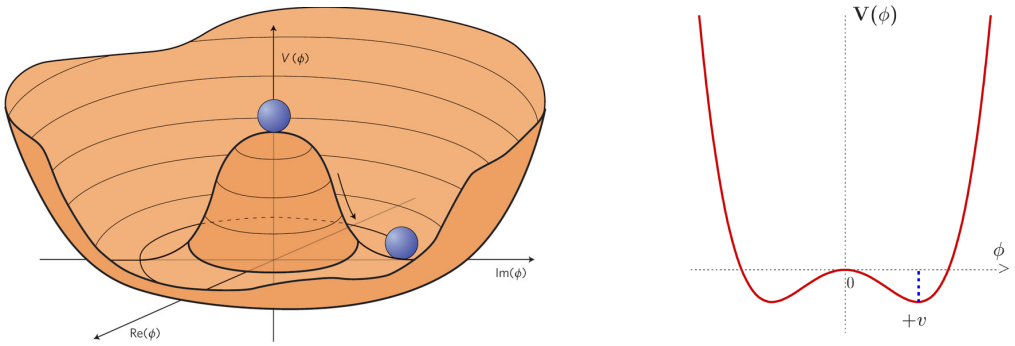

Figure I.3.: Left: Shape of the two-dimensional Higgs potential $V(\Phi)$. Right: One-dimensional projection of the potential for the case $\lambda > 0$ and $\mu^2 < 0$ [33].

With this potential given, there is no single ground state but a continuum of minima in the whole circle with the given radius. The Lagrange density must be formulated in terms of deviations from one of these ground states. This can be done by introducing an excitation, corresponding to small deviations of the field from its ground state:

$$\Phi(x) = \frac{1}{\sqrt{2}} \begin{pmatrix} 0 \\ v + h(x) \end{pmatrix} \exp\{ i\chi(x) \}. \tag{I.30}$$

As there is a continuum of ground states in this potential, an additional degree of freedom is obtained by transforming the system into it, implying the introduction of a new field $\chi(x)$. Spontaneous breaking of a global continuous symmetry always leads to the occurrence of an additional massless scalar field. These fields are called Goldstone bosons according to the *Goldstone theorem*, that connects continuous symmetry breaking with the appearance of scalar fields [34].
A particular choice of the gauge, denoted as "unitary gauge", can be made, so that $\chi = 0$. This is sufficient for the upcoming discussion at tree-level (without including loop diagrams). The Lagrange density of this system can then be written as follows:

$$\mathscr{L}_H = \frac{1}{2}(\partial_\mu h)(\partial^\mu h) + \frac{g}{4}(v+h)^2 W_\mu W^\mu + \frac{g^2}{8\cos^2\theta_W}(v+h)^2 Z_\mu Z^\mu + \frac{\mu^2}{2}(v+h)^2 - \frac{\lambda}{16}(v+h)^4. \tag{I.31}$$

The fields corresponding to the physical $W^\pm$ and Z^0 bosons come from the covariant derivative D_μ in the kinetic term of the newly introduced complex field. Looking at this Lagrange density one can easily see that there are terms like $m_A A_\mu A^\mu$ that represent the mass terms of the gauge fields. Also the additional

scalar field $h(x)$, the Higgs field, acquires a mass term. Apart from couplings to the electroweak gauge fields, the Higgs field has also self-interaction vertices. Expressed in terms of coupling constants, the vacuum expectation value, and the μ parameter of the Higgs potential, the masses of the electroweak and Higgs bosons are given by:

$$m_W = \frac{g\,v}{2}, \qquad m_Z = \frac{m_W}{\cos\theta_W}, \qquad m_H = \sqrt{2}\,\mu. \tag{I.32}$$

Photons and gluons have no mass terms in this model, which is the experimentally observed result. Expressing the Lagrange density in terms of the boson masses and coupling parameters yields:

$$\mathscr{L}_H = \frac{1}{2}(\partial_\mu h)(\partial^\mu h) - \frac{1}{2}m_H^2 h^2 + \frac{1}{2}m_W^2 W_\mu W^\mu + \frac{1}{2}m_Z^2 Z_\mu Z^\mu + g\,m_W\,h W_\mu W^\mu + \frac{g^2}{4}h^2 W_\mu W^\mu \tag{I.33}$$

$$+ g\,\frac{m_Z}{2\cos\theta_W}\,h Z_\mu Z^\mu + g^2\,\frac{1}{4\cos^2\theta_W}\,h^2 Z_\mu Z^\mu - g\,\frac{m_H^2}{4\,m_W}\,h^3 - g^2\,\frac{m_H^2}{32\,m_W^2}\,h^4 + \text{const.} \tag{I.34}$$

Also cubic and quartic interaction terms between the weak vector bosons and the Higgs boson are present. The coupling strength depends on the squared mass of the boson. In addition, cubic and quartic Higgs self-interaction terms appear. This framework allows to quantify all parameters of the GWS model from basic measurements, except for the Higgs boson mass m_H.

The description how fermions acquire mass without violating the electroweak gauge symmetry is achieved by postulating additional terms in the Lagrange density, so-called *Yukawa couplings* [35] which are interaction terms between the left- and right-handed fermions doublets/singlets $\chi_{L,R}$ and the scalar Higgs field Φ. The Lagrange density of the Yukawa interaction terms can be written as follows:

$$\mathscr{L}_{\text{Yukawa}} = \sum_f y_l\,\overline{\chi}_L^l\,\Phi\,\overline{\chi}_R^l - y_u\,\overline{\chi}_L^q\,\Phi^c\,\overline{\chi}_R^u - y_d\,\overline{\chi}_L^q\,\Phi\,\overline{\chi}_R^d + \text{h.c.}, \tag{I.35}$$

where f runs over all quark/lepton generations. The parameters y_l, y_u and y_d are 3×3 matrices and denote the coupling constants of the charged leptons l, the down-type quarks d, and the up-type quarks u. Φ^c is the charge conjugate of the Higgs doublet. The term "h.c." refers to the hermitian conjugate[11] of the full expression.

These terms connect left-handed and right-handed fermions fields, since the Higgs mechanism allows the contraction of the $SU(2)$ indices of the left-handed doublets. The masses of the fermions can be obtained by transforming the fields into mass-bases with unitary gauge and diagonal mass-matrices. The coupling constants of the Yukawa terms are then proportional to the fermion masses:

$$m_f = y_f'\,\frac{v}{\sqrt{2}}. \tag{I.36}$$

Note that the mass-bases, so the bases build by the mass eigenstates of the quark fields, are not the same as the bases build by the eigenstates of the weak interaction. The transformations are given by the unitary matrices U_u and U_d introduced in Section I.3. Due to the connection of left- and right-handed chiral fields, this mechanism cannot be applied for neutrinos which remain therefore massless in this model.

[11] The "h.c." part is required to ensure that the whole expression fulfills the conditions for a hermitian operator: self-adjoint in a complex Hilbert space.

I.7. LIMITATIONS OF THE STANDARD MODEL

The Standard Model provides in most cases a very good description of all known processes in particle physics. Also, the predictions of the SM have so far always been found compatible with the experimental results. However, there are different reasons why the Standard Model cannot be a complete theory of all fundamental processes in the universe. They imply that the current Standard Model is only an effective theory valid at low-energy particle interactions. Thus, the occurrence of new phenomena at high energies is expected. The primary goal of the LHC project is to search for indications for new physics beyond the Standard Model (often denoted as BSM physics). Many theoretical extensions of the SM (e.g. supersymmetric models) have been proposed in the recent decades.
Many of the arguments why the Standard Model is unsuitable for a complete description of all processes in particle physics come from the fact the SM does not provide a sufficient explanation for some experimentally observed phenomena. Furthermore, the incompleteness of the theoretical framework itself in terms of free parameters and consistency with other physical theories indicates the existence of physics beyond the Standard Model. A brief overview of the main problems is given in this section.

I.7.1. UNIFICATION OF FORCES AND DESCRIPTION OF GRAVITY

As described in the previous sections, the current Standard Model is based on a $SU(2)_L \otimes U(1)_Y$ Yang-Mills theory for the electroweak interaction, plus a $SU(3)$ group for quantum chromodynamics. A more general description could potentially incorporate both theories and provide a common description of electroweak and QCD effects. In such a theory, the known interactions are only low-energy approximations of one more fundamental force. In this unification scheme, the three Standard Model coupling constants are derived from one unified coupling and the gauge groups corresponding to the strong and electroweak interactions might be embedded in one unified interaction described by a single, larger symmetry group G_{GUT}. The effective couplings strengths, which are energy dependent in a renormalizable group theory [30], are supposed to unify to a common parameter at large energy scales. A theory satisfying these conditions is called *Grand Unified Theory* (GUT) and is a big challenge in theoretical particle physics:

$$SU(3) \otimes SU(2) \otimes U(1) \subset G_{\mathrm{GUT}}. \tag{I.37}$$

There are several theoretical approaches, such as $SU(5)$ or $SO(10)$-based gauge symmetries [36]. The consequence of such models would be the introduction of additional gauge fields and interaction processes leading to the postulation of new particles. Also, the properties of the known particles would change significantly. Since every proposal of a Grand Unified Theory has to be compatible with previous experimental results, there are no promising GUT candidates yet.

Another crucial topic is the description of gravity within the SM. In the current theory, it is not possible to explain gravitational effects at an elementary level in terms of particle interactions. In the recent decades, the General Theory of Relativity (GTR) has been tested with a high level of precision and is believed to be a very good description of astronomical phenomena. One of the most recent achievements was the direct detection of gravitational waves by the LIGO Collaboration in 2016, which was always a prediction of the GTR [37]. For a fundamental description of the GRT at particle-level, a new hypothetical particle, the *graviton*, needs to be introduced. However, unlike as for the strong and electroweak interactions of the Standard Model, there is no way of consistently describing all effects of the GTR in terms of a quantum field theory. There are different theoretical proposals for a quantum field theory of gravity, but most

of them are either not self-consistent or not compatible with observations from high-energy physics or cosmology.

I.7.2. NEUTRINO MASSES AND OSCILLATIONS

The mechanism of electroweak symmetry breaking gives an explanation for non-vanishing fermion and gauge boson masses in the SM. However, this model makes no prediction for neutrino masses. From the observation of neutrino oscillations it is known that the differences between the squares of the masses of differently flavored neutrinos cannot be zero [12].
Neutrino oscillations describe a periodic conversion between the neutrino flavor (electron, muon, or tau neutrinos). Although a neutrino was originally created with a specific flavor, a subsequent measurement can show a different flavor. Accordingly, the flavor eigenstates of the neutrinos cannot be the same as their mass eigenstates. The mass and flavor eigenstates for the three neutrino generations are related via the *Pontecorvo-Maki-Nakagawa-Sakata matrix* (PMNS matrix) [38] containing the oscillation probabilities U_{ij} between the neutrino flavors. These probabilities are proportional to the differences of the mass squares of the neutrino types:

$$\begin{pmatrix} \nu_e \\ \nu_\mu \\ \nu_\tau \end{pmatrix} = U_{\text{PMNS}} \begin{pmatrix} \nu_1 \\ \nu_2 \\ \nu_3 \end{pmatrix}, \qquad U_{\text{PMNS}} = \begin{pmatrix} U_{e1} & U_{e2} & U_{e3} \\ U_{\mu 1} & U_{\mu 2} & U_{\mu 3} \\ U_{\tau 1} & U_{\tau 2} & U_{\tau 3} \end{pmatrix}, \tag{I.38}$$

with ν_ℓ, $\ell \in \{e, \mu, \tau\}$ representing the flavor and ν_i, $i \in \{1,2,3\}$ defining the mass eigenstates of the three neutrino generations. Similar to the CKM matrix described in Section I.3, the PMNS matrix can be fully defined with four free parameters from which all physically observable properties of the matrix can be determined. Since the oscillations have been observed and the probabilities were measured by different experiments in the past, there are estimations about the mass differences between the neutrino generations. This strongly implies that at least two of the three neutrino types need to have masses.
Furthermore, upper limits on neutrino masses can be set by examining the spectra of $\beta^\pm$ decays for specific isotopes [11]. However, precise measurement of neutrino masses has not been achieved yet and is an important enterprise in modern experimental physics, as it would provide meaningful indications on how physics beyond the Standard Model might look like. It could also clarify in which way neutrinos can contribute to the dark matter fraction in the universe.

I.7.3. MATTER-ANTIMATTER ASYMMETRY AND STRONG CP PROBLEM

The existence of antiparticles is a direct consequence of the Dirac equation, since the antifermion fields build an equivalent solution for it. Consequently, the Standard Model predicts antiparticles that possess (except from their electrical charges) the same properties as their associated particles. Indeed, results from previous experiments yield an almost identical behavior of ordinary particles and their respective antimatter particles. Assuming an equal amount of matter and antimatter produced directly after the Big Bang, it is actually a surprising fact that our universe is dominated by usual matter whereas there is almost no detectable antimatter in the universe.
Many approaches trying to explain why the universe is dominated by usual matter assume a violation of the CP-symmetry, which would lead to minor differences in the behavior of matter and antimatter. The CP-symmetry (charge-conjugation-parity-symmetry) is the combination of C-symmetry (charge-conjugation-symmetry) and P-symmetry (parity-symmetry). Since a combination with the T-symmetry

(time-reversal-symmetry) has to be invariant for all physical systems according to the CPT-Theorem[12], a CP-violation implies a different behavior of particle-antiparticle processes in the *Feynman-Stueckelberg interpretation* of antiparticles as the corresponding particles traveling backwards in time. A violation of this term has been demonstrated already in the experiments by Cronin and Fitch in 1963 where CP-violating decays of neutral kaons to pions could be observed [39]. Also in b-meson systems, CP-violation has been observed by the BABAR and Belle experiments [40, 41]. It is possible to accommodate a CP-violating term in the SM by introducing complex phases in the CKM or PMNS matrix, leading to distinct production rates for the same process before and after a CP transformation. However, such a term cannot be sufficient to explain the complete matter-antimatter imbalance in the universe.

CP-violation is in principle also possible in quantum chromodynamics. Assuming generic CP-violating terms, the QCD Lagrange density can be written as:

$$\mathscr{L}_{\text{QCD}} = \mathscr{L}^0_{\text{QCD}} + \mathscr{L}_\theta, \qquad \mathscr{L}_\theta = \theta \frac{g_s^2 n_f}{32\pi^2} G^n_{\mu\nu} \widetilde{G}^{\mu\nu}_n, \tag{I.39}$$

where $\mathscr{L}^0_{\text{QCD}}$ denotes the QCD Lagrange density without CP-violating terms, as discussed in Section I.4 and $\mathscr{L}_\theta$ represents the additional CP-violating term depending on the θ parameter. n_f is the number of quark flavors. The expression $G^n_{\mu\nu}\widetilde{G}^{\mu\nu}_n$ with the dual gluon field strength tensor $\widetilde{G}^n_{\mu\nu} = {}^1\!/_2\,\varepsilon_{\mu\nu\alpha\beta}\,G^{n\alpha\beta}$ is not invariant under a CP transformation. However, there are no experimental indications of any CP-violation in strong processes. Upper limits on the electric dipole moment of the neutron strongly imply that there is no (or only an extremely small) CP-violation in QCD, corresponding to a very small value of θ. On the other hand, there is no theoretical argument why CP should be conserved in QCD only. This issue is commonly referred to as *strong CP problem*.
A possible solution for this is the postulation of new dynamic fields that cancel the θ parameter in the Lagrange density. As a consequence, new particles, so-called axions, have to be introduced [42]. The search for axions is another important topic in many high-energy physics experiments, since they can provide also a possible candidate for dark matter if they lie in a specific mass range.

I.7.4. DARK MATTER AND DARK ENERGY

Since the early 1930 years, there have been indications that the mass of the visible matter in the galaxy is not large enough to explain all experimentally observed gravitational effects [43].
The rotational speed of stars around the galactic center is much higher than it would be expected by applying the normal laws of gravity[13], as shown schematically in Figure I.4 (left). With the velocities observed, the stars in the galaxies would drift apart and could not stick together as galaxy cluster. Thus, it is assumed that the mass keeping the stars in orbit due to its gravity was miscalculated and the total mass in a galaxy is way larger than the visible mass from the stars. Also in other cases of astronomical observations, like in systems of two colliding clusters of galaxies, so-called *Bullet Clusters*, the problem of some missing, non-detectable matter has been found. Figure I.4 (right) shows the distribution of the visible and invisible mass in such a cluster. This phenomenon is commonly called *dark matter* because it does not belong to the ordinary types of matter which emit light and can, therefore, be observed by telescopes or detectors. A related problem occurs also in the observation of the expansion rate of the universe

[12] The CPT-Theorem states that any Lorentz invariant local quantum field theory with a hermitian Hamilton function must fulfill CPT-symmetry.
[13] According to Newtons gravitational law, an evolution as $v \propto 1/\sqrt{r}$ is expected.

which has found to be an accelerating expansion, so the receding velocity continuously increases with time. Experiments using type-Ia supernovae as standard candles to measure the acceleration confirmed this hypothesis [44]. This acceleration causes a stronger expansion of the universe than predicted by established cosmological theories and seems to be induced by a non-detectable energy. Analogously to dark matter, this energy is called *dark energy*. Latest experimental results indicate that the total mass-energy of the universe amounts to 4.9% of ordinary matter, 26.8% of dark matter, and 68.3% of dark energy [45]. Exploring the nature and origin of dark matter and dark energy is currently one of the biggest, but also one of the most challenging problems in modern physics.

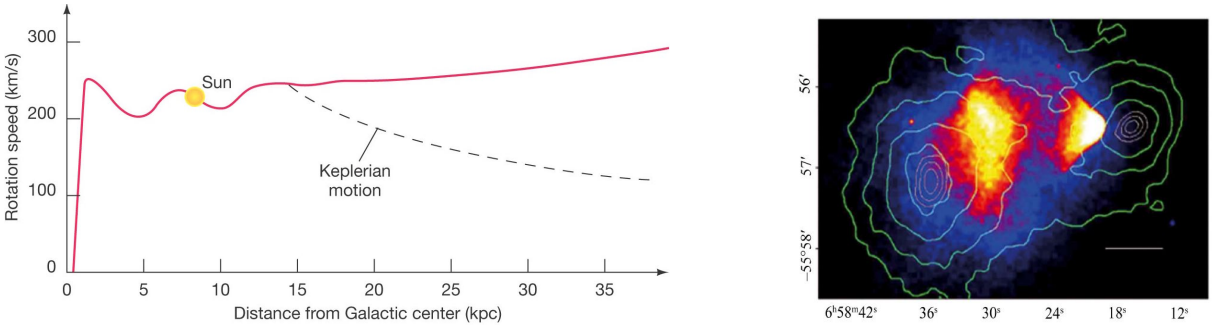

Figure I.4.: Left: Rotational speed of stars versus their distance from the galactic center as it is observed and expected from classical gravitational laws. Right: Visible and invisible mass distribution in Bullet Cluster. The invisible mass distribution is indicated by the green lines [46].

Although some theoretical approaches try to explain the observed discrepancies using modifications of the standard Newtonian gravitational laws or the General Theory of Relativity, most explanations assume that the dark matter/energy is caused by an unknown particle which cannot be detected by astronomical instruments. Therefore, the dark matter/energy problem affects also particle physics research fields and motivates numerous BSM searches at the Large Hadron Collider.

II. Supersymmetry and other Theories Beyond the Standard Model

Undoubtedly, the Standard Model of particle physics is one of the most successful theories in modern science, validated with a high degree of precision during the last decades. However, the problems and unresolved questions of the current Standard Model presented at the end of the previous chapter imply that new physics beyond the SM is required to address these issues.
This chapter gives an overview of possible ways to extend the Standard Model and to provide answers to some of the open problems of the SM. The emphasis of this chapter is on the concept of supersymmetry which is explained in Section II.1. Alternative models and theoretical approaches are briefly addressed in Section II.2.

II.1. Supersymmetry

II.1.1. Introduction to Supersymmetry

The concept of supersymmetry (SUSY) has been firstly introduced by several independent publications in the early 1970s [47–52], presenting a first example of an interacting quantum field theory in four dimensions including supersymmetry. SUSY is a postulated spacetime symmetry and an extension of the Standard Model that connects fermions and bosons with their corresponding superpartners, an associated boson to each fermion and a fermion to each boson. Every theory that fulfills this condition can be called supersymmetric.
The major difference between a supersymmetric theory and the SM as quantum field theory is that fermions and bosons are grouped in the same so-called supermultiplets, combining their spin and internal degrees of freedom. In the SM, fermions and bosons are strictly separated. This formulation is possible because supersymmetry can be expressed as Lie-superalgebra[1] and the supermultiplets are defined in terms of superfields embedded in a superspace[2]. An important condition in QFT is the *Coleman-Mandula theorem* [53] which states that spacetime (mass, momentum, spin) and internal symmetries (quantum numbers associated with the gauge symmetries like electric charge, color, weak isospin) cannot be combined. However, supersymmetry, which involves transformations changing bosons into fermions represents a class of symmetries which is excepted from the conditions set by the Coleman-Mandula theorem [54]. This makes SUSY a unique possible extension of the known spacetime symmetries.
Besides the rich phenomenology which makes supersymmetric models to useful benchmarks for many experimental searches, there are several theoretical aspects why SUSY is one of the most favored candidates for physics beyond the Standard Model. An important characteristic of SUSY is that it provides a convenient solution for a problem in the SM, denoted as *hierarchy problem* [55]. In general, this refers to the large discrepancy between the scales of the electroweak force and the gravity. It arises especially in the stabilization of the Higgs mass, which determines the electroweak scale. The full mass calculation is affected by virtual fermionic interactions with the Higgs field, leading to quadratically divergent quantum corrections to the mass term. Therefore, the stabilization of the Higgs mass requires a big so-called "fine-tuning" (cancellations between the large contributions of the high-order corrections compared to the

[1] A Lie-superalgebra is a $\mathbb{Z}_2$-graded algebra with a decomposition into "even" and "odd" parts including a multiplication operator that respects the grading.
[2] A superspace is an extension of the normal spacetime including also anti-commuting dimensions in addition to the ordinary spacetime dimensions.

relatively small value of the Higgs mass). By adding the contributions from virtual SUSY particles, this problem is solved in a natural way, since the corrections from SUSY particles contribute in an opposite sign than the SM corrections. A simplified view of this effect with a top quark loop[3] is depicted in Figure II.1. Since the masses of the superpartners are obviously not the same as the masses of their SM counterparts (otherwise these particles would have already been observed), it cannot be an exact cancellation of the contributions. However, they can be reduced to logarithmic divergent corrections.

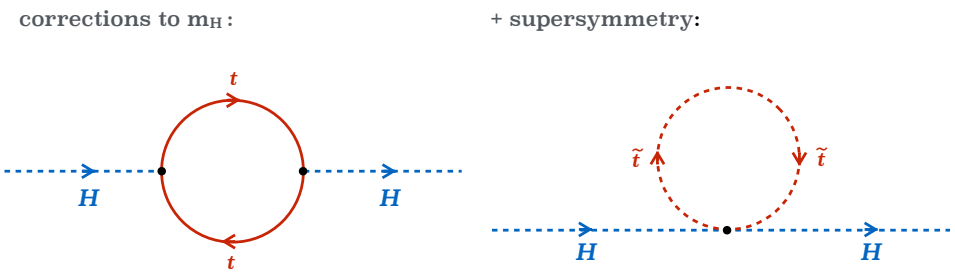

Figure II.1.: Cancellation of the Higgs boson mass renormalization between a fermionic top quark loop (left) and the contribution from the scalar superpartner $\tilde{t}$ of the top (right).

Another advantage is a possible unification of the electromagnetic, weak, and strong coupling constants at large energy scales, since the running of the couplings is affected by the contribution of the supersymmetric particles [56]. A schematic view how the introduction of supersymmetry would change the energy dependencies of the coupling strengths with respect to the SM is given in Figure II.2. In the SM, the three lines showing the inverse values of the coupling parameters for the electromagnetic α_1, the weak α_2, and the strong force α_3, do not meet at one point. With the introduction of SUSY (in this example for the minimal supersymmetric extension of the SM) and assuming the masses of the superpartners to be larger than 1 TeV, the effective couplings can be modified to make them converge at high energy scales.

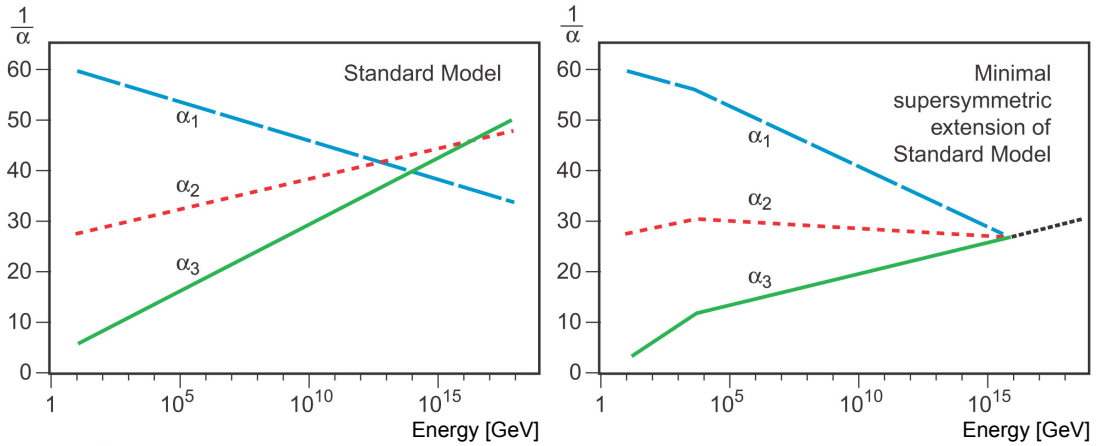

Figure II.2.: Energy dependent evolution of the inverse coupling constants α_1, α_2, α_3 for the three forces in the SM (left) and with the introduction of supersymmetry (right) [57].

Also for the dark matter problem raised in the last chapter, some supersymmetric scenarios can provide a potential solution. In order to be consistent with experimental observations, especially with the

[3] Since the coupling of the Higgs field is proportional to the fermion masses, the contribution from top quark loops is dominant compared to other fermions.

conservation of lepton- and baryon-numbers and the non-observed proton decay, processes producing an uneven number of supersymmetric particles can be suppressed by introducing a new, multiplicative quantum number and postulate its invariance. It is called the *R-parity* P_R and is defined as:

$$P_R = (-1)^{3B+L+2S}, \tag{II.1}$$

where B is the baryon-number, L is the lepton-number, and S is the spin quantum number. All Standard Model particles have $P_R = +1$, while supersymmetric particles have $P_R = -1$. Invariance of the R-parity implies that SUSY particles are always produced in pairs and the lightest supersymmetric particle (LSP) is stable, neutral, and only weakly interacting with ordinary matter. Therefore, the LSP can be a suitable candidate for dark matter and supersymmetric models with conserved R-parity (referred to as RPC SUSY) are attractive scenarios also considering aspects of cosmology. Furthermore, assuming R-parity conservation, a large amount of missing transverse energy in a collider experiment is expected from the LSP escaping the detector volume undetected. Since a large amount of missing energy is a typical event signature in many SUSY searches, RPC SUSY is a more common presumption among the supersymmetric scenarios investigated.

II.1.2. THE SUPERSYMMETRIC ALGEBRA AND SUPERMULTIPLETS

The most simple version of a supersymmetric extension of the Standard Model can be formulated by introducing the Weyl spinor[4] operators Q_α, $Q_\alpha^\dagger$ as generators of the supersymmetry transformations:

$$Q_\alpha \,|\psi_{\text{boson}}\rangle = |\psi_{\text{fermion}}\rangle, \qquad Q_\alpha^\dagger \,|\psi_{\text{fermion}}\rangle = |\psi_{\text{boson}}\rangle. \tag{II.2}$$

The index $\alpha \in \{1,2\}$ denotes the spinor components of the fields. The operators should fulfill the conditions given by the so-called *super-Poincaré algebra*, an extension of the normal Poincaré algebra to incorporate the relation between the bosons and fermion fields. It is given by the general definition of a Poincaré algebra plus the following commutation and anti-commutation relations:

$$\left[Q_\alpha, P_\mu\right] = \left[Q_\alpha^\dagger, P_\mu\right] = 0, \qquad \{Q_\alpha, Q_{\dot\beta}^\dagger\} = 2\,\sigma^\mu_{\alpha\dot\beta} P_\mu, \tag{II.3}$$

$$\{Q_\alpha, Q_{\dot\beta}\} = \{Q_\alpha^\dagger, Q_{\dot\beta}^\dagger\} = 0, \qquad [M^{\mu\nu}, Q_\alpha] = -i\,(\sigma^{\mu\nu})_\alpha^\beta\, Q_\beta. \tag{II.4}$$

The matrices σ^μ are the Pauli matrices. The objects P_μ and $M^{\mu\nu}$ represent the four-momentum operator and the generator of Lorentz transformations, respectively. The $\dot\beta$ index transforms according to the inequivalent conjugate spinor representation. The operator Q increases the spin quantum number of a field by $1/2$, while $Q^\dagger$ lowers it by $1/2$. This is the only non-trivial extension of the Poincaré algebra in a renormalizable quantum field theory with massive particles [54].

In a supersymmetric theory, the particles and their superpartners are grouped in supermultiplets which are represented by superfields in superspace. Two types of supermultiplets are necessary to formulate a supersymmetric extension of the SM:

- *Chiral-supermultiplets* consist of a complex scalar field and a Weyl spinor. The Standard Model fermions are grouped to chiral-supermultiplets with their scalar superpartners (sleptons, squarks). Scalar Higgs bosons build chiral-supermultiplets with their spin-$1/2$ superpartners (Higgsinos).

[4] A Weyl spinor is a simpler version of a Dirac spinor not composed of a left- and right-handed part.

- *Vector-supermultiplets* are formed by a vector field and a Weyl spinor. The Standard Model gauge bosons belong to vector-supermultiplets with their fermionic superpartners (gauginos).

In the SM, left- and right-handed fermions transform differently under the gauge transformation. Only chiral-supermultiplets can contain fermions whose left-handed components transform differently from their right-handed partners under a gauge group. Therefore, all fundamental particles in a supersymmetric extension of the SM must be either in a vector- or a chiral-supermultiplet.

II.1.3. THE MINIMAL SUPERSYMMETRIC STANDARD MODEL

The so-called Minimal Supersymmetric Standard Model (MSSM) is the most simple extension to the Standard Model that realizes supersymmetry. It has been firstly proposed to provide a natural solution for the hierarchy problem and predicted superpartners in the mass range of 100 GeV up to 1 TeV [55].
In the MSSM, the SM fermions and antifermions are assigned to chiral-supermultiplet and the SM gauge fields are assigned to the vector-supermultiplets. The supermultiplets contain always the SM particles and their superpartners. The gauge symmetries remain unchanged with respect to the Standard Model, namely a $U(1)_Y \otimes SU(2)_L \otimes SU(3)_C$ symmetry. Therefore, the gauge interactions of the MSSM are already adapted to the SM. However, since a single Higgsino would lead to gauge anomalies, an additional Higgs doublet has to be introduced:

$$H_u = \begin{pmatrix} H_u^+ \\ H_u^0 \end{pmatrix}, \qquad H_d = \begin{pmatrix} H_d^0 \\ H_d^- \end{pmatrix}. \tag{II.5}$$

The chiral-superfields are grouped in left-handed quark doublets, right-handed antiquark singlets for up-like and down-like quark types, left-handed lepton doublets, right-handed antilepton singlets, as well as two Higgs doublets. The vector-superfields correspond to the SM gauge fields for the electroweak (weak isospin, hypercharge) and strong (color) interactions. The superfields of the MSSM and their most important properties are summarized in Table II.1.

Chiral/vector-superfield		Type	Multiplicity	$P_{\mathbb{Z}_2}$	$(SU(3), SU(2)_L)$	Y
Left-handed quarks	Q	doublet	3	$-$	$(3, 2)$	$1/3$
Right-handed u-type antiquarks	U^c	singlet	3	$-$	$(3, 1)$	$-4/3$
Right-handed d-type antiquarks	D^c	singlet	3	$-$	$(3, 1)$	$2/3$
Left-handed leptons	L	doublet	3	$-$	$(1, 2)$	-1
Right-handed antileptons	E^c	singlet	3	$-$	$(1, 1)$	$+2$
Higgs	H_u	doublet	3	$+$	$(1, 2)$	$+1$
Higgs	H_d	doublet	3	$+$	$(1, 2)$	-1
Hypercharge	V^Y					
Weak-isospin	V^W					
Color	V_g^a					

Table II.1.: Chiral- and vector-superfield content of the MSSM. Properties of the fields like their multiplicity, $\mathbb{Z}_2$-parity, weak hypercharge Y, and representation in $SU(3) \otimes SU(2)_L$ are also stated.

A useful parametrization for the interactions of the superfields is the *superpotential* W [58], which is a

holomorphic[5] function only depending on the chiral-superfields. The superpotential of the MSSM can be written as:

$$W_{\text{MSSM}} = y_u U^c Q H_u - y_d D^c Q H_d - y_e E^c L H_d - \mu H_u H_d, \tag{II.6}$$

where y_u, y_d and y_e are dimensionless 3×3 matrices, corresponding to Yukawa coupling parameters. The μ term quantifies the Higgsino mass, similarly to the Higgs mass in the Standard Model. Note that the superpotential quoted here implies already an invariance of the R-parity, as explained in Section II.1.1. This is phenomenologically motivated, to incorporate that neither a violation of the lepton- nor the baryon-number have been experimentally observed yet. There are additional terms that could be added to the superpotential which are gauge and Lorentz invariant but lead to a violation of those numbers:

$$W_{\Delta L=1} = \frac{1}{2}\lambda^{ijk} L_i L_j L_k E^c_k + \lambda'^{ijk} L_i Q_j L_k D^c_k + \mu'^i L_i H_u, \qquad i,j,k \in \{1,2,3\}, \tag{II.7}$$

$$W_{\Delta B=1} = \frac{1}{2}\lambda''^{ijk} U^c_i D^c_j D^c_k. \tag{II.8}$$

In an R-parity preserving version of the MSSM, the coefficients violating the lepton-number λ, λ', μ' and the baryon-number λ'' are accordingly zero. In scenarios that allow a violation of P_R (denoted as RPV SUSY), these terms contribute to the superpotential. However, this entails significant phenomenological changes of the models, as no stable LSP is present producing a large amount of missing energy in a collider experiment. While the analysis described in this thesis was originally designed to investigate RPC scenarios, both classes of SUSY models were explored in later versions of the search.
As it is the case in the SM, the gauge eigenstates of the fields are not necessarily equivalent to their mass eigenstates. The Higgs doublets mix to two charged Higgs particles $H^\pm$, two neutral scalar Higgs particles h^0, H^0 and a pseudo-scalar particle A^0. The charge-neutral Higgsinos and gauginos (also denoted as binos and winos) mix to four neutralinos ($\widetilde{\chi}^0_i$ with $i \in \{1,2,3,4\}$). Accordingly, the charged Higgsinos and winos mix into two charginos $\widetilde{\chi}^\pm_1$, $\widetilde{\chi}^\pm_2$. The mixing of the left- and right-handed gauge eigenstates for the squarks and sleptons is neglected in this model. An exception are the third-generation fermions, where the left- and right-handed components mix to the mass eigenstates $\widetilde{t}_{1,2}$, $\widetilde{b}_{1,2}$ for top, bottom squarks and $\widetilde{\tau}_1$, $\widetilde{\tau}_2$, $\widetilde{\nu}_\tau$ for tau slepton, tau sneutrino. Like in the SM, the superpartner of the gluon, the gluino $\widetilde{g}$, does not mix with the other gauginos. The superpartners of the Standard Model particles in the MSSM are summarized in Table II.2. This table includes also the gravitino, the supersymmetric version of the graviton.

II.1.4. SUPERSYMMETRY BREAKING

If supersymmetry was a feature of the underlying laws of nature, the Standard Model particles and their superpartners would have identical masses obtained by the supersymmetric version of the Higgs mechanism. Since various experiments in the past showed that there are no such particles in these mass ranges, a realistic phenomenological model has to contain a supersymmetry breaking mechanism.
The most simple approach to construct a model with such a mechanism is to add soft-breaking terms to the effective Lagrange density so that the squarks, sleptons, and the gauginos acquire higher masses than their SM counterparts:

$$\mathscr{L} = \mathscr{L}_{\text{SUSY}} + \mathscr{L}_{\text{soft}}. \tag{II.9}$$

[5] Unlike a classical potential, W can also be complex valued. The holomorphy-condition means that the superpotential depends only on the chiral-superfields, not their complex conjugates.

Particles	Spin	P_R	Gauge eigenstates	Mass eigenstates
Higgs bosons	0	$+1$	$H_u^0 \;\; H_d^0 \;\; H_u^+ \;\; H_d^-$	$h^0 \;\; H^0 \;\; A^0 \;\; H^\pm$
Squarks	0	-1	$\widetilde{u}_L \;\; \widetilde{u}_R \;\; \widetilde{d}_L \;\; \widetilde{d}_R$ $\widetilde{s}_L \;\; \widetilde{s}_R \;\; \widetilde{c}_L \;\; \widetilde{c}_R$ $\widetilde{t}_L \;\; \widetilde{t}_R \;\; \widetilde{b}_L \;\; \widetilde{b}_R$	(same) (same) $\widetilde{t}_1 \;\; \widetilde{t}_2 \;\; \widetilde{b}_1 \;\; \widetilde{b}_2$
Sleptons	0	-1	$\widetilde{e}_L \;\; \widetilde{e}_R \;\; \widetilde{\nu}_e$ $\widetilde{\mu}_L \;\; \widetilde{\mu}_R \;\; \widetilde{\nu}_\mu$ $\widetilde{\tau}_L \;\; \widetilde{\tau}_R \;\; \widetilde{\nu}_\tau$	(same) (same) $\widetilde{\tau}_1 \;\; \widetilde{\tau}_2 \;\; \widetilde{\nu}_\tau$
Neutralinos	$1/2$	-1	$\widetilde{B}^0 \;\; \widetilde{W}^0 \;\; \widetilde{H}_u^0 \;\; \widetilde{H}_d^0$	$\widetilde{\chi}_1^0 \;\; \widetilde{\chi}_2^0 \;\; \widetilde{\chi}_3^0 \;\; \widetilde{\chi}_4^0$
Charginos	$1/2$	-1	$\widetilde{W}^\pm \;\; \widetilde{H}_u^+ \;\; \widetilde{H}_d^-$	$\widetilde{\chi}_1^\pm \;\; \widetilde{\chi}_2^\pm$
Gluinos	$1/2$	-1	$\widetilde{g}$	(same)
Gravitino	$3/2$	-1	$\widetilde{G}$	(same)

Table II.2.: Summary of SUSY particles predicted by the MSSM.

In this context, "soft" means SUSY breaking terms which maintain the cancellation of the divergences of the Higgs boson mass. As for the electroweak symmetry breaking in the SM, the Lagrange density is supposed to be invariant under a supersymmetric transformation but its vacuum state is not. Accordingly, additional degrees of freedom have to be introduced to generate the supersymmetry breaking. Similar to the Higgs sector in the SM, there has to be a "hidden" sector in which the breaking happens and some interactions to transmit the breaking to the visible sector. Several phenomenological approaches can be used to induce this kind of symmetry breaking, such as breaking via a massive gravitino [59], gauge-mediated SUSY breaking (GMSB) [60], or breaking via anomalous $U(1)$ groups [61].
The expression $\mathscr{L}_{\text{soft}}$ includes many new terms, like scalar mass terms, trilinear scalar interactions, or gaugino mass terms. In the MSSM, 111 parameters have to be added which can be reduced to 105 independent parameters by re-defining some of the fields [58]. If the largest mass scale associated with the soft terms is m_{soft}, the corrections to the Higgs mass can be written as follows:

$$\Delta m_H^2 = m_{\text{soft}}^2 \left[\frac{\lambda}{16\pi^2} \ln\left(\frac{\Lambda}{m_{\text{soft}}} \right) + \dots \right]. \tag{II.10}$$

The parameter Λ denotes the SUSY breaking scale. Since the mass differences between the known SM particles and their superpartners would be determined by m_{soft}, the masses of the lightest SUSY particles cannot be too large, otherwise the hierarchy problem returns. This assumption gives an upper bound of $\mathscr{O}$(TeV) on the expected masses for SUSY particles.

II.1.5. A NATURAL SUSY PARTICLE SPECTRUM

As explained in the previous section, the introduction of supersymmetry does not automatically solve the hierarchy problem since the corrections of the Higgs mass depend on the mass scale of the SUSY particles. Models with a very high SUSY mass spectrum are in principle possible, but they require again a

high level of fine-tuning[6] to stabilize the mass scale of the electroweak symmetry breaking. Scenarios, where SUSY provides a solution of the hierarchy problem are commonly referred to as "natural" SUSY. The measured Higgs mass of around 125 GeV set strong constraints on many supersymmetric scenarios and is actually not preferred in the MSSM, since large radiative corrections, mainly coming from top and top squark loops are necessary to fix the Higgs mass to this value [62]. However, it can be accommodated in the MSSM by modifying the mixing of the left- and right-handed gauge eigenstates of the top squark. The observed Higgs is then typically considered to be the lightest neutral Higgs mass eigenstate predicted by the MSSM, indicated as h^0 in Table II.2. Furthermore, in most supersymmetric models with conserved R-parity, the LSP, is assumed to be the lightest neutralino $\widetilde{\chi}_1^0$.
Since the mixing of the gauge eigenstates of the sleptons and squarks depends in general on the masses of their SM counterparts, it is expected to be significant only for the third generation. Especially for the top squark, a significant mixing of the left- and right-handed gauge eigenstates can occur and induce a large mass splitting between the two mass eigenstates $\widetilde{t}_1$ and $\widetilde{t}_2$. Accordingly, $\widetilde{t}_1$ is supposed to be considerably lighter than the rest of the squarks in most scenarios. Indeed, searches for direct squark production focus primarily on top and bottom squarks. An illustration of the mass scales of different superpartners for a possible SUSY model is presented in Figure II.3. This spectrum respects naturalness with a low amount of fine-tuning. Additionally, the mass of the lightest neutral Higgs field h^0 is supposed to be at around 125 GeV and several other experimental constraints have to be taken into account [63]. The masses of the third-generation squarks/sleptons and the lighter neutralinos are expected to be in the sub-TeV region, whereas the superpartners of the light-flavor quarks are significantly heavier and outside an energy range accessible with the LHC. No strong constraints are set on the mass of the gluino, but it is expected to be heavier than the third-generation squarks and the neutralinos.

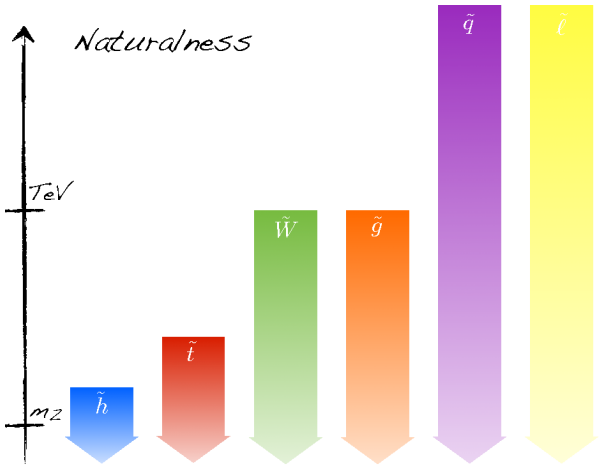

Figure II.3.: Illustration of the mass scales for different superpartners in a natural SUSY model [63].

II.1.6. THE SUPERSYMMETRIC PARAMETER SPACE

EXTENDED SUPERSYMMETRIC MODELS

The MSSM described in the previous sections represents only a subset of possible supersymmetric extensions of the Standard Model. It is constructed assuming only one real spinor representation of the

[6] The acceptable level of fine-tuning, so the size of the correction terms compared to the bare mass is obviously an arbitrary choice. Typically a range of 1–10% is considered as tolerable.

Poincaré group, denoted as $N = 1$ SUSY. Additional superfields can be introduced manually to construct more flexible models, usually referred to as Next-to-Minimal Supersymmetric extension of the Standard Model (NMSSM) [64].
Theories with more than one spinor generator ($N > 1$) are denoted as extended supersymmetry and are allowed according to the *Haag-Lopuszanski-Sohnius theorem* [54]. The super-Poincaré algebra introduced in Section II.1.2 has to be extended by the integers $A, B \in \{1, \dots N\}$:

$$\left\{Q_\alpha^A, Q_\beta^B\right\} = \varepsilon_{\alpha\beta} Z^{AB}, \qquad \left\{Q_\alpha^A, Q_{\dot\beta}^{\dagger B}\right\} = 2\,\sigma^\mu_{\alpha\dot\beta} P_\mu \delta_{AB}. \tag{II.11}$$

The operator Z^{AB} is called "antisymmetric central charge matrix" and commutes with all operators Q_α and P_μ. Models with extended supersymmetry are in general very constrained to find application in realistic scenarios, as they produce a lot of new particles and interactions. However, they show similar dynamics as $N = 1$ SUSY and provide new features, allowing to address problems which are inaccessible in the SM.

CONSTRAINING THE MSSM PARAMETER SPACE

As mentioned above, even the MSSM has more than 100 free parameters, suggesting that the concept of supersymmetry produce at least as many open questions as the Standard Model. However, also the SM has 19 free parameters that need to be determined by experiments. Defining a specific model inside the MSSM that can be probed means making a lot of assumptions about undefined variables and simplifying the model in order to constrain the parameter space.
A constrained version of the MSSM, the pMSSM (phenomenological MSSM) [65], has only 19 free parameters. It can be built by adapting the free parameters to experimental information from various aspects of particle physics, like incorporating constraints from Z^0, $W^\pm$, and Higgs measurements, b-quark physics, astrophysics, as well as limits from dark matter searches. Nevertheless, one still remains with a 19-dimensional parameter space of possible scenarios for which the comparison with experimental data means a comprehensive effort. A further step of simplification is to consider a constrained version of the MSSM (denoted as cMSSM) [66], where the number of independent variables is reduced to five. In an energy region at the GUT scale ($\approx 10^{16}$ GeV), all scalar masses of the MSSM Lagrange density are set to one value m_0, the masses of all gauginos are set to $m_{1/2}$, all trilinear couplings are set to A_0, the ratio of the Higgs doublets is set to $\tan(\beta)$, and the sign of the Higgsino mass parameter is fixed to $\mu = \pm 1$. In such a framework, one specific parameter set of $(m_0, m_{1/2}, A_0, \tan(\beta), \mu)$ defines finally a particular model that can be tested.
Further assumptions, like setting the branching ratio of SUSY decays to 100% or fixing the parameters which are no experimental observables to arbitrary values are also applied in many experimental searches. Consequently, the remaining model is in general not a realistic SUSY scenario anymore. However, these simplified scenarios are nowadays considered rather as benchmark models to point experimentalists to interesting signatures in which physics beyond the SM may hide. A schematic view of the landscape of supersymmetric theories, including different concepts and simplifications like the pMSSM and cMSSM is given in Figure II.4.

II.2. OTHER THEORIES BEYOND THE SM

Besides supersymmetry, there are various other theoretical approaches and ideas how to extend the Standard Model in order to address its primary problems. Due to their high number and their complexity, it is not possible to describe all of them in detail here. A common property of these models is that they

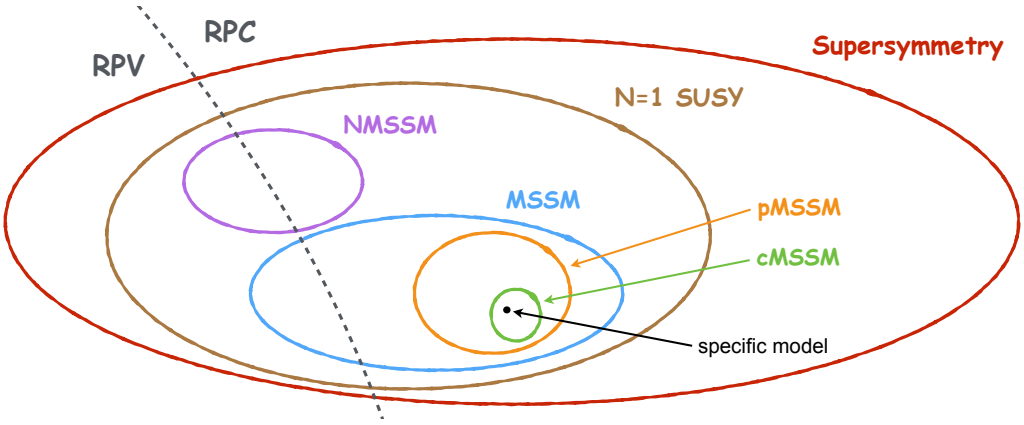

Figure II.4.: Schematic view on the supersymmetry parameter space and associated theories.

usually try to describe the SM as an effective theory only valid for low energies. Therefore, many of these models are adapted phenomenologically to constrain the predictions of the model with respect to the previous results observed in experiments. A brief overview of some of them is given in this section.

II.2.1. Extra Dimensions and String Theory

Many theories about new physics beyond the SM assume the existence of extra dimensions in addition to the four known spacetime dimensions. The ordinary Standard Model, as well as the Special and General Theory of Relativity are formulated using a Minkowski space, a combination of a three-dimensional Euclidean space and the time to a four-dimensional manifold[7]. Thus, if existing, these extra dimensions cannot be visible in most physics phenomena. They must either be very compressed or possess a non-trivial topological structure preventing them from expanding.
One prominent example of this class of theories is the *Kaluza-Klein theory* [67, 68], which was firstly developed already in the 1920s in order to unify classical electromagnetism and gravity in a five-dimensional parameter space with a compactified fourth space dimension. In the 1970s, this concept has been rediscovered for theories trying to provide a common description of quantum physics and the GTR, like loop quantum gravity or string theories. In this formalism, additional dimensions can be added to the field equations if they are compactified, meaning if periodic boundary conditions are assigned to the extra dimensions. For a simple scalar field ϕ, the equation of motion would look like:

$$\left(\partial_n \partial^n + m^2\right) \phi(x^n) = 0, \qquad n \in \{0, \dots N\}. \tag{II.12}$$

The number $N > 3$ indicates the possible number of dimensions. The periodicity-condition for the non-spacetime-like dimensions allows a Fourier-decomposition of the scalar field:

$$\phi(x^n) = \sum_j \phi_j(x^\mu) \exp\left\{-i\frac{2\pi j}{R}\right\}, \qquad \mu \in \{0,1,2,3\}, \tag{II.13}$$

with R describing the expansion radius of the extra dimensions. The equation of motion can be written as:

$$\left(\partial_\mu \partial^\mu + k_j^2 + m^2\right) \phi_j(x^\mu) = 0, \qquad k_j = \frac{j}{R}. \tag{II.14}$$

[7] A Minkowski space $\mathbb{M}$ is isomorphic to $\mathbb{R}^4$ but equipped with a distinct metric to describe the relativistic spacetime.

This implies an additional set of possible massive particles, referred to as Kaluza-Klein particles, which can be interpreted as excitations of the compactified (wrapped) extra dimensions. Some theories predict these excitations to be visible as resonances in invariant mass spectra or other electroweak observables i.e. the forward-backward asymmetry of gauge bosons [69].
Although the original idea can be attributed to the Kaluza-Klein theory, the concept of reducing a higher dimensional theory to four dimensions was re-addressed by many other theoretical approaches in the last decades. An example is the *Randall-Sundrum model* [70], which tries to describe the universe as a five-dimensional anti-de Sitter space[8] and elementary particles as multi-dimensional, compactified objects, so-called "branes".
Another popular approach which was discussed frequently in the last years is string theory. The concept of string theory as a common description of the fundamental elementary forces has been firstly introduced in the 1970s [71, 72]. It describes a class of related models assuming one-dimensional elementary strings as fundamental objects. This is in contrast to established models of quantum field theory, assuming zero-dimensional elementary particles. In this framework, signatures of elementary particles can be seen as vibrational excitation states of these strings. In further developments of the theory, the considered basic objects are not only one-dimensional strings but also higher-dimensional objects. String theory avoids the problems of singularities in the classical quantum field theories and renormalization. These problems arise in particular for point-like particles from their self-interaction terms, which for one-dimensional extended objects are "smeared" and thus mitigated. To include fermions, string theory has to be connected with supersymmetric principles, which is done in so-called *super-string theories* [73]. Since string theory has the potential to address many fundamental problems of the SM, like a theoretical description of gravity at particle-level, it is a popular research field in theoretical particle physics.

II.2.2. TECHNICOLOR AND COMPOSITE HIGGS MODELS

Many theories assume the Higgs boson to be actually a composite object and the Higgs potential the result of pair condensations of fermion-like constituents. In these theories, the electroweak symmetry breaking and a solution for the hierarchy problem can be obtained dynamically from a strongly coupled theory at an energy scale of $\mathcal{O}$(TeV). These models were already proposed in the early 1980s and are usually referred to as *Technicolor theories* (TC) [74].
Technicolor introduces new massless fermion fields, called techniquarks and new gauge bosons, called technigluons. Analogous to the Standard Model, the right-handed components are assigned to electroweak singlets whereas the left-handed components are described by electroweak doublets. The interactions between the techniquarks are similar to the strong interactions but include additional color charges with respect to QCD. The electroweak symmetry breaking is induced by the dynamics of the interactions between left- and right-handed techniquarks. Simple TC models can describe the $W^{\pm}$ and Z^0 boson masses but not the mass terms for quarks and leptons.
More elaborated models accommodate the TC gauge groups and SM gauge groups as subgroups into a superordinate group, which provides also a prediction for the interactions between SM particles and the techniquarks. These types of models are denoted as *extended Technicolor* [75]. The interactions between SM particles and techniquarks can lead to flavor changing neutral currents (FCNC), a process which is highly suppressed in the SM[9]. Also, multi-charged leptons are possible in these models. The interplay

[8] An anti-de Sitter space is a maximally symmetric Lorentzian manifold with constant negative scalar curvature, to describe a spacetime with negative cosmological constant.
[9] While flavor changing charged currents are possible at tree-level in the SM via the exchange of a $W^{\pm}$ boson, FCNC can only occur at higher-orders including loop-diagrams.

between the techniquarks and SM particles changes the effective coupling constants and provides an alternative way to solve the hierarchy problem. Thus, it is an interesting topic for many new physics searches. On the other hand, strong upper limits have been set already on many TC scenarios, as previous experiments measuring the FCNC did not show any significant deviation from the SM prediction.

II.2.3. AXIONS

The concept of axions provides a solution for the strong CP problem described already in Section I.7.3. The existence of axions was firstly postulated in the context of the *Peccei-Quinn theorem* [42], introducing a new spontaneously broken chiral symmetry $U(1)_{PQ}$ which can cancel the θ parameter in the QCD Lagrange density and, therefore, abolish the CP-violating term in the strong interaction. According to the Goldstone theorem, this symmetry breaking induces the appearance of new massive scalar fields, which can be identified as axions.
Since the masses of the axions are not predicted by this model, they can also represent a possible dark matter candidate if their masses are sufficiently large. Thus, many experiments are motivated by axion searches, like the CAST [76] or the ADMX experiment [77]. A generic feature of axions is their interaction with photons. The axion-photon interaction term of the Lagrange density $\mathscr{L}_{a\gamma}$ has the form:

$$\mathscr{L}_{a\gamma} = -\frac{1}{4} g_{a\gamma} F_{\mu\nu} \widetilde{F}^{\mu\nu} \phi_a, \tag{II.15}$$

where ϕ_a denotes the scalar axion field and $g_{a\gamma}$ is the axion-photon coupling parameter. $F_{\mu\nu}$ and $\widetilde{F}^{\mu\nu}$ are the electromagnetic field strength tensor and its dual. As a consequence, photons can be converted to axions in strong electromagnetic fields (and vice versa). Accordingly, the sun could be a potential axion source by transforming thermal photons in the fluctuating electromagnetic field of the stellar plasma[10].
Many of the experimental axion searches rely on the *Primakoff effect*, which describes an interaction of high-energy photons originating from a strong external electromagnetic field with the axions. These are converted to photons via an axion-photon coupling. A simplified diagram of this process is shown in Figure II.5 (left). This approach is used for example at the CAST experiment, where a decommissioned LHC magnet is used as an axion helioscope in order to search for solar axions utilizing the Primakoff effect. Also, many generic dark matter searches can set strong limits on axion masses. So far, no indication for the existence of axions has been found in any of these experiments.

II.2.4. ADDITIONAL PARTICLE GENERATIONS AND EXTENDED GAUGE GROUPS

A Standard Model extension examined frequently is the inclusion of a fourth generation of fermions, i.e. a four-generation Standard Model (SM4) [78] as shown in Figure II.5 (right). This is possible as the number of particle generations is (similar to the conservation of baryon- and lepton-numbers) an empirical fact and the SM can also be formulated with more than the currently known three generations. These models are mostly motivated by cosmological arguments, since the postulated fourth generation particles could be suitable dark matter candidates. Although the number of light neutrino generations can be quantified with a high level of precision using the invisible decay width of the Z^0 boson, this measurement cannot cover the case of neutrinos heavier than $m_\nu > m_Z/2$. However, the most recent measurements of the Higgs boson properties strongly disfavor this class of models [79].

[10] This axion type is usually denoted as "solar axion".

Models which extend the SM by the introduction of superordinate gauge groups often feature additional $U(1)'$ symmetries with corresponding heavy spin-1 bosons. These bosons, generally referred to as Z' and W', would manifest as resonances in leptonic invariant and transverse mass spectra[11]. This class of models is mostly inspired by Grand Unified Theories, as described in Section I.7.1. An example is the Sequential Standard Model (SSM) [80], which is a simplified Standard Model extension where the Z' and W' have the same couplings to fermions as their light SM partners. Also, models like $O(10)$ or E_6 which are based on larger underlying symmetry groups containing the SM gauge groups as subgroups predict additional heavy particles which might be found at collider experiments. Since the number of additional gauge bosons is given by the group generators, models based on these extended symmetries predict many additional gauge fields with respect to the SM. Thus, these models have usually be adapted to phenomenological parameters and accurately harmonized with experimental constraints.
Although these theories are still important topics and motivate a lot of different new physics searches, no indications for these particles have has been found so far and many models are nowadays strongly constrained by various experimental results.

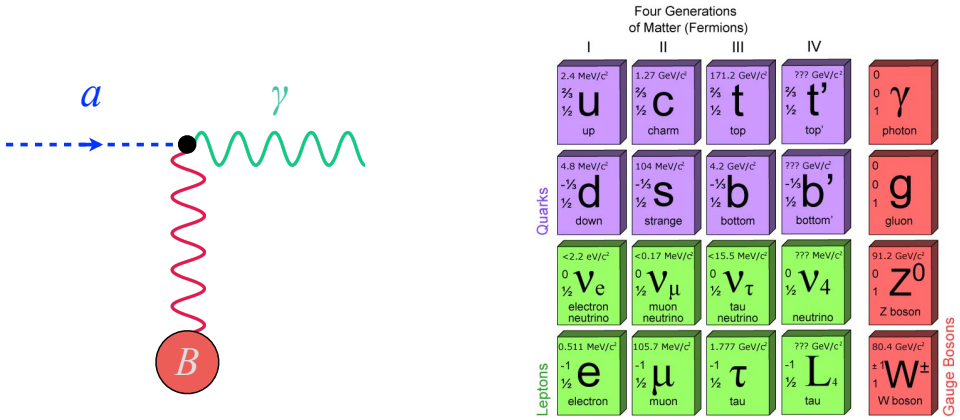

Figure II.5.: Left: Diagram of an axion-photon conversion induced by a magnetic field B via the Primakoff effect. Right: Illustration of the simplest four-generation Standard Model [81].

II.2.5. SEESAW MECHANISM FOR NEUTRINOS

In the previous chapter it was mentioned that the current Standard Model cannot provide an explanation for neutrino masses. However, experimental evidence for neutrino oscillations implies that at least two neutrino generations have masses [12]. There are several Standard Model extensions trying to give an explanation how neutrinos acquire mass. A popular theoretical approach is the *seesaw mechanism* [82], which can be formulated in several variations. The most simple version is the type-I seesaw mechanism, that extends the SM by postulating additional right-handed neutrino fields for each neutrino generation. Also the mass-matrix for the neutrinos has to be extended:

$$\phi_\nu = \begin{pmatrix} \nu_L \\ \nu_R \end{pmatrix}, \qquad M = \begin{pmatrix} 0 & M_D \\ M_D^T & M_R \end{pmatrix}. \tag{II.16}$$

The field ϕ_ν consists of the neutrino part of left-handed lepton isospin doublet ν_L and the postulated right-handed neutrino spinor ν_R, which is a singlet under the weak isospin. The extended mass-matrix

[11] As it is the case in the SM, these particles can also decay hadronically. However, most experimental searches focus on the cleaner leptonic signatures.

consists of the Dirac mass-matrix $M_D^{(T)}$ and the Majorana mass-matrix M_R. Majorana masses are a consequence of the *Majorana equation* [83] and are only possible for neutrinos, since both the neutrino and the antineutrino are electrically neutral. Therefore, Majorana mass terms are not forbidden due to charge conservation[12]. Since, for the sake of simplicity, this example assumes only one neutrino generation, M is given by a 2×2 matrix with the eigenvalues:

$$\lambda_\pm = \frac{M_R \pm \sqrt{M_R^2 + 4M_D^2}}{2}, \qquad \text{if } M_R \gg M_D: \quad \lambda_+ \approx M_R,\ \lambda_- \approx -\frac{M_D^2}{M_R}. \tag{II.17}$$

The mass terms in the Lagrange density can be written as follows:

$$\mathscr{L}_{m(\nu)} = \phi_\nu^T\, M\, \phi_\nu = \begin{pmatrix} \nu_L & \nu_R \end{pmatrix} \begin{pmatrix} 0 & M_D \\ M_D^T & M_R \end{pmatrix} \begin{pmatrix} \nu_L \\ \nu_R \end{pmatrix}. \tag{II.18}$$

If the mass-matrix is diagonalized, the mass term for the left-handed neutrinos is given by λ_-, while for the hypothetical right-handed neutrinos, it is λ_+. Therefore, the small masses of the left-handed neutrinos in the SM can be explained with a suppression coming from the large mass scale of M_R.
This concept is very popular because it is able to explain how neutrinos acquire masses and provides in terms of the heavy neutrinos also a suitable dark matter candidate. Furthermore, it explains the relatively small neutralino masses compared to other SM leptons. The seesaw mechanism can be interpreted in terms of a Grand Unified Theory, motivating the large value of M_R which has chosen to be at the GUT scale. It can also be extended using additional neutrino fields and embedding the model in more complex symmetry groups, referred to as type-II(III) seesaw models [84].

[12] The Majorana equation is equivalent to the Dirac equation if a field is its own charge conjugate $\psi = \psi^c$. Among the SM fermions, only the neutrinos can fulfill this condition.

III. Phenomenology of Proton-Proton Collisions

Scattering experiments performed at particle colliders are of crucial importance to understand the fundamental interactions between elementary particles, to test the predictions of the Standard Model, and to search for new physics beyond the SM. Inelastic (hard) scattering processes between particles, where new particles are created are in this regard of particular interest. This chapter gives an overview of the phenomenology of the proton-proton collisions taking place at the Large Hadron Collider at CERN.
A description of the conditions in a hadron collider and how they can be quantified is given in Section III.1. Section III.2 introduces the concept of parton distribution functions which is crucial for simulating hadron collisions with a sufficient level of precision. A brief description how events are simulated with the usage of Monte Carlo generators and how the interaction of these events with the detector material is simulated, is given in Section III.3 and III.4.

III.1. Description of Collider Conditions

Particle colliders are machines that accelerate particle beams by electromagnetic fields in an evacuated beam pipe and let them collide at specific points. The colliding particles in the beam pipe are cumulated into numerous compressed collections, so-called "bunches".
A quantity used for the description of particle interactions in scattering processes is the cross-section σ[1]. It can be interpreted as effective area, corresponding to the reaction probability of the scattering process. Detailed knowledge about the conditions inside the collider is needed to determine the cross-section of a particular process in a pp collision. A useful parametrization in collision experiments with a rotational symmetry is the differential cross-section $d\sigma/d\Omega$, defined as the cross-section per solid angle. The cross-section in a specific region can then easily be obtained by integrating over the corresponding angular range:

$$\sigma_{\vartheta'} = \int_0^{\vartheta'} \int_0^{2\pi} \left(\frac{d\sigma}{d\Omega}\right) \sin(\vartheta)\, d\phi\, d\vartheta, \qquad \vartheta' \in [0,\, \pi], \tag{III.1}$$

with ϑ' corresponding to the coverage of the scattering angle. The total cross-section is independent from the experimental setup and is determined by the scattering amplitude $\mathscr{M}$ of the process. This quantity is usually referred to as *matrix element*, since it is defined by the S-matrix that relates the initial and the final state of a scattering process:

$$\sigma_{\text{tot}} = \int \left(\frac{d\sigma}{d\Omega}\right) d\Omega = \int \frac{1}{F} \left|\mathscr{M}\right|^2 dQ. \tag{III.2}$$

The variable F denotes the particle flux in the interaction process. The parameter dQ describes an element of the kinematic phase space, which can be integrated to add up all possible momentum states of the particles.
The relation between the event rate $\dot{n}$ and the cross-section is given by the *instantaneous luminosity* L of a collider[2]. The time-integrated total luminosity $\mathscr{L}$ yields accordingly the total number of events produced

[1] In particle physics, the unit of σ is barn (b). $1\,\text{b} \mathrel{\widehat{=}} 10^{-28}\,\text{m}^2$.
[2] The unit of L is $\text{m}^{-2}\,\text{s}^{-1}$, but typically it is quoted in units of the inverse cross-section $\text{b}^{-1}\,\text{s}^{-1}$.

in an interaction process:

$$n = \mathscr{L} \cdot \sigma, \qquad \mathscr{L} = \int L dt. \tag{III.3}$$

The instantaneous luminosity can be obtained from the intristic properties of the pp collisions. If n_b bunches, each containing N particles, collide with the revolution frequency f_c, the instantaneous luminosity of the interaction is given by the formula:

$$L = f_c n_b \frac{N^2}{4\pi \sigma_x \sigma_y} R, \tag{III.4}$$

where σ_x and σ_y are the transverse beam widths in horizontal and vertical directions [11]. This relation is, however, just an approximation assuming that the transverse profiles of the bunches are identical and given by two independent Gaussian distributions along the x- and y-axis. The factor R includes corrections to account for dependencies on the bunch length and the beam crossing angle. Since the expected number of events is proportional to the luminosity, a precise determination of the luminosity is crucial for reliable measurements of the event rates.
A stable beam can be characterized in terms of its initial conditions and a *beta function* β [85], which is a beam optics quantity and is determined by the magnet configuration of the accelerator. The horizontal and vertical beam widths $\sigma_{x,y}$ can be quantified with the horizontal and vertical component of the beta function $\beta_{x,y}$ depending on the nominal beam trajectory s and the transverse beam emittance ε:

$$\sigma_{x,y}(s) = \sqrt{\varepsilon \, \beta_{x,y}(s)}. \tag{III.5}$$

At the interaction point, the instantaneous luminosity needs to be maximized, thus the beam width has to be small. To achieve this, the beta function is adjusted to have local minima at these points. Around the minimum, the evolution of $\beta(s)$ can be written as:

$$\beta(s) = \beta^* + \frac{s^2}{\beta^*}. \tag{III.6}$$

The variable β^* describes the gradient of the beta function before and after the interaction point. This implies that a strong compression of the beam size is associated with a fast widening of the beam after the interaction point. An illustration of the $\beta(s)$ evolution for two different values of β^* is shown on the left of Figure III.1. In a realistic configuration, the aperture of the focusing magnets around the interaction point limits to which extent β can be minimized.

III.2. PARTON DISTRIBUTION FUNCTIONS

The concept of parton distribution functions (PDFs) is essential for describing proton-proton interactions with a high precision. Unlike leptons, protons are composite objects consisting of quarks and held together by the strong force (generally referred to as hadrons). Besides two up quarks and one down quark determining quantum numbers like charge, spin, and baryon-number of a proton (valence quarks), they contain also gluons and virtual quark-antiquark pairs which arise from vacuum fluctuations (sea quarks). Collisions of these composite systems cannot be described as simply as interactions between point-like particles since all constituents of the colliding protons (partons) are involved in the interaction.

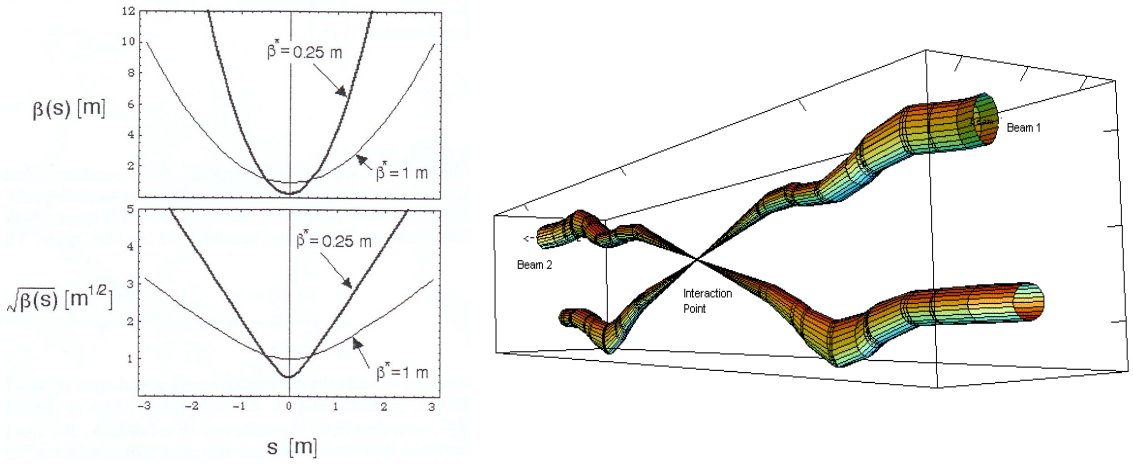

Figure III.1.: Left: The evolution of the beta function $\beta(s)$ around the interaction point for two different values of β^*. Right: Three-dimensional illustration of the beam compression at the collision [86].

A parton distribution function $f_{a/A}(x,Q^2)$ is defined as the probability density function for finding a parton a inside the hadron A with a certain momentum fraction $x = p_a/p_A$ at a specific energy scale Q^2. The *factorization theorem* [87] states that the dynamics of the hadronic substructure can be fully described by the PDF, independent from the type of the underlying scattering process. Due to the energy dependence of the interaction strength in QCD (see Section I.5), the parton densities themselves cannot be calculated using the methods of perturbation theory. However, they can be measured at a fixed scale and the evolution of the parton density depending on Q^2 can be extrapolated with the *Dokshitzer-Gribov-Lipatov-Altarelli-Parisi equation* (DGLAP equation) [87–89]. A specific choice of the energy scale, referred to as "factorization scale" has to be made to define whether partons are absorbed in the PDFs or regarded as part of the hard scattering process. The cross-section of a hadron-hadron scattering process with two hadrons A and B is given by the formula:

$$\sigma(A/B \to X) = \sum_{a,b} \int_x dx_a\, dx_b\; f_{a/A}(x_a, Q^2)\; f_{b/B}(x_b, Q^2) \times \widehat{\sigma}(a/b \to X), \tag{III.7}$$

where a and b denote the parton constituents of their corresponding hadrons A and B. Their PDFs are given by the functions $f_{a/A}(x_a,Q^2)$ and $f_{b/B}(x_b,Q^2)$. The terms $\widehat{\sigma}(a/b \to X)$ are the contributions of the individual cross-sections of the partons a, b to the reaction product X. The cross-sections of all processes expected at a pp collision at the LHC can be computed with this function. However, for an explicit calculation of the total cross-section, a complete and accurate prediction from the PDF is required. It can be determined by taking the experimental information about a particular process and applying it to obtain predictions for other processes. The distribution functions plotted against x for two different energy scales are shown in Figure III.2.

According to the choice of the dataset used for the measurement, the reference value for the energy scale, and different perturbative orders, several strategies how to determine a PDF exist [90]. Different collaborations, such as CT, MSTW, NNPDF, or LHAPDF [91–94], perform these measurements (mainly from deep inelastic $e^{\pm}p$ scattering experiments) and provide PDFs which can be used for physics analyses. The dominant uncertainties associated with the PDFs are typically the experimental uncertainties of the input datasets, theoretical uncertainties of the coupling parameters, or the uncertainty of the perturbative calculations.

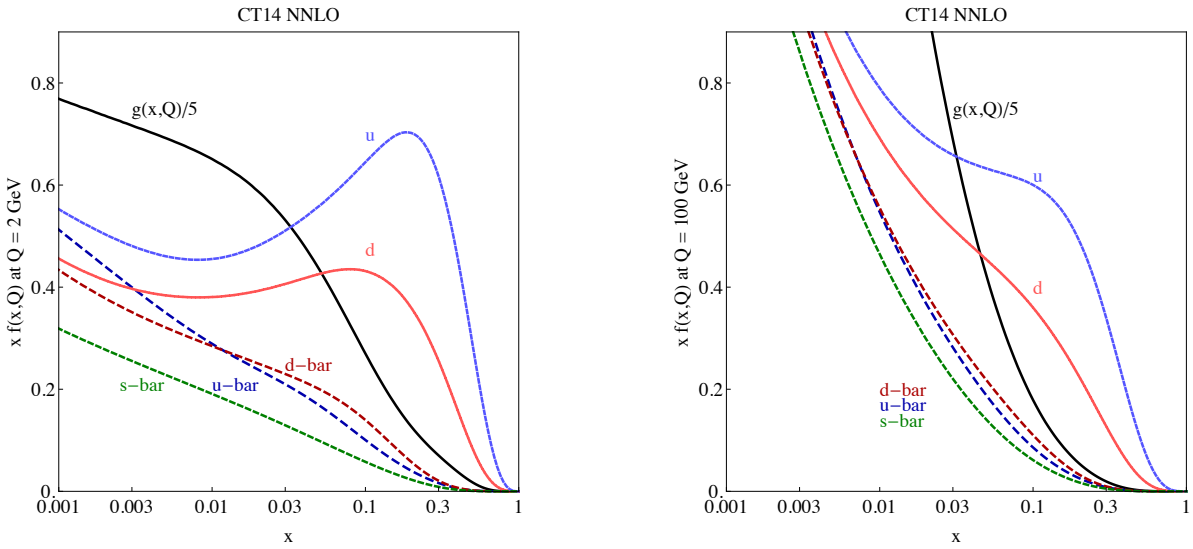

Figure III.2.: Parton distribution functions $x\,f(x,Q^2)$, plotted against x for gluons and different quark flavors. The PDFs are calculated with CT14 at NNLO for $Q = 2$ GeV (left) and $Q = 100$ GeV (right) [91].

III.3. Event Simulation and Monte Carlo Generators

For every physics analysis, it is essential to have a reliable simulation of the underlying Standard Model processes. This is done with so-called Monte Carlo (MC) event generators which are an important tool in particle physics. MC generators are used to simulate events of both signal and background processes. These simulations are also indispensable for the development and optimization of an analysis, since they serve as a basis to decide which analysis techniques are most appropriate to separate possible signal processes from the Standard Model background.
A Monte Carlo simulation starts from the fundamental interaction given by the matrix element of the process (denoted as hard scattering). The final result is a prediction for the stable particles which are visible in a detector. To accomplish this, several steps of initial/final-state radiation, parton shower evolution, hadronization, and interaction with the detector environment have to be simulated [95], as simplified illustrated in Figure III.3. This section gives an overview of the steps that have to be performed in order to obtain a fully generated event.

III.3.1. Hard Scattering Process

The cross-section of the hard scattering interaction can be fully calculated within the theoretical framework provided by the SM. However, many different processes described at this level can lead to the same initial and final states and can, therefore, contribute to the total cross-section of the interaction.
Depending on the power of the coupling constant arising in the matrix element of the term, the processes can be categorized into leading order (LO), next-to-leading order (NLO), next-to-next-to-leading order (NNLO) and higher orders[3]. Thus, the total cross-section σ_{tot} can be written as follows:

$$\sigma_{\text{tot}}(\mu_F) = \sum_{n=1}^{\infty} \alpha^n(\mu_R)\,\sigma_n(\mu_F, \mu_R), \tag{III.8}$$

with σ_n denoting the cross-section for a specific order n, depending on renormalization and factorization

[3] Orders higher than NNLO are usually denoted as NXLO, where X is the given order (e.g. N3LO).

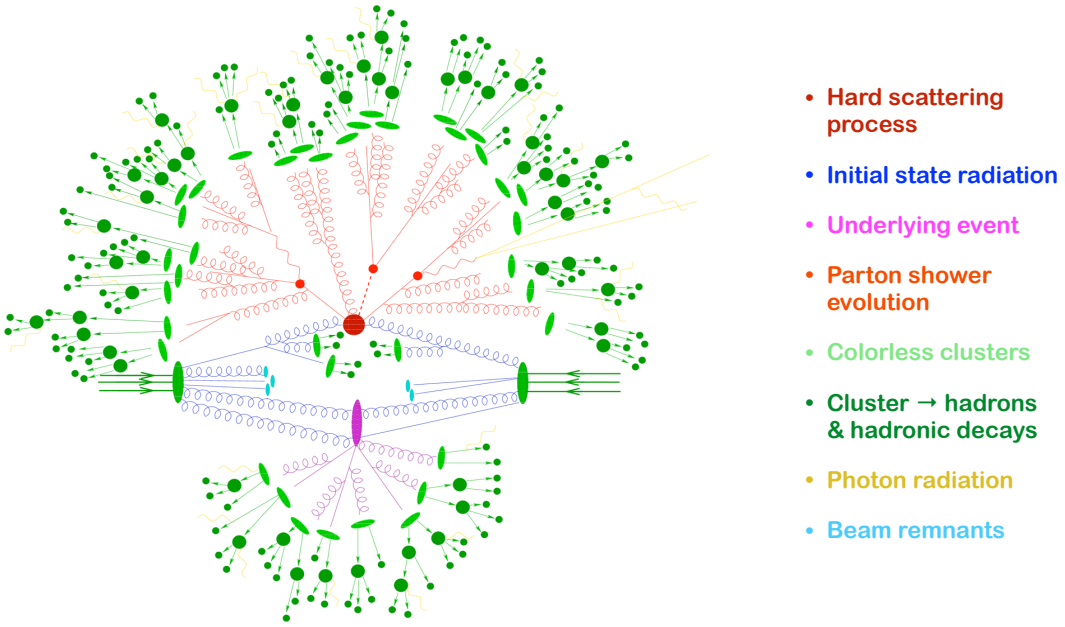

Figure III.3.: Illustration of a pp collision as simulated by an MC event generator: Hard scattering (dark red), parton shower evolution (light red), initial-state radiation (blue), underlying event (purple), hadronization (light/dark green), and photon radiation (yellow) have to be simulated in a full event generation [96].

scale μ_R, μ_F as described in Section I.5 and III.2. The quantity $\alpha(\mu_R)$ states the coupling constant derived for a specific renormalization scale.
Since the SM is a renormalizable theory, the energy-dependent coupling constant absorbs divergences arising in the calculation of σ_n for specific orders. So for $n \to \infty$, the result is independent from the renormalization scale. However, in a calculation for a specific order, residual dependencies on μ_R remain. Accordingly, the final result depends on the choice of μ_R and μ_F. Usually, variations on the renormalization and factorization scale are applied in order to derive theoretical uncertainties associated with calculations at a fixed order. For the most common processes, MC generators using NLO calculations of the matrix element became standard within the last few years, while applications with NNLO calculations are presently under development[4].

III.3.2. PARTON SHOWERS

The partons involved in the hard scattering process induce cascades of radiation, referred to as parton showers (PS). One can distinguish two types of parton showers. Color-charged particles such as quarks and gluons, emit further gluons or produce quark-antiquark pairs leading to the formation of hadronic parton showers. From QED processes, scattered electric charges radiate photons which can produce again lepton-antilepton pairs. These formations are called electromagnetic showers. The structure of these two shower types is in general very different due to the self-interaction properties of gluons and the generation of many low-energy (soft) gluons, leading to an extended shower shape of hadronic parton showers compared to electromagnetic showers.
Calculations for real emissions included in higher order corrections to the hard process can show divergences for very small opening angles between the emitted objects and the emitting parton (collinear

[4]Since calculations at NNLO are very CPU intensive with the available methods, NLO will most likely remain the standard also for the coming years.

limit) and emissions of partons with very low energies (soft limit). These divergences would be canceled by corresponding interference terms in higher orders. To describe processes for a fixed order in these phase space regions, parton shower algorithms simulate the radiations based on a resummation of the leading logarithms to all orders. Divergences arising in these calculations are absorbed in the PDFs. If the calculated matrix element takes already into account terms with higher order, a double-counting with the simulated PS has to be avoided. Several approaches for different MC generators exist to combine the higher order emissions and the simulated parton showers in terms of an NLO+PS or NNLO+PS matching [97].
The PS algorithms simulate sequentially an evolution depending on the momentum transfer scale. The evolution starts from the hard scattering process and is gradually simulated to lower and lower momentum scales up to a point where perturbative methods cannot be applied anymore. The parton splitting probability (e.g. for a quarks emitting a gluon) is described by a splitting function $P_{i,jk}$[5] for the splitting process $(i \longmapsto j,k)$ which depends on flavor and spin. If the n-parton differential cross-section before the splitting is $d\sigma_n$, after the splitting it becomes:

$$d\sigma_{n+1} \approx d\sigma_n \frac{\alpha_s}{2\pi} \frac{d\theta^2}{\theta^2} P_{i,jk}(z)\, dz\, d\phi. \tag{III.9}$$

The parameter z denotes the transferred energy fraction and the variables θ and ϕ define the opening angle of the splitting. The PS algorithm follows an ordered evolution of splittings, starting with the original final-state partons and complying a specific ordering scheme which depends on the algorithm. A resolution criteria defines where the splitting procedure is stopped. The probability for having no splitting during the evolution from one energy scale to another scale is given by so-called *Sudakov form factors* [98]. These terms can be written as:

$$\Delta_i(q_1^2, q_2^2) = \exp\left\{ -\int_{q_2^2}^{q_1^2} \frac{dq^2}{q^2} \frac{\alpha_s(q^2)}{2\pi} \int_{Q_0^2/q^2}^{1-Q_0^2/q^2} \int_0^{2\pi} P_{i,jk}(z)\, dz\, d\phi \right\}, \tag{III.10}$$

where q_1 and q_2 denote the two energy scales between which the evolution is done and Q_0^2 constitutes the cutoff scale. Also, initial state radiation (ISR), meaning radiation emitted by the incoming partons before the hard scattering process can be modeled with PS algorithms. Therefore, a backward evolution, starting at the scale directly after the hard scattering back to the initial partons has to be performed [99].
Different algorithm types such as PYTHIA, SHERPA, or HERWIG [100–102] use different ordering schemes and different resummation methods which usually leads to slightly different, but consistent results. Comparisons between different algorithms can, therefore, be utilized to obtain an uncertainty associated with the parton shower algorithm.

III.3.3. HADRONIZATION

During the parton shower evolution, the energy scale decreases leading to an increase of the QCD coupling constant. Thus, at a certain point of the evolution, perturbation theory breaks down, leading to the formation of colorless bound states [13]. For a realistic simulation of the hadronization process, non-perturbative approaches are necessary, such as different phenomenological models. An alternative approach is provided by lattice gauge theories [103, 104], where spacetime is quantized to a discrete lattice

[5] The terms $P_{i,jk}$ are also referred to as *Altarelli-Parisi splitting kernels*.

structure[6] is a method to address the non-perturbative processes happening during hadronization. Most of the phenomenological prescriptions rely on the fact that hadronization can be treated independently from the perturbative physics at lower energy scales.
A commonly used approach is the *cluster-hadronization model* [105], as it is used for instance in the HERWIG generator. In this model, gluons split into quark-antiquark pairs at the shower cutoff scale to form colorless superpositions of different mesonic states, denoted as clusters. These clusters subsequently decay to stable hadrons based on properties like spin, mass, and lifetime of their constituents. The choice of the cutoff scale is a crucial parameter of this method. An alternative method is the *Lund string model* [106], used e.g. for the simulation with PYTHIA. This method is based on a linear effective potential $V(r) = \kappa \cdot r$ defining the quark-antiquark splitting threshold. The $q\bar{q}$ splitting is repeated iteratively until colorless hadrons are built, as illustrated in Figure III.4. This condition is given by the kinetic energy of the partons which has to be sufficiently low to allow the formation of a bound state.

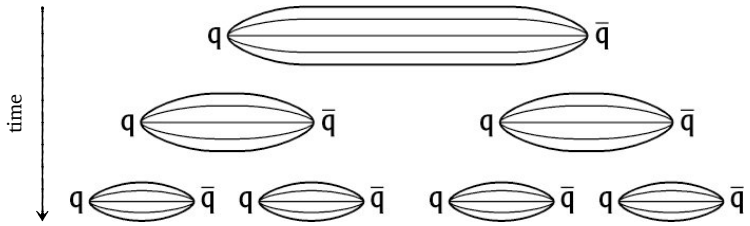

Figure III.4.: Illustration of the lund string model: the string breaking is induced by the consecutive creation of $q\bar{q}$ pairs in the string field.

There are also other phenomenological models which can be used as an implementation for MC generators. They all have in common that they are only simplified approximations and do not allow an accurate description of the full hadronization process. Furthermore, they rely on free parameters and need to be tuned with experimental data in order to produce realistic results.

III.3.4. UNSTABLE PARTICLE DECAYS

The produced hadrons can be unstable and thus decay to lighter particles (such as $\pi^0 \to \gamma\gamma$). The final stage of event generation is the simulation of sequential decays of any unstable hadrons produced in the hadronization process.
This step is essential, as in most phenomenological hadronization models the case that the outcoming hadrons are stable is indeed unlikely. These decays are incorporated using the branching ratios and lifetimes of the unstable particles obtained theoretically from the matrix elements of the decay processes. Furthermore, properties of the decay products such as masses and spin configurations have to be considered for the computation. Especially for multi-body decays, the matrix elements are highly non-trivial and appropriate models have to be constructed for them. The decay models and the theoretically derived parameters have a significant effect on the hadron yields and event characteristics, like transverse momentum spectra or event shapes. Thus, the parameters of the decay model are also often tuned with experimental data. The values for the branching ratios are frequently taken from decay tables obtained from experimental measurements and documented in the PDG [11]. A commonly used framework for

[6] The advantage of a formalism based on a discrete spacetime is that the path-integrals needed for the calculation can be reduced to expressions with finite dimensionality (while they are infinite-dimensional in a continuous spacetime). Thus, they can be a numerically solved with stochastic simulation techniques.

these simulations is EVTGEN [107], which was developed to model the decay of b-mesons but can be used also for other decay modes.

III.3.5. UNDERLYING EVENT AND PILE-UP

An additional feature of event generators is the modeling of the so-called underlying event. It describes all types of hadronic activity in addition to what can be associated with the hadronization of partons involved in the hard scattering process (including its ISR and FSR activities). In case of multiple parton scattering processes happening simultaneously in the same event, it can be attributed to activities not coming from the interaction with the highest $\sum p_{\mathrm{T}}^2$ of the outcoming objects [108]. The simulation of these effects is done with phenomenological approaches. Typically, distributions sensitive to the properties of underlying events are measured and cuts on them are defined[7]. The optimal discrimination is achieved by tuning the prediction from MC generators with experimental data.
Besides the underlying event, an effect denoted as *pile-up* can be another source of soft hadronic interactions in addition to the hard scattering. The expression pile-up refers to multiple proton-proton interactions in the same bunch crossing (in-time pile-up) or from consecutive bunch crossings (out-of-time pile-up) and yields substantial hadronic activities in addition to the hard scattering process. The average number of interactions per bunch crossing $\langle\mu\rangle$ is in first approximation proportional to the instantaneous luminosity. Usually, it lies between 0 and 40 for the current ATLAS luminosities. For the combined $\sqrt{s}$ = 13 TeV data from 2015 and 2016, its mean value is around 23.7 [109]. An event with high pile-up environment is shown on the left of Figure III.5. Actually, the hard scattering happening in this event is found to be a $Z^0 \to \mu\mu$ process, highlighted by the yellow bold lines. However, the pile-up conditions cause a high number of additional reconstructed vertices and hadronic activities in the event which makes the identification of the hard process a challenging task. Although a trigger-based object identification and kinematic requirements in the event selection can help to mitigate the impact of pile-up in data, a proper modeling of these effects is still essential for a reasonable Monte Carlo prediction.
Pile-up conditions can be simulated by generating an inclusive sample of proton-proton collision events and superimpose them with the hard scattering process. The number of overlaid events is varied and later reweighted to match the actual distribution of the number of pp interactions per bunch crossing in data. The reweighting of the $\langle\mu\rangle$ distributions is translated into a modified weight of the generated MC event. This procedure is called "pile-up reweighing" and is a crucial step to achieve a realistic description of pile-up effects in data.

III.4. DETECTOR SIMULATION

Generated events including additional implementations such as parton showering, hadronization, as well as the simulation of underlying event and pile-up effects do still not take into account the interaction of the outcoming particles with the detector material.
In order to be fully comparable to the real data collected with a detector, the generated events have to pass a detailed detector simulation which is capable of reproducing the impact of the different detector parts on the produced objects. This is done with a special detector simulation framework, called GEANT4 [110, 111]. The simulation takes into account different functionalities like tracking, calorimetry, and a full implementation of the detector geometry. It is able to model detector-related effects in a wide energy range, starting from $\mathcal{O}$(100 eV) up to the TeV scale for electromagnetic and hadronic processes. It can

[7] Variables sensitive to underlying event properties are e.g. η, ϕ, or the multiplicity of charge particles.

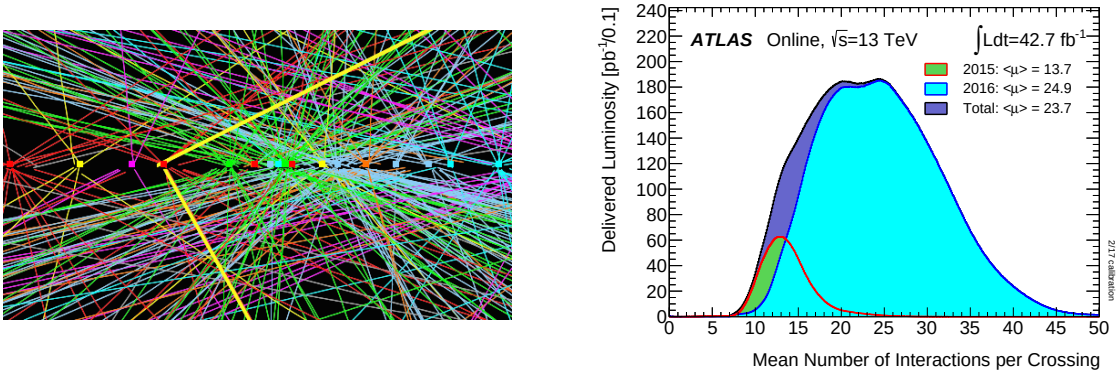

Figure III.5.: Left: Event display showing a $Z^0 \to \mu\mu$ event (yellow bold lines) with high pile-up environment recorded at ATLAS in 2012. Right: Average number of pp interactions per bunch crossing for the combined 13 TeV data from 2015 and 2016 [109].

also consider changes of the trigger conditions in different data taking periods as well as known detector defects, such as inactive or dead readout modules. Newer developments like multithreading, reversed Monte Carlo[8], improved visualization techniques, or faster geometry primitives have been implemented in more recent extensions of the framework. Simulated events and real data are processed with the same reconstruction software to obtain comparable physics objects like leptons or jets.

The complete simulation infrastructure for the ATLAS experiment is more elaborated using different software packages to reproduce the response of the various subdetectors and triggers. The flexible simulation framework allows changing the detector conditions and particular simulation parameters also during runtime. Furthermore, it is able to cope with uncertainties associated with the performance of the detector or particular subdetectors. The physics validation of the simulation infrastructure is performed with dedicated validation tools and is a continuous activity within the collaboration.

Besides the full simulation based on GEANT4, a fast simulation framework denoted as ATLASFASTII [112] exists, which uses all simulation steps for the inner detector and the muon spectrometer, but only a simplified approach for the calorimeter system based on a parametrization of its response for different types of particles. This framework provides a significantly faster event generation[9] compared to the full simulation and is mainly used for the generation of signal events. The ATLASFASTII simulation is also taken for the signal samples used in the analysis described in this thesis.

[8] Reversed Monte Carlo (RMC) is a modeling method in which the initial conditions of a simulation are adjusted until the final observables have the biggest consistency with experimental data.

[9] Compared to a full simulation, ATLASFASTII can reduce the average simulation time of physics processes by a factor 10–20, depending on the complexity of the process [112].

IV. The ATLAS Experiment at the Large Hadron Collider

This chapter is dedicated to the technical design of the Large Hadron Collider and the ATLAS detector. The proton-proton collision data needed to conduct physics analyses is delivered by these machines. Therefore, a sufficient understanding of their layout and working methods is essential for any meaningful interpretation of the analysis results.
A comprehensive overview of the CERN research facility and its largest and most powerful particle accelerator, the Large Hadron Collider, is given in Section IV.1 and IV.2, respectively. The ATLAS detector including its different components and subsystems is described in Section IV.3. Section IV.4 explains how the luminosity delivered to the detector is measured with dedicated forward detectors. Finally, Section IV.5 provides a summary of the run conditions and the ongoing performance of the experiment during Run II.

IV.1. CERN

The European Organization for Nuclear Research, called CERN (named after its foundation council *Conseil Européen pour la Recherche Nucléaire*) was founded in 1954 and was one of the first international research organizations in Europe. It has currently 22 member states and more than 2500 permanent staff members. In addition, more than 12000 fellows, associates, visiting scientists, and engineers from about 600 institutes and research facilities are involved in the various experiments [113]. The biggest collaborations among them are the ones working on the general-purpose detectors ATLAS and CMS, each including around 2800 members. This makes them some of the largest and most important scientific organizations.
The CERN research facility is placed in Meyrin in the canton of Geneva in Switzerland. The instruments primarily used at CERN are particle accelerators and detectors to explore the fundamental structure of matter and to provide insights into the most elementary laws of nature. Accelerators propel charged particles to very high energies in collimated beams and make them collide at stationary interaction points (IPs). Detectors installed at these points observe and record the results of the particle collisions. Besides high-energy physics, many other nuclear research projects and experiments are located at CERN, such as neutrino experiments, mass spectrometry, experiments investigating antimatter, or dark matter searches. CERN hosts also a large computing facility, which major purpose is to store and analyze data from the different experiments as well as generate simulated events.
Several outstanding achievements and discoveries have been made through experiments at CERN within the recent decades. Prominent examples are the discoveries of the Z^0 and $W^\pm$ boson with the UA1 and UA2 experiments in 1983 [114–117], the first observation of direct CP-violation with the NA48 experiment in 1999 [118], or the discovery of a particle compatible with the SM Higgs boson by the ATLAS and CMS experiments in 2012 [14, 15]. This demonstrates the remarkable scientific capacity and the variety of research projects which have been accomplished by this organization in the past.

IV.2. The Large Hadron Collider

The Large Hadron Collider (LHC) [119] is the most modern and powerful particle accelerator in the world. It is located at the CERN complex and installed in an approximately 26.7 km long circular tunnel at about

100 m below ground. This tunnel was once built for the Large Electron-Positron Collider (LEP) [120] at CERN which was used from 1989 until 2000 for electron-positron collisions. For the LHC, the collider ring was redesigned to perform proton-proton collisions. However, it can also be used for beams of lead nuclei. The particles are accelerated and steered in opposite directions by electric and magnetic fields maintained by superconducting electromagnets. At the four interaction points located in the ring, the detectors are placed and the particle beams are made to collide.

The protons are accelerated gradually in several smaller accelerator rings in order to reach the nominal beam energy. Many of these smaller accelerators are used for other experiments located at CERN. An overview of the different accelerators and detectors at CERN is shown in Figure IV.1. The generation of protons happens at the LINAC2 linear accelerator which sends them to the Proton Synchrotron Booster (PSB). At the PSB they are accelerated to an energy of 1.4 GeV. In the Proton Synchrotron (PS), a further boost is applied and the beam energy is increased to 25 GeV. During this step, the proton beams are also cumulated and compressed to form separated bunches. Before being injected into the LHC main ring, the Super Proton Synchrotron (PSP) brings the protons up to 450 GeV. After entering the LHC beam pipe, they are accelerated to the nominal beam energy of 6.5 TeV, corresponding to a center-of-mass energy of $\sqrt{s} = 13$ TeV at the collision[1].

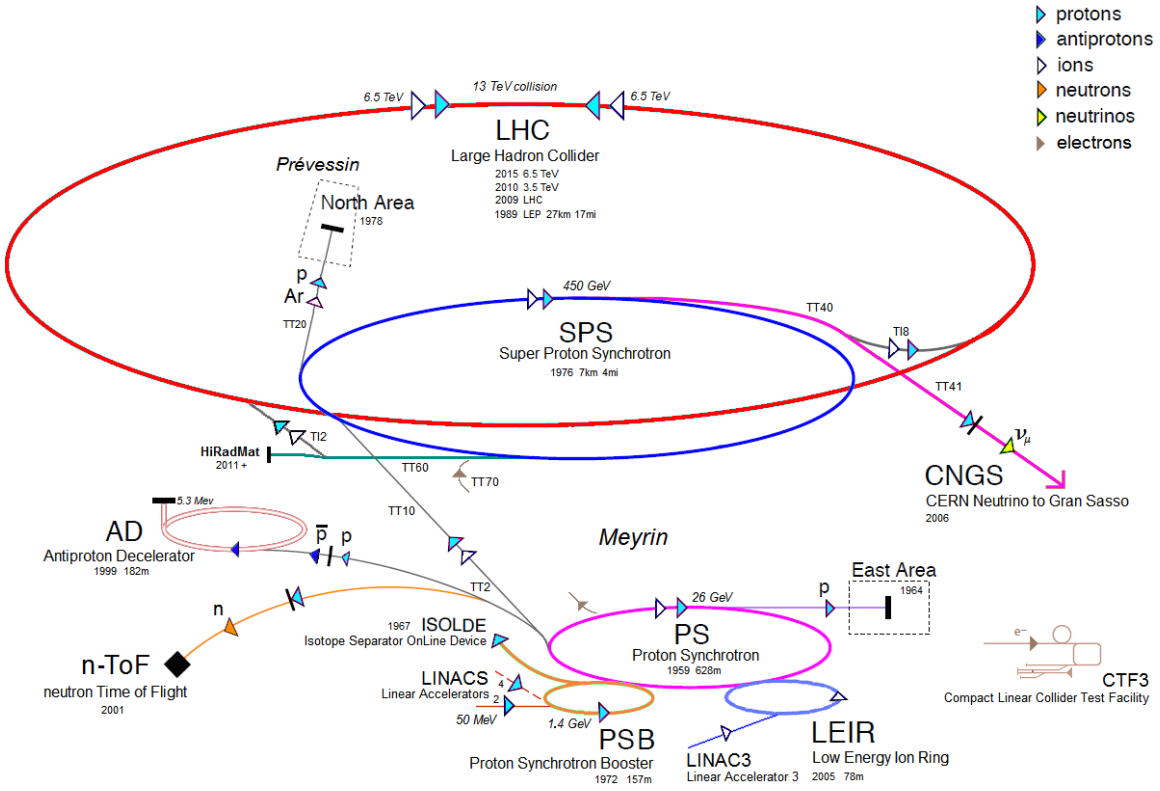

Figure IV.1.: Overview of the accelerator and detector complex at CERN. The colors of the arrows indicate the particle types which can be injected into the different accelerators [121].

The high-energy protons are steered by 1232 superconducting dipole magnets. Each magnet has two apertures for the two separated proton beam pipes. The diameter of the beam pipes is around 53 mm and 858 quadrupole magnets are operated for the focusing of the proton beams. In order to obtain a collimation of the proton bunches in both horizontal and vertical plane, a system of several subsequent

[1] Before the Run II upgrade in 2015, the maximal center-of-mass energy of the LHC was $\sqrt{s} = 8$ TeV.

quadrupole magnets with an alternating polarity is used. Analogously to an optical system with a sequence of divergent and convergent lenses, this makes the protons oscillate around the center of the pipe. With this arrangement, which is typically referred to as FODO pattern[2], an optimal collimation of the circulating protons can be achieved. The setup of a FODO cell and a cross-section of an LHC quadrupole is shown in Figure IV.2. Additional multipole magnets (sextupoles, octupoles) are installed for the beam focusing and counteract perturbations of the trajectory. A further compression of the beam at the interaction points is achieved with eight special magnets, called inner triplets. In total, there are more than 9000 magnets surrounding the LHC ring. The different magnet types are cooled by superfluid helium to the operating temperature of 1.9 K and can reach field strengths up to 8.3 Tesla.
The proton bunches circulating in the LHC ring are separated by a time-spacing of 25 ns in Run II[3]. Each bunch contains around 10^{11} protons and has an approximate scale of 30 cm length and 20 µm width at the collision point. As explained above, the bunch size is not constant along the ring. In order to maximize the instantaneous luminosity of the collision, the bunch is squeezed to reach minimal width and maximal length at the interaction point (see Section III.1). The average collision frequency of the bunches for the ongoing runs is around 31.6 MHz[4]. In the ongoing Run II, the highest instantaneous luminosity achieved so far was $2.06 \cdot 10^{34}$ cm^{-2}s^{-1} and was reached in autumn 2017.

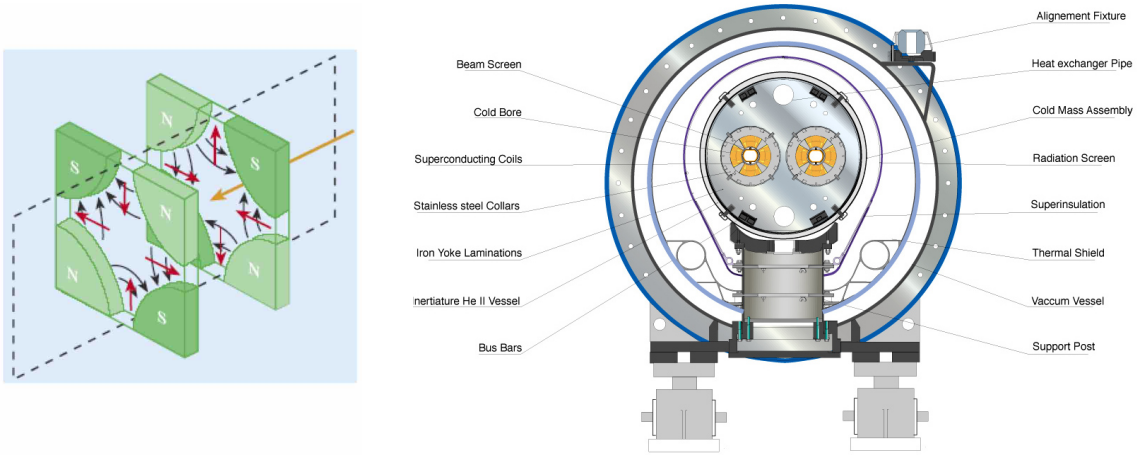

Figure IV.2.: Left: Quadrupole magnets with alternating polarity are used for focusing along the horizontal and vertical plane. Right: Cross-section of a LHC quadrupole [122].

There are seven experiments located at the LHC main ring. Besides the general-purpose detectors ATLAS and CMS [2, 3], the ALICE experiment [123] is dedicated to investigations of strongly interacting matter at extreme energy densities and quark-gluon plasma, which is studied from the collisions of lead nuclei (*Pb-Pb* collisions). For this experiment, LHC has to run in a different operating mode, accelerating lead ions instead of proton bunches. The LHCb experiment [124] investigates the interactions of *b*-hadrons and focuses on effects related to *b*-physics, such as CP-violation or branching ratio measurements of rare *b*-decays. These four detectors are located at the different collisions points of the LHC.
In addition to the four main experiments, the LHCf, TOTEM, and MoEDAL experiments [125–127] perform more specific research, like calibration studies, searches for magnetic monopoles, or elastic cross-section measurements.

[2]The "F" and the "D" in FODO stand for focusing and defocusing. The letter "O" denotes the drift path without a field.
[3]During Run I, the LHC was mostly operated with a bunch spacing of 50 ns.
[4]A 25 ns bunch crossing rate corresponds to 40 MHz. Due to gaps in the bunch trails, the average crossing rate is usually lower.

IV.3. THE ATLAS DETECTOR

The ATLAS (A Toroidal LHC ApparatuS) detector is one of the two general-purpose particle detectors at the LHC ring, installed at interaction point-1 in a large cavern about 100 m below ground. The detector has a length of approximately 44 m and a diameter of 25 m. Its total weight is about 7000 tonnes and it covers a solid angle of almost 4π. The detector system is able to process up to one billion collisions per second, with a data volume of more than 60 million megabytes per second. Since November 2009, it records pp collision generated at the Large Hadron Collider.
The physics program of the ATLAS Collaboration covers a wide range of different topics, including precision measurements of Standard Model processes, searches for new particles and effects predicted by the SM, as well as searches for new physical phenomena beyond the Standard Model. In the design of the detector, different experimental aspects had to be considered to achieve the desired performance goals. The most important features are:

- Maximal geometrical coverage to achieve the best possible detector acceptance.
- High resolution of the electromagnetic calorimeter for a precise electron and photon identification. In addition, a hadronic calorimetry with full coverage for accurate jet and $E_{\mathrm{T}}^{\mathrm{miss}}$ measurements.
- Fine segmentation of the calorimeters to obtain a good angular resolution for reconstructed electrons, jets, and photons.
- High spatial resolution in vertex reconstruction for an efficient identification of the primary interaction vertex and secondary vertices needed for identification of b-jets and τ leptons.
- Precise determination of the muon momentum by the inner detector, with the possibility of an accurate independent measurement with the muon spectrometer.
- A fast and efficient trigger system to select interesting events and to process the large amount of data, according to the high luminosities delivered by the LHC [2].

A schematic view of the ATLAS detector and its different subdetector systems is shown in Figure IV.3. The detector can be subdivided into an inner tracking chamber (inner detector), an electromagnetic and hadronic calorimeter, and a muon spectrometer in the outermost part of the detector. Each of these subdetectors consists again of several separate components designed for specific applications.
The magnet system of the detector is composed of a central solenoid surrounding the inner detector and three toroid magnets (one barrel and two end-caps) placed around the muon spectrometer. The central solenoid generates a constant magnetic field of 2 Tesla parallel to the beam axis to bend the trajectories of charged particles, allowing a momentum and charge measurement by the tracking system. The barrel and end-cap toroid magnets (eight coils each) supply the muon system with an inhomogeneous magnetic field of approximately 0.5 and 1 Tesla in the central and end-cap regions, respectively. This provides an advanced precision of the muon momentum measurements due to additional bending of the muon trajectories[5]. The luminosity delivered to ATLAS is measured by several dedicated luminosity detectors located at the beam pipe before and after the interaction point, as explained in Section IV.4.
A more detailed description of the different ATLAS subdetectors and the trigger system used for data acquisition is given in the following sections.

[5] The additional magnetic field allows an independent momentum measurement by the muon spectrometer, which can be combined with the information from the inner detector.

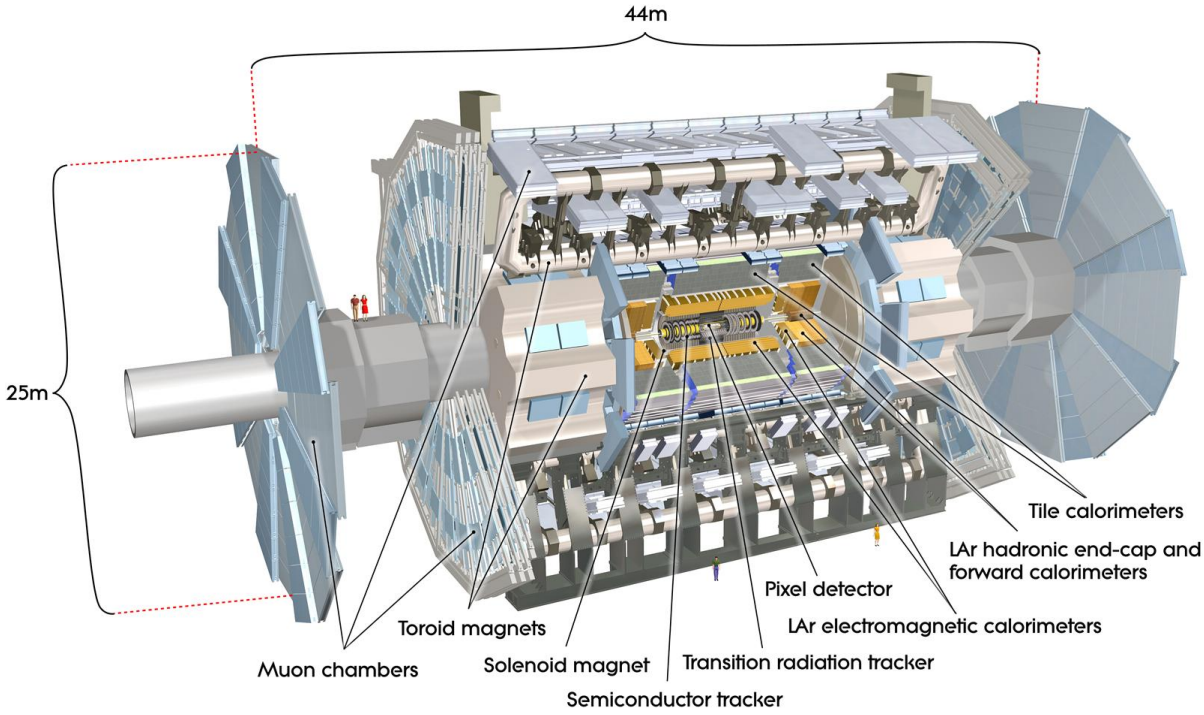

Figure IV.3.: A schematic view of the ATLAS detector and its different subdetector systems [128].

IV.3.1. Detector Coordinate System and Important Variables

To quantify the position of the objects in the detector, ATLAS uses a right-handed coordinate system with its origin at the nominal interaction point of the particles in the center of the detector. The z-axis is defined along the beam pipe, the x-axis is parallel to the plane of the LHC ring pointing to its center, and the y-axis goes upwards. Matching the geometry of the detector, the coordinate system typically used in ATLAS is a spherical coordinate system (r, ϕ, θ), where r is the radius, ϕ is the azimuthal angle around the beam pipe, and θ is the polar angle from the beam axis. Since θ is not invariant under Lorentz transformations, this coordinate is often parametrized in terms of the *rapidity* y or *pseudorapidity* η. They are defined as:

$$y = \frac{1}{2}\ln\left(\frac{E+p_z}{E-p_z}\right), \qquad \eta = -\ln\left[\tan\left(\frac{\theta}{2}\right)\right], \tag{IV.1}$$

with E as the total energy and p_z stating the z-component of the particle momentum. For massless particles, the definitions of rapidity and pseudorapidity are equivalent. In the highly relativistic case, where their masses become negligible, y and η are converging towards the same values. However, since η can be computed more easily, the quantification of the position of an object in a detector is more commonly done with the coordinates ϕ and η. The angular separation ΔR between objects in the (ϕ, η) space can be quantified as:

$$\Delta R = \sqrt{(\Delta\phi)^2 + (\Delta\eta)^2}. \tag{IV.2}$$

This quantity is also used to indicate e.g. the extension of jets cones, the size of electromagnetic and hadronic showers, or the resolution of reconstructed objects.
Since the partons participating in the hard scattering process carry only a fraction of the total momenta of the colliding protons (see Section III.2), the outcoming particles can have a residual boost in the

z-direction. Thus, the only well-known kinematic variable of the interaction is the transverse momentum $\vec{p}_{\mathrm{T}}$, which is the projection of the momentum to the x-y plane of the detector. Its magnitude p_{T} can be calculated from the x- and y-components of the momentum vector:

$$\vec{p}_{\mathrm{T}} = \begin{pmatrix} p_x \\ p_y \end{pmatrix}, \qquad p_{\mathrm{T}} = \sqrt{(p_x)^2 + (p_y)^2}. \tag{IV.3}$$

Since the value of p_z can be obtained from combining p_{T} and the rapidity (or pseudorapidity), the momentum vector of a particle is fully defined by a point in the $(p_{\mathrm{T}}, \eta, \phi)$ parameter space. The scalar sum of the transverse momenta of all selected particles in an event is typically referred to as H_{T}. A variable denoted as the (inclusive) effective mass m_{eff} can be calculated by adding the missing transverse energy $E_{\mathrm{T}}^{\mathrm{miss}}$ (as comprehensively explained in Section V.4) to this value.

$$H_{\mathrm{T}} = \sum_i |p_{\mathrm{T}}|^i, \qquad m_{\mathrm{eff}} = H_{\mathrm{T}} + E_{\mathrm{T}}^{\mathrm{miss}}, \tag{IV.4}$$

with the index i iterating on all selected particles[6]. In most cases, these quantities are expected to be fairly sensitive to new physics phenomena. Therefore, they are commonly used in physics analyses to evaluate the compatibility between data and the predicted SM background.

IV.3.2. The Inner Detector

The inner detector (ID) [129, 130] is the innermost part of the ATLAS detector and provides the tracking system for charged particles. Therefore, it is the most important part for measuring momenta and charges, as well as reconstructing track vertices with a high precision. It is built directly around the interaction point of the beam pipe and has a diameter of 2.1 m and a total length of 6.2 m. Including its different components, it covers a pseudorapidity up to $|\eta| = 2.5$. The p_{T} threshold for momentum measurements with the ID is about 400 MeV. The track momentum resolution using the combined detector information is approximately $\sigma_{p_{\mathrm{T}}}/p_{\mathrm{T}} = 0.05\%\, p_{\mathrm{T}} \oplus 1\%$[7].

The inner detector is composed of three complementary subdetectors: the pixel detector, the semiconductor tracker (silicon microstrip tracker), and the transition radiation tracker. Several parts of the detector system were upgraded after Run I to cope with the higher instantaneous luminosities expected for future runs and to improve the precision of the track reconstruction. In particular, a new pixel layer, the insertable B-Layer (IBL) [131], has been added to the pixel detector. In Figure IV.4, a detailed layout of the inner detector system with its three components and the new IBL is shown.

The Pixel Detector

The original pixel detector instrumented for Run I is a silicon detector with three cylindrical layers located at radii of 50.5 mm, 88.5 mm, and 122.5 mm around the center of the beam pipe. In addition, it has two end-caps with three disc layers each. In total, 1744 modules with 46080 readout channels per module ($\approx$8.4 million channels) are installed[8]. This is about 50% of all the readout channels in the entire detector. Each layer consists of several staves containing 13 modules each. The pixel sensors have a thickness

[6] The definitions of H_{T} and m_{eff} depend obviously on the selection criteria for the particles considered for the computation. Thus, these variables are very analysis-specific quantities.

[7] Throughout the rest of this thesis, the symbol $\oplus$ means that the relative uncertainties are added in quadrature.

[8] Due to inactive or dead cells in the detector, the number of operating channels is always slightly below the nominal numbers quoted in the Technical Design Report.

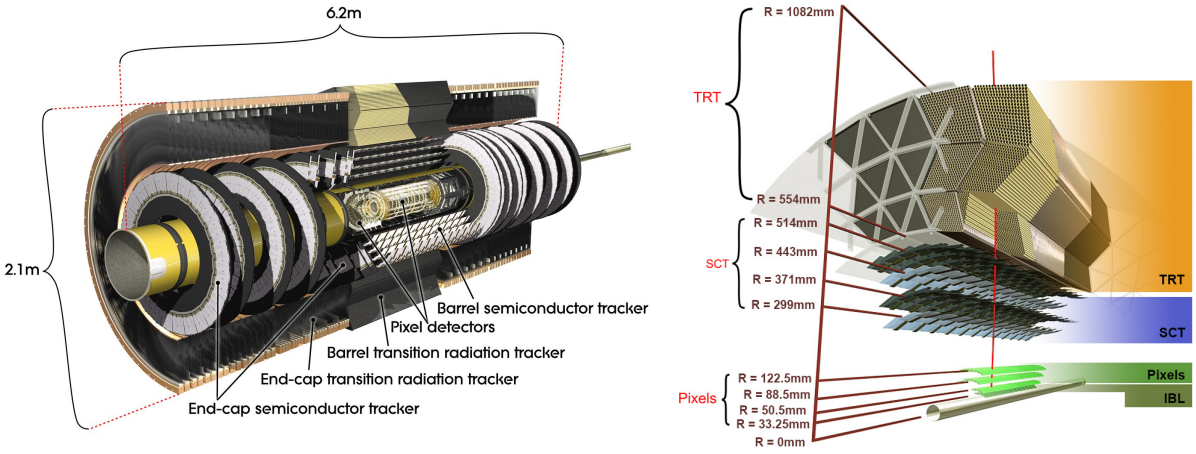

Figure IV.4.: Left: Detailed layout of the ATLAS inner detector. Right: A sector of the ID showing the different subdetectors and the new insertable B-Layer [132].

of around 250 µm, a size of 50×400 µm^2, and a resolution of 14×115 µm^2 in the (R, ϕ) plane and the z-direction, respectively[9]. A cooling system keeps the modules at a low temperature of around 0 °C to suppress electronic noise in the detector.

For Run II, several upgrades and improvements were applied on the pixel detector, like new optical connections, new service quarter panels and also software updates, such as new track reconstruction algorithms. Also, a fourth pixel layer, the new IBL, was inserted at a radius of 33.25 mm. The IBL consists of 14 staves, each with 20 modules. In total it has more than 12 million pixels with a size of 50×250 µm^2 and covers a pseudorapidity range of $|\eta| < 2.9$. Improvements attributed to the IBL are an enhanced tracking accuracy by providing an additional measurement point and a mitigation of inefficiencies in the three original layers due to radiation damage.

THE SEMICONDUCTOR TRACKER

The semiconductor tracker (SCT) is built around the pixel detector. It consists of four cylindrical barrel layers located at radii of 299, 371, 443, and 554 mm with respect to the beam axis. Nine planar end-caps discs are placed on each side. The layout of the SCT is very similar to the pixel detector, but instead of pixels, silicon microstrip sensors are used for the measurements.

It has 4088 modules covering an area of approximately 63 m^2. The 2112 barrel modules are two-sided and use microstrip sensors. Two sensors, each containing 768 active strips, with a nominal thickness of 285 µm and a strip pitch of 80 µm are mounted on both sides the modules. The end-cap disks use 1976 wedge-shaped modules of three different sizes. The modules in the barrel layer are tilted with a stereo angle of $\approx$40 mrad. This angle breaks the degeneracy along the z-direction and allows to measure three-dimensional space points. The same rotation angle is applied also for the end-cap discs. This sort of arrangement provides a very good position resolution for charged tracks and, therefore, a good momentum reconstruction. Including all active readout strips, the SCT layers have more than 6.3 million readout channels in total. The resolution of one channel is approximately 70×580 µm^2. A pseudorapidity range of $|\eta| < 1.5$ is covered by the barrel layers of the SCT, while the end-cap discs cover a region up to $|\eta| = 2.5$. The system is operated at temperatures between -10 °C and -5 °C in order to attenuate different types of electronic noise.

[9] The first number indicates the resolution in the (R, ϕ) plane, while the second number gives the resolution in z-direction.

THE TRANSITION RADIATION TRACKER

The transition radiation tracker (TRT) is the outermost part of the ID. Its basic detector elements are straw tubes with 4 mm diameter and a 0.03 mm diameter gold-plated tungsten wire in the center of the tube. In the barrel part, these tubes are arranged parallel to the beam axis placed at a radial region between 554 mm and 1082 mm with respect to the beam axis. It contains 50000 straw tubes with a length of 144 cm, divided into two parts with separate readout systems. The end-caps contain 250000 radial straw tubes of 37 cm length with the readout system connected to the outer radius.
The tracking in the TRT is based on transition radiation, which is emitted by charged particles traversing a boundary of two dielectric materials. The tubes are filled with a gas mixture of $Xe(70\%)$, $CO_2(27\%)$ and $O_2(3\%)$. A potential difference of 1.5 kV is applied to the central wire and the surface of the tube, producing an electric current via gas ionization induced by the transition radiation photons produced in polymer fibers (barrel) and foils (end-caps) surrounding the tubes. This current is detectable as a count in the readout system. Accordingly, this setup allows only to obtain an (R,ϕ) information. The single hit resolution is around 120 µm in the barrel region and 130 µm in the end-caps. Compared to the other parts of the inner detector, this is rather low. However, for each track, the TRT records around 30 hits, which significantly improves the spatial resolution of the track reconstruction if the information of the TRT is combined with the pixel detector and the SCT.
The TRT allows also particle identification by distinguishing between two different types of transition radiation thresholds for the signal readout. A low-threshold, optimized to detect direct ionization from particles penetrating the tube, whereas a high-threshold is sensitive to transition radiation photons. Emission of transition radiation is much more likely for electrons than for charged hadrons, meaning that the high-threshold probability is different over a wide energy range. This allows a discrimination of those particle types which is important, especially for an efficient separation between $\pi^{\pm}$ and $e^{\pm}$ tracks. The total number of readout channels in the TRT is approximately 351000. The barrel part covers pseudorapidities with $|\eta| < 1.1$. Including the end-caps, its total range is extended to $|\eta| < 2.0$.

IV.3.3. THE CALORIMETER SYSTEM

Calorimeters are intended to provide precise measurements of particle energies by absorbing them and to characterize the properties of the electromagnetic and hadronic showers induced by the particles. The shower properties can also be used for particle identification, in particular for particles which do not produce any tracks in the ID. Also for a reliable $E_{\mathrm{T}}^{\mathrm{miss}}$ measurement, an accurate energy determination with the calorimeter is essential.
The calorimeter system of ATLAS is built around the inner detector and is composed of two main subsystems. The inner part is the electromagnetic calorimeter [133] which is a liquid argon sampling calorimeter[10]. The outer part is an iron scintillator tile calorimeter sensitive to hadronic activities [134]. Both calorimeters consist of a barrel part and end-caps. The calorimeters are finely segmented, both in longitudinal and azimuthal direction to provide a good spatial resolution of the energy deposits and to get detailed information about the shower shapes. The total calorimeter system provides a pseudorapidity coverage up to $|\eta| = 4.9$. A cut-away view of the barrel part and the end-caps of the electromagnetic and hadronic tile calorimeter is given in Figure IV.5. Unlike particles producing electromagnetic or hadronic showers, muons do not strongly interact with the calorimeters and are mostly visible in the muon spectrometer instead. Thus, it is important that most of the energy of the detected particles is absorbed by the calorimeters to assure an uninhibited operation of the muon system.

[10] Sampling calorimeters consist of alternating layers of active and passive materials to subdivide (sample) the energy deposits.

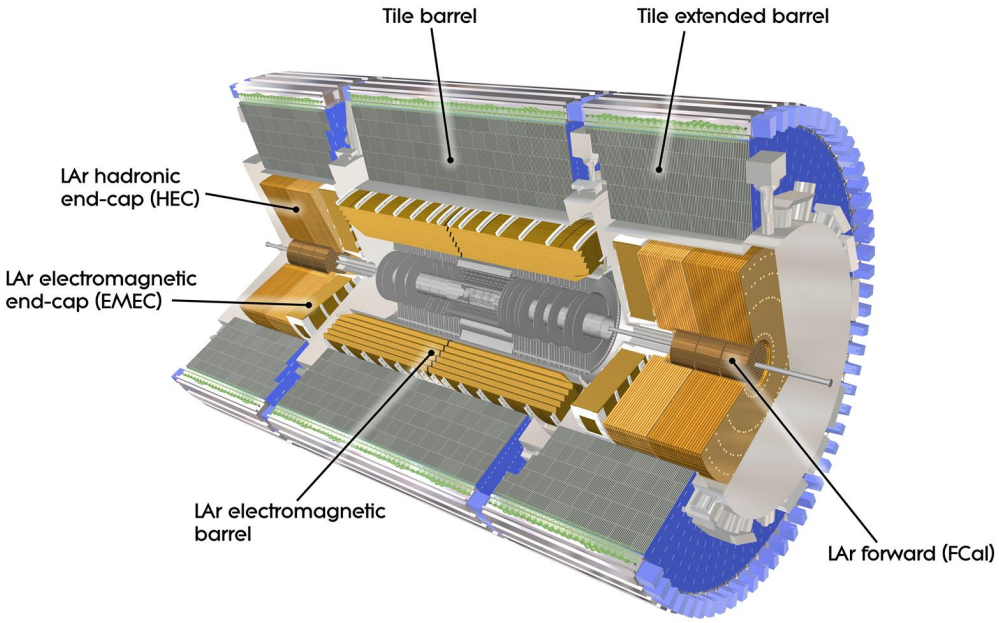

Figure IV.5.: Overview of the ATLAS calorimeter system: electromagnetic and hadronic calorimeter are divided into a barrel part, forward calorimeters, and end-caps [128].

ELECTROMAGNETIC CALORIMETER

The electromagnetic (EM) calorimeter is a high-granularity liquid argon (LAr) sampling calorimeter intersected with absorber plates made out of lead. To ensure a sufficient azimuthal coverage, the EM calorimeter has an accordion-like geometry. The readout electrodes and the lead absorbers are laid out radially and folded, such that particles cannot pass the calorimeter without traversing the active material and the absorbers. The structure is held in position by 2.1 mm honeycomb-shaped spaces. The liquid argon used as active medium is placed in the gaps between absorbers and readout electrodes and is cooled down to a temperature of $-183\,^{\circ}\mathrm{C}$. A potential difference of 2 kV between the electrodes and the absorbers is applied so that the charges induced by ionization of the argon drift towards the electrodes. The average drift time of the ionization products is about 450 ns.

The barrel part has a length of 6.4 m, an inner diameter of 2.8 m, and an outer diameter of 4 m. It consists of two identical half-barrels, separated by a small gap (4 mm) at $|z| = 0$ and covers pseudorapidities up to $|\eta| = 1.475$. Longitudinally, the barrel part is divided into three layers with different granularity which allows a more elaborated analysis of the shower shape. The first layer (strip-layer) has a granularity of $\Delta\eta \times \Delta\phi = 0.0031 \times 0.098$. Due to its fine η segmentation, it is suitable for distinguishing prompt photons from $\pi^0 \to \gamma\gamma$ processes. The second layer (middle-layer) has a granularity of $\Delta\eta \times \Delta\phi = 0.025 \times 0.0245$ and records the central part of the shower. It is also the thickest layer among the three. The third layer (back-layer) has a granularity of $\Delta\eta \times \Delta\phi = 0.0245 \times 0.05$ and measures the tails of high-energy electromagnetic showers. It can be used to distinguish electromagnetic from hadronic deposits. An additional 11 mm LAr layer (denoted as presampler) with a fine η segmentation of 0.2 is placed in front of the EM calorimeter in the region $|\eta| < 1.8$, which is used to correct for energy losses in the ID and in the central solenoid. On the left-hand side of Figure IV.6, a schematic view of a barrel module with its three layers is given.

The end-caps for the EM calorimeter (EMEC) extend the pseudorapidity coverage to $|\eta| < 3.2$ and are divided into inner and an outer end-caps, with a spacing of approximately 3 mm between them. The inner

end-caps consist of three layers (as the barrel part), while the outer end-caps have only two layers with a coarser transverse granularity.
At high energies, the absorption power of a calorimeter can be quantified in a material-independent way by using the *radiation length* X_0 of its medium, which is defined as the distance over which the particle energy is reduced by a factor $1/e$ due to radiation losses. In terms of radiation lengths, the thickness of the electromagnetic calorimeter is 22 X_0 in the barrel part and 24 X_0 in the end-caps. Including the presampler and the different layers in the barrel part and the end-caps, the EM calorimeter has in total about 170000 readout channels. It provides a high intrinsic energy resolution of $\sigma_E/E = 10\%/\sqrt{E} \oplus 0.7\%$.

HADRONIC CALORIMETER

The hadronic calorimeter is located around the EM calorimeter. Since the average particle interaction length of hadronic showers is larger than for particles interacting electromagnetically, the hadronic calorimeter needs to be larger.
The barrel part can be subdivided into a central barrel with a length of 5.8 m and two extended barrels, 2.6 m in length, each having an inner diameter of 4.6 m and an outer diameter of 8.5 m. A small gap ($\approx$60 cm) between the central and the extended barrels where LAr pipes and readout cables are routed provides only limited instrumentation. It uses steel as absorber and scintillator plastic tiles as active medium. The scintillating tiles emit light when charged particles pass through them and are read out by photomultiplier tubes at the tile edges using wavelength shifting fibers. The central and both extended barrels consist of 64 wedge-shaped modules containing several tiles and covering a sector of $\Delta\phi = 0.1$. In total, about 500000 tiles are installed in the barrels. The right-hand side of Figure IV.6 shows a module of the tile calorimeter with the alternating steel-scintillator structure and the photomultiplier. Similar to the EM calorimeter, the barrels are longitudinally divided into three layers. The first two layers have a granularity of $\Delta\eta \times \Delta\phi = 0.1 \times 0.1$, while the third layer has $\Delta\eta \times \Delta\phi = 0.2 \times 0.1$. The barrel part can cover pseudorapidities up to $|\eta| = 1.7$.
The end-caps of the hadronic calorimeter consist of two parts: the hadronic end-cap (HEC) and the forward calorimeter (FCal)[11] [135]. Unlike the barrel part, the HEC and the FCal are LAr calorimeters. The hadronic end-cap calorimeter consists of two independent wheels per end-cap placed behind the end-caps of the EM calorimeter. They are made of 32 wedge-shaped modules with a similar structure as the EMEC calorimeters and cover a range of $1.5 < |\eta| < 3.1$. The segmentation of the modules is $\Delta\eta \times \Delta\phi = 0.1 \times 0.1$ for the region $|\eta| < 2.5$ and twice as coarse for larger pseudorapidities. The forward calorimeter covers a range of $3.1 < |\eta| < 4.9$ and is placed approximately 4.5 m from the interaction point, behind the EMEC and surrounded by the HEC. It has three complementary layers and is sensitive to both electromagnetic and hadronic signatures. The first layer uses copper as absorber material and is optimized for electromagnetic interactions, whereas the second and third layer are mainly made out of tungsten to detect hadronic showers. The FCal layers use a structure of copper/tungsten rods centered in tubes which are arranged parallel to the beam axis. Small gaps (0.27–0.51 mm) between the rods and the outer perimeter of the tubes are filled with LAr as the active medium for the particle detection. The smaller gap size leads to a lower LAr drift time of approximately 60 ns and therefore to a faster readout (higher time resolution) compared to the electromagnetic calorimeter.
Including the HEC, the FCal, and the tile calorimeter, the hadronic calorimeter has almost 20000 readout channels. In the barrel and the end-caps, the energy resolution is $\sigma_E/E = 50\%/\sqrt{E} \oplus 3\%$. The forward region ($3.1 < |\eta| < 4.9$) has a resolution of $\sigma_E/E = 100\%/\sqrt{E} \oplus 10\%$.

[11] Since the FCal is also sensitive to EM signatures, it is technically a separate system and not part of the hadronic calorimeter.

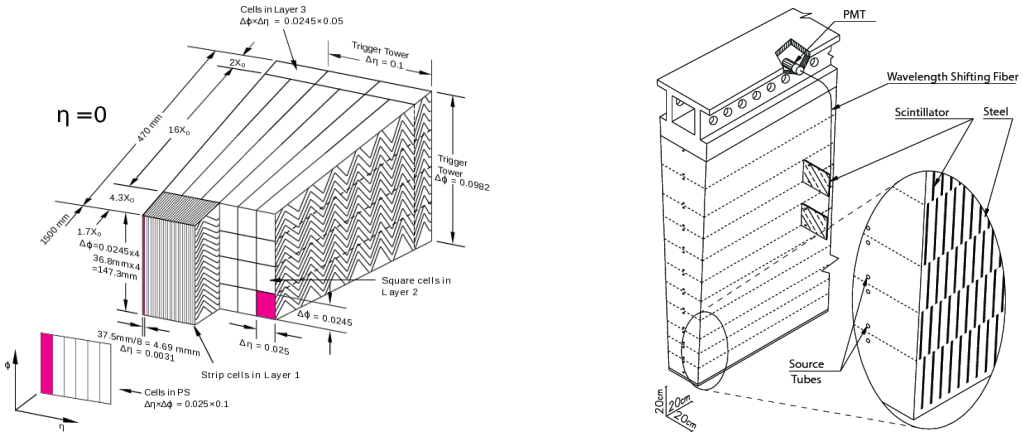

Figure IV.6.: Left: Schematic view of a barrel module of the LAr calorimeter including its three different layers. Right: A module of the tile calorimeter with its alternating steel-scintillator structure [2].

IV.3.4. THE MUON SPECTROMETER

The muon spectrometer (MS) [136] is the outermost system of the ATLAS detector. It is designed especially for an efficient muon identification and high-precision momentum measurements of muons tracks, complementary to the information provided by the inner detector. The MS is built around the outer calorimeters and has a volume of around $1.9 \cdot 10^4\,\mathrm{m}^3$ which is almost 90% of the total detector volume. The system is composed of a barrel part and three sets of end-cap discs with increasing diameter (referred to as small, big, and outer-wheel). The barrel part has a length of 24 m and a diameter of 20 m. The three types of end-caps have diameters of 10, 23, and 25 m and are located at distances of around 7.5, 13.5, and 21.5 m from the interaction point[12]. Figure IV.7 shows the layout of the muon spectrometer including all subsystems (left) as well as a cross-section of its barrel part (right).

The trajectories of the muons are recorded with monitored drift tubes (MDT). They are assembled in several chambers which are arranged around the barrel part and in the end-cap discs. At large pseudorapidities, cathode strip chambers (CSC) are used which are multi-wire proportional chambers with cathodes segmented into strips. Resistive plate chambers (RPC) mounted together with the MDT chambers in the barrel part and thin gap chambers (TGC) instrumented around the second end-cap can identify potential muon tracks and are used as fast trigger detectors. They also provide an additional coordinate measurement of the muon track complementary to the other systems.

The muon spectrometer covers a pseudorapidity range of $|\eta| < 2.7$ with the full information from the trigger systems available up to $|\eta| = 2.4$. It provides muon momentum measurements starting from 3 GeV to 1 TeV. The momentum resolution of the spectrometer is $\sigma_{p_\mathrm{T}}/p_\mathrm{T} = 2-4\%$ in the p_T range of 10–200 GeV and $\sigma_{p_\mathrm{T}}/p_\mathrm{T} = 10\%$ at $p_\mathrm{T} = 1$ TeV.

MONITORED DRIFT TUBES

The monitored drift tube chambers are installed in the barrel part and in the end-cap discs of the muon spectrometer. They have rectangular shapes in the barrel and are trapezoidal shaped in the end-caps. In the barrel part, the chambers are arranged in three subsequent layers which are embedded in the toroid magnet system of the detector. On the right-hand side of Figure IV.7, the arrangement of the chambers around the toroid coils is illustrated. Each chamber contains several (typically 3–8) layers of muon drift

[12] An additional layer, denoted as extended end-cap (EE) is located at a distance of 10.5 m from the IP between the small and big wheel with an inner(outer) diameter of 12(18) m.

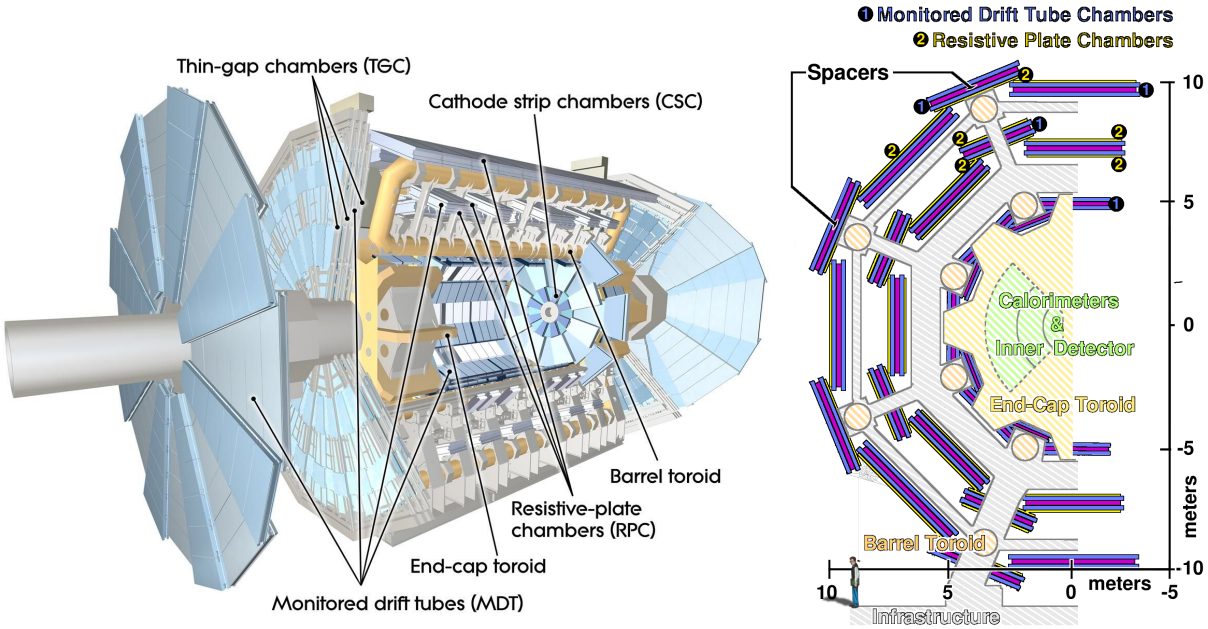

Figure IV.7.: Muon spectrometer magnets and subsystems of the ATLAS detector: a cut-away view (left) and a cross-section of the barrel part (right) [128].

tubes used for the reconstruction of muon tracks. The full $|\eta| < 2.7$ range of the muon system is covered by MDT chambers[13]. In total, 1108 chambers with more than 350000 drift tubes are instrumented in the spectrometer. In 2015, some additional chambers were installed at the end-caps. The absolute number of MDT readout channels is around 339000.

The muon drift tubes have a diameter of 3 cm and a length varying from 0.85 to 6.5 m, depending on the position of the chamber in the detector. They have an aluminum surface and a tungsten-rhenium wire with a diameter of around 50 µm running through the center. The tubes are filled with a gas mixture of $Ar(93\%)$ and $CO_2(7\%)$ with a pressure of 3 bar. A voltage of 3080 V is applied between the tubes surface and the wire. A muon traversing the tube ionizes the Ar/CO_2 gas and the produced electrons drift towards the central tungsten wire where they are amplified and detected as a signal by the readout system. The average drift time of the tubes is about 700 ns. In the z-direction, the resolution is around 80 µm for a single tube and 35 µm per chamber.

Cathode Strip Chambers

The cathode strip chambers are part of the innermost end-cap discs and cover a region with large pseudorapidities of $2.0 < |\eta| < 2.7$. They are multi-wire proportional chambers with multiple closely separated anode wires and cathode strips orthogonal to the wires. Similar to the MDT chambers, they are filled with an Ar/CO_2 gas mixture but with a higher CO_2 fraction ($\approx 20\%$).

Due to their higher resolution and lower response time they are more suitable than the MDT chambers in the forward region of the detector, where the event rates are typically higher. Furthermore, with their orthogonal layout it is possible to measure the charge distribution in both x- and y-direction, allowing a two-dimensional spatial resolution of the detected objects. The chambers are operated with a nominal voltage of 1.9 kV. Smaller anode-cathode distances (2.5 mm) yielding much lower drift times with respect to the MDT chambers, resulting in an enhanced time resolution of around 7 ns. The spatial resolution

[13] Except the innermost end-cap, where the MDT chambers cover only a region $|\eta| < 2.0$ due to the CSC.

of a chamber is 40 µm in the bending plane and about 5 mm in the transverse direction. Including both end-caps, the MS has 32 cathode strip chambers with approximately 30000 active readout channels.

RESISTIVE PLATE CHAMBERS

Resistive plate chambers provide the muon trigger system in the barrel part of the MS. Three RPC layers (trigger stations) are installed in the barrel attached to the second and third layer of MDT chambers covering a pseudorapidity of $|\eta| < 1.05$. Each station consists of two independent detector layers, measuring the ϕ and η coordinates of the track.
A layer is build of two parallel resistive plates, made of phenolicmelaminic plastic laminate. The 2 mm gap between the plates is filled with a mixture of $C_2H_2F_4(94.7\%)$, Iso-$C_4H_{10}(5\%)$ and $SF_6(0.3\%)$ which is ionized by the muons crossing the layers. They are operated with an electric field of 4.9 kV between the two plates. The readout of the signal works via capacitive coupling to metallic strips which are attached to the outer surface of the resistive plates. A muon penetrating all three trigger stations delivers six hits with a ϕ and η information.
The RPCs are used to identify muon tracks and also provide a second coordinate measurement complementary to the MDT chambers in the central region. The spatial resolution is 10×10 mm in z- and ϕ-direction, while the time resolution is ≈ 1.5 ns. The 544 chambers provide around 360000 readout channels in the spectrometer.

THIN GAP CHAMBERS

A higher occupancy and radiation level in the forward region demands a separate system for identifying muon tracks. The trigger system of that region is built by thin gap chambers covering a range of $1.05 < |\eta| < 2.4$. In addition, they provide a determination of the azimuthal coordinate of the track in the bending direction complementing the information given by the MDT chambers.
Nine TGC layers are installed at the end-caps of the MS. Two at the first and seven at the second end-cap disc. They work similar to the CSC modules (multi-wire proportional chambers) with graphite layers as cathodes and tungsten wires as anodes. However, the distance between wire and cathode (1.4 mm) is smaller than the wire-to-wire distance (1.8 mm) yielding a higher resolution than the CSCs. A gas mixture of $CO_2(55\%)$ and n-$C_5H_{12}(45\%)$ with a gain of $\approx 3 \cdot 10^5$ allows an operation in quasi-saturated mode. A potential difference of 2.9 kV is applied between anodes and cathodes, with strips connected to the outer surface of the graphite layers performing the signal readout.
The spatial resolution per chamber is 3–12 mm in z-direction and about 8 mm in ϕ-direction, while the time resolution is around 4 ns. The 3588 chambers mounted at the end-caps provide in total around 318000 readout channels.

IV.3.5. TRIGGER SYSTEM IN ATLAS

A highly efficient trigger system is required by the ATLAS detector to reduce the overwhelming amount of data delivered by the LHC and to select potentially interesting events.
The trigger system used in RunI was three-level trigger system using a successive selection of events with interesting topologies by different trigger stages [137]. The system consisted of a hardware-based trigger (L1), a high-level software trigger (L2), and event filter triggers (EF) which was capable to reduce the rate of processed events during a nominal run from initially around 1 GHz to below 200 Hz. The L1 trigger implemented in the muon system (L1Muon) and the calorimeters (L1Calo) were based on coincident hits in the muon trigger stations or on local energy deposits in the calorimeters in order to

select the detector area with a potentially interesting event, the so-called Region of Interest (RoI). The L2 software trigger retrieved the information about the RoI provided by L1 and reconstructed the event in this area using the full resolution data, including also tracking information from the ID. At the EF level, the complete information about the accepted event (not only in the RoI) with the full capabilities of all detector subsystems was considered[14]. This allowed an event selection based on more complex object definitions, comparable to the objects reconstructed offline.
For Run II, the trigger and data acquisition system has been revised in order to cope with the increased trigger rates while maintaining its efficiency in selecting physics processes of interest [138, 139]. The diagram in Figure IV.8 outlines the ATLAS trigger and readout system as it is used for the current data taking.

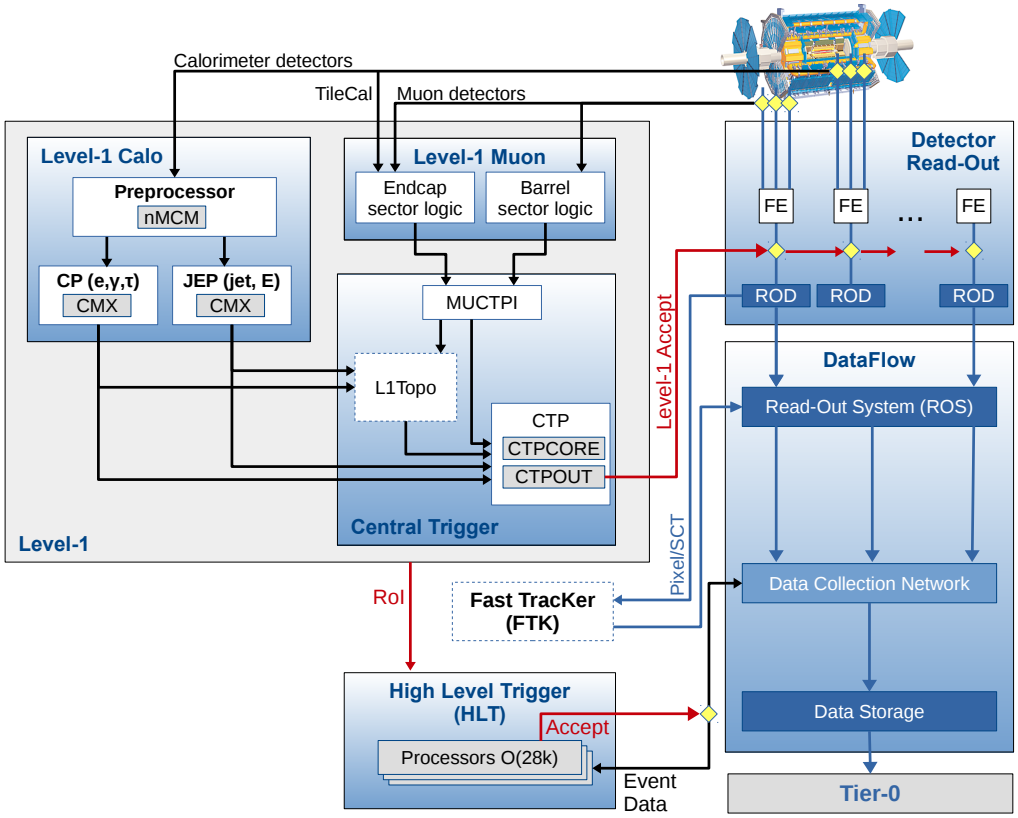

Figure IV.8.: The trigger and readout system as it is used in ATLAS since Run II. The trigger system can be subdivided into a level-1 part and a high-level trigger (HLT) [139].

The main difference is that the formerly separated L2 and the EF frameworks were merged into a single homogeneous high-level trigger system (HLT), which reduces the complexity and allows for dynamic resource sharing between the algorithms of the two trigger levels. The L1Muon and L1Calo triggers were not significantly changed with respect to Run I. The level-1 muon trigger system consists of a barrel part and two end-caps and makes a decision based on coincidences of hits in the RPC and TGC layers (see Section IV.3.4). Coincident hits are defined by the positions of the tracks as well as the p_T of the muon candidates. The installation of additional trigger chambers and an updated coincidence-logic for Run II increased the acceptance and mitigated the rate of non-prompt muons in the trigger system.

[14] A system called event builder (EB) was used to recombine the event fragments selected by L2 with the buffered full event information.

The L1Calo trigger uses a sliding-window algorithm on calorimeter segments with a coarse granularity of $\Delta\eta \times \Delta\phi = 0.1 \times 0.1$, denoted as *trigger towers* to identify considerable energy deposits. Separate algorithms are responsible for the identification of jet, $E_{\mathrm{T}}^{\mathrm{miss}}$ objects, and $e^{\pm}$, γ, or $\tau^{\pm}$ candidates. The latter objects are defined by 2×2 trigger tower clusters in the EM calorimeter for which the sum of the transverse energy from at least one of the four possible pairs of nearest neighbor towers exceeds a predefined threshold. The neighbor towers around the selected cluster need to fulfill specific isolation requirements. Jet candidates are defined by 4×4 or 8×8 clusters in the electromagnetic and the hadronic calorimeter with a threshold on the transverse energy of the central 2×2 cluster in the RoI. Several minors updates were made for Run II, such as using a reduced granularity of the calorimeters, an improved readout system, or updated algorithms which are more stable against pile-up effects.
The level-1 trigger decision is made by the central trigger processor (CTP) using the input from the L1Muon and L1Calo triggers. In 2015, a new topological trigger system (L1Topo) [140] was included in the level-1 decision performing selections based on the combined geometric and kinematic information of trigger objects received from the L1Calo and L1Muon systems. The entire level-1 filter reduces the initial event rate already to around 100 kHz. If an event is accepted by L1, it is further analyzed at the HLT stage, which reprocesses the event using the full granularity detector information. In contrast to the former trigger scheme, where partial event data from L2 had to be recombined with the buffered full event information using a dedicated event building algorithm, a common framework incorporating the event building and the actual trigger selection based on the reconstructed objects is used in the HLT system. For some triggers sensitive to frequent event signatures, *prescales* (selecting only a specific fraction of events) are applied to reduce the final output rate of the trigger.
An additional feature included since the 2017 data taking is a hardware-based track reconstruction at trigger level with the new fast tracker system (FTK) [141]. It was designed to reconstruct tracks in the ID for events passing the L1 trigger. This allows the HLT to have early access to tracking information leading to an enhanced purity of triggered events. In particular, the rejection of objects accidentally reconstructed as electrons can be improved by combining the track information with the L1Calo input. However, due to its late commissioning, the FTK has not been used for the Run II data collected in 2015 and 2016.
Events passing the full trigger chain are eventually stored permanently at the CERN computing facility (Tier-0). They are also replicated and distributed to numerous smaller national computing centers (Tier-1 and Tier-2)[15] using the worldwide LHC computing grid [142].

IV.4. Forward Detectors and Luminosity Determination

An accurate measurement of the luminosities delivered to the detector is crucial for a precise cross-section determination of any kind of physics process. The luminosity measurements are performed by different dedicated luminosity detectors placed at the beam pipe before and after the collision point, such as the ALFA[16] [143] or the LUCID[17] [144] detectors.
The LUCID detectors are designed to monitor instantaneous luminosities in real time. They are located at distances ± 17 m with respect to the interaction point. Each detector has 16 photomultipliers close to the beam pipe and four quartz fiber bundles. The photomultipliers detect the Cherenkov light produced if charged particles traverse the quartz window. This setup allows determining the number of charged

[15] Tier-1 centers are usually large national computing facilities with a big storage capacity, while Tier-2 centers are universities and other scientific institutes with smaller resources.
[16] ALFA: Absolute Luminosity For ATLAS.
[17] LUCID: LUminosity measurement using Cherenkov Integrating Detector.

particles in the far forward region. It can be translated into the luminosity during specific time intervals were it is assumed to be constant (so-called "lumi-blocks"). For Run II, the electronic readout system of the Cherenkov detectors was updated to cope with the higher bunch crossing rate, an increased pile-up environment, as well as higher instantaneous luminosities [145].
The ALFA setup is installed at distances ± 240 m from the interaction point. It consists of four so-called *Roman pot* [146] stations, special movable devices, which are connected to the accelerator vacuum via bellows and can be inserted directly into the beam pipe. The Roman pot detectors use scintillating fiber modules as active material and can be moved to a distance of 1 mm towards the proton beam. Figure IV.9 shows a simplified illustration of this setup. The purpose of the ALFA detector is to determine the absolute luminosity scale by measuring elastic pp scattering at very small angles, which can be related to the total cross-section using the optical theorem. The measurements are performed during dedicated beam-separation scans, denoted as *van der Meer scans* [147], since the angular separation of the elastic scattering processes (≈ 3 µrad) is smaller than the beam divergence during normal runs.

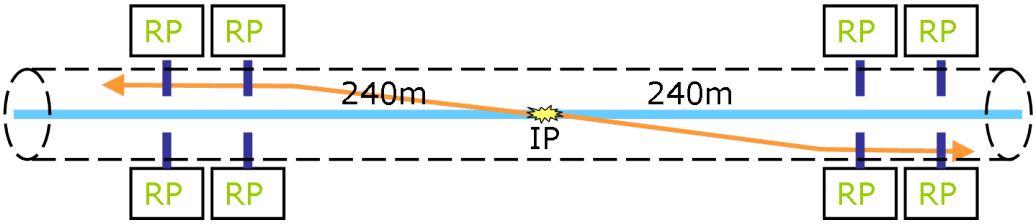

Figure IV.9.: The ALFA setup with the four Roman pot detectors at each side of the interaction point. The orange line illustrates the elastic pp interaction at small scattering angles [143].

The final luminosity determination works with a combination of the absolute luminosity scale and the relative luminosities measured during data taking. With this method, the luminosities recorded by ATLAS during Run I and II could be measured with a high level of precision. The relative uncertainty of the 20.3 fb^{-1} of physics data collected in Run I during 2012 was 2.8% [148]. For the 36.1 fb^{-1} taken in 2015 and 2016, the uncertainty is approximately 3.2% [109].

IV.5. Run II Performance of the ATLAS Experiment

After Run I was completed in 2013, the accelerator complex shut down for two years of maintenance of the superconducting magnets in the collider ring and preparation for higher center-of-mass energies (Long Shutdown 1). As already discussed, numerous updates on the different detector systems have been applied during this period as well. Run II started in 2015 and completed in the meanwhile two and a half years of successful data taking, collecting more than 80 fb^{-1} of data. Run II is planned to be finalized at the end of 2018 expecting 100–150 fb^{-1} of recorded data [149]. Afterwards, another long shutdown is scheduled to prepare for Run III which is planned to be commissioned in 2021.
In the first year after the shutdown, the amount of collected data was moderate with respect to the performance in 2016. Since many systems were still in commissioning phase and the accelerator had to be consolidated with the increased center-of-mass energies, only around 3.5 fb^{-1} of data could be recorded by ATLAS in 2015. In the second year, the LHC operated under more stable conditions and more than ten times of the data taken in 2015 could be collected[18]. In Run II, the data taking efficiency (ATLAS

[18] Note that the amount of data recorded by ATLAS is usually lower than the data delivered by the LHC due to temporary standby modes of the detector and inefficiencies of the data acquisition system.

recorded versus LHC delivered) was typically 92–94%. The final integrated luminosities used in physics analyses are usually also slightly lower than the ones recorded by the detector, since specific data quality criteria are applied beforehand.
On the left-hand side of Figure IV.10, the cumulative luminosity versus time delivered by the LHC (green) and recorded by the ATLAS detector (yellow) during the year 2016 is shown. On the right, a comparison of these evolutions for all years of pp collision data taking (2011–2012[19] for Run I and 2015–2017 for Run II) is given, demonstrating the improved performance of the LHC and ATLAS within the recent years.

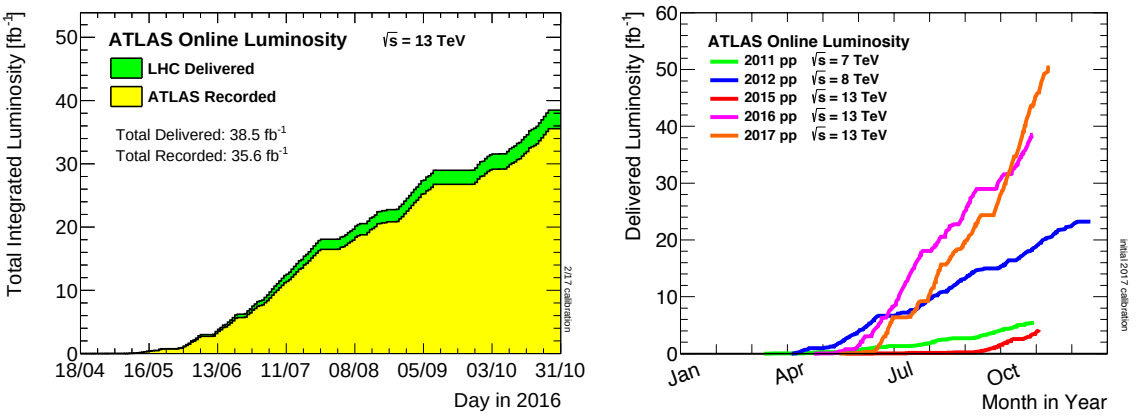

Figure IV.10.: Left: Cumulative luminosity versus time delivered to (green) and recorded by ATLAS (yellow) in 2016. Right: Comparison of the cumulative luminosities versus time for the years 2011–2017 [109].

Also in terms of the instantaneous luminosities, higher values could be achieved over the past few years. While the peak luminosity was $5 \cdot 10^{33}$ cm^{-2}s^{-1} in 2015, it could be increased to $1.38 \cdot 10^{34}$ cm^{-2}s^{-1} and $2.06 \cdot 10^{34}$ cm^{-2}s^{-1} in 2016 and 2017, respectively. The higher instantaneous luminosities naturally cause an intensification of the pile-up conditions (see Section III.3.5). The average number of interactions per bunch crossing increased from about 14 in 2015 to $\approx$25 in 2016. In the year 2017, a mean value of around 38 was reached. However, this issue can be addressed with more sophisticated trigger systems and improved offline calibrations of the reconstructed physics objects. Table IV.1 summarizes the main parameters for the recent years of LHC data taking, showing that the performance could be continuously improved during Run II, with 2017 being the most successful year so far.

	Run I		Run II		
Year	2011	2012	2015	2016	2017
$\sqrt{s}$ [TeV]	7	8	13	13	13
Bunch spacing time [ns]	50	50	25	25	25
$\langle\mu\rangle$	9.1	20.7	13.5	24.9	38.3
Peak luminosity [10^{33} cm^{-2}s^{-1}]	3.65	7.73	5.0	13.8	20.6
Total luminosity [fb^{-1}]	4.6	20.3	3.2	32.9	43.8

Table IV.1.: Summary of the run conditions during pp collision data taking for Run I and II. The total luminosities are the values used for physics analyses with data quality criteria applied.

[19] Already in 2010, 45 pb^{-1} of data have been recorded by ATLAS. However, this can be neglected with respect to the amount of data recorded in the subsequent years.

V. Object Reconstruction and Particle Identification in ATLAS

The variety of different particle types which can be created at a proton-proton collision is enormous. A crucial task for all physics analyses is a reliable reconstruction and identification of the physics objects out of the raw data delivered by the different detector subsystems. In particular for analyses looking at signatures with multiple leptons, as it is the case for the same-sign or three-lepton search described in this thesis, an adequate identification of electrons and muons is essential for a stable background estimation and a reliable interpretation of the results. Also, the reconstruction of jets and a precise estimation of the missing transverse energy is necessary, since the jet topology and the $E_{\mathrm{T}}^{\mathrm{miss}}$ are important quantities for the definitions of many signal regions used in this analysis.
In this chapter, the methods of object identification and reconstruction as they are used in ATLAS for Run II are presented. Furthermore, the techniques used for the calibration of these objects and how to estimate their efficiencies in data and Monte Carlo are briefly reviewed. Section V.1 and V.2 describe the identification of muons and electrons, how their reconstruction efficiencies are obtained, and which approaches are used to correct the momentum scale/resolution of simulated events in order to be comparable to data. The reconstruction and calibration of jets are explained in Section V.3. Also, the most recent approaches how to identify (tag) jets originating from b-hadrons (b-jets) are addressed. Finally, Section V.4 is dedicated to the estimation of the missing transverse energy which can only be done properly if the momenta of all other objects in an event are computed precisely[1].

V.1. Muons

Since the analysis discussed in this thesis focuses on multi-lepton signatures, muons are some of the key objects for this type of search. They are also crucial for many Standard Model measurements, like the determination of important properties of the Higgs boson. In contrast to most other particle types produced in pp collisions, muons traverse usually the entire detector without significant energy losses. However, as they are electrically charged, they leave tracks in the inner detector and the muon spectrometer. Since the MS is permeated with an additional magnetic field generated by the outer toroids, it provides complementary p_{T} measurements of the muons. The information from the individual subdetectors is then usually combined to improve the precision of muons tracks used for physics analyses [150].

V.1.1. Reconstruction and Identification

The reconstruction of muon tracks is performed with separate methods in the inner detector and the muon spectrometer. Both of them are essential for a high-quality muon identification.
In the ID, muon tracks are reconstructed like any other charged particle with dedicated tracking algorithms [151, 152] which can build tracks for particles with a momentum threshold of $p_{\mathrm{T}} > 400$ MeV in a region up to $|\eta| = 2.5$. Hits in the pixel detector are directly translated into space points, while for the SCT, two hits are needed to reconstruct one space point. The drift time information from the TRT is used to construct so-called drift circles around the wires which can be juxtaposed to obtain a two-dimensional resolution of the trajectory. Two types of tracking algorithms are used: an *inside-out* and an *outside-in* approach. The inside-out algorithm starts the track reconstruction with the space point information from

[1] Since tau leptons and photons are of minor relevance for the analysis presented in this thesis, they are not discussed here. However, they are needed for a correct $E_{\mathrm{T}}^{\mathrm{miss}}$ computation.

the pixel detector and the SCT, extrapolates it to the TRT considering the magnetic field configuration, and merges the initial track seed with the TRT hits to complete it. The outside-in approach works the other way around, starting the track building from the TRT hits, extrapolates it to the interaction point, and combines the track components with the hits in the SCT and the pixel detector. While the inside-out approach is the baseline algorithm for track building, the purpose of the outside-in algorithm is to reconstruct trajectories which cannot be associated with a vertex close to the IP (originating e.g. from photon conversions). In Run II, the spatial resolution and efficiency of the tracking algorithms could be improved due to additional hits recorded with the new insertable B-Layer.
Track vertices are defined by selecting the maxima of track distributions along the beam axis and re-fitting all trajectories under the assumption that they originate from these points. The quality of the fit is given by its χ^2-value[2] which has to satisfy specific selection criteria. Each partial track has to be associated with a reconstructed vertex, otherwise it is discarded by the algorithms. A matching with the primary interaction vertex[3] discriminates primary from secondary tracks. The identification of the primary vertex allows to define longitudinal and transverse impact parameters z_0, d_0 of the tracks. They are given by the closest distance of the fitted trajectory to the reconstructed primary vertex in the longitudinal and transverse plane. Requirements on these parameters provide an efficient identification of tracks originating from the primary vertex which is relevant e.g. for the rejection of cosmic muons.
The reconstruction in the muon spectrometer is done with the MDT chambers: a linear fit is performed according to the hits recorded in each layer. The hits in the RPC and TGC layers allow measuring the coordinate orthogonal to the bending plane. The measurements from the CSC segments complement the MDT information for a pseudorapidity range of $|\eta| < 2.0$. Muon track candidates are built by performing a combined fit with hits from segments in different layers. The fitted track seeds are then consecutively extended to other layers and matched to each other, according to their hit multiplicity and fit quality. At least two matching segments are needed to build a track. A subsequent algorithm selects the best assignment for each fitted trajectory and removes overlapping tracks candidates. The global fit result is afterwards either accepted or discarded according to its χ^2 distribution.

The combined muon reconstruction is done with to the information provided by the ID and the MS using the *Chain 3* algorithm [153] by default since Run II. Muon candidates can be categorized according to the subdetectors used in the combined reconstruction. For the muons used in physics analyses, overlaps between the categories are removed. Four different muon types are defined:

- **Segment-tagged (ST) muons:**

  Segment-tagged muons are reconstructed from ID tracks and have to fulfill a matching requirement with at least one local track segment in the MDT or CSC chambers. This muon type is used when muons pass only one layer in the spectrometer due to a low p_{T} or if the track is in a pseudorapidity region with a reduced acceptance of the muon system.

- **Calorimeter-tagged (CT) muons:**

  Calorimeter-tagged muons are identified similar to ST muons, but with the matching requirement between the ID track and an energy deposit in the calorimeter. The calorimeter deposit has to be compatible with the signature of a minimum-ionizing particle. The identification for CT muons is

[2]The value of χ^2 is defined according to the *goodness-of-fit* test: for n hits (measurements) $\chi^2 = \sum_{i=1}^{n} \frac{(x_i - f_i)^2}{\sigma_i^2}$, where x_i denote the observed space points and f_i, σ_i the expected mean values (variances) asserted by the fit hypothesis.
[3]The primary vertex is defined as the vertex with the largest $\sum p_{\mathrm{T}}^2$ of the associated tracks.

optimized for a momentum range from 15 to 100 GeV and a pseudorapidity region of $|\eta| < 0.1$. In this region, the MS is only partially operated to allow for cabling and services to the calorimeters and the ID. Therefore, this identification method intends to recover the acceptance of the MS, although its purity is lower with respect to other muon types.

- **Extrapolated (ME) muons:**

  The identification of extrapolated muons relies only on the track from the muon spectrometer. The extrapolated MS track has to be (to some extent) compatible with the location of the interaction point. The parameters of the muon track are defined at the IP, taking into account the calculated energy loss of the muons in the calorimeter system. The muon candidate is required to pass two (three) layers in the barrel region (end-caps) of the MS. This approach allows to extend the muon reconstruction acceptance to large pseudorapidities $2.5 < |\eta| < 2.7$ that are not covered by the ID anymore.

- **Combined (CB) muons:**

  The constituents of combined muon tracks are reconstructed independently in the ID and MS. The CB track is built with a global refit that uses the hit information from the ID and MS subdetectors. The global fit follows an outside-in pattern recognition, in which the muons are first reconstructed in the MS and then extrapolated and matched to an ID track. An inside-out combined reconstruction, where ID tracks are matched to MS tracks is used as a complementary approach to improve the efficiency of the track combination. During this fit procedure, MS hits can be added to or removed from the track to improve the overall fit quality. The muon momentum is recalculated using the curvature of the combined track.

The identification of muon candidates is done by applying quality requirements in order to suppress background e.g. from meson decays or photon conversions. According to the criteria applied, several default muon identification selections (muon qualities) can be defined. In 2015 and 2016, four distinct muon qualities were provided to address the specific conditions of different physics analyses. They are based on the following criteria:

- ***Loose*** is the lowest quality criteria used for muon identification. All muon types described above are used for the *loose* selection. Selected CB tracks need to have >2 hits in at least two MDT layers. ME tracks are required to have hits in at least three MDT/CSC layers and are only used in a region $2.5 < |\eta| < 2.7$. Furthermore, the p_{T} measured in the ID and the MS have to fulfill a compatibility requirement. The q/p significance[4] of the trajectory has to be less than seven. CT and ST muons are used in the $|\eta| < 0.1$ region to extend the total acceptance.

- ***Medium*** is the default muon quality and used for most physics analyses. It is defined similar to the *loose* configuration but using only CB and ME tracks.

- ***Tight*** is the highest muon quality criteria with the largest purity of prompt muons. Only CB muons satisfying the *medium* conditions are used. Additionally, the fit has to fulfill a more stringent χ^2 requirement of <8 and a p_{T} dependent cut on the q/p significance is applied to improve the rejection of non-prompt muons at low momenta. Also, a stricter condition on the relative momentum

[4]The q/p significance is defined as the difference between the ratio of the charge and momentum of the muons measured in the ID and MS divided by the quadratic sum of their uncertainties.

difference measured in the ID and the MS ($|p_{\mathrm{T}}^{\mathrm{ID}} - p_{\mathrm{T}}^{\mathrm{MS}}|/p_{\mathrm{T}}^{\mathrm{CB}}$) with respect to *medium* is set to reduce the impact of mismeasured tracks.

- ***High-p_T*** is a special quality criteria designed to improve the momentum resolution for muons with a high transverse momentum of $p_{\mathrm{T}} > 100$ GeV. Only CB muons passing the *medium* selection and having at least three hits in three distinct MS layers are selected. This selection is optimized especially for Z' and W' searches.

V.1.2. EFFICIENCY MEASUREMENTS AND CORRECTIONS

Not all muons created in a pp collision can be reconstructed or identified with the methods described above. The reconstruction efficiencies for the different muon quality types have to be derived with specific approaches depending on their transverse momentum and their position in the detector. Furthermore, the difference between the efficiencies measured in real data and in simulated events has to be determined and corrected in Monte Carlo in order to reproduce the data efficiency.
The reconstruction efficiency for muons is obtained with a so-called *tag-and-probe* method. This technique relies on preselected $Z^0 \to \mu\mu$ or $J/\psi \to \mu\mu$ samples with a very high purity of prompt muons. One leg of the two-body decay has to be selected by a muon trigger and is identified using the *medium* requirements (tag muon), while the other leg has to be reconstructed according to the object selection to be measured. The invariant mass of both objects needs to be compatible with a Z^0 or J/ψ decay. The actual efficiency ε is calculated by dividing the number of selected probe muons by the total number of probes matched to the tag muons in the sample after subtracting the expected number of background (bkg) events from the Z^0 or J/ψ resonance, respectively:

$$\varepsilon = \frac{N_P^{Rec}(\text{data}) - N_P^{Rec}(\text{bkg})}{N_P(\text{data}) - N_P(\text{bkg})}, \tag{V.1}$$

where N_P denotes the total number of probe muons in the sample and N_P^{Rec} is the number of reconstructed probes with the certain muon quality criteria applied. The measured efficiencies are binned in p_{T} and η of the muons. For muons with $p_{\mathrm{T}} > 10$ GeV, the $Z^0 \to \mu\mu$ sample is used by selecting muon pairs with an invariant mass of $m_{\mu\mu} \in [m_Z \pm 10\,\text{GeV}]$. In addition, a stricter preselection on the tag muon is applied to increase the purity of the sample and to ensure that the muon trigger is fully efficient. For muons with 5 GeV $< p_{\mathrm{T}} <$ 20 GeV, the $J/\psi \to \mu\mu$ sample is used. The sample is preselected by requiring an invariant mass window of $m_{\mu\mu} \in [2.7\,\text{GeV}, 3.2\,\text{GeV}]$ for the muon pairs and some further criteria on the tag muon to suppress the non-resonant background.
The efficiency measurements are performed in real data samples as well as in simulated POWHEG [154] $Z^0 \to \mu\mu$ and PYTHIA8 [100] $J/\psi \to \mu\mu$ MC samples. The difference of the efficiencies obtained from data and MC can be expressed as the ratio of these two values, denoted as "efficiency scale factor" (SF):

$$\text{SF} = \frac{\varepsilon_{\text{data}}(Q)}{\varepsilon_{\text{MC}}(Q)}, \qquad [\, Q = \mathit{medium} \,|\, \mathit{tight} \,|\, \mathit{high}\text{-}p_{\mathrm{T}} \,]\,. \tag{V.2}$$

These scale factors are calculated for different muon qualities Q independently and are provided binned in p_{T} and η of the muons. Scale factors can be applied to the event weight of Monte Carlo samples in order to reproduce the data efficiencies. Systematic uncertainties of the scale factors are obtained from varying the invariant mass windows used for the preselection or changing between different background subtraction models.

The muon reconstruction efficiencies computed with the tag-and-probe method for data and Monte Carlo are shown in Figure V.1 as a function of the transverse momentum (left) and the pseudorapidity (right). The plots show the efficiency values for the *medium* selection and are obtained from the Z^0 or J/ψ resonance according to the p_T range of the tag muon. The bottom panels show the ratio between data and MC including statistical and systematic uncertainties. The efficiencies amount to $>99\%$ for most p_T and η values. The scale factors vary in most cases between 0.99 and 1.01. For $|\eta| < 0.1$, the efficiency shows the expected decrease due to the reduced operation of the MS in that region.

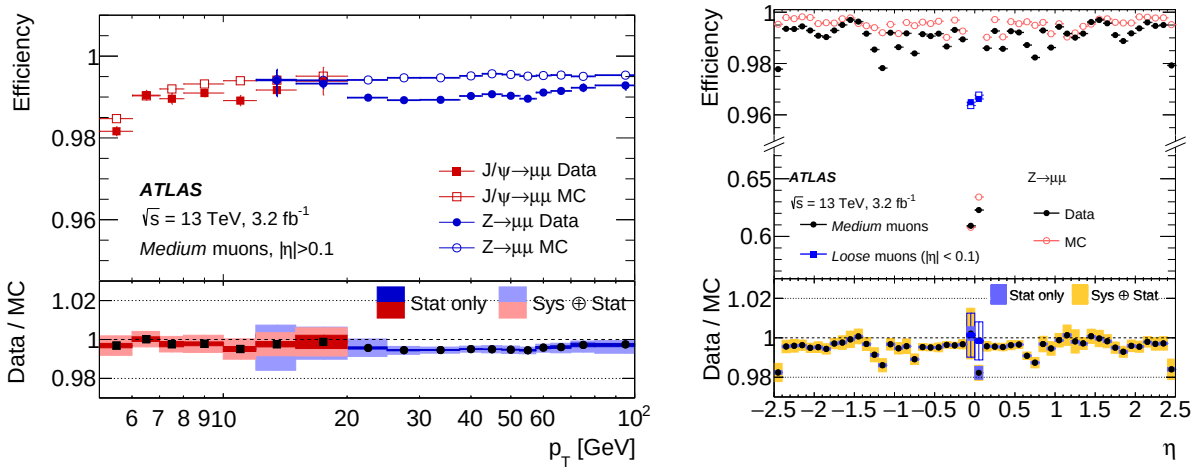

Figure V.1.: The reconstruction efficiencies for *medium* muons as a function of p_T (left) and η (right). The values are obtained from the Z^0 or J/ψ resonance according to the p_T range of the tag muon [150].

Besides the efficiency associated with the pure quality selection, an additional component of the total efficiency comes from the isolation requirement that can be applied to the muons. The term "isolation" typically refers to a condition set on a particle that there are no other objects such as tracks or energy clusters in a specific ΔR cone around the selected particle. For muons, track- and calorimeter-based isolation variables are defined. They are calculated by adding up all transverse momenta (or calorimetric energy clusters) in the cone excluding the contribution from the muon itself and requiring an upper limit on this energy. One can specify several sets of cuts on isolation variables, denoted as isolation working points (WPs) which can be applied in addition to the muon quality cuts. The measurement of the isolation efficiencies works equivalent to the method explained above, just that the efficiency is defined as the number of probe muons fulfilling the isolation requirement divided by the total number of probe muons (while the muon quality stays fixed). Scale factors are provided for seven different isolation WPs which have to be applied on top of the reconstruction SF to get the total efficiency. A common feature in Run II is to apply isolation requirements for p_T dependent cone sizes (p_T^{varcone}), starting with wider cones at low energy ranges and using more narrow cones for muons with high momenta[5].

V.1.3. MUON MOMENTUM SCALE AND RESOLUTION

The transverse momentum of a muon is determined by measuring the curvature of its associated track. Since the default muon selections include χ^2-based quality requirements of the fitted track, the trajectories in the ID and the MS can be determined with a high precision, corresponding to a low uncertainty of the p_T computation. However, this process cannot be modeled with sufficient accuracy in simulated events to

[5] Additionally, it increases the efficiency for high-p_T muons where the isolation requirement can be relaxed.

describe the muon momentum scale at permille and the momentum resolution at percent level. Specific corrections have to be applied to the simulated muon p_{T} to obtain this level of agreement between data and Monte Carlo. The corrections are applied to the ID and MS track separately and have to be recombined subsequently to build CB tracks[6]. The corrected transverse momentum for the ID/MS component of the track is given by the following formula:

$$p_{\mathrm{T}}^{\mathrm{ID/MS}}(\mathrm{corr.}) = \frac{p_{\mathrm{T}}^{\mathrm{ID/MS}}(\mathrm{MC}) + \sum_{n=0}^{1} s_n^{\mathrm{ID/MS}}(\eta,\phi)\left(p_{\mathrm{T}}^{\mathrm{ID/MS}}(\mathrm{MC})\right)^n}{1 + \sum_{m=0}^{2} \Delta r_m^{\mathrm{ID/MS}}(\eta,\phi)\left(p_{\mathrm{T}}^{\mathrm{ID/MS}}(\mathrm{MC})\right)^{m-1} \cdot g_m}, \qquad n,m \in \mathbb{N}, \tag{V.3}$$

with $p_{\mathrm{T}}^{\mathrm{ID/MS}}(\mathrm{MC})$ denoting the uncorrected momentum in the corresponding subdetector part obtained from simulation. The parameters $s_n^{\mathrm{ID/MS}}(\eta,\phi)$ and $\Delta r_m^{\mathrm{ID/MS}}(\eta,\phi)$ are derived empirically for different p_{T}, η ranges and take into account inaccuracies of the magnetic field description and the estimated energy losses due to the detector material. g_m is a normally distributed random variable with its mean at zero and a variance of one. The s_n and Δr_m correction parameters are extracted from data using a maximum-likelihood fit [155] on simulated templates in order to maximize their agreement. The systematic uncertainties of the momentum corrections come from the errors of the fit parameters and from additional terms derived from variations of the invariant mass windows or the background subtraction methods.

VALIDATION OF THE MUON MOMENTUM CORRECTIONS

Figure V.2 shows the $m_{\mu\mu}$ distributions of $J/\psi \to \mu\mu$ (left) and $Z^0 \to \mu\mu$ (right) test samples for data, uncorrected Monte Carlo (black dashed lines), and corrected MC (red solid lines). After applying the corrections, the improvement in terms of data/MC agreement is clearly visible.

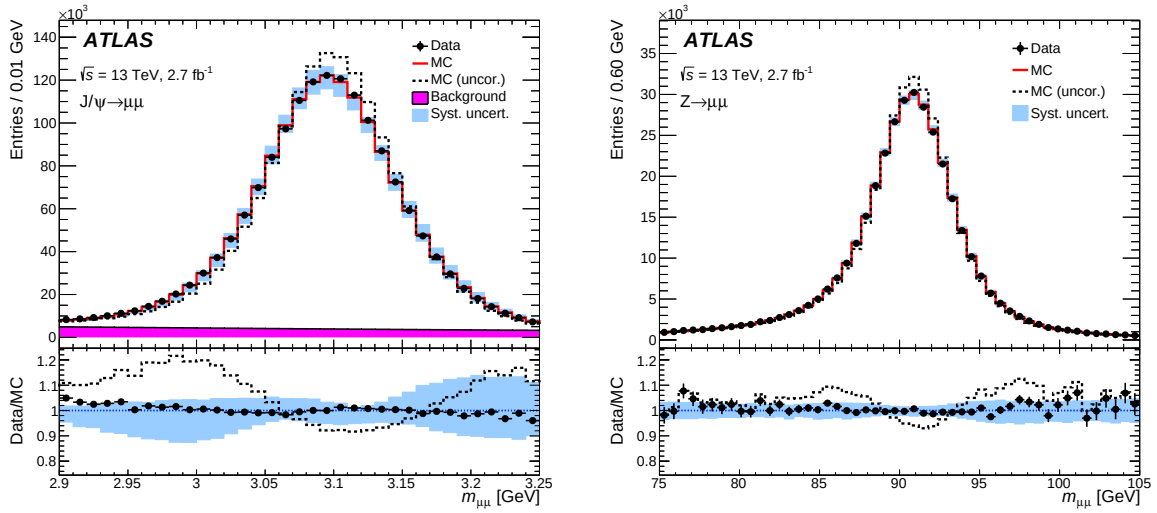

Figure V.2.: Invariant mass distributions of preselected $J/\psi \to \mu\mu$ (left) and $Z^0 \to \mu\mu$ (right) samples for data and MC. The black dashed line is the original MC, while the red solid line shows the MC with the momentum corrections applied. The blue area indicates the systematic uncertainty of the corrections [150].

[6] The combination is a weighted average of the momenta. The weight depends on the relative contribution of the ID and MS to the particular track.

The improved agreement between data and Monte Carlo after applying the momentum corrections can be demonstrated by fitting the invariant mass distributions at the Z^0 and J/ψ resonance in data and MC and extracting the fit parameters of interest. The invariant mass scale and resolution (position and width of the peak) of the corrected MC can be compared to data in different η and p_{T} ranges. The fit template used for the Z^0 peak is a convolution of a Breit-Wigner distribution and a Crystal-ball function [156] to model asymmetries in the shape of the resonance due to energy losses in the detector. For the J/ψ peak, it is a Gaussian distribution convoluted with the Crystal-ball function since the intrinsic width of the resonance is negligible compared to the experimental $m_{\mu\mu}$ resolution. The non-resonant background is modeled with an exponential function.
Figure V.3 shows the invariant mass scale (left) and resolution (right) of the $Z^0 \to \mu\mu$ peak obtained from the fit and plotted versus the pseudorapidity of the leading muon. The mass scale is in almost all η and p_{T} regions compatible with data to a level of $<0.5\%$. For the mass resolution, the level of agreement is in most cases in a range of 5–10%. These differences are covered by the systematic uncertainties of the muon momentum corrections.

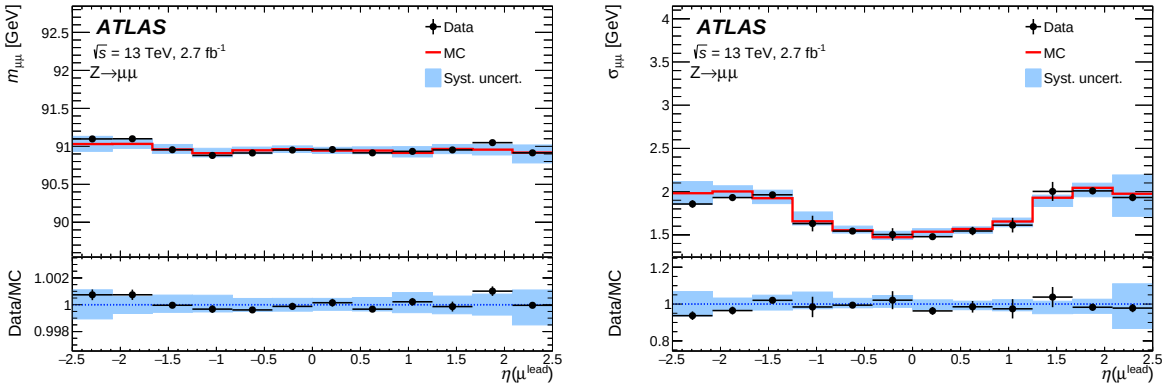

Figure V.3.: Invariant mass scale (left) and resolution (right) versus η of the leading muon. The values are obtained from a preselected $Z^0 \to \mu\mu$ sample for data (black) and corrected MC (red) [150].

V.2. ELECTRONS

As it is the case for muons, electrons are of particular importance for the analysis described in this thesis. The track signature left by electrons in the inner detector is basically the same as for muons, but contrary to them, they are absorbed typically in the electromagnetic calorimeter producing a characteristic electromagnetic shower. The reconstruction of this shower and its association with a compatible ID track builds the central component of the electron object identification. Especially the evaluation of the shower shape and its discrimination from hadronic activities is a crucial task in the selection process to assure a low misidentification probability of the electrons used for physics analyses.

V.2.1. RECONSTRUCTION AND IDENTIFICATION

The reconstruction of electrons can be subdivided into several complementary steps: the selection of a seed-cluster in the electromagnetic calorimeter, the track selection and fitting in the ID, a geometrical track-cluster matching, and the final reconstruction of the electron candidate [157].

The seed-clusters are selected by a sliding-window scan with a size of 3×5 segments in the EM calorimeter middle layer (see Section IV.3.3) looking for deposits above an energy threshold of 2.5 GeV. The correct position and kinematics of the clusters are computed using a dedicated clustering algorithm [158]. The reconstruction of electron tracks in the ID is performed in the same way as it is done for muons (explained in Section V.1.1). However, a modified pattern recognition of the ID hits is used which takes into account the higher energy loss of the particles while traversing the detector material. This allows discriminating $e^{\pm}$ tracks from $\pi^{\pm}$ or $\mu^{\pm}$ signatures and can be regarded as an electron-specific utilization of the standard track reconstruction. The fitted tracks are extrapolated to the middle layer of the EM calorimeter, matched to the seed-cluster and re-fitted with stricter conditions under the assumption that the cluster originates from the track. The effect of bremsstrahlung is included in the re-fitted tracks using a Gaussian Sum Filter algorithm [159]. If several tracks can be matched to one cluster, one track is selected as primary track according to the cluster-track distance and χ^2-based quality criteria of the fit. Furthermore, cuts on the longitudinal and transverse impact parameter are applied to ensure that the track is compatible with the primary interaction vertex of the collision. The measured energy of the cluster[7] is then calibrated to the original electron energy with multivariate techniques [160, 161]. Due to the better spatial resolution in the ID, the η and ϕ coordinates of the electron candidate are taken from the reconstructed track, whereas the transverse energy E_{T} is obtained from the calibrated cluster.
The identification is based on several properties of the electron candidate, such as calorimeter shower shapes, track quality, track-cluster compatibility, or information from the TRT (as explained in IV.3.2). These algorithms were re-optimized for Run II, considering the higher center-of-mass energy and the increased pile-up conditions. The probability density functions of these discriminating variables are used to construct a combined likelihood function $L(\vec{x})$ on which a cut is applied for the electron selection:

$$L(\vec{x}) = \prod_{i=1}^{n} P_i(x_i), \qquad \vec{x} = (x_1, \ldots x_n), \tag{V.4}$$

where $\vec{x}$ is the vector of discriminating variables (with components x_i) and $P_i(x_i)$ is the value of the probability density function of variable i evaluated at point x_i. A requirement on the likelihood function defines an identification working point. Several identification WPs are defined according to different purities of prompt electrons and background rejection rates, respectively: *looseLH*, *mediumLH*, and *tightLH* (the suffix *LH* indicates that the identification is likelihood-based).
In addition to the likelihood-based selection, an isolation requirement is set for electrons in most physics analyses. Equivalent to muons, the isolation is defined as the energy deposited in a specific ΔR cone around the electron without the E_{T} from the particle itself. Also for electrons, the isolation can be track-based, calorimeter-based, or both. With respect to muons, the probability for photon conversions and light-flavor hadrons misidentified as electrons is much higher due to a stronger interaction with the detector material. Accordingly, strict isolation criteria, especially at low energies, are crucial for an efficient background suppression.

V.2.2. ELECTRON EFFICIENCY MEASUREMENTS AND CORRECTIONS

The measurement of the electron efficiencies relies on a tag-and-probe technique similar to the muon measurement described above. Analogous to the methodology used for muons, the measurements are separated into an $J/\psi \to ee$ and a $Z^0 \to ee$ sample, corresponding to the E_{T} range of the electrons. For

[7] The clusters matched to tracks are re-build by the clustering algorithm using slightly bigger EM calorimeter segments of 3×7 or 5×5 units.

electrons with a low E_T from 7 to 20 GeV, the values obtained from the J/ψ sample are taken, while for $E_T > 15$ GeV, the Z^0 sample is used [157]. Furthermore, the measurements are binned in η and E_T of the electrons. The total efficiency can be subdivided into several components for reconstruction, identification, isolation, and trigger selection which are evaluated independently:

$$\varepsilon_{tot} = \varepsilon_{reco} \times \varepsilon_{id} \times \varepsilon_{iso} \times \varepsilon_{trig}. \tag{V.5}$$

The reconstruction efficiency ε_{reco} is given by the ratio between the electrons reconstructed according to the previous section and the total number of clusters in the EM calorimeter selected by the clustering algorithm. The other components of the total efficiency are measured with respect to the previous step using the tag-and-probe method with different preselection criteria applied to the probe electrons. Measurements are done for *looseLH*, *mediumLH*, and *tightLH* electrons, different isolation working points and trigger selections, each provided as two-dimensional efficiency map parametrized in (E_T, η) bins. The differences between the values obtained from data and simulation are expressed as multiplicative correction factors which are applied to the Monte Carlo event weight.
The uncertainties of the measurements are obtained from variations on the invariant mass windows, changing the selection requirements for the tag electrons and varying between different methods to subtract the non-resonant background. The errors associated with the total efficiencies are derived from the uncertainties of the individual measurements using pseudo-experiments (done independently for each E_T, η bin). Figure V.4 shows the combined electron reconstruction and identification efficiencies as a function of E_T (left) and η (right) of the leading electron. The filled dots show the data values while the circles are the values obtained from $Z^0 \to ee$ Monte Carlo.

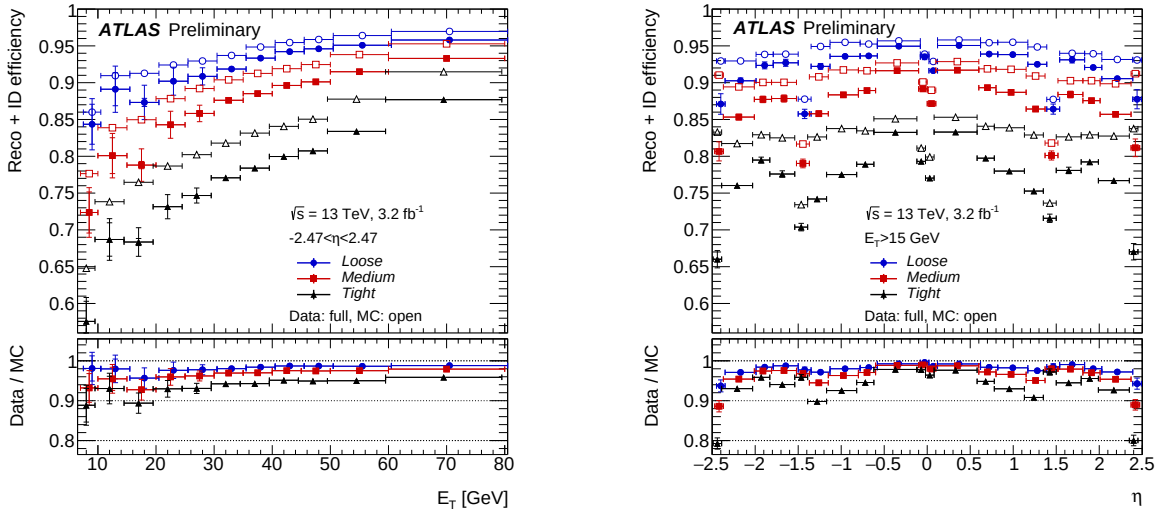

Figure V.4.: Combined electron reconstruction and identification efficiencies, measured in $J/\psi \to ee$ and $Z^0 \to ee$ samples for data (filled dots) and MC (circles). The efficiencies are shown for different identification WPs as a function of E_T (left) and η (right) of the leading electron [157].

For all three working points, the reconstruction efficiency improves with increasing E_T values. For *tightLH* electrons, the efficiency in data is around 60% for $E_T < 10$ GeV and reaches up to 85% for high E_T values. For *mediumLH* and *looseLH* electrons, the efficiency varies between 75–90% and 85–95%, respectively. If the efficiency is plotted against η, it shows the expected decrease in the region $|\eta| \approx 0$ where the EM calorimeter is divided into its two half-barrels. In the transition region (crack region) between the barrel part of the electromagnetic calorimeter and the EM end-caps $(1.37 < |\eta| < 1.52)$, the

efficiency drops by 5–10%, depending on the electron quality. The scale factors (data-MC ratio, bottom panels in Figure V.4) for all electron types vary typically between 0.95 and 1.00 with small dependencies on E_{T} and η of the electrons.

V.2.3. ENERGY CALIBRATION

The energy calibration of electron candidates is done in several steps. Data-driven uniformity adaptions are applied to data to correct the difference in the response of the longitudinal EM calorimeter layers between data and simulation. A multivariate calibration procedure based on Monte Carlo is applied to data and simulation. It corrects the E_{T} value measured in the calorimeter taking into account the energy loss between the interaction point and the reconstructed cluster, using the information from the inner detector. As a last step, an in-situ correction based on $Z^0 \to ee$ events is applied to Monte Carlo in order to adjust residual disagreements with data of the energy scale and resolution [161].
The difference between the energy scale in data and MC for a specific pseudorapidity region i can be parametrized with an correction factor α_i. The energy resolution difference, which does not directly depend on the total energy, can be addressed with an additional correction term c_i'. The energy scale and resolution in data can be written as:

$$E_i^{\mathrm{data}} = E_i^{\mathrm{MC}}\,(1+\alpha_i)\,, \qquad \left(\frac{\sigma(E)}{E}\right)_i^{\mathrm{data}} = \left(\frac{\sigma(E)}{E}\right)_i^{\mathrm{MC}} \oplus c_i'. \tag{V.6}$$

The parameters α_i and c_i' are obtained from a comparison of simulated $Z^0 \to ee$ events and a preselected data sample collected in 2015. Systematic uncertainties of these parameters are derived from varying the selection criteria of the candidate electrons, changing the invariant mass window for the Z^0 requirements and using different models to evaluate the non-resonant background. Furthermore, many other error sources, like for the description of the detector material or statistical uncertainties of the template samples have been taken into account. An additional uncertainty is introduced to account for differences in the pile-up conditions between 2015 and 2016 data.

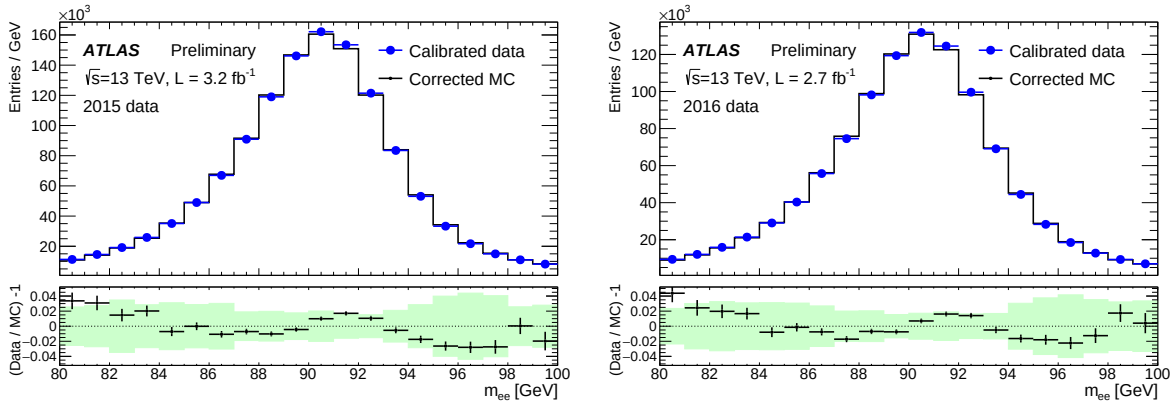

Figure V.5.: Invariant mass distributions of preselected $Z^0 \to ee$ samples, comparing calibrated data from 2015 (left) and 2016 (right) with corrected MC. The green area shows the uncertainty of the calibration [161].

A comparison between calibrated data and corrected Monte Carlo is shown in Figure V.5 for preselected $Z^0 \to ee$ samples. This validation is done separately for the 3.2 fb^{-1} of data collected in 2015 (left) and the first part of the 2016 data, corresponding to 2.7 fb^{-1} (right). The separated validation is done in order to show the functionality of the correction parameters obtained from 2015 data also for the

increased pile-up environment in the 2016 data taking. The error bars in the bottom panel include the full uncertainty associated with the calibration and correction procedure. The corrected Monte Carlo describes the calibrated data to a level of $<5\%$, whereby the observed deviations are in most cases covered by the systematic uncertainties assigned to the MC prediction.

V.3. JETS

Objects denoted as jets are the most frequent signatures produced in pp collisions. They are formed by radiation of quarks or gluons which hadronize inside the detector and deposit energy clusters in the electromagnetic and hadronic calorimeters. Since many of the hadrons producing jets are electrically charged, they can also create tracks in the inner detector. Jets can be categorized into objects originating from light quark types (u, d, s, c) or gluons, denoted as *light-flavor* jets and jets coming from b-quarks, denoted as *heavy-flavor* jets[8].
Both light- and heavy-flavor jets are key ingredients for many new physics searches including especially analyses looking for strong production of SUSY particles, like squarks and gluinos. Also, they are of particular importance for many SM measurements and studies of Higgs properties, e.g. investigations of the $H \to bb$ decay channel.

V.3.1. JET RECONSTRUCTION ALGORITHMS

For the reconstruction of jets in ATLAS, jet algorithms are used that cluster several energy deposits in the calorimeters to one single object. There are various jet algorithms, using different methods of clustering and reconstruction [162]. The most appropriate choice depends on the desired properties of the selected jets, given by the jet requirements of the analysis.
Two main categories of jet reconstruction algorithms exist: *cone algorithms* and *sequential clustering algorithms*. Cone algorithms basically add up the energy deposits in rigid areas defined by a given ΔR parameter resulting in jets with circular boundaries. Most of them have the disadvantage that they cannot provide stable results including very soft (low-p_{T}) parton emissions or effects from collinear splittings, features denoted as "infrared-safety" and "collinear-safety". The more common approach for physics analyses is to use sequential clustering algorithms for the jet reconstruction which combine topological energy clusters (topo-clusters) [163] iteratively based on energy and angular variables of the constituents. Sequential clustering algorithms widely used are the k_t, the anti-k_t, or the Cambridge/Aachen (CA) algorithm [164–166]. For the analysis described in this thesis, jets reconstructed with the anti-k_t algorithm are used as implemented in the FASTJET [167] software package.
The anti-k_t algorithm works by consecutively combining topologically connected energy clusters depending on their distance to each other. For two clusters i and j, one can define the distance parameter d_{ij} as follows:

$$d_{ij} = \min\left(\frac{1}{k_{t,i}^2}, \frac{1}{k_{t,j}^2}\right) \cdot \frac{\Delta_{ij}^2}{R^2}, \qquad \Delta_{ij} = \sqrt{(y_i - y_j)^2 + (\phi_i - \phi_j)^2}, \tag{V.7}$$

where Δ_{ij} is the geometrical distance between the cluster cells defined by their rapidity and azimuthal difference and $k_{t,i}$ is transverse momentum of the cluster i. Two particles with $d_{ij} < R$ can be merged to a common object.

[8] The top quark belongs also to the heavy-flavor quarks. However, due to its short lifetime of $\approx 5 \cdot 10^{-25}$ s [11], it decays before forming any bound state.

The clustering process starts from a group of objects and proceeds by combining the two topo-clusters i and j with the smallest d_{ij}. If the distance parameter between remaining cluster cells reached a minimum value of $d_{Bi} = k_{t,i}^{-2}$, the combination sequence is stopped and merged clusters are assigned as jet. The procedure is repeated until all clusters in the default jet radius are merged into one object, which is eventually considered as jet. An advantage with respect to the normal k_t algorithm is that the k_t^{-2} dependency of the distance parameter makes the clustering sequence start with the hardest (largest k_t) component and subsequently adds softer objects which leads to a more conical jet shape[9]. The radius parameter R determines the actual extension of the jet cone and can be specified according to the analysis requirements. The jets used for the analysis presented in this thesis have $R = 0.4$. Larger values like $R = 1.0$ are mainly relevant in searches sensitive to jet substructures but were also tested within the optimization studies for this analysis.

V.3.2. ENERGY CALIBRATION AND RESOLUTION

For a valid and meaningful information of the jet energy and direction, a calibration procedure has to be applied to the reconstructed jets. The determination of the jet energy scale (JES) and jet energy resolution (JER) consists of several consecutive steps derived from different of Monte Carlo based methods and in-situ techniques [168].
The calibrations based on MC correct the reconstructed jet four-momentum to the information from particles taken from simulated jets. They are applied to correct for detector effects, biases in the jet reconstruction algorithm, as well as pile-up contaminations. The purpose of the in-situ calibration is to measure the difference in the jet response (energy of the generated initial particles versus energy at reconstruction-level) between data and simulation, with residual energy corrections applied to jets in data only. The diagram in Figure V.6 summarizes the different stages of the jet calibration procedure which will be explained in the following.

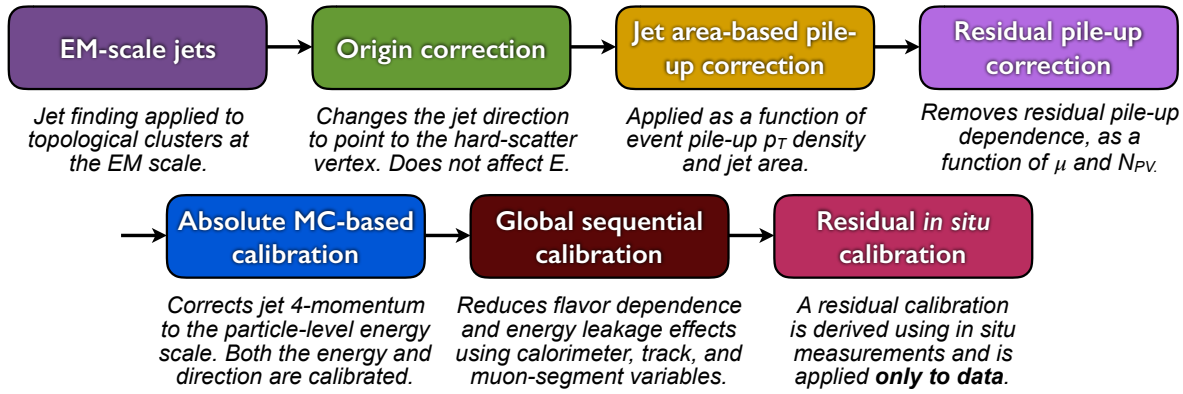

Figure V.6.: The different calibration stages applied in the EMTopo scheme. Each step of the procedure affects either the position (η, ϕ) or the energy scale of the input jets [168].

As already noted, the jets considered for the analysis discussed in this thesis are reconstructed with the anti-k_t algorithm with $R = 0.4$. The reconstruction starts from energy deposits measured at the electromagnetic energy scale (EM scale). A collection of three-dimensional and massless topological

[9] The usual k_t and the Cambridge/Aachen algorithm are based on the same principle, defining distances $d_{ij} = \min(k_{t,i}^{2p}, k_{t,j}^{2p}) \cdot \frac{\Delta_{ij}^2}{R^2}$ with $p = 1$ for the k_t and $p = 0$ for the CA algorithm.

clusters at this energy scale are used as input for the algorithm. This approach is typically denoted as EMTopo scheme[10].

A jet origin correction recomputes the four-momentum of the jet taking into account the difference between the centroid position of the jet and the nominal interaction point. This correction improves only the spatial resolution of the jet (η, ϕ) without modifying their energy. The subtraction of pile-up effects is done with a so-called jet-area method [169]. It works by computing the expected average contribution of pile-up jets in the relevant detector region and subtracting it in the area where the selected jet was reconstructed. Since a residual pile-up dependence remains, an additional correction has to be applied using scale factors from simulated jets without imposing detectors effects (truth jets). The absolute JES calibration corrects the four-momentum of the jet to the energy scale of jets reconstructed from the generated initial particles. The corresponding correction factors are obtained from truth jets in simulated dijet events and affect direction and energy scale of the input jet. Afterwards, a so-called "global sequential calibration" is applied which uses information from the inner detector and the muon spectrometer complementary to the calorimeter system. This is done to mitigate remaining dependencies of the JES on the particle composition and their energy distributions within the jet.

As a final step, an in-situ calibration is used to correct for differences in the jet response between data and simulation. This is done by balancing the p_{T} of a jet against another reference object which is measured with a high precision. Typically, these measurements are done in γ+jets or Z+jets events, as the p_{T} of the photon or the Z^0 boson can be determined very accurately compared to the recoiling jet. Furthermore, it is possible to derive corrections from a high-p_{T} jet balanced against several well-calibrated jets with lower momentum with the "multi-jet balance method". The different in-situ calibration methods are done separately for several p_{T} and η ranges and their results are statistically combined afterwards. The difference between the precisely measured jets in the central detector region and forwards jets is addressed with an extrapolation of the η dependent correction factors to the forward region (η-intercalibration) [170]. The resulting JES corrections are applied to the four-momentum of the input jets and vary from a level of 4% for jets with $p_{\mathrm{T}} = 20$ GeV to around 2% at $p_{\mathrm{T}} = 2$ TeV. The JER corrections are around 3% for jets with $p_{\mathrm{T}} = 20$ GeV and $< 1\%$ for $p_{\mathrm{T}} > 100$ GeV.

SYSTEMATIC UNCERTAINTIES OF THE CALIBRATION

The subsequent calibration stages and methods used for the in-situ corrections are affected by individual sources of systematic uncertainties. They are estimated with different approaches and propagated to the total uncertainty assigned to the fully calibrated jets. In total, more than 80 partially correlated uncertainty parameters have to be considered for the entire process. Among many others, they include theoretical uncertainties from the Monte Carlo modeling, statistical errors of the calibration samples, and specific uncertainties associated with the in-situ techniques derived with various methods (jet flavor, pile-up corrections, η-dependence, etc.). For the sake of simplicity and computing time, several correlation models and grouping-approaches exist to reduce the number of free uncertainty parameters without a sizable effect on the results (as it is also done for the analysis presented here). The total uncertainty amounts to around 4.5% for jets with $p_{\mathrm{T}} = 20$ GeV, decreases to about 1% for $p_{\mathrm{T}} = 200$ GeV and inflates again to $\approx 2\%$ for $p_{\mathrm{T}} = 2$ TeV. These numbers remain almost constant for all η values of the calibrated jets, with small increases for large pseudorapidities ($|\eta| > 3.0$) and in the transition region.

The total fractional uncertainty of the calibration procedure for anti-k_t ($R = 0.4$) jets is shown in Figure V.7, on the left as a function of the jet transverse momentum for jets with ($\eta = 0$) and on the right as a function

[10] A particular jet collection is typically named by the reconstruction algorithm, the jet radius parameter, and the energy calibration scheme (e.g. AntiKt4EMTopo).

of η for jets with $p_{\mathrm{T}} = 80$ GeV. Also, the individual contributions from different categories of uncertainties are shown by the colored lines superimposed.

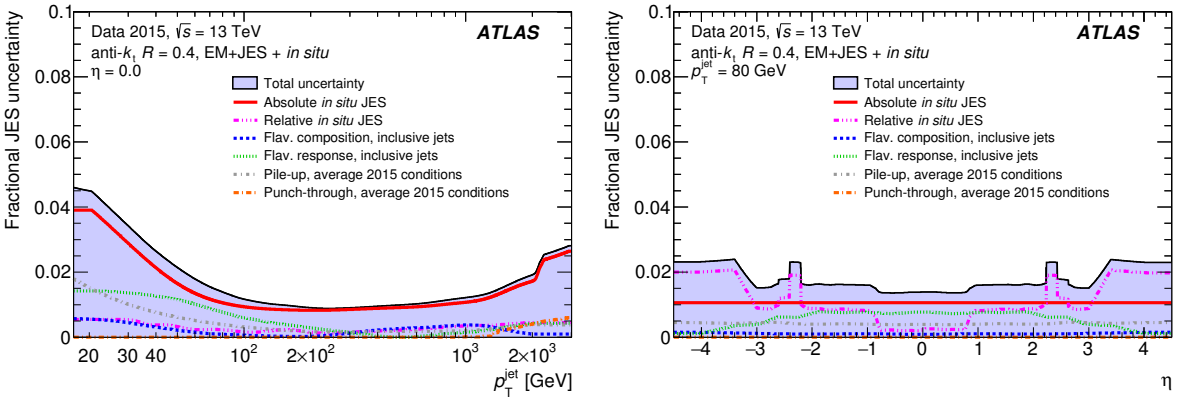

Figure V.7.: Total fractional uncertainty of the calibration procedure (for AntiKt4EMTopo jets) as a function of the jet p_{T}. It is shown for central jets ($\eta = 0$) (left) and as function of η for jets with $p_{\mathrm{T}} = 80$ GeV (right). The total uncertainty can be subdivided into different categories shown by the colored lines [168].

V.3.3. IDENTIFICATION OF B-JETS

Jets originating from b-quarks have specific attributes which make them distinguishable from jets originating from light quark types or gluons. Thus, it is possible to identify these jets with dedicated approaches, referred to as *b-tagging*. A solid and efficient b-jet identification is an important tool in many physics analyses allowing the suppression of major background processes or increasing the sensitivity to possible BSM signatures [171].
There are several b-tagging algorithms based on different, partially complementary, approaches:

- **Secondary vertex taggers:** These algorithms are based on the reconstruction of a secondary vertex (SV) besides the primary vertex. The average lifetime of hadrons containing b-quarks ($\approx 1.5 \cdot 10^{-12}$ s [11]) allows them to travel a measurable distance (3–5 mm) through the detector before decaying. Thus, the resulting secondary vertex can be used as an identifier for jets containing b-quarks, as shown on the illustration in Figure V.8 (left).

  Tagging algorithms like *SV0* or *SV1* [172] use this information and compute the b-jet probability based on the distance between primary and secondary vertex divided by the uncertainty of the vertex position. With respect to *SV0*, the *SV1* tagger uses an improved computation based on a likelihood ratio formalism and additional input variables.

- **Impact parameter taggers:** The tracks from b-hadron decays have on average larger impact parameters than light-flavor quark decays. This distinctive signature is used by algorithms like *IP2D* and *IP3D* [172]. While the *IP2D* tagger only uses the transverse impact parameters, *IP3D* uses both the transverse and longitudinal impact parameters, taking also into account their correlations[11].

- **Decay chain taggers:** Some algorithms, like *JetFitter* [173] try to reconstruct the full decay chain to separate light- from heavy-flavor jets. They use both track and vertex variables to define a

[11] Due to the additional information in the longitudinal plane, *IP3D* has a higher rejection power of light-flavor jets. However, *IP2D* is more robust against pile-up effects.

likelihood function based on the simulated ideal decay chain of *b*- and *c*-hadrons which is used a discriminating variable. Furthermore, the output from other tagging algorithms can be used to provide an enhanced rejection of light-flavor jets, as it is done in the combined *IP3D+JetFitter* framework.

- **Combined tagging algorithms:** The tagging algorithms most commonly used in ATLAS rely on the input of several complementary *b*-taggers and combine them to maximize their performance.

  In Run I, *MV1* [174] was the standard algorithm used for most of the physics analyses. It is based on an artificial neural network using the information from the *IP3D*, *SV1*, and *IP3D+JetFitter* taggers as input and computes the probabilities for a given jet to originate from a *b*-, *c*-, or light-flavor quark. For Run II, the performance of *MV1* has been revisited and the neural network was replaced by a boosted decision tree (BDT) [175], resulting in an improved performance and shorter computation times. Also, further variables were added to supplement the information given by the input taggers. The new algorithm, denoted as *MV2* [176] is the standard approach for the Run II physics analyses[12].

The performances of some of those *b*-tagging algorithms (*b*-jet efficiency versus light-jet rejection) are shown on the right of Figure V.8. Independent from the choice of the algorithm, *b*-jets can never be discriminated from light-flavor jets without a certain misidentification probability. The higher the requirements on the *b*-tagging decision are chosen by applying a cut on the BDT score, the greater the *b*-jet purity (light-jet rejection rate), but the lower the efficiency for the tagged jets. Typically, a set of operation points (OPs), corresponding to specific *b*-tagging efficiencies is defined for the various taggers. The efficiency differences between data and simulation can be expressed in *b*-tag scale factors that are assigned to every *b*-, *c*-, and light-flavor jet[13].

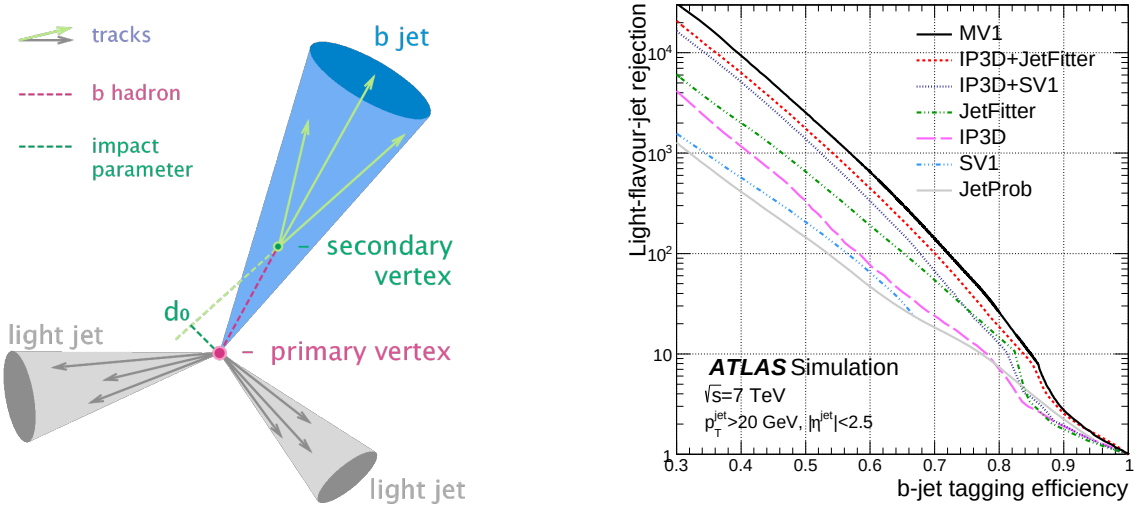

Figure V.8.: Left: Illustration showing the principle of *b*-jet identification. Right: *b*-tagging efficiency versus light-jet rejection (for jets with $p_{\mathrm{T}} > 20$ GeV, $|\eta| < 2.5$) plotted for different algorithms [171].

Efficiency measurements in data and Monte Carlo have to be performed to obtain scale factors for heavy- and light-flavor jets. There are several methods to determine the *b*-tag efficiency and the misidentification

[12] Several variants of the *MV2* algorithm exist optimized with different *c*-jets fractions in the initial training samples. They are denoted as *MV2cXX*, where $XX = 00, 10, 20$ denote different fractions of *c*-jets.

[13] Since light-flavor jets are identified by an inverse *b*-jets requirement (*b*-veto), a SF has to be assigned also to them.

rates in data from $t\bar{t}$ or dijet events. The $p_{\mathrm{T}}^{\mathrm{rel}}$ method relies on the relative p_{T} of muons in jets as a discriminating variable to estimate the fraction of b-jets in a control sample before and after the tagging procedure. Another approach is the so-called *System8* method [177] which uses two control samples with different b-jet fractions and two uncorrelated tagging algorithms. The efficiency can then be obtained by solving a system of eight non-linear equations.
For the *MV2* tagger that is used for the analysis described in this thesis, scale factors are provided for four different OPs, corresponding to fixed b-jet efficiencies of 60, 70, 77, and 85%. They are parametrized in p_{T}, $|\eta|$, and ΔR of the input jets and vary mostly from 1.00 to 1.05, with a relative uncertainty of 5–10% for the 70% OP [178].

V.4. MISSING TRANSVERSE ENERGY

For many physics analyses, in particular for new physics searches like supersymmetric phenomena, the missing transverse energy ($E_{\mathrm{T}}^{\mathrm{miss}}$) is one of the most important quantities.
Assuming the sum of the momenta in the plane transverse to the beam axis is zero before the collision, it can be defined as the momentum imbalance in this plane taking into account all other calibrated objects in the detector. A schematic view of the principle for an event with one muon and two jets is given in Figure V.9. The only physics objects inside the Standard Model which can produce real missing energy are neutrinos, which traverse all detector layers without interacting with their material. The x- and y-components of the missing transverse energy can be computed as:

$$E_{x,y}^{\mathrm{miss}} = \sum_{\mu} E_{x,y}^{\mathrm{miss},\mu} + \sum_{e} E_{x,y}^{\mathrm{miss},e} + \sum_{\tau} E_{x,y}^{\mathrm{miss},\tau} + \sum_{\gamma} E_{x,y}^{\mathrm{miss},\gamma} + \sum_{j} E_{x,y}^{\mathrm{miss,jet}} + E_{x,y}^{\mathrm{miss,soft}}. \tag{V.8}$$

The total $E_{\mathrm{T}}^{\mathrm{miss}}$ is given by the negative sum of the transverse momenta of all calibrated and corrected physics objects (muons, electrons, tau leptons [179, 180], photons [181], and jets), denoted as "hard term". Furthermore, it takes into account additional energy contributions that cannot be assigned to any of the hard objects, referred to as "soft term" ($E_{x,y}^{\mathrm{miss,soft}}$). Several approaches exist how to reconstruct the total $E_{\mathrm{T}}^{\mathrm{miss}}$ from the input objects and the soft term. The soft term contributions can be either calculated from ID tracks, denoted as track-based soft term (TST) or energy deposits in the calorimeters, called calorimeter-based soft term (CST) [182]. The CST $E_{\mathrm{T}}^{\mathrm{miss}}$ definition uses a soft term reconstructed from energy clusters in the calorimeter not associated with any of the hard objects. This definition is typically not very stable against pile-up effects and, therefore, less suitable for the high $\langle\mu\rangle$ collisions in Run II. As alternative option, the TST $E_{\mathrm{T}}^{\mathrm{miss}}$ uses a soft term based on tracks but combines it with calorimeter information from the hard objects. To maintain stability against pile-up effects, all tracks used in the soft term are required to be associated with the primary vertex, but not with any of the physics objects considered for the hard term. This approach is used as the default method for the $E_{\mathrm{T}}^{\mathrm{miss}}$ calculations in most of the Run II physics analyses [183].
From its corresponding x- and y-components, the magnitude $E_{\mathrm{T}}^{\mathrm{miss}}$ and the azimuthal angle ϕ^{miss} of the missing transverse energy vector can be calculated:

$$E_{\mathrm{T}}^{\mathrm{miss}} = \sqrt{\left(E_x^{\mathrm{miss}}\right)^2 + \left(E_y^{\mathrm{miss}}\right)^2}, \qquad \phi^{\mathrm{miss}} = \arctan\left(\frac{E_y^{\mathrm{miss}}}{E_x^{\mathrm{miss}}}\right). \tag{V.9}$$

An *overlap removal* (OR) between all baseline objects used for the hard term is applied to avoid double-countings of objects which may be selected by more than one category (e.g. an electromagnetic energy

cluster reconstructed as both an electron and a jet). The OR is mainly based on geometrical conditions, like p_{T} dependent minimal distances (ΔR values) between objects. It follows a well-defined sequence, favoring objects that can be reconstructed with a higher level of confidence and discarding other overlapping objects. However, the specific configuration of the OR procedure depends on the analysis specifications and is usually part of the optimization process.
The $E_{\mathrm{T}}^{\mathrm{miss}}$ is calibrated according to the object-specific schemes described in the previous sections. Systematic uncertainties on the calibrated hard term objects passing the OR are evaluated and propagated to the total $E_{\mathrm{T}}^{\mathrm{miss}}$ uncertainty. The remaining soft term uncertainties are estimated from comparisons between data and Monte Carlo in preselected $Z^0 \to \mu\mu$ events with residual $E_{\mathrm{T}}^{\mathrm{miss}}$ along the flight-direction of the Z^0 boson [184].

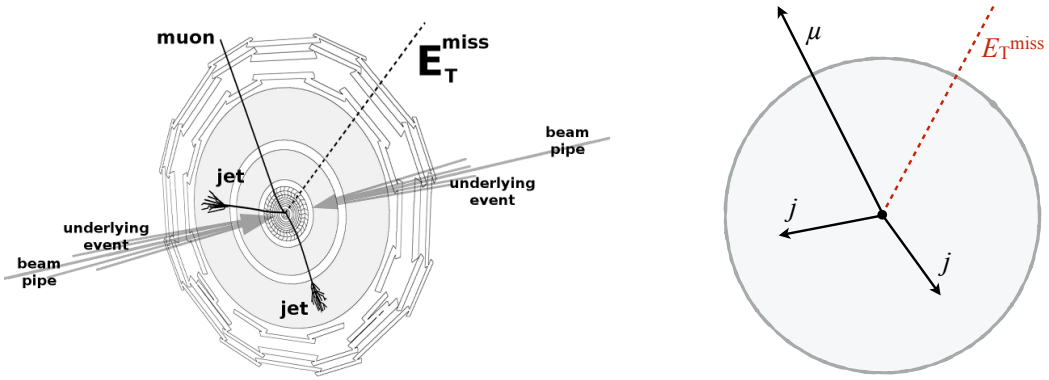

Figure V.9.: Simplified view of a detector event with one muon, two jets and a large amount of missing transverse energy (dashed line).

Apart from the actual physical processes which produce missing transverse energy, many other sources, such as limited detector coverage, finite detector resolution, mismeasured objects, or inactive readout modules can contribute to the total $E_{\mathrm{T}}^{\mathrm{miss}}$ value (denoted as fake $E_{\mathrm{T}}^{\mathrm{miss}}$). An important requirement on any analysis which relies on $E_{\mathrm{T}}^{\mathrm{miss}}$ signatures is to minimize the impact of these effects.

VI. Previous Supersymmetry Searches at ATLAS

The search for supersymmetric phenomena is one of the main research fields in the physics program of the ATLAS experiment. Accordingly, many different analyses dedicated to this topic have been conducted and published since the commissioning of the LHC.
Section VI.1 provides a short summary of the results of former SUSY analyses and their status after Run I. The previous same-sign or three-lepton search performed with the full $\sqrt{s} = 8$ TeV data is briefly reviewed in Section VI.2. The aim of this chapter is to get a general overview of the status of the SUSY searches performed in the ATLAS Collaboration and allows to evaluate the achievements of the analysis discussed in this thesis in the context of former results.

VI.1. Supersymmetry Searches at ATLAS: Status after Run I

In Run I, 20.3 fb^{-1} of pp collision data[1] at $\sqrt{s} = 8$ TeV have been collected by the ATLAS detector. Various analyses used this data to search for supersymmetric phenomena in different final states and experimental signatures.
SUSY analyses in ATLAS can be categorized in four different thematic fields trying to address specific classes of supersymmetric models: searches for inclusive strong production of squarks and gluinos, searches for direct production of third-generation squarks, searches for electroweak production of SUSY particles, and searches for R-parity violating SUSY scenarios. However, these categories are not strictly separated and are only used to classify the analyses thematically. Also, a particular analysis typically intends to investigate explicit final states which are decisive for the background estimation strategy and the choice of the SUSY models being explored. Prominent examples are SUSY searches in final states with no leptons, jets, and $E_{\mathrm{T}}^{\mathrm{miss}}$ (0-lepton) [185] or 1-lepton, jets and $E_{\mathrm{T}}^{\mathrm{miss}}$ [186]. Usually, these signatures are obliged to be distinct (orthogonal) in order to allow a statistical combination of the results after the individual analysis has been fully conducted [187]. The SUSY scenarios explored are typically simplified models, corresponding to a single production mode with a branching ratio of 100% for a specific decay chain[2]. The masses of the SUSY particles not involved in the process are set to very high values (effective models). However, also dedicated scans on the full parameter space for different pMSSM and cMSSM scenarios are performed [188].
The results from the various searches can be interpreted in the context of the simplified models considered and upper limits (usually calculated at 95% confidence level (CL), as described in Section VII.8.2) can be set on the masses of SUSY particles, such as gluinos, neutralinos, and squarks. The inclusive searches are usually the most competitive ones for models with large gluino masses. Different analyses could exclude masses up to a range of 900–1400 GeV for models with very small neutralino masses. The searches for third-generation squarks (which are assumed to be the lightest in many models) excluded top and bottom squark masses below 500–700 GeV. Electroweak SUSY analyses could exclude sleptons and electroweak gauginos with masses up to 400–600 GeV [189].
Figure VI.1 (left) shows the observed (solid red line) and expected (dashed red line) exclusion limit (at 95% CL) in the $(m_{\widetilde{g}}, m_{\widetilde{\chi}_1^0})$ mass plane for a benchmark model where a pair of gluinos decays promptly via on- or off-shell top squarks to four top quarks and two lightest neutralinos (simplified $\widetilde{g} \to t\bar{t}\,\widetilde{\chi}_1^0$ scenario).

[1] Not all results include the full Run I data. It can vary from 4.6–20.3 fb^{-1}, depending on the publication time.
[2] A branching ratio of 100% makes it more easy to interpret the models and to compare the results from ATLAS and CMS.

The limits are obtained from the statistical combination of the results from the different orthogonal searches, such as the aforementioned 0-lepton and 1-lepton analyses. The observed and expected limits from the individual analyses used for the combination are shown as well. The summary of the Run I searches for direct top squark pair production (Figure VI.1, right) is presented in a $(m_{\tilde{t}_1}, m_{\tilde{\chi}_1^0})$ mass plane and is separated into different decay modes of the top squark, for which individual analyses have been performed.

Since this summary covers results from different analyses and a lot of far-reaching assumptions (parameter space, branching ratios, neutralino masses, etc.) have been made to obtain them, they can obviously only give a rough idea about the overall achievements of the Run I SUSY searches in ATLAS. However, they provide a useful benchmark for understanding and evaluating the performance of the Run II analysis discussed in the following chapters.

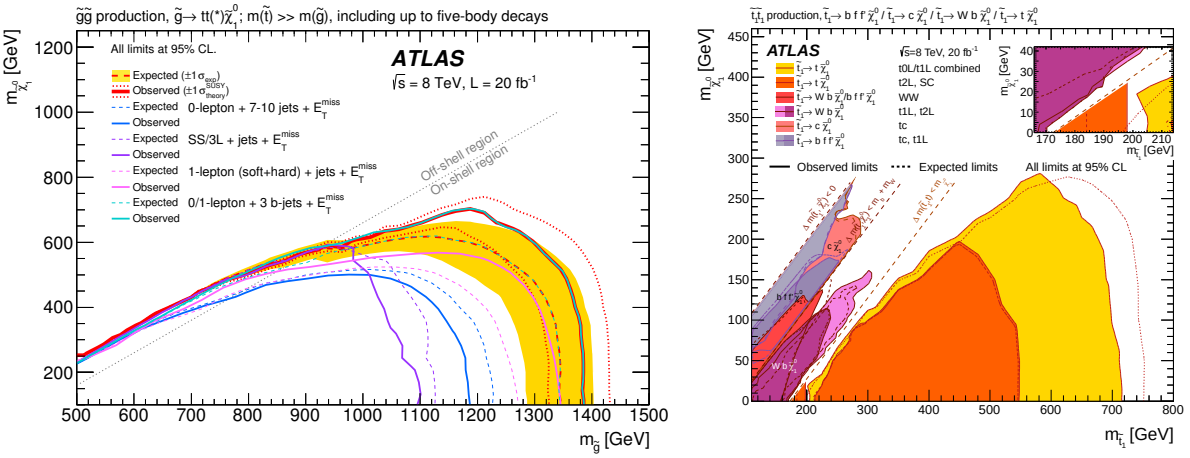

Figure VI.1.: Left: Exclusion limits in the $(m_{\tilde{g}}, m_{\tilde{\chi}_1^0})$ plane for the $\tilde{g} \to t\bar{t}\tilde{\chi}_1^0$ scenario. Expected limits from the individual analyses as well as the combined expected and observed limit are shown [187]. Right: Summary of the Run I searches for direct top squark pair production in the $(m_{\tilde{t}_1}, m_{\tilde{\chi}_1^0})$ plane. Different decay modes of the top squark are considered separately, each with a branching ratio of 100% [190].

VI.2. SAME-SIGN/3L SEARCH RESULTS FROM RUN I

The analysis described in this thesis is a resumption of the Run I search for strongly produced supersymmetric particles in final states with two same-sign (SS) leptons or three leptons (3L), which has been conducted using data from the full 2012 data taking period (20.3 fb^{-1} at $\sqrt{s} = 8$ TeV) [4]. Apart from the new developments presented in the following chapters, these were also the latest results for SUSY searches in this event signature. A brief summary of this analysis is given here.

The analysis focused on signatures with multiple energetic jets (light-flavor or b-jets), $E_{\mathrm{T}}^{\mathrm{miss}}$, and either two isolated leptons (electrons or muons) with the same electric charge or three leptons. Different kinematic requirements on m_{eff}, $E_{\mathrm{T}}^{\mathrm{miss}}$, or m_{T}[3] and selections on the event signatures (N_ℓ, N_{jets}) were used to define signal regions (SRs) sensitive to particular SUSY benchmark models. Two signal regions requiring a same-sign signature and b-jets were optimized for gluino-mediated top squark and direct bottom squark production. A region with a b-jet veto was targeted for gluino-mediated production of first- and second-generation squarks. Two SRs had a three-lepton requirement and were designed for SUSY scenarios with

[3]The transverse mass m_{T} is defined as: $m_{\mathrm{T}} = \sqrt{2p_{\mathrm{T}}^{\ell} E_{\mathrm{T}}^{\mathrm{miss}} \cdot (1 - \cos(\Delta\phi(p_{\mathrm{T}}^{\ell}, p_{\mathrm{T}}^{\mathrm{miss}})))}$.

multi-step decay chains. These five regions were kept orthogonal to allow a statistical combination of the results from each SR. The contribution from prompt Standard Model backgrounds in the SRs was estimated purely with Monte Carlo. Dominant SM processes were $t\bar{t}$+Z, $t\bar{t}$+W for the regions with b-jets and diboson production for the SRs with a b-veto. The reducible background can be separated into two categories. The first type is caused by so-called fake or non-prompt leptons, denoting arbitrary objects misidentified as leptons, such as light-flavor hadrons creating lepton-like signatures or leptons originating from heavy-flavor hadron decays. The second source is caused by leptons with misidentified charge, referred to as "charge-flip". This effect can occasionally convert opposite-sign events in same-sign final states. The reducible background sources were estimated with different data-driven techniques which will be comprehensively explained in the following chapter, since the Run II version of this analysis follows in general still the same strategy for the background estimation.
No significant deviation from the total Standard Model prediction has been observed in any of the five signal regions[4]. Accordingly, model-independent upper limits on the cross-section of possible BSM contributions to the signal regions were computed. Furthermore, model-dependent exclusion limits were set on a wide variety of supersymmetric models. Interpretations have been done in the context of R-parity conserving and violating scenarios. In total, exclusion limits were placed for 14 different SUSY models (including GMSB [60], mSUGRA/cMSSM [66] and bRPV [191]) using the statistical combination of the results from all signal regions. In addition, an interpretation in the context of one mUED (minimal Universal Extra Dimension) scenario [192] was done. The observed and expected limits for two commonly used benchmarks models ($\widetilde{g} \to t\bar{t}\widetilde{\chi}_1^0$ and $\widetilde{b}_1 \to tW^{\pm}\widetilde{\chi}_1^0$) are shown in Figure VI.2 in the $(m_{\widetilde{g}}, m_{\widetilde{\chi}_1^0})$ (left) and $(m_{\widetilde{b}_1}, m_{\widetilde{\chi}_1^0})$ (right) plane. The exclusion limits for gluino, squark, and neutralino masses depend strongly on the benchmarks model considered and specific assumptions made for each model. Thus, the numbers can in general not be compared to the values achieved in other searches. Gluino masses below 600–1200 GeV and squark masses below 400–500 GeV could be excluded at 95% CL. Neutralino masses could be excluded up to a range of 300–600 GeV for several scenarios.

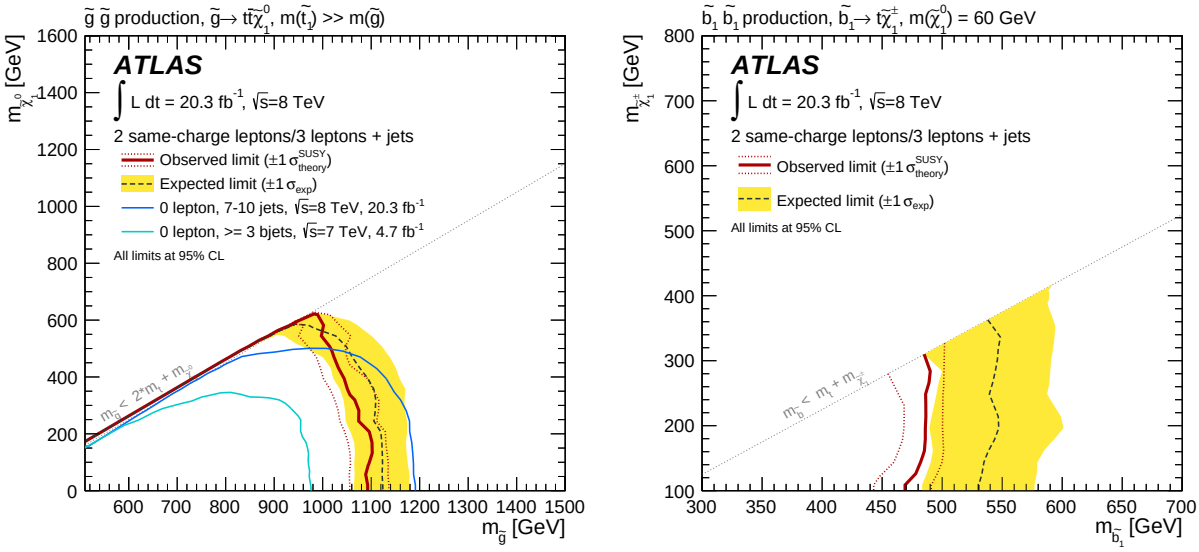

Figure VI.2.: Observed and expected exclusion limits (at 95% CL) of the Run I SS/3L analysis, derived for a $\widetilde{g} \to t\bar{t}\widetilde{\chi}_1^0$ (left) and $\widetilde{b}_1 \to tW^{\pm}\widetilde{\chi}_1^0$ (right) benchmark model. The results are compared with other Run I searches exploring the same model [4].

[4]The most significant region showed a p-value of 0.03, corresponding to a significance of 1.9 σ over the SM expectation.

VII. Search for SUSY with two same-sign Leptons or three Leptons in 2015

The Run II resumption of the search for supersymmetry in final states with either two same-sign leptons or three leptons, jets and $E_{\mathrm{T}}^{\mathrm{miss}}$ started beginning of 2015 with the intention to benefit from the increased cross-sections predicted for the production of SUSY particles at $\sqrt{s} = 13$ TeV [5]. While events with two same-sign or three-lepton final states are a frequent signature in many different BSM scenarios, most Standard Model processes leading to such events have rather low cross-sections. Thus, looser kinematic requirements with respect to other new physics searches can be applied while preserving a similar sensitivity to the most relevant SUSY scenarios.
The following chapter is dedicated to the same-sign/3L analysis, as it was conducted for the first time after the Long Shutdown 1 with the dataset collected in the year 2015. This analysis builds also the baseline for all further developments that followed during Run II. Besides a short summary of the SUSY benchmark models used to motivate the analysis (Section VII.1), the generic event selection, signal region definition and the background estimation strategy are described in detail in the Sections VII.2–VII.6. The results for the 2015 data and their interpretation in the context of the aforementioned simplified SUSY model are presented in Section VII.7 and VII.8, respectively. The personal contributions from the author of this thesis in the context of the analysis are summarized in the list of publications.

VII.1. Analysis Motivation and Signal Scenarios

Final states with two same-sign leptons or three leptons accompanied by multiple jets and large missing transverse energy are sensitive to a wide variety of new physics scenarios. In particular in supersymmetric models, such signatures can be created by pair production of heavy superpartners with subsequent decays involving top quarks, sleptons, or massive electroweak gauge bosons.
Four supersymmetric benchmark scenarios that can lead to same-sign or three-lepton + jet + $E_{\mathrm{T}}^{\mathrm{miss}}$ signatures are used for the optimization of the analysis and the design of the signal regions:

- Gluino pair production with prompt decay via off-shell top squarks $\widetilde{t}_1$ to four top quarks and two lightest neutralinos $\widetilde{\chi}_1^0$ with 100% branching ratio (simplified $\widetilde{g} \to t\bar{t}\widetilde{\chi}_1^0$ model). In this model, top squarks are considered to be much heavier than gluinos ($m_{\widetilde{t}_1} = 5$ TeV). Thus, the virtual $\widetilde{t}_1$ mediator can be expressed as an effective coupling and the gluinos decay directly to a $t\bar{t}\widetilde{\chi}_1^0$ triplet. The neutralinos produce a substantial amount of missing transverse energy. Due to the multiple top quark decays, several b-jets in addition to the same-sign signature are expected in the final state. The representative diagram of the process is depicted in Figure VII.1a.

- Direct pair production of light bottom squarks $\widetilde{b}_1$ with a subsequent chargino-mediated decay to top quarks, $W^{\pm}$ bosons, and neutralinos, referred to as $\widetilde{b}_1 \to t\,W^{\pm}\,\widetilde{\chi}_1^0$ model. In this model, the mass difference between the chargino $\widetilde{\chi}_1^{\pm}$ and neutralino is fixed to 100 GeV to allow on-shell $W^{\pm}$ boson production in the decay chain. Typically, b-jets originating from the top decays are expected in the final state as top quarks decay almost exclusively to $bW^{\pm}$. The process is shown in Figure VII.1b.

- Gluino pair production with generic decays to light-flavor quarks mediated by a cascade involving the lightest chargino $\widetilde{\chi}_1^{\pm}$ and the second-lightest neutralino $\widetilde{\chi}_2^0$, with two Z^0, two $W^{\pm}$ bosons, and two neutralinos in the final state (denoted as $\widetilde{g} \to q\bar{q}W^{\pm}Z\widetilde{\chi}_1^0$ model). The mass differences between

the particles in the decay chain allow on- and off-shell production of the massive gauge bosons. The gluinos decay via an effective coupling to a $q\bar{q}\widetilde{\chi}_1^{\pm}$ triplet, since the squark masses are assumed to be very large with respect to the gluino masses. The production of heavy-flavor quarks is suppressed in this scenario. Thus, it is used as benchmark to define signal regions with a b-jet veto. The model is illustrated in Figure VII.1c.

- Gluino pair production with a decay to light-flavor quarks and a two-step decay chain involving the second-lightest neutralino and light sleptons $\widetilde{\ell}/\widetilde{\nu}$ with multiple leptons and neutralinos in the final state. Also in this case, an effective coupling between the gluinos and a $q\bar{q}\widetilde{\chi}_2^0$ triplet is assumed. The branching ratios of the $\widetilde{\chi}_2^0 \to \widetilde{\ell}/\widetilde{\nu}$ decays are set to 50%. Compared to the $\widetilde{g} \to q\bar{q}W^{\pm}Z\widetilde{\chi}_1^0$ model, it has fewer jets in the final state but typically higher lepton multiplicities and is accordingly used as a benchmark for the signal regions with three leptons. The scenario is referred to as $\widetilde{g} \to q\bar{q}(\ell\bar{\ell}/\nu\nu)\widetilde{\chi}_1^0$ model and is shown in Figure VII.1d.

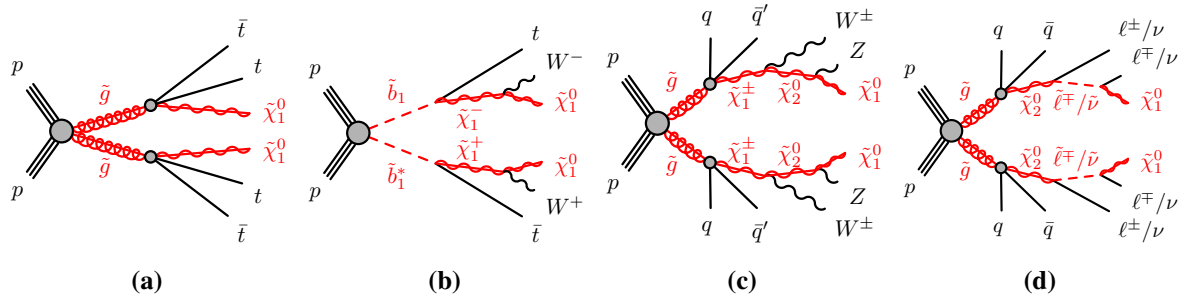

Figure VII.1.: Simplified SUSY benchmark models considered for the 2015 version of this analysis. The processes feature gluino (a,c,d) or bottom squark (b) pair production.

VII.2. Analysis Inputs, Object Definitions and Event Selection

This section gives a summary of the input data and simulated Monte Carlo samples used by the analysis and presents the definitions of the considered objects: muons, electrons, jets, b-jets, and $E_{\mathrm{T}}^{\mathrm{miss}}$ (hadronically decaying tau leptons are not considered). Furthermore, the preselection of candidate events and the trigger strategy is explained.

VII.2.1. Data and Monte Carlo Samples

The proton-proton collision data used for the analysis were collected during the year 2015 and correspond to a total integrated luminosity of 3.2 fb^{-1}. The nominal bunch spacing is 25 ns with an average number of additional pp interactions per bunch crossing of $\langle\mu\rangle = 14$. Requirements on beam stability, detector- and data-quality are applied, as described in Section VII.2.3.

Simulated Monte Carlo samples are used to model the prompt SM background and the different SUSY signal processes. Considering the experiences from the SS/3L search in Run I, the biggest SM contributions are expected to originate from diboson production in the signal regions without b-jets and from the production of top-antitop pairs plus one associated heavy gauge boson ($t\bar{t}$+W/Z) in the SRs with b-jets. The frameworks used for the event generation, the parton showering algorithms and the set of tuned parameters (MC tune) are stated in Table VII.1 for all background and signal processes. Also, the

associated PDF sets used in the simulation and the production cross-sections are presented. The values used for the MC normalization are actually given by the product of the production cross-section σ, the branching ratio (BR) of the decay, the generator filter efficiency ε_f[1], and the k-factor[2] of the process. The category "Rare" quoted in the table includes several SM backgrounds leading to a SS/3L signature, but with notably smaller cross-sections compared to the dominant diboson and $t\bar{t}+W/Z$ processes (tZ, $tW^{\pm}Z$, $t\bar{t}VV$ ($V = W/Z$), $tt\bar{t}$ (3-top), $t\bar{t}t\bar{t}$ (4-top), $W/Z+H$, $t\bar{t}+H$ and triboson production). The different signal samples are simulated with the same configuration, calculating the cross-section to NLO in the strong coupling constant and adding the resummation of soft gluon emission at next-to-leading-logarithmic accuracy (referred to as NLO+NLL scheme) [194]. Whereas the background samples are produced with the full GEANT4 simulation, the signal samples are mostly generated using the simplified ATLASFASTII framework (see Section III.4). A detailed list of all Monte Carlo samples used for signal and prompt background modeling, including the relevant numbers can be found in Appendix A.

Process	$\sigma \cdot \mathrm{BR} \cdot k \cdot \varepsilon_f$ [pb]	Event generator	Parton shower	σ order	MC tune	PDF set
Diboson						
ZZ	11.8	SHERPA2.2.1 [101]	SHERPA	NLO	SHERPA	CT10 [91]
$W^{\pm}Z$	4.62	SHERPA2.2.1	SHERPA	NLO	SHERPA	CT10
$W^{\pm}W^{\pm}jj$	$6.29 \cdot 10^{-2}$	SHERPA2.1.1	SHERPA	NLO	SHERPA	CT10
$t\bar{t}+W/Z$						
$t\bar{t}+W$	0.603	MG5_aMC@NLO2.2.2 [195]	PYTHIA8.186 [100]	NLO	A14 [196]	NNPDF23 [93]
$t\bar{t}+Z$	0.124	MG5_aMC@NLO2.2.2	PYTHIA8.186	NLO	A14	NNPDF23
Rare						
tZ	0.24	MADGRAPH5	PYTHIA6	LO	P2012 [197]	NNPDF23
$tW^{\pm}Z$	$1.55 \cdot 10^{-2}$	MG5_aMC@NLO2.2.2	PYTHIA8.186	NLO	A14	NNPDF23
$t\bar{t}VV$	$1.01 \cdot 10^{-2}$	MG5_aMC@NLO2.2.2	PYTHIA8.186	NLO	A14	NNPDF23
$t\bar{t}+H$	0.507	MG5_aMC@NLO2.3.2	HERWIG++2.7 [102]	NLO	UEEE5 [198]	NNPDF23
$W/Z+H$	2.25	PYTHIA8.186	PYTHIA8.186	NLO	A14	NNPDF23
3,4-top	$1.07 \cdot 10^{-2}$	MG5_aMC@NLO2.2.2	PYTHIA8.186	LO, NLO	A14	NNPDF23
Triboson	$1.47 \cdot 10^{-2}$	SHERPA2.1.1	SHERPA	NLO	SHERPA	CT10
Signal	–	MG5_aMC@NLO2.2.3	PYTHIA8.186	NLO+NLL	A14	NNPDF23

Table VII.1.: Simulated background and signal samples. The corresponding event generator, parton shower, cross-section, PDF set, and MC tune are listed for each sample. The signal cross-sections depend on the mass parameters of the SUSY particles and are obtained from [199].

VII.2.2. OBJECT DEFINITIONS

ELECTRONS AND MUONS

Lepton candidates (muons or electrons) can be identified according to a baseline definition in order to select leptons considered for the overlap removal, as well as more stringent identification requirements for

[1] Many MC generators use internal event filters to increase the purity of desired topologies (e.g. leptons or b-jets) for the randomly generated events.

[2] Simulated processes at leading order can be rescaled to NLO(NNLO) by applying correction factors, denoted as k-factors to the LO cross-section [193].

the objects used to build same-sign pairs for the signal regions (referred to as baseline and signal leptons). The selection requirements (working points) for the baseline and signal definitions have been chosen to obtain the optimal expected sensitivity to the targeted signal processes.

Baseline muons have to pass the *medium* [150] quality criteria and need to have $p_{\mathrm{T}} > 10$ GeV and $|\eta| < 2.5$. A lepton-jet isolation requirement is applied after the electron-jet overlap removal (see detailed explanation of OR). A signal muon candidate is required to pass additional isolation cuts defined by the *FixedCutTightTrackOnly*[3] isolation WP. Furthermore, the muon track has to fulfill conditions on the transverse and longitudinal impact parameters.

Baseline electrons are selected according to the likelihood-based *looseLH* [157] quality cuts with $E_{\mathrm{T}} > 10$ GeV and $|\eta^{\mathrm{clust}}| < 2.47$[4]. Electron candidates in the transition region between the barrel and end-cap electromagnetic calorimeters ($1.37 < |\eta| < 1.52$) are removed since the rate of non-prompt electrons was found to be significantly higher than in other detector regions. A requirement on the transverse impact parameter of the track is also applied to the baseline electron in order to further mitigate to contribution of electrons with misidentified charge. Signal electrons are identified according to the *tightLH* quality WP and are only selected within a reduced acceptance of $|\eta| < 2.0$, as the largest contributions from reducible background sources (see Section VII.4) are observed at large pseudorapidities. In addition, they have to pass isolation requirements (using the *FixedCutTight*[5] isolation WP) and a cut on the longitudinal impact parameter.

The criteria for the muon and electron selection are summarized in Table VII.2, including the baseline definitions and the additional requirements for signal leptons.

	Baseline electrons	**Baseline muons**
Acceptance	$E_{\mathrm{T}} > 10$ GeV, $\lvert\eta^{\mathrm{clust}}\rvert < 2.47$ except $1.37 < \lvert\eta^{\mathrm{clust}}\rvert < 1.52$	$p_{\mathrm{T}} > 10$ GeV, $\lvert\eta\rvert < 2.5$
Quality WP	*looseLH*	*medium*
ℓ-jet Isolation	$\Delta R(e, jet) > 0.4$	$\Delta R(\mu, jet) > 0.4$
Impact parameter	$\lvert d_0/\sigma(d_0)\rvert < 5.0$	
	Signal electrons	**Signal muons**
Quality WP	*tightLH* $\lvert\eta\rvert < 2.0$	(same as baseline)
Isolation WP	*FixedCutTight*	*FixedCutTightTrackOnly*
Impact parameter	$\lvert z_0 \cdot \sin(\theta)\rvert < 0.5$ mm	$\lvert z_0 \cdot \sin(\theta)\rvert < 0.5$ mm $\lvert d_0/\sigma(d_0)\rvert < 3.0$

Table VII.2.: Summary of the criteria for the electron (left) and muon (right) selection. The signal selection requirements are applied in addition to the baseline definition.

JETS AND B-TAGGED JETS

Jets are reconstructed using the anti-k_t algorithm [164] with a distance parameter of $R = 0.4$ and calibrated with the EMTopo scheme (AntiKt4EMTopo collection) [168]. The jet-area method [169] is applied to

[3] FixedCutTightTrackOnly: $p_{\mathrm{T}}^{\mathrm{varcone30}}/p_{\mathrm{T}} < 0.06$ with $p_{\mathrm{T}}^{\mathrm{varcone}R} = \min(R, \frac{10\,\mathrm{GeV}}{p_{\mathrm{T}}})$.

[4] For electrons, η^{clust} is the pseudorapidity measured from the EM energy cluster. The ordinary η is measured from the tracks.

[5] FixedCutTight: $p_{\mathrm{T}}^{\mathrm{varcone20}}/p_{\mathrm{T}} < 0.06$ and $E_{\mathrm{T}}^{\mathrm{Topo,varcone20}}/p_{\mathrm{T}} < 0.06$ with $E_{\mathrm{T}}^{\mathrm{Topo,varcone}R} = \min(R, \frac{10\,\mathrm{GeV}}{E_{\mathrm{T}}^{\mathrm{Topo}}})$.

subtract the contribution from pile-up effects. The selected jets need to have $p_T > 20$ GeV and $|\eta| < 2.8$. A further rejection of pile-up and displaced jets is attained with the jet vertex tagger (JVT) tool [200], which ensures that a significant fraction of the tracks associated with each jet must have an origin compatible with the primary vertex.
The identification of b-jets is done with the *MV2c20* [176] algorithm with a 70% efficiency operating point (see Section V.3.3). A slightly looser OP of 80% is used in the overlap removal procedure. The selected b-jets need to have $p_T > 20$ GeV and $|\eta| < 2.5$. The jet selection criteria and the b-jet requirements are summarized in Table VII.3.

	Jets
Collection	AntiKt4EMTopo
Acceptance	$p_T > 20$ GeV, $\|\eta\| < 2.8$
Jet vertex tagger	JVT > 0.64 for jets with $p_T < 50$ GeV, $\|\eta\| < 2.4$ (after OR)
	***b*-jets**
Acceptance	$p_T > 20$ GeV, $\|\eta\| < 2.5$
Identification	*MV2c20* at 70% OP (80% OP for OR)

Table VII.3.: Summary of the jet selection criteria and the b-jet requirements.

MISSING TRANSVERSE ENERGY

The E_T^{miss} is computed using all identified and calibrated physics objects, except from tau leptons (electrons, muons, photons, and jets), as well as the TST-based soft term as described in Section V.4.

OVERLAP REMOVAL

After the identification, overlaps between objects are resolved in order to avoid double-counting of physics objects. The OR procedure is performed as follows:

- Any jet within a distance closer than $\Delta R_y = 0.2$[6] to an electron candidate is discarded, unless the jet is identified as a b-jet according to the conditions from Table VII.3. In this case, the electron is removed since it is likely originating from a semileptonic b-hadron decay.
- Any remaining electron or muon closer than $\Delta R_y = 0.4$ to a jet is discarded.
- If a jet has less than three associated tracks, the muon is kept and the jet is removed to avoid inefficiencies for high-p_T muons undergoing significant energy losses in the calorimeter system.
- In case a muon and an electron with $\Delta R_y < 0.01$ are identified, the electron is likely to originate from muon bremsstrahlung. In this case, the electron is non-prompt and the muon momentum cannot be measured correctly, so both objects are rejected.

[6] For the sake of accuracy, the computation of geometrical distances in the OR procedure is done with the regular rapidity y instead of the pseudorapidity (denoted as ΔR_y).

- Finally, if two (or more) electrons with $\Delta R_y < 0.05$ are identified, the EM showers were most likely induced by the same initial object. Therefore, the electron with the highest p_T is kept and the others are discarded.

VII.2.3. PRESELECTION AND EVENT CLEANING

Events considered for the analysis are selected according to the criteria listed below. The cuts are applied consecutively in the same order as described in the list:

- **Good Run List:** Data events are only selected if they come from lumi-blocks with sufficient beam- and data-quality and ensured functionality of all detector systems [201]. These events are listed in an official recommended Good Run List (GRL). Events which do not fulfill these conditions are rejected. This requirement is not applied to simulated events.
- **Primary vertex:** Events are required to have at least one reconstructed vertex with ≥ 2 associated tracks with $p_T > 400$ MeV. The vertex with the largest $\sum p_T^2$ of the associated tracks is defined as the primary vertex.
- **Trigger:** Events are selected using a logical "or" combination of dilepton and E_T^{miss} triggers. The detailed trigger strategy is explained in Section VII.2.4.
- **Error-flags:** Events with error-flags indicating temporary non-functionality of the LAr or tile calorimeter are removed.
- **Bad muon/jet veto:** Events are rejected if they contain at least one muon with $\sigma(q/p)/|q/p| > 0.2$ (see Section V.1.1) before the OR.

  Particular jet quality criteria are defined to remove events with significant energy deposits in the calorimeters due to instrumental effects, like cosmic rays, non-collision particles, or electronic noise [168]. If events contain jets failing these quality criteria after the OR, they are removed.
- **Cosmic muon veto:** Cosmic muon candidates are identified if their tracks cannot fulfill $|z_0| < 1.0$ mm and $|d_0| < 0.2$ mm. Events containing a cosmic muon candidate are rejected.
- **Two leptons:** Selected events are required to contain at least two signal leptons with $p_T > 20$ GeV (two-lepton event). If the events contain a third signal lepton, it needs to have $p_T > 10$ GeV to be considered as three-lepton final state. These p_T requirements were found to be the most sensitive ones, as shown in Section VII.3.1.
- **Same-sign lepton pair:** For two-lepton events, the leading leptons are required to have the same electric charge (independent from the flavor combination of the lepton pair).

  Three-lepton final states are always considered as a same-sign event. For events with more than one possibility to select a same-sign pair (e.g. $e^+\mu^-\mu^-e^+$), the pair including the lepton with the largest p_T is chosen.

VII.2.4. TRIGGER STRATEGY

Since many aspects of the ATLAS trigger system changed significantly in Run II (as described in Section IV.3.5), the trigger strategy used to select potentially interesting events had to be fully revisited with simulated test samples.

Based on the approach used for the Run I version of the analysis, the strategy was chosen with consecutive checks of performance and efficiency of single-lepton, dilepton, and $E_{\mathrm{T}}^{\mathrm{miss}}$ triggers. Efficiency studies were performed on several single electron/muon triggers, same- and opposite-flavor dileptons triggers, and $E_{\mathrm{T}}^{\mathrm{miss}}$ triggers taken from the 2015 trigger menu. Offline cuts on the missing transverse energy and the p_{T} of the triggered objects have been applied to ensure to be on the efficiency plateaus of the corresponding triggers.

MISSING TRANSVERSE ENERGY TRIGGERS

To select events with large missing transverse energy, the trigger that was chosen is `HLT_xe70`, with an online $E_{\mathrm{T}}^{\mathrm{miss}}$ threshold of 70 GeV. This was the lowest unprescaled $E_{\mathrm{T}}^{\mathrm{miss}}$ trigger in the 2015 menu[7]. Figure VII.2 shows its efficiency evolution (plotted against the total missing E_{T} value) in a $t\bar{t}$ Monte Carlo sample with an additional preselection of ≥ 2 signal leptons applied. The efficiency is shown for different requirements on the jet multiplicity (left) and compared with the performance of the `HLT_xe80` ($E_{\mathrm{T}}^{\mathrm{miss}} > 80$ GeV) and `HLT_xe80_tc_lcw`[8] triggers, which are also unprescaled (right). In all cases, the efficiency turn-on curves are similar and the triggers are fully efficient at $E_{\mathrm{T}}^{\mathrm{miss}}$ values of around 250 GeV.

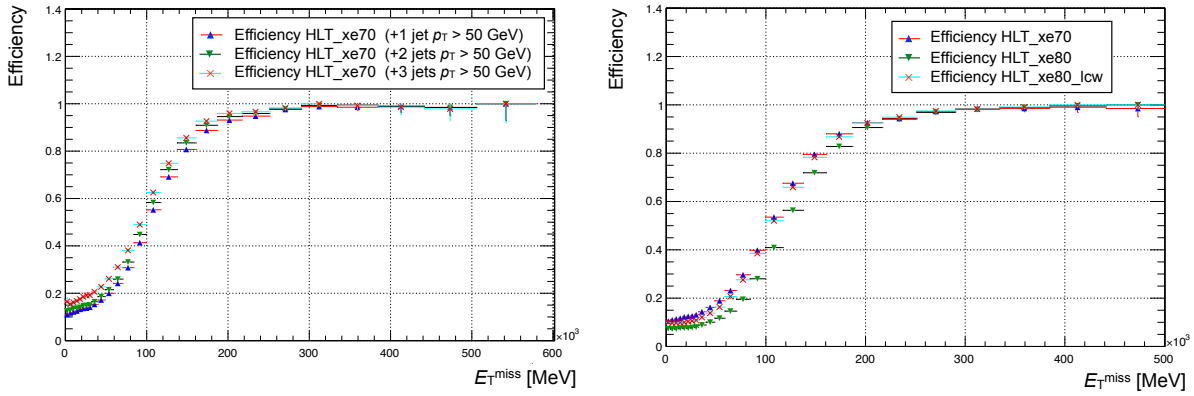

Figure VII.2.: Efficiency evolution of the trigger `HLT_xe70` versus $E_{\mathrm{T}}^{\mathrm{miss}}$ for different jet multiplicities (left) and compared to `HLT_xe80` and `HLT_xe80_tc_lcw` (right). The efficiencies are derived from simulated $t\bar{t}$ samples for preselected events with at least two signal leptons.

DILEPTON TRIGGERS

For the selection of dilepton events, it was decided to use a combination of a dimuon, a dielectron, and an electron-muon trigger. For each lepton topology, the lowest unprescaled trigger available in the menu was chosen: `HLT_2e12_lhloose_L12EM10VH` (two electrons with $p_{\mathrm{T}} > 12$ GeV), `HLT_mu18_mu8noL1` (two muons, $p_{\mathrm{T}}^{1(2)} > 18(8)$ GeV) and `HLT_e17_lhloose_mu14` (one electron, $p_{\mathrm{T}} > 17$ GeV and one muon, $p_{\mathrm{T}} > 14$ GeV).

On the left-hand side of Figure VII.3, the efficiency of the dielectron trigger plotted against the p_{T} of the leading electron is shown[9]. The plot on the right-hand side shows the efficiency for the combination of the dilepton and $E_{\mathrm{T}}^{\mathrm{miss}}$ triggers for preselected $t\bar{t}$ events with two signal muons ($p_{\mathrm{T}} > 20$ GeV) plotted against the p_{T} of the leading muon. The efficiency stays at an almost constant value of around 95%.

[7] In order not to discard potentially interesting events in data, unprescaled triggers are used.

[8] The difference between them is the calibration scheme of the jets used for the $E_{\mathrm{T}}^{\mathrm{miss}}$ calculation (EMTopo vs. LCTopo).

[9] The efficiency is computed in two dimensions binned in the momenta of the two triggered leptons and then projected to the p_{T} of the leading lepton.

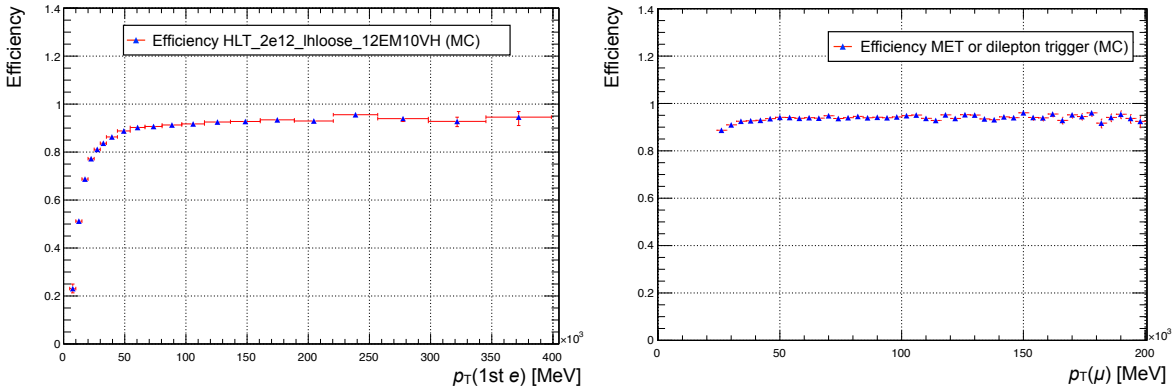

Figure VII.3.: Left: Efficiency of `HLT_2e12_lhloose_L12EM10VH` plotted against the p_T of the leading electron. Right: The total efficiency for the "or" combination of dilepton and E_T^{miss} triggers versus the p_T of the triggered muon.

TRIGGER YIELDS AND FINAL CONFIGURATION

The total event yields for different trigger configurations have been investigated in order to understand the gain of the several trigger types and their combinations. These tests were performed on a simulated $t\bar{t}$ sample.

The results are shown in Figure VII.4, separately for events with $E_T^{miss} < 200$ GeV and $E_T^{miss} > 200$ GeV and for several "or" combinations of triggers (dilepton triggers, dilepton or E_T^{miss} triggers, dilepton or E_T^{miss} or single-lepton triggers[10]). For the events with low E_T^{miss}, the single-lepton triggers yield an increase of the selected events by about only 1.5%. Also the measurement for high-E_T^{miss} events shows only a negligible improvement by adding single-lepton triggers to the configuration. The most significant improvement is achieved by adding the E_T^{miss} trigger to the dilepton trigger chain for events with $E_T^{miss} > 200$ GeV, with a $\approx$6% increase of the events selected by the triggers. For simplicity and due to the minor improvement they could provide, it has been decided not to include single-lepton triggers in the final configuration.

Accordingly, the final trigger strategy to be used for this analysis is based on a combination of several dilepton triggers and an E_T^{miss} trigger:

- For events with $E_T^{miss} < 250$ GeV, a logical "or" combination of the following dilepton triggers is used: `HLT_2e12_lhloose_L12EM10VH`, `HLT_mu18_mu8noL1` and `HLT_e17_lhloose_mu14`. Additionally, a trigger matching between the signal leptons ($p_T > 20$ GeV) and the triggered objects is applied[11].
- For events with $E_T^{miss} > 250$ GeV, an "or" between the aforementioned dilepton triggers and the E_T^{miss} trigger `HLT_xe70` is used.

VII.3. SIGNAL REGIONS

The definition of the signal regions is the result of a dedicated optimization procedure performed to achieve the maximal discovery sensitivity to each of the four supersymmetric benchmark models. However, in

[10] The bin "all triggers" is a control indicator showing the event yields for all triggers (also prescaled ones) from the 2015 menu.
[11] The object that activates one of the lepton triggers might not always be identical with one of the selected signal leptons. To avoid a misidentification, a geometrical matching (trigger matching) as to be applied if an event is selected by a lepton trigger.

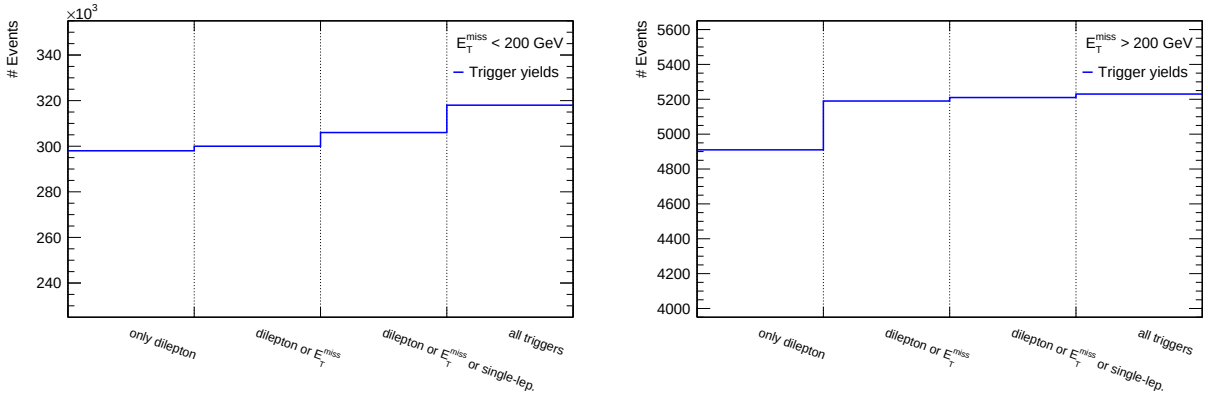

Figure VII.4.: Total number of selected events in a simulated $t\bar{t}$ sample for several trigger configurations (dilepton, dilepton or $E_{\mathrm{T}}^{\mathrm{miss}}$, dilepton or single-lepton or $E_{\mathrm{T}}^{\mathrm{miss}}$). The event yields are measured separately for events with $E_{\mathrm{T}}^{\mathrm{miss}} < 200$ GeV (left) and $E_{\mathrm{T}}^{\mathrm{miss}} > 200$ GeV (right).

order to allow model-independent interpretations of the results, the selection should not be too specific. The optimization effort and the final definition of the analysis signal regions are described in this section.

VII.3.1. OPTIMIZATION PROCEDURE

The optimization was performed independently for the four SUSY scenarios described in Section VII.1 by scanning on different cut values for kinematic quantities and object multiplicities. All these scans included already the generic preselection listed in Section VII.2.3, in particular the SS/3L requirement. The set of cuts with the best expected sensitivity for discovering a specific scenario was used to define a signal region, with the purpose of the procedure to reach the best possible discovery potential across the entire signal grid with a single cut configuration. It should be mentioned that different signal points in one SUSY grid have in general distinct kinematic properties due to the various mass differences between the squarks/gluinos and neutralinos. Thus, obtaining the optimal sensibility to an entire grid with one fixed cut configuration is hardly achievable and the best SR definition was typically chosen as the best possible compromise across the signal grids to cover regions with large mass splittings between the superpartners, as well as compressed scenarios.

Signal regions targeting the $\widetilde{g} \to t\bar{t}\widetilde{\chi}_1^0$ and $\widetilde{b}_1 \to tW^{\pm}\widetilde{\chi}_1^0$ scenarios include b-jet requirements whereas the SRs aiming for the $\widetilde{g} \to q\bar{q}W^{\pm}Z\widetilde{\chi}_1^0$ and $\widetilde{g} \to q\bar{q}(\ell\bar{\ell}/\nu\nu)\widetilde{\chi}_1^0$ signals have b-jet vetos. The background estimation for the optimization studies relied purely on Monte Carlo simulation. Simulated $t\bar{t}$+W/Z samples have been used for the regions with b-jet requirements while diboson MC was used for the SRs with b-jet vetos. The reducible background processes were modeled with $t\bar{t}$ samples. The expected sensitivity was computed with the ROOSTATS framework [202] using a simplified approach assuming an overall 40% systematic uncertainty on the background prediction with the significance Z_n defined in terms of one-sided Gaussian standard deviations.

The parameters examined during the optimization were kinematic quantities, such as $E_{\mathrm{T}}^{\mathrm{miss}}$, m_{eff}, and the p_{T} of the leptons and jets, but also the number of signal leptons $N_{\ell}^{\mathrm{signal}}$, the jet multiplicity N_{jets} and the number of b-tagged jets $N_{b\text{-jets}}$ in an event. For the sake of simplicity and to avoid being too specified to the simplified benchmark models, these were the only discriminant variables in the 2015 version of the analysis[12]. Figure VII.5 shows the expected significances of the signal regions optimized for the $\widetilde{g} \to t\bar{t}\widetilde{\chi}_1^0$

[12] If a signal region is too optimized to a particular model, it typically loses its general sensitivity to a broad range of other BSM scenarios. This effect, commonly denoted as "over-optimization", has to be avoided.

and $\widetilde{b}_1 \to tW^{\pm}\widetilde{\chi}_1^0$ scenarios (left-hand side), as well as for the $\widetilde{g} \to q\bar{q}W^{\pm}Z\widetilde{\chi}_1^0$ and $\widetilde{g} \to q\bar{q}(\ell\bar{\ell}/\nu\nu)\widetilde{\chi}_1^0$ scenarios (right-hand side) for different lepton multiplicities and p_{T} requirements on the leptons. A specific benchmark point from the respective scenario is used to find the most sensitive lepton selection for each of the four signal regions. It was found that in most cases (except from the $\widetilde{g} \to q\bar{q}(\ell\bar{\ell}/\nu\nu)\widetilde{\chi}_1^0$ process), an inclusive selection of ≥ 2 signal leptons with $p_{\mathrm{T}}(\ell_{1,2}) > 20$ GeV and $p_{\mathrm{T}}(\ell_3) > 10$ GeV is more sensitive than requiring explicitly two leptons or at least three leptons.

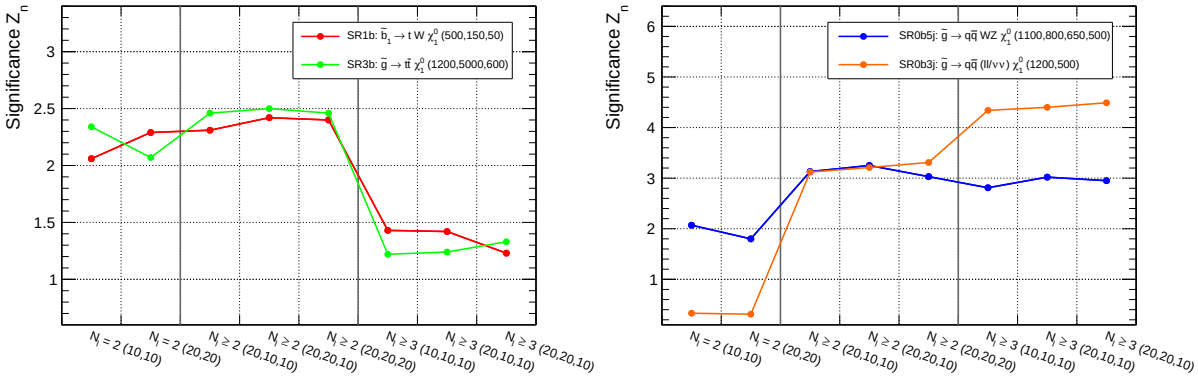

Figure VII.5.: Expected significances of the signal regions optimized for the $\widetilde{g} \to t\bar{t}\widetilde{\chi}_1^0$ and $\widetilde{b}_1 \to tW^{\pm}\widetilde{\chi}_1^0$ scenarios (left), as well as for the $\widetilde{g} \to q\bar{q}W^{\pm}Z\widetilde{\chi}_1^0$ and $\widetilde{g} \to q\bar{q}(\ell\bar{\ell}/\nu\nu)\widetilde{\chi}_1^0$ scenarios (right) for different lepton multiplicities (N_ℓ) and p_{T} thresholds (in GeV). The numbers in brackets indicate the p_{T} cuts for the first, second, and third lepton, respectively. For each SR, a specific benchmark point from the corresponding SUSY scenario was used for the optimization.

VII.3.2. SIGNAL REGIONS DEFINITIONS

The four signal regions are defined as summarized in Table VII.4. Selection cuts on the effective mass and the missing transverse energy are applied to all signal regions. The regions optimized for the $\widetilde{b}_1 \to tW^{\pm}\widetilde{\chi}_1^0$ and $\widetilde{g} \to t\bar{t}\widetilde{\chi}_1^0$ scenarios have one and three b-jets requirements, respectively. Accordingly, they are denoted as "SR1b" and "SR3b". Also, a minimum number of jets with $p_{\mathrm{T}} > 50$ GeV (light-flavor or b-tagged) is required. The regions targeting the $\widetilde{g} \to q\bar{q}(\ell\bar{\ell}/\nu\nu)\widetilde{\chi}_1^0$ and $\widetilde{g} \to q\bar{q}W^{\pm}Z\widetilde{\chi}_1^0$ models have b-jet vetos, but also requirements on the number of light-flavor jets. They are named "SR0b3j" and "SR0b5j". It was found that no substantial gain would be achieved by considering three-lepton final states separately, as it was done in the Run I analysis [4]. Only for SR0b3j, which aims explicitly for the $\widetilde{g} \to q\bar{q}(\ell\bar{\ell}/\nu\nu)\widetilde{\chi}_1^0$ scenario, a three-lepton requirement was found to be significantly more sensitive.

Signal region	N_ℓ^{signal}	N_{jets}^{50}	$N_{b\text{-jets}}^{20}$	$E_{\mathrm{T}}^{\mathrm{miss}}$ [GeV]	m_{eff} [GeV]	Targeted signal
SR1b	≥ 2	≥ 4	≥ 1	> 150	> 550	$\widetilde{b}_1 \to tW^{\pm}\widetilde{\chi}_1^0$
SR3b	≥ 2	–	≥ 3	> 125	> 650	$\widetilde{g} \to t\bar{t}\widetilde{\chi}_1^0$
SR0b3j	≥ 3	≥ 3	$= 0$	> 200	> 550	$\widetilde{g} \to q\bar{q}(\ell\bar{\ell}/\nu\nu)\widetilde{\chi}_1^0$
SR0b5j	≥ 2	≥ 5	$= 0$	> 125	> 650	$\widetilde{g} \to q\bar{q}W^{\pm}Z\widetilde{\chi}_1^0$

Table VII.4.: Summary of the 2015 signal region definitions and their targeted SUSY scenarios. The superscript in the jet multiplicity denotes the p_{T} threshold of the corresponding jets.

VII.4. BACKGROUND ESTIMATION

Due to the small number and relatively low cross-sections of Standard Models processes leading to a same-sign or three-lepton + jets + $E_{\mathrm{T}}^{\mathrm{miss}}$ signature, the signal regions of this analysis have in general a rather low background contamination. However, several reducible and irreducible background sources exist. A stable and precise estimation of these background processes is an essential task in order to obtain reliable results. The background can be subdivided into three categories for which different estimation methods are utilized:

- **Prompt SS/3L background:** Although processes leading to same-sign or three-lepton final states have small cross-sections compared to many other SM processes, their contribution to the SRs cannot be neglected.
- **Fake or non-prompt leptons:** This denotes different objects misidentified as leptons, such as light hadrons with lepton-like signatures, electrons from photon conversions or leptons originating from heavy-flavor hadron decays. Events with one of these objects in addition to a real lepton can occasionally create same-sign final states.
- **Charge-flip leptons:** This background comes from leptons where the electric charge was misidentified, commonly referred to as "charge-flip". In this case events with opposite-sign (OS) lepton pairs can be unintentionally identified as SS events.

The methods for estimating the contributions of these background sources to the signal regions are described in the following.

VII.4.1. PROMPT LEPTON BACKGROUND

The estimation of the SM background processes leading to prompt same-sign or three-lepton final states is performed using the Monte Carlo samples listed in Table VII.1. As it was mentioned already, the main sources are the associated production of $t\bar{t}$ pairs plus massive gauge bosons ($t\bar{t}$+W/Z) in the signal region with at least one b-jet and diboson production in the SRs with a b-jet veto. Figure VII.6 depicts the representative tree-level diagrams for some of the most relevant diboson (a,b), $t\bar{t}$+Z (c), and $t\bar{t}$+W (d) production mechanisms.

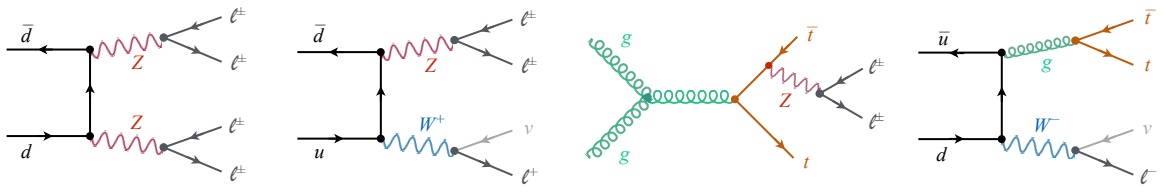

Figure VII.6.: Diagrams for some fundamental processes featuring $ZZ \to \ell\ell\ell\ell$ (a), $WZ \to \ell\ell\ell\nu$ (b), $t\bar{t}$+Z (c), and $t\bar{t}$+W (d) production. The processes are only shown tree-level (without including higher order corrections).

The MC prediction is normalized to the total data luminosity using the best known theoretical cross-sections. Dedicated validation regions (VRs) with an enhanced contribution from these processes and only a small signal contamination were defined to verify the background predictions from the simulation. These regions are introduced in Section VII.6. Contributions from SM processes with low production

rates (summarized and labelled as "Rare" for the rest of this chapter) come from single top production plus one (or two) associated massive gauge bosons, $t\bar{t}$ plus two massive gauge bosons, production of a Higgs boson in association with a $t\bar{t}$ pair or a massive gauge boson, multi-top, and triboson production. Due to their subordinate role with respect to $t\bar{t}$+W/Z and diboson production, no VRs dedicated to these processes were designed.

VII.4.2. FAKE/NON-PROMPT LEPTON BACKGROUND AND MATRIX METHOD

The expression "fake lepton" describes arbitrary objects accidentally misidentified as a lepton. They can originate from different sources, such as leptons from pion or kaon decays, electrons from photon conversions, or light jets with parts of the electromagnetic shower selected by a lepton identification algorithm. Non-prompt leptons originate typically from heavy-flavor hadron decays with associated production of $W^{\pm}$ or Z^0 bosons which decay subsequently to leptons. Examples of such processes are schematically illustrated in Figure VII.7. These effects can in general not be modeled sufficiently by Monte Carlo.

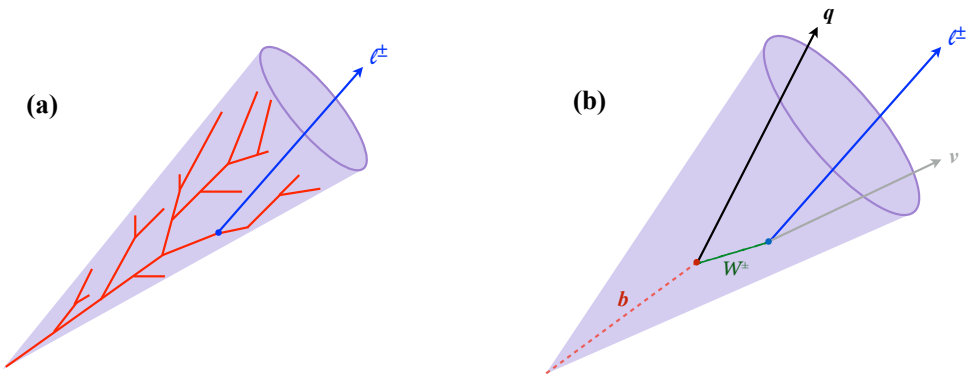

Figure VII.7.: Illustration of processes that can lead to fake/non-prompt leptons: lepton coming from the electromagnetic shower of a jet (a) or a non-prompt lepton from a heavy-flavor quark decay (b).

The contribution from fake or non-prompt (FNP) leptons to the signal regions is estimated with a purely data-driven approach, referred to as *matrix method* [4]. This method has been successfully used already in the RunI version of the analysis. It relies basically on the difference in the response of identification, isolation and impact parameters for prompt and non-prompt leptons. The efficiencies for FNP leptons are in general lower than for real leptons. The method uses the baseline[13] and signal lepton collections, as they are defined in Table VII.2. For cases with only one lepton per event, one can relate the numbers of prompt or FNP leptons passing the signal or baseline requirements by a 2×2 matrix Λ, containing the efficiencies for the two leptons types to pass the signal requirements:

$$\begin{pmatrix} N_S \\ N_B \end{pmatrix} = \Lambda \times \begin{pmatrix} N_P \\ N_F \end{pmatrix}, \qquad \Lambda = \begin{pmatrix} \varepsilon & \zeta \\ (1-\varepsilon) & (1-\zeta) \end{pmatrix}, \tag{VII.1}$$

where N_P and N_F denote the numbers of prompt and FNP leptons. N_B and N_S state the numbers of leptons passing the baseline or signal requirements. The parameters ε and ζ are the probabilities that a real or FNP lepton fulfills the signal requirements (denoted as real and fake rates). The quantity of interest is the number of fake/non-prompt leptons passing the signal requirements in the signal region. Therefore, the

[13] For consistency with the acceptance used for signal electrons, only baseline electrons with $|\eta| < 2.0$ are considered.

efficiency matrix has to be inverted:

$$\begin{pmatrix} N_P \\ N_F \end{pmatrix} = \Lambda^{-1} \times \begin{pmatrix} N_S \\ N_B \end{pmatrix}, \qquad \Lambda^{-1} = \frac{1}{\varepsilon - \zeta} \begin{pmatrix} (1-\zeta) & -\zeta \\ (\varepsilon - 1) & \varepsilon \end{pmatrix}. \tag{VII.2}$$

The number of fake or non-prompt leptons passing the signal requirements $N_{\{F|S\}}$ can be calculated from the total number of FNP leptons and the fake rate:

$$N_{\{F|S\}} = \zeta \cdot N_F = \frac{\zeta}{\varepsilon - \zeta} \left(N_S (\varepsilon - 1) + \varepsilon N_B \right). \tag{VII.3}$$

This equation yields the total number of leptons entering a signal region. Due to its linearity, the total event yields can be obtained by applying a weight $w = \frac{\zeta}{\varepsilon - \zeta}(\varepsilon - \mathbb{I}_\ell)$ to each event, depending if the lepton passed ($\mathbb{I}_\ell = 1$) or failed ($\mathbb{I}_\ell = 0$) the signal requirements. The predicted total event yields from fake/non-prompt leptons are then given by the sum of these weights.
For the two-lepton case, the equation has to be extended to cover all possible combinations of prompt and FNP leptons passing or failing the signal requirements. Accordingly, a 4×4 matrix including the fake and real rates for the first and the second lepton $\varepsilon_{1,2}$, $\zeta_{1,2}$ has to be used:

$$\begin{pmatrix} N_{SS} \\ N_{SB} \\ N_{BS} \\ N_{BB} \end{pmatrix} = \Lambda \times \begin{pmatrix} N_{PP} \\ N_{PF} \\ N_{FP} \\ N_{FF} \end{pmatrix}, \; \Lambda = \begin{pmatrix} \varepsilon_1 \varepsilon_2 & \varepsilon_1 \zeta_2 & \zeta_1 \varepsilon_2 & \zeta_1 \zeta_2 \\ \varepsilon_1 (1-\varepsilon_2) & \varepsilon_1 (1-\zeta_2) & \zeta_1 (1-\varepsilon_2) & \zeta_1 (1-\zeta_2) \\ (1-\varepsilon_1) \varepsilon_2 & (1-\varepsilon_1) \zeta_2 & (1-\zeta_1) \varepsilon_2 & (1-\zeta_1) \zeta_2 \\ (1-\varepsilon_1)(1-\varepsilon_2) & (1-\varepsilon_1)(1-\zeta_2) & (1-\zeta_1)(1-\varepsilon_2) & (1-\zeta_1)(1-\zeta_2) \end{pmatrix}. \tag{VII.4}$$

However, the methodology remains the same as in the one-lepton case explained. The formalism can also be extended to an arbitrary number of leptons, denoted as *dynamic matrix method* which is the default approach in this analysis. For events with >3 leptons, the contribution from fake/non-prompt leptons has a negligible effect on the signal regions. The different sources of FNP leptons (light hadrons, heavy-flavor decays, photon conversions, etc.) cannot be disentangled by this method. However, an additional uncertainty is assigned to the prediction to account for potential differences in the composition of FNP lepton sources between the regions used for the rate measurements and the actual signal regions.
The application of this method demands a precise measurement of the fake and real rates ε and ζ. The real rates are measured in a pure $Z^0 \to \ell\ell$ data sample. A tag-and-probe method is used similarly to the one described in Section V.1.2. The tag leptons have to fulfill the signal requirements and need to have $p_{\mathrm{T}} > 25$ GeV. The probe leptons are selected by building same-flavor lepton pairs which are required to be in an invariant mass range of 80 GeV $< m_{\ell\ell} <$ 100 GeV. If a tag-and-probe pair is selected, both leptons are alternatively considered to be the potential tag object, as this allows to improve the statistical precision of the measurement and to remove any possible bias in the choice of the tag lepton.
The fake rates also determined from data in a control region enriched with $t\bar{t}$ events. Events in this region have to contain at least one b-jet, one signal muon with $p_{\mathrm{T}} > 40$ GeV[14] and an additional baseline lepton. The signal muon and the other lepton need to build a same-sign pair. Assuming the signal muon is most likely a prompt lepton and the dominant process in the data sample is indeed $t\bar{t}$ production (which cannot promptly produce same-sign final states), the additional baseline lepton has to originate from a heavy-flavor decay[15]. Before measuring the rates, the expected contributions from prompt leptons and

[14] The high p_{T} requirement of 40 GeV is chosen to ensure a high probability that this muon is not a fake lepton.
[15] Measuring the fake rates in this way assumes that heavy-flavor decays are the only source of FNP leptons (which is not completely correct). However, investigating the sources of FNP leptons in MC confirmed that this is the dominant process.

charge mismeasured electrons (which are estimated separately) are subtracted from the observed event yields of the control region.
Both rates are measured separately for electrons and muons. Furthermore, the measurements are done for several p_T and η ranges and applied as a function of the positions and momenta of the leptons. The real rates are in most cases $>60\%$ and close to 100% for leptons with $p_T > 50$ GeV. The fake rates depend to a large extent on the lepton flavor and on properties like the event topology, the η range and the p_T of the leptons. They are typically between 10 and 20%. The systematic uncertainties associated with this method are described in Section VII.5.

VII.4.3. CHARGE-FLIP BACKGROUND

A misidentification of the electric charge of a lepton can be induced by different effects. The main processes responsible for a mismeasured electron charge are so-called "trident events": electrons which emit a hard bremsstrahlung photon and the photon subsequently converts to an electron-positron pair ($e^{\pm} \to e^{\pm}\gamma \to e^{\pm}e^{+}e^{-}$), with the main fraction of the original momentum transferred to the positron[16]. Another potential source are errors on the track charge assignment itself, which occurs especially for high-p_T tracks with a small curvature. The impact of this effect is, however, smaller than the contribution from the trident process. An illustration of these processes is shown in Figure VII.8 (on the left-hand side the trident event and on the right-hand side the wrong charge assignment of the track).

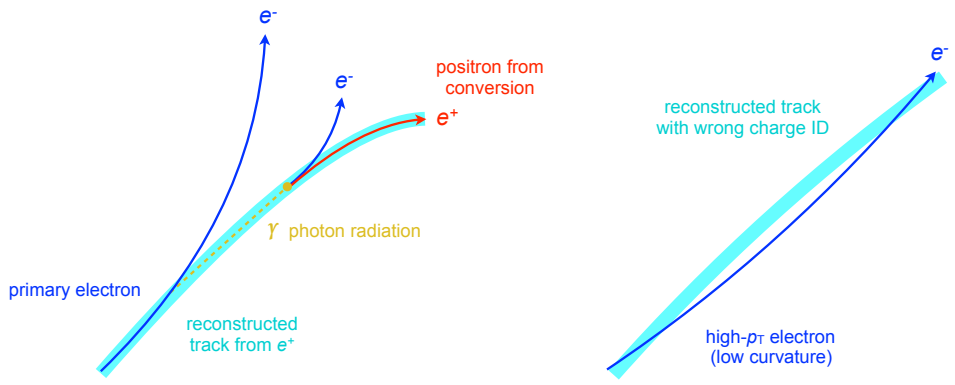

Figure VII.8.: Processes leading to a charge misidentification: emittance of a bremsstrahlung photon with subsequent $e^{+}e^{-}$ conversion (left). Wrong curvature reconstruction of a high-p_T track (right).

Both effects are found to happen primarily for electrons. The probability of misidentifying the charge of a muon was determined in simulation and can be neglected in the kinematic range relevant to this analysis (0.2–0.3‰). For signal regions with a three-lepton requirement, this background type is also ignored, since a charge misidentification has obviously no consequences there.
The size of the charge-flip process can be exhibited by looking at $Z^0 \to \ell\ell$ events for opposite-sign and same-sign lepton pairs, as shown on the plots in Figure VII.9, on the left for electron pairs and on the right for muon pairs. These plots consider only pairs of signal leptons ($N_\ell = 2$) with $p_T > 20$ GeV. The fact that the Z^0 resonance at around 91 GeV is clearly visible also in the invariant mass spectrum for same-sign electrons demonstrates that the charge of one of these electron has been misidentified. For muons, these effects are several orders of magnitude smaller and can, therefore, be ignored. By comparing the simulated $Z^0 \to \ell\ell$ events to data, it is noteworthy that the MC prediction of the charge-flipped electrons is about

[16]The identical process can obviously happen also vice versa, with a positron mismeasured as electron.

30% too high in the region around the Z^0 resonance. Thus, a data-driven approach is indeed needed to describe this effect.

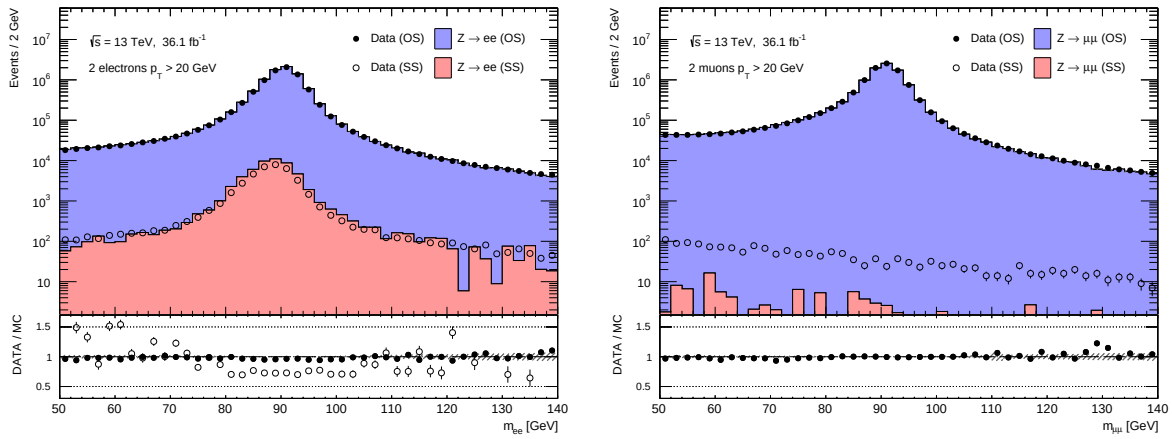

Figure VII.9.: Invariant mass distributions of opposite-sign and same-sign electron (left) and muon (right) pairs: the data is compared to simulated $Z^0 \to \ell\ell$ OS (blue) and SS (red) events. The bottom panel shows the ratio between data and MC for OS and SS signatures.

A data-driven method is used also for estimating the charge-flip background. Assuming the charge-flip rates of the first and the second electron $\xi_{1(2)}$ (equivalent to the probability of a charge to be misidentified) are known, the event yields can be predicted by selecting events with pairs of opposite-sign leptons in data and assign them a weight w_{CF}. Since the aforementioned processes responsible for the charge mismeasurement depend on momentum and position of the particles, the rates are assumed to be functions of p_{T} and η of the first and second electron:

$$w_{\mathrm{CF}} = \xi_1 \cdot (1-\xi_2) + (1-\xi_1) \cdot \xi_2, \qquad \xi_{1(2)} = \xi(p_{\mathrm{T},1(2)}, \eta_{1(2)}). \tag{VII.5}$$

The contribution of charge-flip electrons can be computed by assigning these weights to the events passing the same kinematic cuts as defined for the signal regions but with an opposite-sign instead of a same-sign requirement. The effect is neglected for muons $\xi(\mu) = 0$. The electron charge-flip probabilities are extracted from a $Z^0 \to ee$ data sample using a likelihood-based parameter estimation. The likelihood function L takes as input the Poisson-expected event yields of same-sign and opposite-sign electron pairs observed in an invariant mass range between 75 and 100 GeV. The charge-flip probabilities are free parameters of the fit and obtained as a function of the electron p_{T} and η:

$$L(\{N_{\varpi}^{\mathrm{SS,obs}}\} \,|\, \{\xi(\eta, p_{\mathrm{T}})\}) = \prod_{\varpi} \mathscr{P}\left(N_{\varpi}^{\mathrm{SS,obs}} \,|\, w_{\mathrm{CF}}(\xi(\eta_1, p_{\mathrm{T},1}), \xi(\eta_2, p_{\mathrm{T},2})) \times N_{\varpi}^{\mathrm{OS+SS,obs}}\right). \tag{VII.6}$$

The variable $\varpi = (p_{\mathrm{T},1}, \eta_1, p_{\mathrm{T},2}, \eta_2)$ indexes the various p_{T} and η bins (with $p_{\mathrm{T},1} > p_{\mathrm{T},2}$). The numbers N_{ϖ} denote the observed OS or SS events in that bin. This calculation assumes that the expected same-sign event yields are given by the total number of OS+SS events in a certain ϖ bin multiplied by w_{CF}. The probabilities $\mathscr{P}$ are given by Poisson distributions.

For the nominal estimate of the charge-flip background, only events with exactly two opposite-sign signal electrons are considered. However, since the charge-flip contribution has to be subtracted from the control samples used for the fake rates to avoid interferences between the two data-driven methods,

additional measurements have to be performed involving one electron failing the signal requirements[17]. An advantage of this method is a good statistical precision since many more OS than SS events are present in the regions where the weights are applied. Furthermore, this method relies only on data, so it does not depend on any simulated processes and their related uncertainties. Obviously, a precise determination of the rates for all p_{T} and η bins is required for a reliable prediction.
The measured charge-flip rates amount to 0.1–0.5%, moderately increasing with higher p_{T}, for electrons reconstructed in the barrel part of the EM calorimeter ($|\eta| < 1.37$). Electrons with higher pseudorapidities have significantly larger rates, reaching about 3% for $p_{\mathrm{T}} > 100$ GeV[18].

VII.4.4. ALTERNATIVE: MC TEMPLATE METHOD

As an alternative to the data-driven approaches described in VII.4.2 and VII.4.3, the so-called "MC template method" is used. This is a semi data-driven method that relies partially on data and on simulation. It assumes that the kinematic distribution of the FNP lepton and charge-flip backgrounds can be modeled by Monte Carlo, except from global normalization factors which can be obtained from data. This assumption makes the MC template method a suitable check of the matrix method, which assumes that the fake rates are the same in control and signal regions regardless of the selection requirements. Another assumption is that the fake rates are uncorrelated in events with more than one fake or non-prompt lepton, which can also be validated with this alternative approach.
Six orthogonal control regions (CRs) are used to rescale the MC prediction to data. The CRs are defined to cover topologies with b-jets and b-vetos, as well as different flavor combinations of the same-sign lepton pairs. They are defined as follows:

- CR0b: $N^{20}_{b\text{-jets}} = 0$, $E_{\mathrm{T}}^{\mathrm{miss}} > 25$ GeV, separated in same-sign ee, μμ and eμ channels.
- CR1b: $N^{20}_{b\text{-jets}} \geq 1$, $E_{\mathrm{T}}^{\mathrm{miss}} > 25$ GeV, separated in same-sign ee, μμ and eμ channels.

The generic event cleaning and the object definitions are the same as for the signal regions. Furthermore, all events satisfying the requirements for one of the signal regions are vetoed to ensure orthogonality between control and signal regions. The MC prediction for these regions is classified according to the lepton origin, using the truth-information[19] of the simulated samples. Correction factors are applied for five categories of lepton sources (charge-flip, electron-LF, muon-LF, electron-HF, muon-HF). The suffixes "LF" and "HF" indicate if an electron/muon candidate is produced by a light- or heavy-flavor jet.
A simultaneous fit to data in all six control regions is performed to obtain the correction factors. It is based on a likelihood function defined as the product of the Poisson probabilities describing the observed events in the binned distributions from the expected number of events rescaled by the five correction factors, which are the free parameters of the fit. The kinematic variables for the binned distributions are chosen to provide the best individual separation between prompt and non-prompt processes (N_{jets}, m_{eff}, $E_{\mathrm{T}}^{\mathrm{miss}}$, or the leading lepton p_{T}). Finally, these correction factors are applied to the fake/non-prompt and charge-flip MC predictions in the signal regions to get an estimation of the fake/non-prompt and charge-flip backgrounds. The systematic uncertainty of the MC template method is evaluated by comparing the estimated event yields for different choices of MC generators.

[17] Charge-flipped electrons are more likely to fail impact parameter or isolation requirements. Therefore, they are partially estimated also with the matrix method, which utilizes this difference.
[18] This is an understandable effect, as the electrons traverse a higher amount of detector material which increases the probability to emit bremsstrahlung.
[19] "MC-truth information" is metadata providing information about the origin and decay of simulated events.

The size of the correction factors is in general between 1.05 and 2.26 with relative uncertainties of 20–30%. The low amount of data in the kinematic edges of some control regions lead to these rather large uncertainties. In addition, one has to consider the already limited statistical precision of the MC prediction in the SRs, which is the main reason why this approach is not used as one of the nominal methods. Thus, it is intended to be primarily used to confirm the numbers from the previously described data-driven techniques. However, in the updated version of the analysis, it will be also used to reduce the uncertainties of the predictions from the matrix method since their results are consistent (see Section VIII.2.4).

VII.5. UNCERTAINTIES ON THE BACKGROUND ESTIMATION

The result of the analysis is affected by statistical and different sources of systematic uncertainties. Statistical uncertainties arise from the fact that an analysis is actually a counting experiment following a Poisson probability density function. On the other hand, systematic uncertainties come from inaccuracies attributed to the measurement process or from uncertainties of theoretical predictions. The different sources of uncertainties considered for this analysis are explained and quantified in this section.

VII.5.1. THEORETICAL UNCERTAINTIES

The theoretical uncertainties of the prompt SM processes contributing to the signal regions are composed of cross-section uncertainties corresponding to the normalization and inaccuracies of the Monte Carlo modeling, which can affect also the kinematic shape of a simulated process.
To take into account the former, the cross-sections used to normalize the MC samples are varied according to the uncertainty in the cross-section calculation, which is approximately 6% for diboson, 13% for $t\bar{t}$+W, and 12% $t\bar{t}$+Z production [193]. The component to account for the MC modeling are evaluated by comparing the predictions from the MG5_aMC@NLO and SHERPA generators for $t\bar{t}$+W/Z in the SR and taking the relative differences in the signal regions as uncertainties. For diboson, this component is estimated by varying the renormalization, factorization and resummation scales used to generate these samples. An additional component uncorrelated to the aforementioned sources is the systematic uncertainty inherent in the choice of PDF sets used for the simulated samples. This is addressed by varying different PDF parameters by $\pm 1\,\sigma$ and propagating the results to the MC event weights, using the LHAPDF6 framework [203].
The different sources of theoretical uncertainties are added up quadratically and treated as a common nuisance parameter (NP). The uncertainties for $t\bar{t}$+W/Z and diboson amount to 30–35% and are evaluated independently for each SR. For the subdominant processes (Rare), a more conservative value of 50% is assumed, including cross-section, MC modeling, and PDF uncertainties.

VII.5.2. EXPERIMENTAL UNCERTAINTIES

All relevant experimental systematic uncertainties associated with the prompt SS/3L processes in the signal regions are considered. Furthermore, systematic uncertainties for the data-driven approaches used to estimate to non-prompt and charge-flip background are derived. The experimental systematic uncertainties for the prompt backgrounds are:

- **Luminosity:** For the total integrated luminosity an error of 5% is used. It is derived following a prescription similar to that described in [148], from a calibration of the luminosity scale using beam-separation scans.

- **Jet energy scale/resolution:** The uncertainties of the jet energy scale are estimated by varying the scale up and down by $\pm 1\,\sigma$ for each nuisance parameter and scaling each individual jet energy accordingly. Additional uncertainties are considered related to jet flavor, pile-up corrections, and η-dependence, yielding a total of 88 independent NPs [168]. For this analysis, a strongly reduced uncertainty set, not taking into account jet-by-jet correlations and combining several parameters is used. It reduces the numbers of independent NPs to three[20]. The resulting scale factors are provided in bins of p_{T} and η of the jets. The JES uncertainty amounts to 5–15% in the SRs.

  An additional momentum smearing is added to the jets based on their η and p_{T} to account for a potential underestimate of the jet energy resolution in the MC simulation. The JER uncertainty is typically 1–3% in the SRs.

- **Flavor tagging:** Variations of the b-, c-, and light-jet efficiency scale factors (as described in V.3.3) are applied. They are binned in p_{T} and η of the jets. The uncertainties of the flavor tagging SFs are in most cases smaller than 10%. In the SRs with a b-jet veto, they are below 1%.

- **Jet vertex tagger:** Scale factor variations are applied to the jets to account for efficiency differences in the jet vertex tagger between different MC generators and to cover residual pile-up dependences. In all SRs, the JVT uncertainty is below 1%.

- **Egamma scale/resolution:** Uncertainties are used to address inaccuracies of the E_{T} scale and resolution after the electron/photon energy calibration process [161]. Also for this case, a strongly reduced uncertainty set, reducing the originally 67 NPs to one NP for scale and resolution, is used, as it was found to not affect the final results. These uncertainties are usually $< 1\%$ in the SRs.

- **Electron efficiency:** These uncertainties are associated with the electron efficiency scale factors (see Section V.2.2). In the reduced uncertainty set, one separate nuisance parameter is provided for electron reconstruction, identification, and isolation efficiency. They are typically between 1 and 3% in the SRs.

- **Muon scale/resolution:** Similar to the electrons, uncertainties are used to address imperfections of the muons momentum scale and resolution corrections ($< 1\%$). They are evaluated by applying $\pm 1\,\sigma$ variations on the reconstructed combined tracks from the inner detector and the muon spectrometer [150]. An additional uncertainty is considered related to the muon track-to-vertex-association (TTVA).

- **Muon efficiency:** These uncertainties corresponds to the statistical and systematic uncertainties of the muon efficiency SFs, as described in Section V.1.2. A separate nuisance parameter is applied for muon reconstruction and isolation efficiency. The uncertainties of the total SFs in the SRs are in most cases 1–3%.

- $E_{\mathrm{T}}^{\mathrm{miss}}$ **hard/soft term:** Imperfections in the calibrations of hard objects do also affect the $E_{\mathrm{T}}^{\mathrm{miss}}$ value. Their associated uncertainties (mainly JES and JER) are propagated to the $E_{\mathrm{T}}^{\mathrm{miss}}$ and corresponding variations are derived [183]. The uncertainty of the soft term is evaluated with data-MC comparisons in $Z^0 \to \mu\mu$ events [184]. The soft term uncertainties amount to 1–5% in the SRs.

[20] Several reduced uncertainty sets, applying different types of correlation models are provided by the Jet/EtMiss group. It was checked that the choice of the uncertainty set has no significant effect on the total JES uncertainty in the SRs.

- **Trigger:** Scale factors correct for the trigger efficiency difference between data and MC. Uncertainties of these trigger SFs are evaluated for all triggers ($<1\%$). For multi-object triggers and trigger combinations, the total uncertainty is computed from the individual uncertainties for each trigger.
- **Pile-up reweighting:** A correction on $\langle\mu\rangle$ is applied to account for differences to data in the simulation of pile-up processes. The uncertainty is obtained by rescaling the $\langle\mu\rangle$ value to cover the full difference between applying and not-applying the nominal $\langle\mu\rangle$ correction (as up/down variation in the MC event weight). The pile-up uncertainty is below 1% in all SRs.

All these experimental uncertainties are applied also on the simulated signal samples when exclusion limits on supersymmetric scenarios are computed.

FAKE/NON-PROMPT LEPTON AND CHARGE-FLIP BACKGROUND

The systematic uncertainty of the matrix method is evaluated from the uncertainties of the fake and real rate measurements which are propagated to the final estimation for the fake/non-prompt lepton background in the signal regions. Uncertainties are assigned to the rates to account for potentially different compositions of fake or non-prompt lepton types (light hadrons, heavy-flavor decays, photon conversions, etc.) between the region used to measure the rates and the signal regions. These differences were studied and quantified in simulated MC samples and led to errors of 50–60% for the measured rates. The measurements are also affected by statistical uncertainties due to the limited number of data events with loose and tight leptons in the regions used for the measurements. The overall uncertainties of the fake/non-prompt leptons in the total background estimates are between 18 and 21%, depending on the signal region.

A systematic uncertainty associated with the estimation of the charge-flip background is derived by varying the invariant mass window and the background subtraction models in the $Z^0 \to ee$ data sample, from which the charge-flip rates are obtained. The rates are measured for different configurations of m_{ee} ranges and side-band subtraction methods (typically varying the ranges for the nominal measurement by ± 5 GeV). For each $\xi(p_{\mathrm{T}}, \eta)$ bin, the largest difference from the nominal measurement is taken as corresponding uncertainty. However, the dominant uncertainty is the statistical error of the observed same-sign events in $Z^0 \to ee$ data leading to uncertainties between 25 and 50%. The overall error of the charge-flip process amounts only to 1–8% of the total background yields in the signal regions.

VII.6. VALIDATION OF BACKGROUND MODELING

To check the validity and robustness of the background estimation, the distributions of several discriminating variables is compared to data in regions similar to the signal regions but with looser requirements on $E_{\mathrm{T}}^{\mathrm{miss}}$, the number of jets, or the number of b-jets. Examples of such distributions are presented in the Figures VII.10a–VII.10d. All the selection criteria include a SS/3L requirement but vary for each of the distributions to enhance different background types (the actual selection cuts are specified in the subtitles of the individual plots). For the regions validating the charge-flip background, only same-sign electron pairs (ee) are selected. The agreement between data and the background prediction is in most cases fairly good, confirming that the simulated samples, as well as the data-driven methods, work sufficiently well. In particular, the number of jets with $p_{\mathrm{T}} > 50$ GeV shown in Figure VII.10a and the p_{T} spectrum of the leading lepton in Figure VII.10d validate the techniques used to estimate the FNP lepton and the charge-flip component of the background.

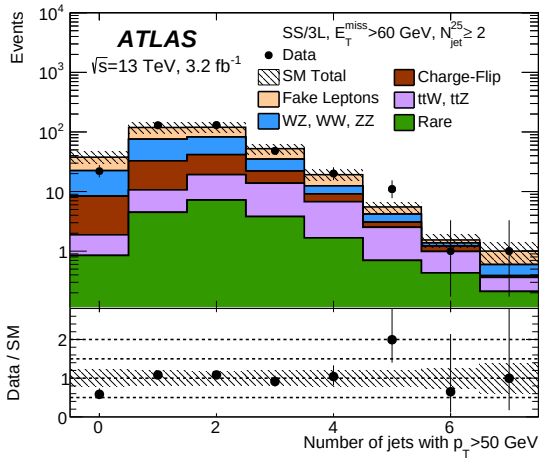

(a) SS/3L, $E_{\mathrm{T}}^{\mathrm{miss}} > 60$ GeV, $N_{\mathrm{jets}}^{25} \geq 2$

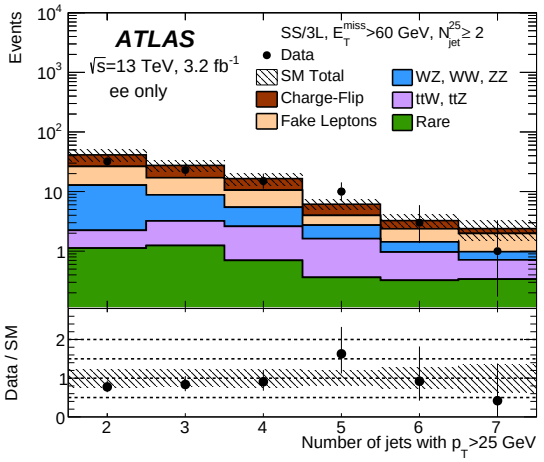

(b) SS/3L(ee), $E_{\mathrm{T}}^{\mathrm{miss}} > 60$ GeV, $N_{\mathrm{jets}}^{25} \geq 2$

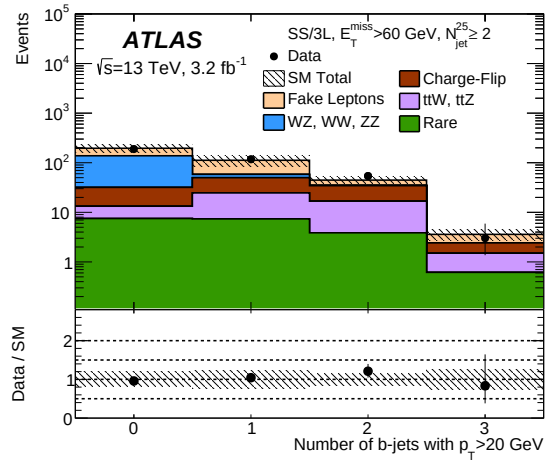

(c) SS/3L, $E_{\mathrm{T}}^{\mathrm{miss}} > 60$ GeV, $N_{\mathrm{jets}}^{25} \geq 2$

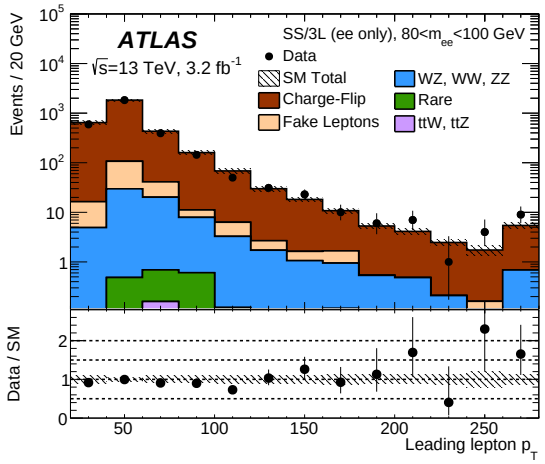

(d) SS/3L(ee), 80 GeV $< m_{ee} <$ 100 GeV

Figure VII.10.: Comparison between data and the predicted background for the number of jets with $p_{\mathrm{T}} >$ 50 GeV or 25 GeV (a,b), the number of b-jets with $p_{\mathrm{T}} > 20$ GeV (c) or the leading lepton p_{T} (d) for regions close to the SR but with slightly looser requirements. The actual selection cuts are specified in the subtitles. The bottom panel shows the data-to-background ratio. The error bands include only statistical uncertainties and the systematic uncertainties associated with the data-driven methods [6].

The estimates of the prompt background processes are validated with four dedicated validation regions, denoted as VR-WW, VR-WZ, VR-ttV, and VR-ttZ[21]. They were defined after a refined optimization procedure to obtain the maximal purity for the targeted processes and avoiding signal contaminations. The definitions are summarized in Table VII.5. Events passing the requirements for any of the signal regions are vetoed from the validation regions to ensure their orthogonality to the signal regions. Furthermore, events where the leading or subleading lepton is an electron with $|\eta| > 1.37$ are rejected to mitigate the contributions from charge-flip and FNP leptons. Two VRs dedicated to the most relevant diboson processes ($W^{\pm}Z$ and $W^{\pm}W^{\pm}jj$), one region for $t\bar{t}$+W/Z, and one region optimized for $t\bar{t}$+Z[22] are defined.

[21] The second part of the name indicates the targeted process.

[22] While it is possible to select $t\bar{t}$+Z events by requiring a SFOS pair in the Z-mass range, it is more difficult to get a similar purity for the $t\bar{t}$+W process. Thus, one specific $t\bar{t}$+Z VR and another VR optimized for the overall $t\bar{t}$+W/Z process is used.

Name	N_ℓ^{S} (N_ℓ^{BL})	N_{jets}^{25}	$N_{b\text{-jets}}^{20}$	$E_{\mathrm{T}}^{\mathrm{miss}}$ [GeV]	m_{eff} [GeV]	Other
VR-WW	$=2\,(=2)$ $=1$ SS pair	≥ 2	$=0$	35−200	300−900	$m_{j_1 j_2} > 500$ GeV $p_{\mathrm{T}}(j_2) > 40$ GeV $p_{\mathrm{T}}(\ell_2) > 30$ GeV $m_{ee} \notin [80, 100]$ GeV
VR-WZ	$=3\,(=3)$	1−3	$=0$	30−200	< 900	$p_{\mathrm{T}}(\ell_3) > 30$ GeV
VR-ttV	≥ 2 ≥ 1 SS pair	≥ 5 (ee, eμ) ≥ 3 (μμ)	≥ 2	20−200	200−900	$p_{\mathrm{T}}(\ell_2) > 25$ GeV $E_{\mathrm{T}}^{\mathrm{miss}} < 125$ GeV or $m_{\mathrm{eff}} < 650$ GeV
VR-ttZ	≥ 3 ≥ 1 SFOS pair	≥ 4 (=1 b-jet) ≥ 3 (>1 b-jet)	≥ 1	20−150	100−900	$p_{\mathrm{T}}(\ell_2) > 25$ GeV $p_{\mathrm{T}}(\ell_3) > 20$ GeV (if $e^{\pm}$) $m_{\mathrm{SFOS}} \in [80, 100]$ GeV

Table VII.5.: Summary of the 2015 validation region definitions. N_ℓ^{S} and N_ℓ^{BL} denote the number of signal and baseline leptons, respectively. The three leading leptons are denoted as $\ell_{1,2,3}$. The variable $m_{j_1 j_2}$ is the invariant mass of the two leading jets and m_{SFOS} describes the invariant mass of same-flavor opposite-sign lepton pairs (if present in the event).

The numbers of observed data and expected background events in the validation regions are shown in Table VII.6. The errors indicated include all statistical and systematic uncertainties, as described in Section VII.5. The purity of the targeted processes is between 50 and 80%. There is a good agreement between data and the total estimated background for all of the VRs. The largest deviation occurs in the region VR-ttV, with a discrepancy corresponding to a significance of around 1.5 σ.

Name	VR-WW	VR-WZ	VR-ttV	VR-ttZ
Observed events	4	82	19	14
Total background	3.4 ± 0.8	98 ± 15	12.1 ± 2.7	9.7 ± 2.5
Fake/non-prompt leptons	0.6 ± 0.5	8 ± 4	2.1 ± 1.4	0.6 ± 1.0
Charge-flip	0.26 ± 0.05	–	1.14 ± 0.15	–
$t\bar{t}$+W	0.05 ± 0.03	0.25 ± 0.09	2.4 ± 0.8	0.10 ± 0.03
$t\bar{t}$+Z	0.02 ± 0.01	0.72 ± 0.26	3.9 ± 1.3	6.3 ± 2.1
$W^{\pm}Z$	1.0 ± 0.4	78 ± 13	0.19 ± 0.10	1.2 ± 0.4
$W^{\pm}W^{\pm}jj$	1.3 ± 0.5	–	0.02 ± 0.03	–
ZZ	0.02 ± 0.01	8.2 ± 2.8	0.12 ± 0.15	0.30 ± 0.19
Rare	0.10 ± 0.05	2.8 ± 1.4	2.3 ± 1.2	1.1 ± 0.6

Table VII.6.: The numbers of observed data events and expected background contributions in the 2015 validation regions for a luminosity of 3.2 fb^{-1}. Background processes which do not contribute to a given region are shown as "–". The displayed errors include all statistical and systematic uncertainties.

VII.7. RESULTS IN SIGNAL REGIONS

The plots in Figure VII.11a–VII.11d show the missing transverse energy distributions for observed data and the predicted background in regions with all selection cuts as in the signal regions applied, besides the $E_{\mathrm{T}}^{\mathrm{miss}}$ requirement. Accordingly, the last (inclusive) bins of those plots show the actual results in the SRs (indicated by the red solid line). A benchmark point from the most relevant SUSY scenario is superimposed for each of the plots to illustrate the sensitivity of the SRs to the different models used to motivate this analysis.
Table VII.7 shows the detailed event yields in the signal regions for data and the different background components. Depending on the SR, the total uncertainties amount to 22–34% of the background prediction. Although the observed data yields exceed the SM expectation in all four signal regions, no significant deviation can be observed in any of them (as it will be quantified in the next section). The distributions in Figure VII.11 show that the data is also in agreement with the background prediction for lower $E_{\mathrm{T}}^{\mathrm{miss}}$ ranges, confirming that the background modeling performs well, independently from the $E_{\mathrm{T}}^{\mathrm{miss}}$ requirement.

Signal region	SR1b	SR3b	SR0b3j	SR0b5j
Observed events	7	1	3	3
Total background	4.5 ± 1.0	0.80 ± 0.25	1.5 ± 0.4	0.88 ± 0.29
Fake/non-prompt leptons	0.8 ± 0.8	0.13 ± 0.17	< 0.2	0.05 ± 0.18
Charge-flip	0.60 ± 0.12	0.19 ± 0.06	–	0.02 ± 0.01
$t\bar{t}$+W	1.1 ± 0.4	0.10 ± 0.05	0.01 ± 0.01	0.08 ± 0.04
$t\bar{t}$+Z	0.92 ± 0.31	0.14 ± 0.06	0.10 ± 0.04	0.05 ± 0.03
$W^{\pm}Z$	0.18 ± 0.11	< 0.02	1.2 ± 0.4	0.48 ± 0.20
$W^{\pm}W^{\pm}jj$	0.03 ± 0.02	< 0.01	–	0.12 ± 0.07
ZZ	< 0.03	< 0.03	< 0.03	< 0.04
Rare	0.8 ± 0.4	0.24 ± 0.14	0.14 ± 0.08	0.07 ± 0.05

Table VII.7.: The numbers of observed data and expected background events in the 2015 signal regions, obtained for an integrated luminosity of 3.2 fb^{-1}. Background processes shown as "–" do not contribute to the according SR. The indicated errors include all statistical and systematic uncertainties.

VII.8. STATISTICAL INTERPRETATIONS

This section is dedicated to the statistical interpretations of the obtained results. In this regard, some additional terms and definitions have to be introduced before presenting the actual results.

VII.8.1. P-VALUES AND SIGNIFICANCES

In order to quantify the significances of the results in the signal regions, their *p-values* have to be computed. A p-value is a quantity used for the evaluation of statistical measurements and can be obtained from an observed result and a probability density function corresponding to a given statistical model. It indicates how likely it is to obtain this result (or a more unlikely one), assuming if the null hypothesis is true.

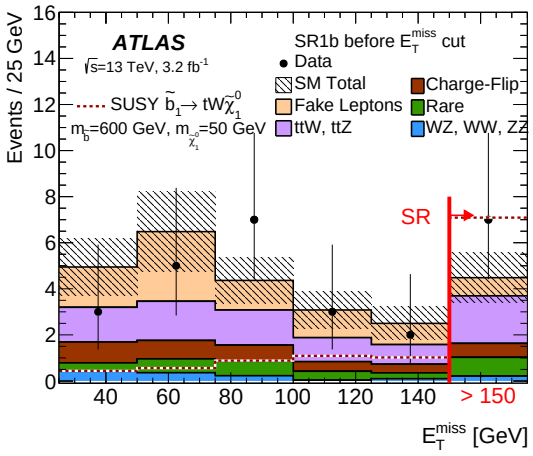

(a) SR1b before $E_{\mathrm{T}}^{\mathrm{miss}}$ cut

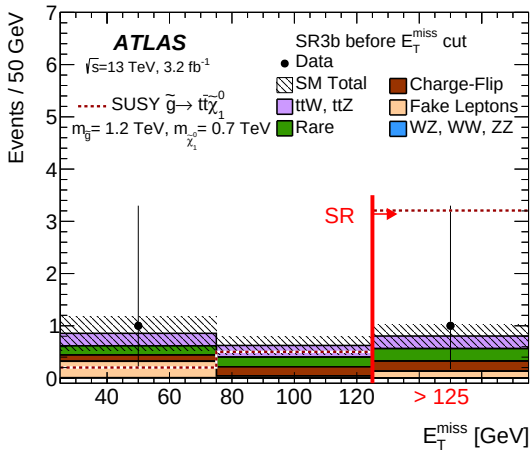

(b) SR3b before $E_{\mathrm{T}}^{\mathrm{miss}}$ cut

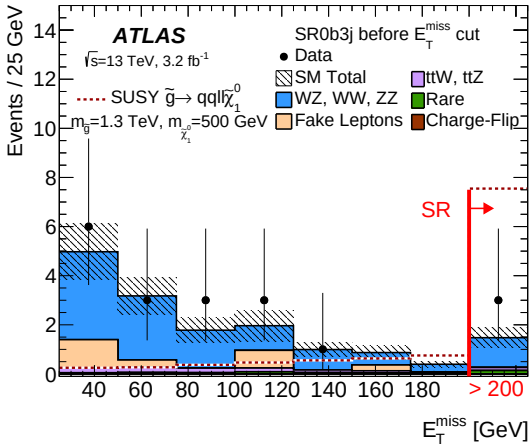

(c) SR0b3j before $E_{\mathrm{T}}^{\mathrm{miss}}$ cut

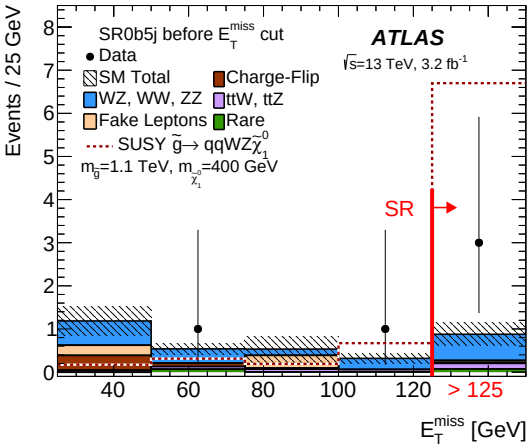

(d) SR0b5j before $E_{\mathrm{T}}^{\mathrm{miss}}$ cut

Figure VII.11.: The $E_{\mathrm{T}}^{\mathrm{miss}}$ distributions in regions with all selection cuts as in the SRs applied, except from the $E_{\mathrm{T}}^{\mathrm{miss}}$ cut. The last (inclusive) bins show the results in SR1b (a), SR3b (b), SR0b3j (c), SR0b5j (d). For each plot, a specific benchmark point from the most relevant SUSY grid is superimposed [6].

The null hypothesis denotes the statement that the measurements follow exactly the default prediction without the presence of a signal (within the tolerance given by the uncertainties). In the context of searches for new physics beyond the Standard Model, it is analogous to the "SM-only" case. The statement "more unlikely" means lower than the actual measurement, if the measurement is already too low with respect to the most likely value (corresponding to the maximum of the PDF) or higher, if the measurement is already too high. Accordingly, the p-value p_0 can be calculated as:

$$p_0 = \int_{x=\mathrm{data}}^{\infty} f_0(x)\,dx \qquad \text{or} \qquad p_0 = \int_{-\infty}^{x=\mathrm{data}} f_0(x)\,dx, \tag{VII.7}$$

with the PDF f_0 representing the null hypothesis and $x = \mathrm{data}$ is the value obtained from observation. The formula to be used changes if the measurement is higher or lower than the most likely value (right- and left-tailed probability). The concept is illustrated in Figure VII.12 for two simple examples with a Gaussian (left) and a Poisson PDF (right) and measurements above the most likely values. In contrast

to the null hypothesis, a p-value can also be defined according to a PDF which describes an alternative hypothesis, such as the "SM+signal" case.

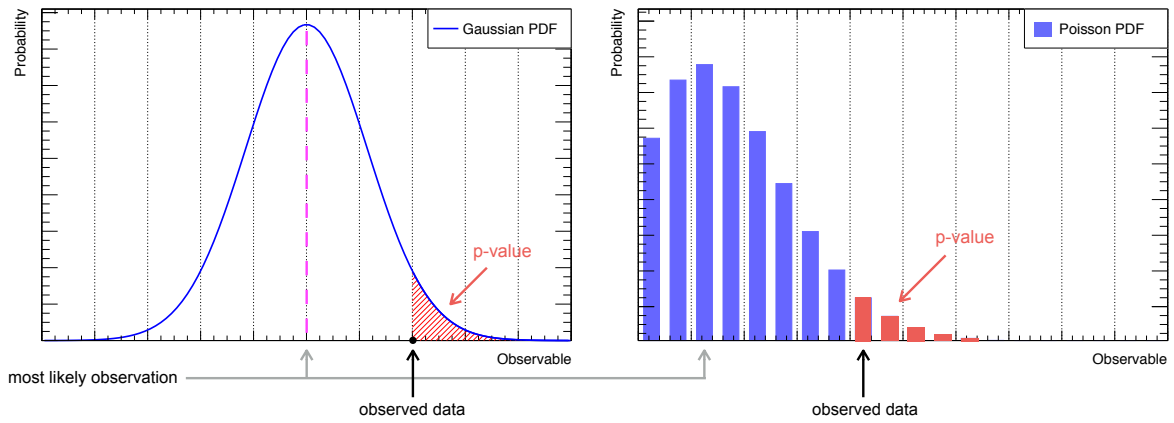

Figure VII.12.: Examples for a p-value computation with a Gaussian (left) and Poisson (right) PDF: the probability to get a result equal or higher than the observed value for a given PDF assuming the null hypothesis is true. The p-value is given by the red area limited by the observed result.

A realistic p-value computation utilizing the results in a set of analysis signal regions is actually more complex, since the PDFs have to be constructed from a Poisson probability density function describing the observed number of events convoluted with a set of Gaussian PDFs constraining the nuisance parameters associated with the systematic uncertainties. Furthermore, potential correlations between different nuisance parameters or correlations of a given nuisance parameter across the different background sources (or between background and signal samples) have to be taken into account.
If a statistical model depends on several independent variables in addition to the parameter of interest, a more advanced method, referred to as profile-likelihood-ratio test [204] has to be applied. The *Neyman-Pearson lemma* [205] states that the most powerful test-statistic[23] to reject the null hypothesis in favor of an alternative hypothesis is given by the likelihood-ratio λ. For testing a specific model, the test-statistic q_μ is defined as follows:

$$q_\mu = \begin{cases} -2\ln\lambda(\mu) & \hat{\mu} < \mu \\ 0 & \hat{\mu} > \mu \end{cases} \qquad \lambda(\mu) = \frac{L(\mu, \hat{\hat{\theta}}(\mu)\,|\,x)}{L(\hat{\mu}, \hat{\theta}\,|\,x)}. \tag{VII.8}$$

The functions L are the likelihood functions for a specific signal strength[24] parameter μ and an observed measurement x. The variable $\theta = (\theta_1, \ldots \theta_n)$ describes a set of nuisance parameters. The $\hat{\hat{\theta}}$ in the numerator denotes the configuration of θ that maximizes L for a fixed μ. The denominator is the maximized (unconditional) likelihood function, with $\hat{\mu}$ and $\hat{\theta}$ as the maximum likelihood estimators. With this approach, the nuisance parameters are profiled out and the test-statistic can be expressed as function of the signal strength only. The nuisance parameters widen the profile-likelihood function which reflects the loss of information about μ accompanied by the introduction of systematic uncertainties. The reason for setting $q_\mu = 0$ for cases with $\hat{\mu} > \mu$ is to ensure that the maximum likelihood estimator is not larger than the signal strength parameter, meaning that no scenario with $\hat{\mu} > \mu$ can be excluded. In this

[23] In general, "test-statistic" denotes an arbitrary function on a sample of measurements which can be used to distinguish (test) different hypotheses against each other.
[24] The signal strength is equivalent to a signal normalization parameter. In SM or Higgs measurements it is usually also scaled in units of the SM prediction.

formalism, the quantity used to define the p-value of an observation is given by the test-statistic:

$$p_\mu = \int_{q_\mu(\text{data})}^{\infty} f(q_\mu|\mu)\, dq_\mu. \tag{VII.9}$$

This quantifies the level of (dis)agreement between the measurements and the hypothesized value of μ (higher values of q_μ correspond to decreasing compatibility between the data and μ). The statistical significance Z for a deviation of a measurement from the null hypothesis can be directly associated with the p-values by translating them back to one-sided standard deviations of Gaussian distributions:

$$Z = \Phi^{-1} \cdot (1 - p_0), \tag{VII.10}$$

where Φ^{-1} defines the quantile function (inverse of the cumulative distribution) of the Gaussian PDF. Unlike the simplified approach used for the optimization studies (Section VII.3.1), all nuisance parameters and their correlations are considered correctly in this prescription. By convention in high-energy physics, no deviation with significance less than $3\,\sigma$ is treated as evident discrepancy, while a disagreement corresponding to $Z > 5\,\sigma$ typically constitutes a discovery.

RESULTS IN THE SIGNAL REGIONS

The p-values and their corresponding significances for the four SS/3L signal regions are listed in Table VII.8. The largest deviation is observed in SR0b5j, corresponding to a significance of $1.8\,\sigma$. As they are far away from any $3\,\sigma$ excess, it can be stated that the results of the 2015 analysis do not show significant deviations from the SM prediction.

Signal region	SR1b	SR3b	SR0b3j	SR0b5j
Observed events	7	1	3	3
Total background	4.5 ± 1.0	0.80 ± 0.25	1.5 ± 0.4	0.88 ± 0.29
p-value	0.15	0.36	0.13	0.04
Significance	$1.0\,\sigma$	$0.4\,\sigma$	$1.1\,\sigma$	$1.8\,\sigma$

Table VII.8.: Summary of the p-values and their corresponding significances in the signal regions. By convention, only deviations $> 3\,\sigma$ are treated as evidence.

VII.8.2. HYPOTHESIS TESTING AND CONFIDENCE LEVELS

In the absence of any significant deviations from the Standard Model predictions, upper limits on potential BSM contributions to the signal regions can be computed, in particular in the context of the four SUSY benchmark scenarios used of the SR optimization.

A variable typically used to quantify upper limits or to reject a hypothesis is the *confidence level* which defines the threshold for an one-sided confidence interval around an observed (or expected) value. The computation of model-dependent and model-independent upper limits in this analysis is performed with the CL_s formalism [206]. The CL_s value is defined as the ratio between the p-value computed for the

SM-only (p_b) and SM+signal (p_{s+b}) hypotheses. It can be written as:

$$CL_s = \frac{CL_{s+b}}{CL_b} = \frac{p_{s+b}}{1-p_b}, \qquad p_b = p_0. \tag{VII.11}$$

The computation of p_b and p_{s+b} is done with the PDFs corresponding to the SM-only and SM+signal case, respectively. If the signal contribution is a free parameter, the upper limit can be defined as the number of signal events (or its associated cross-section) for which the CL_s value gets below a chosen threshold, denoted as α. This prescription can also be used to reject a particular hypothesis with a fixed number of signal events. In most cases the value of α is set to 5% for excluding a signal. An advantage of the CL_s approach with respect to simply demanding $CL_{s+b} < \alpha$ to reject a hypothesis, is that this definition is more robust against anomalies arising for small signal contributions and downward fluctuations of the observed measurements[25].
The full computation of the model-independent and model-dependent 95% upper limits within the CL_s prescription is performed with the HISTFITTER software framework [207].

VII.8.3. MODEL-INDEPENDENT UPPER LIMITS IN THE SIGNAL REGIONS

Model-independent upper limits allow to check whether an arbitrary signal model can be excluded considering the given observed (or expected) results in the signal regions. Therefore, an artificial signal is added to the observed (expected) results in the SRs, with its signal strength treated as a free fit parameter. The upper limit is defined as the number of signal events (more generally, BSM events) that can contribute to the SR until the CL_s value gets below 5%, denoted as N_{BSM}^{obs} (N_{BSM}^{exp}). Normalizing these numbers by the integrated luminosity L of the data sample, they can be interpreted as upper limits on the visible signal cross-section σ_{vis} (in fb), defined as:

$$\sigma_{vis}^{obs(exp)} = \sigma_{prod} \times A \times \varepsilon = \frac{N_{BSM}^{obs(exp)}}{L}, \tag{VII.12}$$

with σ_{prod} denoting the signal production cross-section, A the detector acceptance, and ε the reconstruction efficiency. Observed and expected model-independent upper limits on BSM events (and the corresponding visible cross-sections) are derived for each SR independently and are stated in Table VII.9. Also, the $\pm 1\,\sigma$ variations on the expected limits due to the statistical and systematic uncertainties of the estimated background are shown. The calculations are performed with a frequentist-based approach using 10^4 pseudo-experiments to construct the underlying PDFs.

Signal region	SR1b	SR3b	SR0b3j	SR0b5j
N_{BSM}^{obs} (N_{BSM}^{exp})	$8.8\,(6.0^{+2.6}_{-1.6})$	$3.8\,(3.7^{+1.1}_{-0.5})$	$5.9\,(4.1^{+1.6}_{-0.8})$	$6.4\,(3.6^{+1.2}_{-1.1})$
σ_{vis}^{obs} (σ_{vis}^{exp}) [fb]	$2.8\,(1.9^{+0.8}_{-0.5})$	$1.2\,(1.1^{+0.3}_{-0.2})$	$1.8\,(1.3^{+0.5}_{-0.3})$	$2.0\,(1.1^{+0.4}_{-0.4})$

Table VII.9.: Observed (expected) model-independent upper limits (computed at 95% CL_s) on the number of BSM events N_{BSM}^{obs} (N_{BSM}^{exp}) and on the visible signal cross-section σ_{vis}^{obs} (σ_{vis}^{exp}) in the SR. The $\pm 1\,\sigma$ variations on the expected limits are derived from statistical and systematic uncertainties in the background prediction.

[25] If the number of expected signal events is high with respect to the background and the data observation is below the expectation, simply setting a threshold on CL_{s+b} leads to excluding these cases (even without any sensitivity).

VII.8.4. EXCLUSION LIMITS ON SIGNAL SCENARIOS

Model-dependent exclusion limits can be derived for the four SUSY benchmark scenarios considered in this analysis. The details and features of these scenarios have been explicitly discussed already in Section VII.1. The exclusion ranges depend naturally on the masses of the superpartners involved in these models: the signal cross-sections decrease for larger masses of the gluino or squark pairs produced. For increasing neutralino masses, the p_{T} spectra of the visible particles involved in the decays are lower, which reduces the signal acceptance. Accordingly, the limits are typically presented in a two-dimensional plane for the two independent mass parameters (with the other model parameters either set to fixed values or determined from the variable masses in the plane axes). Figure VII.13 shows the exclusion limits on the mass of the neutralino $\widetilde{\chi}_1^0$ as a function of the gluino $\widetilde{g}$ (or light bottom squark $\widetilde{b}_1$, in case of Figure VII.13b) masses for the four SUSY models. The SRs used to obtain the limits are indicated for each plot.
The lines drawn on the mass planes indicate the kinematic regions up to those a model can be excluded at 95% confidence level. The dashed lines with the yellow bands show the expected limits and their $\pm 1\,\sigma$ variations including the statistical and systematic uncertainties of the background predictions. The red solid lines show the observed limits with their $\pm 1\,\sigma$ variations corresponding to the theoretical uncertainties of the signal cross-sections[26]. If possible, the current limits are compared to existing (observed) limits from the Run I same-sign/3L search [4] (or the combined $\sqrt{s} = 8$ TeV results [187, 190]). The diagonal gray lines indicate model-specific kinematic constraints (forbidden regions) on the decays of the superpartners. Considering the level of agreement between the observed and expected event yields in the signal regions, it is obvious that also the observed and expected exclusion limits are mostly compatible within their uncertainties.

For the $\widetilde{g} \to t\bar{t}\,\widetilde{\chi}_1^0$ scenario (VII.13a), SR3b is used. In this model, gluino masses up to 1.2 TeV and neutralino masses up to 650 GeV can be excluded. This improves already the limit obtained with the Run I version of the SS/3L analysis, using 20.3 fb^{-1} of $\sqrt{s} = 8$ TeV data. SR1b is used for the $\widetilde{b}_1 \to t\,W^{\pm}\,\widetilde{\chi}_1^0$ model (VII.13b) where the observed limit reaches around 540 GeV for the mass of the light bottom squark and around 140 GeV for the mass of the neutralino. For the $\widetilde{g} \to q\bar{q}\,(\ell\bar{\ell}/\nu\nu)\,\widetilde{\chi}_1^0$ model (VII.13c), the region with the three-lepton requirement, SR0b3j, is used. Gluinos up to $m_{\widetilde{g}} \approx 1.32$ TeV can be excluded. The exclusion limit for neutralinos reaches $m_{\widetilde{\chi}_1^0} \approx 840$ GeV for $m_{\widetilde{g}} \approx 1.1$ TeV. Thus, the limit obtained for the $\widetilde{g} \to q\bar{q}\,(\ell\bar{\ell}/\nu\nu)\,\widetilde{\chi}_1^0$ model is the most far-reaching exclusion limit among the four scenarios. Finally, the $\widetilde{g} \to q\bar{q}\,W^{\pm}Z\,\widetilde{\chi}_1^0$ (VII.13d) is addressed with SR0b5j. The exclusion limit reaches around $m_{\widetilde{g}} \approx 1.1$ TeV and $m_{\widetilde{\chi}_1^0} \approx 550$ GeV and surpasses also the limit achieved for this model in Run I.
The gray numbers shown on the plots indicate the upper limits on the signal cross-section (in fb) for a specific mass point. They are determined with a frequentist-based method equivalent to the approach described in Section VII.8.3, where the signal contribution for this point is rescaled by an artificial cross-section, so that a corresponding upper limit at 95% $\mathrm{CL_s}$ can be computed. The difference with respect to the model-independent upper limits listed in Table VII.9 is that signal efficiency and acceptance specific to each individual point in the mass plane is considered for the computation.

[26] This is in fact not an uncertainty of the observed result. By convention, the theoretical uncertainties of the signal cross-sections are presented as a dashed band around the observed result to separate them from the yellow band, which is intended to show only uncertainties associated with the background prediction.

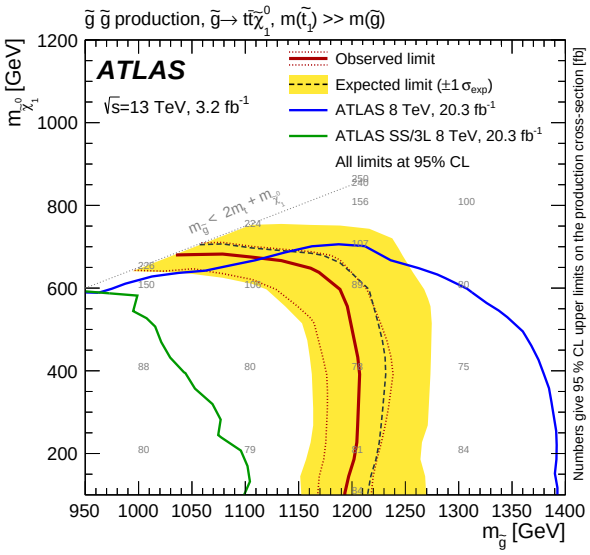

(a) SR3b: $\widetilde{g} \to t\bar{t}\,\widetilde{\chi}_1^0$ scenario

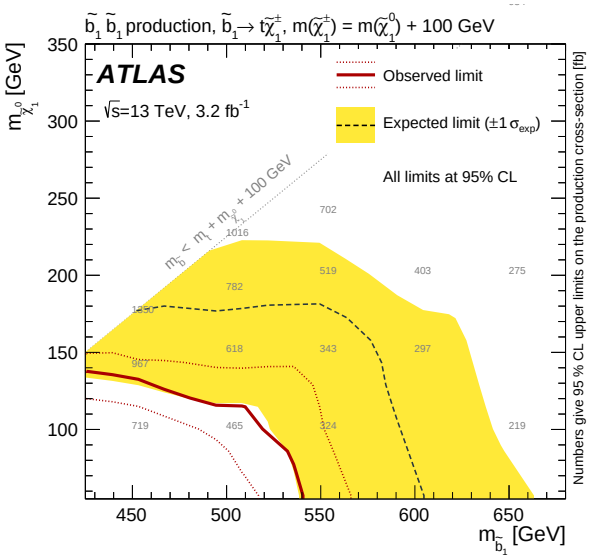

(b) SR1b: $\widetilde{b}_1 \to t\,W^{\pm}\,\widetilde{\chi}_1^0$ scenario

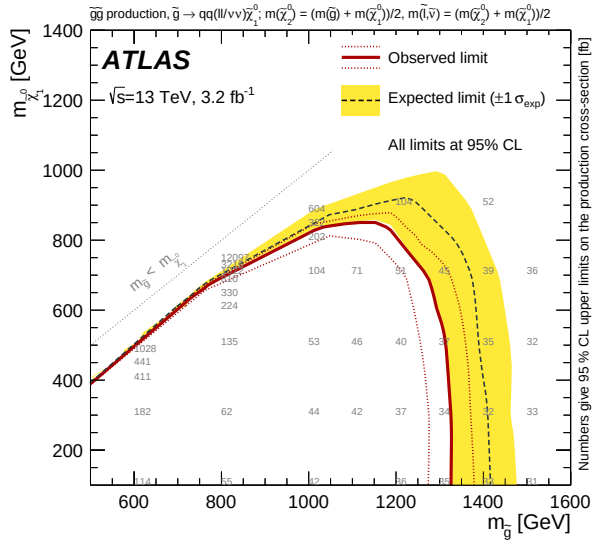

(c) SR0b3j: $\widetilde{g} \to q\bar{q}\,(\ell\bar{\ell}/\nu\nu)\,\widetilde{\chi}_1^0$ scenario

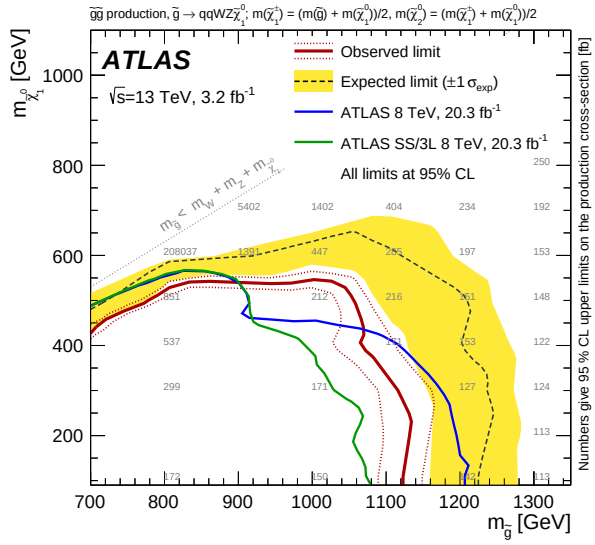

(d) SR0b5j: $\widetilde{g} \to q\bar{q}\,W^{\pm}Z\,\widetilde{\chi}_1^0$ scenario

Figure VII.13.: Observed and expected exclusion limits (computed at 95% CL_s) on the mass of $\widetilde{\chi}_1^0$ as function of the gluino (or light bottom squark) mass in the context of the simplified SUSY benchmark scenarios. The limits are obtained from SR3b for the $\widetilde{g} \to t\bar{t}\,\widetilde{\chi}_1^0$ scenario (a), SR1b for $\widetilde{b}_1 \to t\,W^{\pm}\,\widetilde{\chi}_1^0$ (b), SR0b3j for $\widetilde{g} \to q\bar{q}\,(\ell\bar{\ell}/\nu\nu)\,\widetilde{\chi}_1^0$ (c), and SR0b5j for $\widetilde{g} \to q\bar{q}\,W^{\pm}Z\,\widetilde{\chi}_1^0$ (d). All statistical and systematic uncertainties are included in the error bands. The diagonal gray lines indicate the decay-specific kinematic constraints on a model [6].

VIII. Updates and Improvements of the Analysis in 2016

The analysis conducted in 2015 was the first resumption of the same-sign/3L search in Run II. Therefore, it also built the baseline for further developments associated with successive updates of the analysis during 2016. Preliminary results were released in the middle of 2016 in terms of an intermediate update of the analysis using 13.2 fb^{-1} of data. This was done to benefit from the increased amount of data recorded at the early 2016 operation and to extend the interpretation of the analysis to some additional SUSY scenarios. This update is briefly summarized in Section VIII.1.
The most recent results of the analysis are presented in Section VIII.2 and include the full dataset collected during the years 2015 and 2016, corresponding to an integrated luminosity of 36.1 fb^{-1}. In addition to a full re-optimization of the signal regions to account for the increased amount of data, new signal regions are introduced to explore additional same-sign or three-lepton topologies. Furthermore, several improvements regarding the object reconstruction and the background estimation have been implemented. The interpretation of the search results is extended to a high number of different R-parity conserving and violating SUSY scenarios for which dedicated exclusion limits could be placed. The list of publications at the end of this thesis specifies the personal contributions of the author to the 13.2 fb^{-1} and 36.1 fb^{-1} versions of the analysis.

VIII.1. Updated Analysis Results for 13.2 fb^{-1} of Data

In this updated version of the analysis, the combined 25 ns datasets from 2015 and the first half of 2016 are used [7]. The official recommended Good Run List has been updated accordingly to select suitable runs and lumi-blocks from the 2016 data. Due to the higher instantaneous luminosities, the average number of pp interactions per bunch crossing increased from $\langle\mu\rangle = 14$ to around 22. Several minor improvements regarding the object selection and the evaluation of experimental uncertainties have been implemented during this time period. They will not be discussed in detail here since they did not change the analysis methodology in a significant manner. More details on the intermediate update of the analysis with 13.2 fb^{-1} of data can be found in Appendix B.
The signal regions targeting the four SUSY benchmark scenarios were re-optimized to account for the higher integrated luminosity. A feature limiting the sensitivity already in the 2015 version of the analysis was the practice of choosing only one signal region with fixed kinematic requirements for one supersymmetric model. Since kinematic properties of a SUSY scenario are basically defined by the mass differences between the superpartners involved in the decay, the best sensitivity cannot be obtained by choosing a fixed set of selection cuts across the entire signal grid. Therefore, the signal regions optimized for the $\widetilde{g} \to q\bar{q}W^{\pm}Z\widetilde{\chi}_1^0$ and the $\widetilde{g} \to q\bar{q}(\ell\bar{\ell}/\nu\nu)\widetilde{\chi}_1^0$ models have been subdivided into two partially overlapping SRs[1] with the same topological, but distinct kinematic requirements in order to improve the sensitivity to scenarios with large mass splittings as well as compressed SUSY mass spectra. For each point of the SUSY parameter space, the SR providing the best expected limit is used for the final combined exclusion limits. This strategy is continued and refined also for the latest analysis results described in the next section.

[1] Referred to as SR0b1(2) for the former SR0b5j and SR3L1(2), formerly SR0b3j.

VIII.1.1. INTERMEDIATE UPDATE OF THE EXCLUSION LIMITS

Since the data used for this update is also included in the full 2015+2016 dataset, dedicated results for the signal regions are not shown here (they can be found in Appendix B). No significant excess above the SM background expectation was observed in any of the SRs. The updated exclusion limits on the SUSY processes described in Section VII.1 are presented in Figure VIII.1, showing the exclusion limits in the two-dimensional planes defined by the masses of the superpartners. The specifications of the plots are the same as for Figure VII.13, with the previous limits superimposed as blue lines[2]. In addition, the observed limits from other 2015 searches (multi-b and multi-jet analyses [208, 209]) and previous $\sqrt{s} = 8$ TeV results are stated if available for the same model. In all four scenarios, the observed and expected exclusion limits are still compatible within their uncertainties.
The formerly used $\widetilde{g} \to t\bar{t}\widetilde{\chi}_1^0$ scenario with on-shell top quark production was extended to allow also $t \to bW^{\pm}$ decays via off-shell top quarks. Accordingly, the kinematic constraints for the gluino decay are relaxed from $m_{\widetilde{g}} > 2m_t + m_{\widetilde{\chi}_1^0}$ to $m_{\widetilde{g}} > 2m_W + m_{\widetilde{\chi}_1^0}$, which increases the detectable energy range of neutralino masses by around 185 GeV for all potential gluino masses. Since one of the advantages of the SS/3L search is its superior sensitivity especially in compressed SUSY mass spectra, the investigation of the off-shell top region in the $\widetilde{g} \to t\bar{t}\widetilde{\chi}_1^0$ scenario is an important goal of the analysis.

For the $\widetilde{g} \to t\bar{t}\widetilde{\chi}_1^0$ scenario (Figure VIII.1a), gluino masses $m_{\widetilde{g}} \lesssim 1.45$ TeV are excluded for $m_{\widetilde{\chi}_1^0} \lesssim 700$ GeV and neutralino masses up to approximately 850 GeV are excluded for $m_{\widetilde{g}} \approx 1.25$ TeV. With respect to the results obtained with 3.2 fb^{-1} of data, the limit on the gluino mass is improved by around 250 GeV for neutralino masses below 600 GeV. For the $\widetilde{b}_1 \to tW^{\pm}\widetilde{\chi}_1^0$ model (Figure VIII.1b), the limit for bottom squark masses reaches up to 690 GeV for very light neutralinos and $m_{\widetilde{\chi}_1^0} \lesssim 260$ GeV for $m_{\widetilde{b}_1} \approx 540$ GeV. The previous limit is extended by about 150 GeV, almost independent from the mass of the neutralino or the bottom squark.
The limit for the $\widetilde{g} \to q\bar{q}(\ell\bar{\ell}/\nu\nu)\widetilde{\chi}_1^0$ scenario (Figure VIII.1c) reaches about 1.7 TeV for the gluino mass and about 1.1 TeV for the neutralino mass (for gluinos with $m_{\widetilde{g}} \approx 1.4$ TeV). The improvement regarding the excluded gluino mass range is around 400 GeV for almost all potential neutralino masses. Also, the reach of the excluded neutralino masses can be extended by almost 200 GeV (note that the updated limit is now obtained from two signal regions instead of one). For the $\widetilde{g} \to q\bar{q}W^{\pm}Z\widetilde{\chi}_1^0$ model (Figure VIII.1d), gluino masses $m_{\widetilde{g}} \lesssim 1.6$ TeV and neutralino masses $m_{\widetilde{\chi}_1^0} \lesssim 920$ GeV (for $m_{\widetilde{g}} \approx 1.3$ TeV) can be excluded. Compared to the result obtained with 3.2 fb^{-1}, the limit for gluino masses can be extended by almost 500 GeV for light neutralinos (also in this case, two SRs are used for the updated limit). Among the four scenarios, this is the most evident improvement that could be achieved.

[2]The upper limits on the cross-sections for particular mass points (gray numbers) have not been calculated for this update.

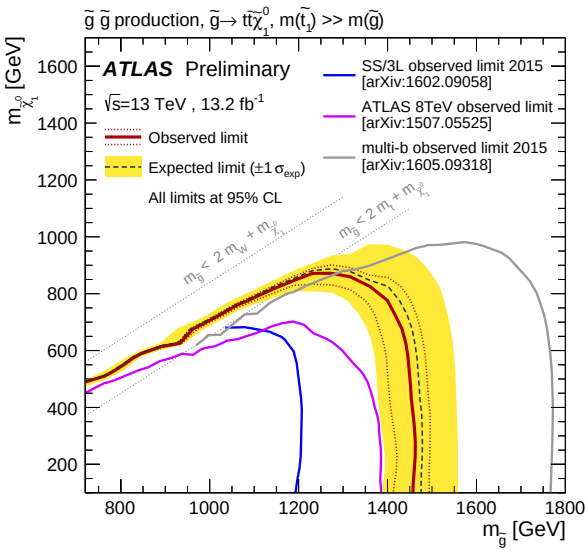

(a) SR3b: $\widetilde{g} \to t\bar{t}\,\widetilde{\chi}_1^0$ scenario

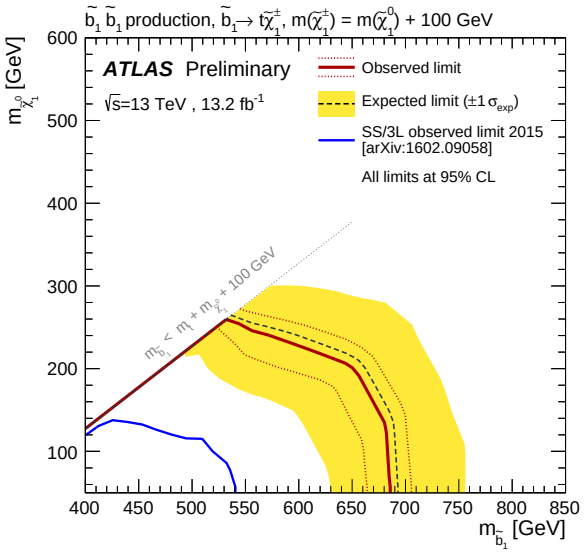

(b) SR1b: $\widetilde{b}_1 \to t\,W^{\pm}\,\widetilde{\chi}_1^0$ scenario

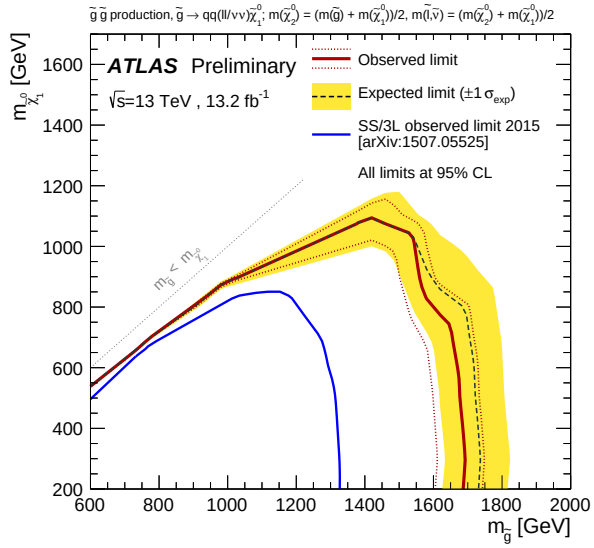

(c) SR3L1(2): $\widetilde{g} \to q\bar{q}\,(\ell\bar{\ell}/\nu\nu)\,\widetilde{\chi}_1^0$ scenario

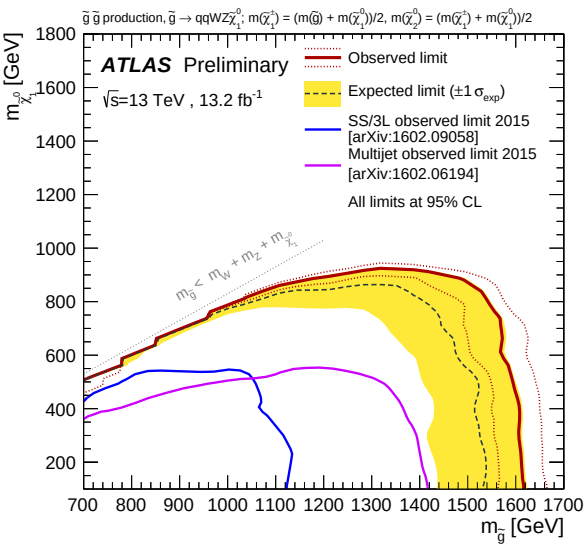

(d) SR0b1(2): $\widetilde{g} \to q\bar{q}\,W^{\pm}Z\,\widetilde{\chi}_1^0$ scenario

Figure VIII.1.: Updated observed and expected exclusion limits on the mass of $\widetilde{\chi}_1^0$ as function of the gluino (or light bottom squark) mass in the context of the SUSY benchmark models introduced in the previous chapter. The limits are obtained for the $\widetilde{g} \to t\bar{t}\,\widetilde{\chi}_1^0$ scenario (a), $\widetilde{b}_1 \to t\,W^{\pm}\,\widetilde{\chi}_1^0$ (b), $\widetilde{g} \to q\bar{q}\,(\ell\bar{\ell}/\nu\nu)\,\widetilde{\chi}_1^0$ (c), and for $\widetilde{g} \to q\bar{q}\,W^{\pm}Z\,\widetilde{\chi}_1^0$ (d). The $\widetilde{g} \to t\bar{t}\,\widetilde{\chi}_1^0$ scenario was extended to allow also off-shell top decays [7].

VIII.2. SAME-SIGN/3L ANALYSIS FOR THE FULL 2015+2016 DATASET

This section is dedicated to the most recent results of the same-sign/3L search including the full datasets from 2015 and 2016 [8]. With respect to the previous section, the update incorporates also the data recorded during the second half[3] of 2016. The mean number of pp interactions per bunch crossing increased to $\langle\mu\rangle \approx 25$ for the updated 2016 data[4]. The data collected in 2015 and 2016 correspond to integrated luminosities of 3.2 fb^{-1} and 32.9 fb^{-1}, respectively. Accordingly, the combined dataset has 36.1 fb^{-1} of data and is, therefore, almost twelve times larger than the initial 2015 dataset used for the first Run II results. The uncertainty of the 2015+2016 integrated luminosity amounts to 3.2% [109]. Besides the larger amount of analyzed data, many new features have been introduced with respect to the 2015 results in order to improve the event selection, the quality of the background estimation, and to extend the scope of the analysis. They will be described in the following sections.

VIII.2.1. ADDITIONAL SIGNAL SCENARIOS

In contrast to the 2015 analysis which used only four R-parity conserving SUSY processes to design the signal regions as well as deriving model-dependent exclusion limits, the intention of the most recent version of the SS/3L search was to extend the possible interpretations to more benchmark processes that can lead to prompt same-sign or three-lepton signatures, including also R-parity violating SUSY models. The decay topologies of these processes are depicted in Figure VIII.2.

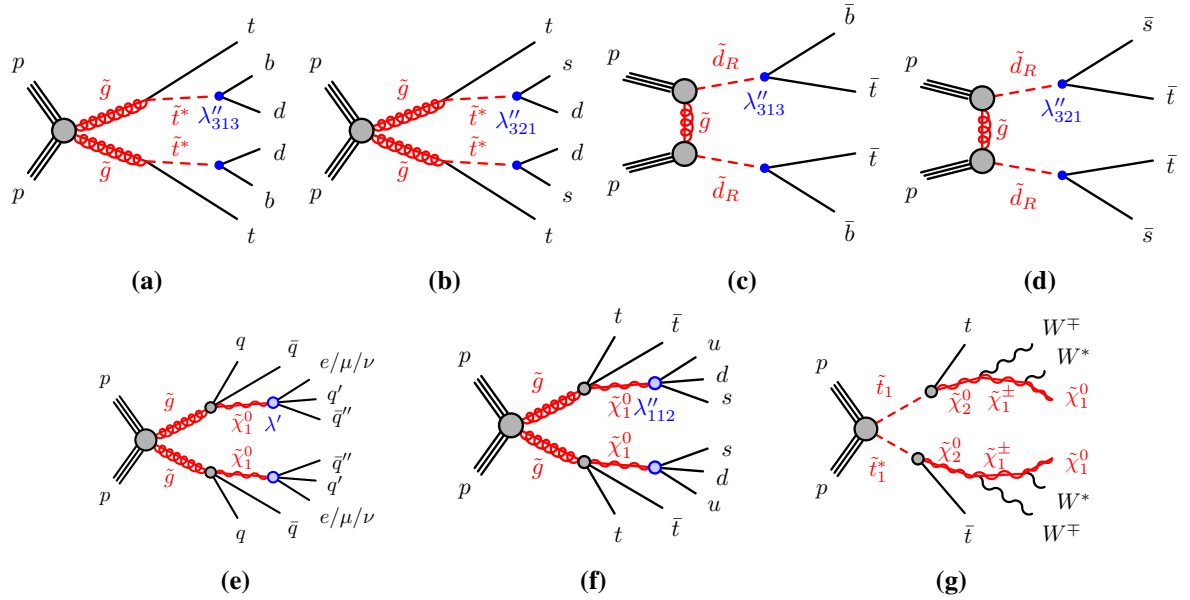

Figure VIII.2.: Additional SUSY benchmark processes considered for the 2015+2016 version of the SS/3L analysis: RPV SUSY models featuring gluino pair production (a,b,e,f), t-channel production of right-handed down squark pairs (c,d), as well as one RPC SUSY scenario featuring direct pair production of top squarks (g).

Besides the same-sign or three-lepton condition all models have in common, other event characteristics, such as the number of jets (b-tagged jets), $E_{\mathrm{T}}^{\mathrm{miss}}$, or the effective mass can vary. This naturally increases the coverage of the search compared to the former 2015 version, since $E_{\mathrm{T}}^{\mathrm{miss}}$ and high-N_{jets} requirements are not necessary in all signal regions. In addition to the four RPC scenarios introduced in Section VII.1,

[3] Separated by a four-week machine development stop (MD1) in July 2016.
[4] For the combined 2015+2015 dataset, it is $\langle\mu\rangle \approx 23.7$ [109].

the following models are considered for the design of the re-optimized and new signal regions, as well as for the model-dependent interpretation of the results:

- Gluino pair production with a top squark $\widetilde{t}_1$ mediated decay to top, bottom, and down quarks, denoted as $\widetilde{g} \to tbd$ scenario (shown in Figure VIII.2a). The top squarks decay via an RPV coupling in the baryonic sector λ''_{313} to bottom and down quarks, as proposed in scenarios with minimal R-parity and flavor violation [210,211]. An equivalent process can be simulated with the top squarks decaying into strange and down quarks via a λ''_{321} coupling ($\widetilde{g} \to tsd$ model, Figure VIII.2b). These processes lead typically to events with same-sign leptons accompanied by b-jets. Since the RPV couplings λ''_{313} (λ''_{321}) lead to experimentally indistinguishable event signatures as processes with the couplings λ''_{323} (λ''_{311}, λ''_{322}), all exclusion limits derived for the former models are also valid for the latter ones.

- Direct production of right-handed same-sign down squark pairs $\widetilde{d}_R\widetilde{d}_R$ in the t-channel. The down squarks decay via the λ''_{313} or the λ''_{321} RPV coupling to antitop and antibottom (or antistrange) quarks, denoted as $\widetilde{d}_R \to \bar{b}\bar{t}$ (or $\widetilde{d}_R \to \bar{s}\bar{t}$) model, as depicted in Figure VIII.2c and VIII.2d, respectively. The mass of the gluino in the t-channel only affects the absolute production cross-section for the scenario. Therefore, these processes are simulated only with a fixed gluino mass of 2 TeV and model-dependent limits are derived in terms of upper limits on the production cross-section depending only on the mass of the down squark.

- Gluino pair production with effective decays to $q\bar{q}\widetilde{\chi}^0_1$ or $t\bar{t}\widetilde{\chi}^0_1$ triplets. The neutralinos subsequently decay via an RPV coupling in the leptonic (λ') or the baryonic sector (λ'') to either leptons and quarks ($\widetilde{g} \to q\bar{q}\widetilde{\chi}^0_1$, $\widetilde{\chi}^0_1 \to q\bar{q}\ell$ model) or only quarks ($\widetilde{g} \to t\bar{t}\widetilde{\chi}^0_1$, $\widetilde{\chi}^0_1 \to uds$ model), as illustrated in Figure VIII.2e and VIII.2f. Typically, these scenarios lead to large multiplicities of light-flavor jets (in case of $\widetilde{g} \to q\bar{q}\widetilde{\chi}^0_1$, $\widetilde{\chi}^0_1 \to q\bar{q}\ell$) or b-jets (for $\widetilde{g} \to t\bar{t}\widetilde{\chi}^0_1$, $\widetilde{\chi}^0_1 \to uds$).

- Production of top squark pairs $\widetilde{t}_1\widetilde{t}_1^*$ with an effective two-step decay involving the second-lightest neutralino $\widetilde{\chi}^0_2$ and a chargino $\widetilde{\chi}^\pm_1$ to top quarks, $W^\pm$ bosons, and the lightest neutralinos $\widetilde{\chi}^0_1$ ($\widetilde{t}_1 \to tW^\mp W^*\widetilde{\chi}^0_1$ model, shown in Figure VIII.2g). The lightest neutralino and chargino are assumed to be nearly mass degenerate ($m_{\widetilde{\chi}^0_1} \approx m_{\widetilde{\chi}^\pm_1}$ with largely off-shell W^*), while the mass difference between the second-lightest neutralino and the chargino is fixed to 100 GeV to allow also on-shell $W^\pm$ boson production[5]. Since the mass of the top squark is the only free parameter in this sort of model, the model-dependent limits are also derived in terms of upper limits on the production cross-section depending only on $m_{\widetilde{t}_1}$. This process is characterized by a unique signature with three leptons, all having the same charge ($\ell^+\ell^+\ell^+$ or $\ell^-\ell^-\ell^-$). The $\widetilde{t}_1 \to tW^\mp W^*\widetilde{\chi}^0_1$ model is a promising candidate to explain a small excess observed in same-sign lepton signatures during Run I [212].

- The two-extra-parameter non-universal Higgs model (NUHM2) [213,214] is a natural (low fine-tuning) SUSY model. In contrast to the cMSSM, it allows the soft SUSY breaking masses of the Higgs multiplets to be different from matter scalar masses at the grand unification scale (non-universality). The scenario is simulated with a set of fixed parameters $(m_0, A_0, \tan(\beta), m_A, \mu)$ leading to a Higgs mass of $m_H = 125$ GeV and the common mass term of the soft SUSY breaking electroweak gauginos $m_{1/2}$ as only free parameter. In addition to same-sign lepton pairs, several b-jets are expected in the final state.

[5] With $m_{\widetilde{\chi}^0_2} - m_{\widetilde{\chi}^\pm_1} = 100$ GeV and $m_{\widetilde{\chi}^0_1} \approx m_{\widetilde{\chi}^\pm_1}$, the production of on-shell Higgs bosons via $\widetilde{\chi}^0_2 \to \widetilde{\chi}^0_1 + H$ is suppressed.

As for the previously introduced scenarios, these signal processes are typically simplified models, assuming a single production mode with a branching ratio of 100% for a specific decay (only the NUHM2 is a full model). Generic decays into light-flavor quarks ($q = u,d,c,s$) or leptons ($\ell = e,\mu,\tau$) are simulated with equal probabilities.

VIII.2.2. UPDATED TRIGGER STRATEGY

The trigger configuration to select same-sign or three-lepton events has been revisited and updated since new high-level triggers became available during the 2016 data taking and formerly unprescaled triggers had prescales applied[6]. Different trigger configurations have to be used for the 2015 and 2016 data to account for these changes.
While the trigger strategy described in Section VII.2.4 is retained for the data recorded in 2015, the 2016 data is selected with the following configuration:

- For events with $E_{\mathrm{T}}^{\mathrm{miss}} < 250$ GeV, a logical "or" combination of the following dilepton triggers is used: `HLT_2e17_lhvloose_nod0` (two electrons with $p_{\mathrm{T}} > 17$ GeV), `HLT_mu22_mu8noL1` (two muons, $p_{\mathrm{T}}^{1(2)} > 22(8)$ GeV), and `HLT_e17_lhloose_nod0_mu14` (one electron, $p_{\mathrm{T}} > 17$ GeV and one muon, $p_{\mathrm{T}} > 14$ GeV).
- For events with $E_{\mathrm{T}}^{\mathrm{miss}} > 250$ GeV, an "or" between the dilepton triggers and the $E_{\mathrm{T}}^{\mathrm{miss}}$ triggers `HLT_xe100_mht_L1XE50` and `HLT_xe110_mht_L1XE50` is used[7].

In MC, the samples are subdivided into two orthogonal subsets to be used for 2015 and 2016 data. The splitting is done randomly, with a trigger configuration chosen according to the relative luminosities and $\langle\mu\rangle$ profiles of the 2015 and 2016 data.
The new triggers used for the 2016 configuration have been validated with dedicated checks of performance and efficiency in data and simulated test samples. Figure VIII.3 shows the efficiency evolution for the dimuon trigger `HLT_mu22_mu8noL1` (left) and electron-muon trigger `HLT_e17_lhloose_nod0_mu14` (right) in simulated $WZ \to \ell\ell\ell\nu$ events, plotted against the p_{T} of the first trigger item (electron or muon) for different lepton preselections applied. For the event signatures considered and the kinematic range relevant to this analysis, the efficiency of this configuration is in almost all cases above 95%.
Trigger scale factors are applied to the simulated events to account for potential efficiency differences between data and simulation. For the dielectron, dimuon, and electron-muon triggers, they are derived from the SFs of the corresponding single-lepton triggers provided by the trigger signature groups which are propagated to provide dilepton trigger SFs. More details about the 2016 trigger studies are given in Appendix C.

[6] This is the case especially for the $E_{\mathrm{T}}^{\mathrm{miss}}$ trigger, where `HLT_xe70` had to be prescaled in order to cope with the increased event rates in 2016.

[7] Since `HLT_xe100_mht_L1XE50` was unprescaled beginning of 2016 but prescaled during the second half of the year (with `HLT_xe110_mht_L1XE50` as lowest unprescaled $E_{\mathrm{T}}^{\mathrm{miss}}$ trigger), it was decided to use their "or" combination to obtain the best possible efficiency for the entire 2016 data taking.

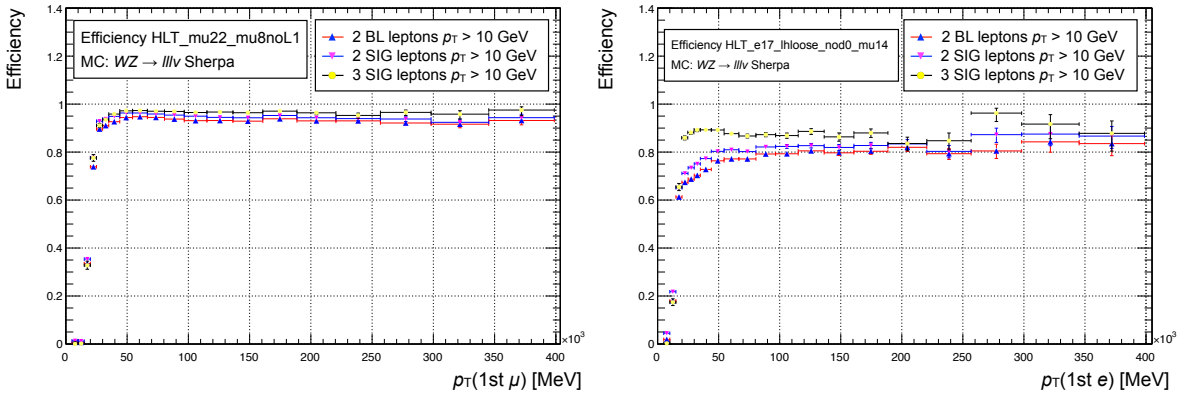

Figure VIII.3.: Efficiency evolution for the dimuon trigger `HLT_mu22_mu8noL1` (left) and the electron-muon trigger `HLT_e17_lhloose_nod0_mu14` (right) in $WZ \to \ell\ell\ell\nu$ MC, plotted against the p_{T} of the first trigger item (electron or muon). The trigger efficiency is compared for different lepton preselections applied.

VIII.2.3. IMPROVED OBJECT SELECTION AND ELECTRON CHARGE IDENTIFICATION

Compared to the object definitions described in Section VII.2.2, some changes have been implemented for the 2015+2016 version of the analysis in order to take into account improvements made in the object selection during 2016 or to increase the sensitivity of the analysis. These modifications are briefly summarized in Appendix D. Dedicated studies have been done for each of them to confirm that they indeed improve the overall analysis performance.

A significant improvement could be attained for the identification of the electron charge, for which a new method based on a boosted decision tree [175] was introduced. The processes leading to charge misidentification of electrons have been already described in Section VII.4.3. In order to obtain a better discrimination between electrons with wrong and correct charge assignments, a BDT using electron cluster and track properties such as impact parameters, electromagnetic shower widths, or cluster-track matching variables, is applied to separate these two types of electrons. Also, standard electron properties like p_{T} or η are used for the BDT input. The BDT was trained with $Z^0 \to ee$ control samples containing electrons with misidentified and correctly measured charges. A selection requirement on the BDT output, corresponding to a 97% efficiency[8] for electrons with correctly measured charge is added to the signal electron definition, using a dedicated selection tool developed by the electron performance group (electron charge ID selector tool). With this method, the rejection of electrons with a wrong charge assignment could be improved by a factor of 7–8 with respect to the standard identification.

The effect of the electron charge ID selector tool is shown in Figure VIII.4. The invariant mass distribution of signal $e^{\pm}e^{\pm}$ pairs around the Z^0 resonance (equivalent to Figure VII.9) with and without the selection requirement on the BDT output applied (at 97% efficiency WP for correct charge assignment). The reduction of the charge-flip process in data (left) as well as in Monte Carlo (right) is remarkable.

Additional scale factors to account for the difference in the selection efficiency of the tool between data and simulation have to be applied to the selected electrons in MC. Although the charge-flip rates can be significantly reduced utilizing the charge ID selector tool, the effect cannot be eliminated completely. Therefore, the data-driven method introduced in the 2015 version of the analysis is still applied in the 2016 version (with adapted measurements of the charge-flip efficiencies).

[8] Corresponding to a background acceptance of ≈8% for the *mediumLH* electron identification WP.

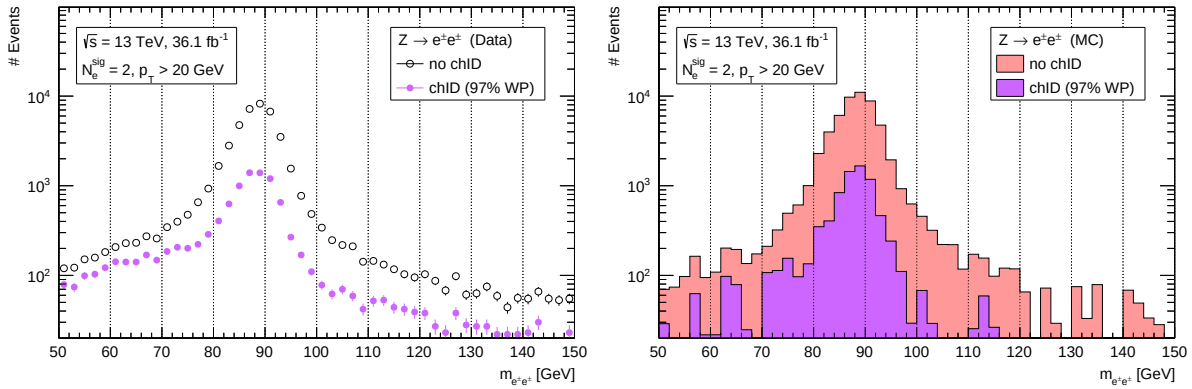

Figure VIII.4.: Invariant mass distribution of signal $e^{\pm}e^{\pm}$ pairs around the Z^0 resonance in data (left) and simulated $Z^0 \to ee$ events (right) with and without the electron charge ID selector tool (chID) applied.

VIII.2.4. CHANGES IN THE BACKGROUND ESTIMATION AND NEW VALIDATION REGIONS

The modeling of the prompt same-sign/3L background relies still fully on simulated Monte Carlo samples. Only marginal modifications have been applied, such as increasing the number of generated events for some MC samples or adapting the pile-up reweighting procedure to the updated $\langle\mu\rangle$ profile of the combined 2015+2016 data.

The theory uncertainties were revisited using varied event weights included within the nominal MC samples (LHE3 weights [215]). The uncertainties of the $t\bar{t}$+Z and $t\bar{t}$+W samples are evaluated by performing a generator comparison between SHERPA and MG5_aMC@NLO independently for each of the new and re-optimized signal regions to account for the theoretical modeling of the kinematic distributions in the MC simulation. For diboson production, uncertainties are estimated by varying the MC normalization, factorization, and resummation scales as well as the parton shower recoil scheme. Including the cross-section uncertainties[9], the values amount to 15–35% for $t\bar{t}$+W/Z and 30–40% for diboson production, depending on the SR. For the remaining prompt processes (tZ, $tW^{\pm}Z$, $t\bar{t}VV$, $tt\bar{t}$, $t\bar{t}t\bar{t}$, W/Z+H, $t\bar{t}$+H and triboson production), a conservative value of 50% is used as in 2015. The impact of $W^{\pm}W^{\pm}$ production via double parton scattering (DPS) to the SRs has been investigated and found to be negligible for the analysis. The dedicated study can be found in Appendix E.

Charge-flip efficiencies, as well as the fake and real rates for the matrix method, have been newly measured with the full 36.1 fb^{-1} dataset, using the updated object definitions. Also, their uncertainties have been revisited with the same approaches as described in Section VII.5.2. Since the fake/non-prompt lepton predictions from the matrix method and the MC template method are consistent with each other, it has been decided to use a weighted average of the results from the two techniques. This makes the prediction in the signal and validation regions more stable and helps to reduce the associated uncertainties. Especially the large statistical uncertainties of the matrix method due to small numbers of events in the control regions used for the fake rate measurements could be mitigated. Figure VIII.5 shows the consistency of the FNP lepton prediction obtained from the two methods in a control region with a simple preselection applied (two same-sign leptons, two jets $p_{\mathrm{T}} > 40$ GeV, ≥ 1 b-jet, and $E_{\mathrm{T}}^{\mathrm{miss}} > 50$ GeV).

Also in this version of the analysis, the background estimation is validated with a set of validation regions optimized for the most relevant Standard Model background processes (VR-ttW, VR-ttZ, VR-WZ4j,

[9] With respect to 2015, the cross-section uncertainties remained basically unchanged at around 12% for $t\bar{t}$+Z, 13% for $t\bar{t}$+W and 6% for diboson production.

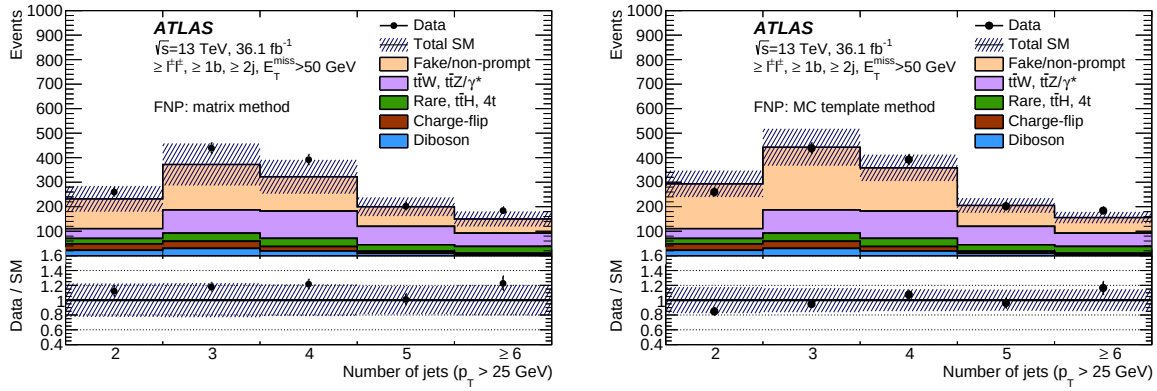

Figure VIII.5.: The N_{jets}^{25} distribution after requiring a same-sign lepton pair, two jets $p_{\text{T}} > 40$ GeV, $N_{b\text{-jets}} \geq 1$, and $E_{\text{T}}^{\text{miss}} > 50$ GeV. The estimation of the FNP lepton contribution is done either with the matrix method (left) or the MC template method (right). The predictions from both methods are consistent within their uncertainties.

VR-WZ5j and VR-W$^{\pm}$W$^{\pm}$jj). Their definitions are summarized in Table VIII.1. Compared to the 2015 validation regions, a particular region targeting the $t\bar{t}$+W process was designed (VR-tt̄W) and the previous VR optimized for the $W^{\pm}Z$ background was subdivided to validate individually different numbers of extra jets in $W^{\pm}Z$ events (VR-WZ4j and VR-WZ5j).

Name	N_{ℓ}^{S}	N_{jets}	$N_{b\text{-jets}}$	$p_{\text{T}}^{\text{jet}}$ [GeV]	$E_{\text{T}}^{\text{miss}}$ [GeV]	m_{eff} [GeV]	Other
VR-tt̄W	$= 2$	≥ 4 (ee,eμ)	≥ 1	> 40	> 45	> 550	$p_{\text{T}}(\ell_2) > 40$ GeV
	$= 1$ SS pair	≥ 3 (μμ)		> 25			$H_{\text{T}}^{b\text{-jet}}/H_{\text{T}}^{\text{jet}} > 0.25$
VR-tt̄Z	≥ 3	≥ 3	≥ 1	> 35	–	> 450	$m_{\text{SFOS}} \in [81, 101]$ GeV
	≥ 1 SFOS pair						
VR-WZ4j	$= 3$	≥ 4	$= 0$	> 25	–	> 450	$E_{\text{T}}^{\text{miss}}/H_{\text{T}}^{\ell} < 0.7$
VR-WZ5j	$= 3$	≥ 5	$= 0$	> 25	–	> 450	$E_{\text{T}}^{\text{miss}}/H_{\text{T}}^{\ell} < 0.7$
VR-W$^{\pm}$W$^{\pm}$jj	$= 2$	≥ 2	$= 0$	> 50	> 55	> 650	$m_{ee} \notin [81, 101]$ GeV
	$= 1$ SS pair						$p_{\text{T}}^{\ell_2} > 30$ GeV
							$\Delta R(\ell_{1,2}, j) > 0.7$
							$\Delta R(\ell_1, \ell_2) > 0.7$

Table VIII.1.: The 2016 validation region definitions. In addition to these requirements, all events entering one of the SRs are vetoed from the VRs to ensure their orthogonality. H_{T}^{ℓ}, $H_{\text{T}}^{\text{jets}}$ and $H_{\text{T}}^{b\text{-jets}}$ denote the scalar sum of the p_{T} of all leptons, jets and b-jets, respectively.

A comparison between the observed and expected results in the 2016 validation regions for 36.1 fb^{-1} is shown in Figure VIII.6. The uncertainty band includes all experimental and theoretical systematic uncertainties as well as the statistical errors. They are in the range of 16–45%. Within the uncertainties, there is good agreement between data and the estimated background. The purity of the targeted background processes is between 35 and 65%, while the expected signal contamination in the VRs amounts to 5–20%. Note that the "Rare" category introduced in the previous chapter does not contain the contributions from $t\bar{t}\,t\bar{t}$ and $t\bar{t}$+H anymore: it has been decided to show them as individual categories, as they represent

important background processes in some of the signal regions. The reasonable results in the VRs confirm that the background estimation strategy is still reliable also for the increased luminosity and the changes in the object definitions.

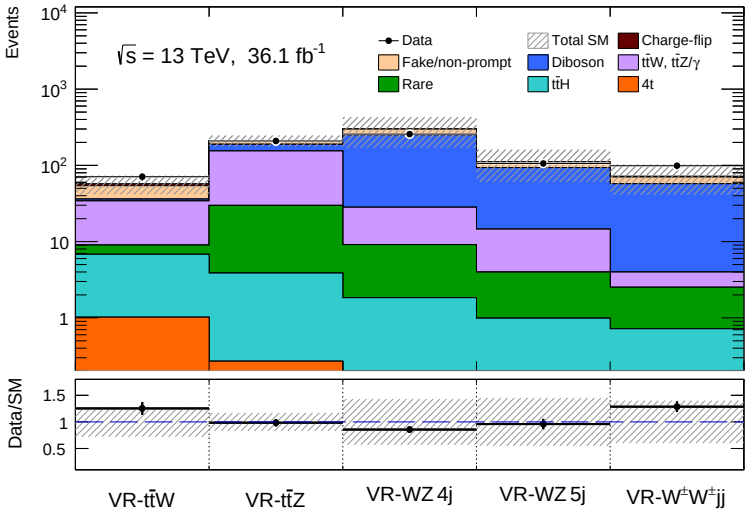

Figure VIII.6.: Observed and expected event yields in the 2016 validation regions for 36.1 fb^{-1}. The bottom panel shows the ratio between data and the background prediction.

VIII.2.5. RE-OPTIMIZED AND NEW SIGNAL REGIONS

The simple prescription used to design the four signal regions in 2015 has been refined already in the intermediate analysis update presented in Section VIII.1. While the original approach was to use only one SR for each of the benchmark models, the recipe has been changed to in order to obtain a good sensitivity to several kinematic regions (different mass splitting between the SUSY particles) within one scenario. The change of the kinematic properties for different signal points from the same scenarios is demonstrated in Figure VIII.7, showing the m_{eff} distributions of two signal points from the $\widetilde{g} \to t\bar{t}\,\widetilde{\chi}_1^0$ (left) and $\widetilde{g} \to q\bar{q}(\ell\bar{\ell}/\nu\nu)\,\widetilde{\chi}_1^0$ (right) grid with the same gluino masses but very different neutralino masses. While the m_{eff} spectra have their maxima at very large values of 1.5–2.0 TeV for points with negligible $m_{\widetilde{\chi}_1^0}$, they are shifted towards lower values ($\approx$500 GeV) if the mass difference between neutralino and gluino is relatively small.

To address this feature, signal regions with same topological, but distinct kinematic requirements were optimized for different kinematic regions and combined subsequently for the model-dependent interpretation. In general, the optimization procedure is performed similarly to the one described in Section VII.3.1 but for higher luminosities[10] and independently for regions with low and high mass differences. For each of the four original benchmark models, two individual SRs have been defined following this approach. Additionally, two separate SRs were designed especially for the $\widetilde{g} \to t\bar{t}\,\widetilde{\chi}_1^0, t \to bW^{\pm}$ scenario with decays via off-shell top quarks. Furthermore, new signal regions were designed targeting the additional RPC and RPV SUSY models introduced in Section VIII.2.1. The diagram in Figure VIII.8 illustrates the evolution of the RPC signal regions, from the simple strategy used in 2015 to the more sophisticated approach from 2016, with dedicated SRs for different kinematic regions within one SUSY scenario.

[10] Optimization studies were performed simultaneously for several expected luminosity values (30 fb^{-1}, 35 fb^{-1}, 40 fb^{-1}). The definitions obtained from the scenario closest to the finally observed value (in this case 35 fb^{-1}) have been taken.

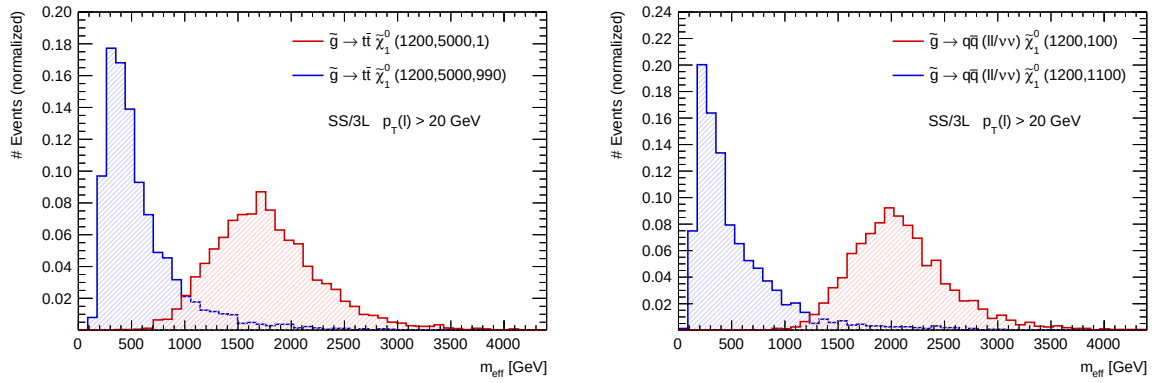

Figure VIII.7.: The m_{eff} distributions of two different signal points from the $\widetilde{g} \to t\bar{t}\widetilde{\chi}_1^0$ (left) and $\widetilde{g} \to q\bar{q}(\ell\bar{\ell}/\nu\nu)\widetilde{\chi}_1^0$ (right) scenario: the spectra are shown for cases where the mass difference between gluino and neutralino is either very large (red) or very small (blue). All distributions are normalized to unity.

The new SRs are labelled according to a more consistent and meaningful naming convention: they typically have the form "RpxNLYbZ", where $x = c, v$ indicates whether the SR targets an RPC or RPV model, $N = 2,3$ gives the number of signal leptons required, Y the number of b-jets in the SR, and $Z = S, M, H$ the severity of the $E_{\text{T}}^{\text{miss}}$ and m_{eff} requirements (Soft, Medium, Hard) to address different kinematic regions of the SUSY signal grid.

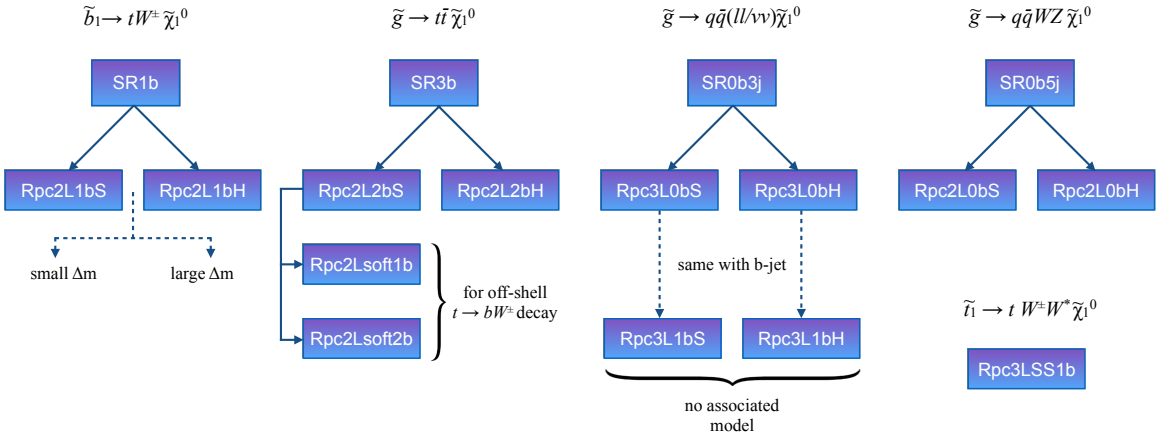

Figure VIII.8.: Evolution of the SR strategy for the RPC models, starting from the simple approach used in 2015 (top) to a more elaborated strategy, using dedicated SRs for different kinematic regions of one model.

The requirement of having three b-tagged jets in the signal regions optimized for the $\widetilde{g} \to t\bar{t}\widetilde{\chi}_1^0$ scenario was relaxed to a $N_{b\text{-jets}} \geq 2$ condition, since a slight disagreement is observed between data and the SM prediction in the opposite-sign 2ℓ+$3b$ channel[11] (most likely due to an insufficiency of the FNP lepton estimation with the matrix method). Furthermore, during the optimization studies, it was confirmed that there is no large sensitivity loss for the targeted model by demanding only two b-jets instead of three. The regions Rpc3L1bS and Rpc3L1bH do not target a particular model and will not be used for any model-dependent interpretation. They are included to cover event signatures with three leptons and

[11] A working background estimation in the opposite-sign 2ℓ+$3b$ channel is crucial for the data-driven estimation of the charge-flip contribution in the according same-sign channel.

b-jets, which cannot be motivated by any specific SUSY scenario but is nevertheless an interesting event signature to explore in the context of this analysis.
The definitions for all new and re-optimized signal regions are listed in Table VIII.2, including also the most relevant signal processes. In total, 19 partially overlapping signal regions, targeting twelve different supersymmetric benchmark scenarios are defined. Unlike the signal regions designed for the RPC models, the RPV regions do not have $E_{\mathrm{T}}^{\mathrm{miss}}$ requirements but typically higher jet multiplicities or larger cuts on m_{eff} instead (motivated by the additional SM particles produced at the $\widetilde{\chi}_1^0$ decays in the RPV models). The regions optimized especially for the off-shell top region in the $\widetilde{g} \to t\bar{t}\widetilde{\chi}_1^0$ scenario (Rpc2Lsoft1b and Rpc2Lsoft2b) target scenarios with very soft lepton p_{T} spectra, which are in general lower than those from the dominant background processes. Thus, these signal regions were found to be more sensitive with an upper cut on the p_{T} of the leptons. For regions where the Z+jets background is relevant (Rpc3LSS1b, Rpv2L0b, and Rpv2L2bH), events with a same-sign electron pair with an invariant mass close to the Z^0 resonance ($m_Z \pm 10$ GeV), are rejected.

Signal region	N_ℓ^{S}	N_{jets}	N_b	$p_{\mathrm{T}}^{\mathrm{jet}}$ [GeV]	$E_{\mathrm{T}}^{\mathrm{miss}}$ [GeV]	m_{eff} [GeV]	$E_{\mathrm{T}}^{\mathrm{miss}}/m_{\mathrm{eff}}$	Other [GeV]	Targeted signal
Rpc2L2bS	≥ 2	≥ 6	≥ 2	> 25	> 200	> 600	> 0.25	–	$\widetilde{g} \to t\bar{t}\widetilde{\chi}_1^0$
Rpc2L2bH	≥ 2	≥ 6	≥ 2	> 25	–	> 1800	> 0.15	–	$\widetilde{g} \to t\bar{t}\widetilde{\chi}_1^0$ & NUHM2
Rpc2Lsoft1b	≥ 2	≥ 6	≥ 1	> 25	> 100	–	> 0.3	$20 < p_{\mathrm{T}}^{\ell_1} < 100$ $10 < p_{\mathrm{T}}^{\ell_2} < 100$	$\widetilde{g} \to t\bar{t}\widetilde{\chi}_1^0,\ t \to bW^{\pm}$
Rpc2Lsoft2b	≥ 2	≥ 6	≥ 1	> 25	> 200	> 600	> 0.25	$20 < p_{\mathrm{T}}^{\ell_1} < 100$ $10 < p_{\mathrm{T}}^{\ell_2} < 100$	$\widetilde{g} \to t\bar{t}\widetilde{\chi}_1^0,\ t \to bW^{\pm}$
Rpc2L0bS	≥ 2	≥ 6	$= 0$	> 25	> 150	–	> 0.25	–	$\widetilde{g} \to q\bar{q}W^{\pm}Z\widetilde{\chi}_1^0$
Rpc2L0bH	≥ 2	≥ 6	$= 0$	> 40	> 250	> 900	–	–	$\widetilde{g} \to q\bar{q}W^{\pm}Z\widetilde{\chi}_1^0$
Rpc2L1bS	≥ 2	≥ 6	≥ 1	> 25	> 150	> 600	> 0.25	–	$\widetilde{b}_1 \to tW^{\pm}\widetilde{\chi}_1^0$
Rpc2L1bH	≥ 2	≥ 6	≥ 1	> 25	> 250	–	> 0.2	–	$\widetilde{b}_1 \to tW^{\pm}\widetilde{\chi}_1^0$
Rpc3L0bS	≥ 3	≥ 4	$= 0$	> 40	> 200	> 600	–	–	$\widetilde{g} \to q\bar{q}(\ell\bar{\ell}/\nu\nu)\widetilde{\chi}_1^0$
Rpc3L0bH	≥ 3	≥ 4	$= 0$	> 40	> 200	> 1600	–	–	$\widetilde{g} \to q\bar{q}(\ell\bar{\ell}/\nu\nu)\widetilde{\chi}_1^0$
Rpc3L1bS	≥ 3	≥ 4	≥ 1	> 40	> 200	> 600	–	–	–
Rpc3L1bH	≥ 3	≥ 4	≥ 1	> 40	> 200	> 1600	–	–	–
Rpc3LSS1b	≥ 3(SS)	–	≥ 1	–	–	–	–	$m_{ee} \notin [81, 101]$	$\widetilde{t}_1 \to tW^{\mp}W^*\widetilde{\chi}_1^0$
Rpv2L0b	$= 2$	≥ 6	$= 0$	> 40	–	> 1800	–	$m_{ee} \notin [81, 101]$	$\widetilde{g} \to q\bar{q}\widetilde{\chi}_1^0, \widetilde{\chi}_1^0 \to q\bar{q}\ell$
Rpv2L1bS	$\geq 2^-$	≥ 4	≥ 1	> 50	–	> 1200	–	–	$\widetilde{d}_R \to \bar{s}\bar{t}$
Rpv2L1bM	$\geq 2^-$	≥ 4	≥ 1	> 50	–	> 1800	–	–	$\widetilde{d}_R \to \bar{s}\bar{t}$
Rpv2L1bH	≥ 2	≥ 6	≥ 1	> 50	–	> 2200	–	–	$\widetilde{g} \to tbd$ & $\widetilde{g} \to tsd$
Rpv2L2bS	$\geq 2^-$	≥ 3	≥ 2	> 50	–	> 1200	–	–	$\widetilde{d}_R \to \bar{b}\bar{t}$
Rpv2L2bH	≥ 2	≥ 6	≥ 2	> 40	–	> 2000	–	$m_{ee} \notin [81, 101]$	$\widetilde{g} \to t\bar{t}\widetilde{\chi}_1^0, \widetilde{\chi}_1^0 \to uds$

Table VIII.2.: Summary of the final 2016 signal regions. The naming convention was changed to provide more details about the selection requirements and the targeted signal model. The regions Rpc3L1bS(H) are not inspired by a particular model and are just added to cover the 3ℓ+b-jet topology.

For the SRs targeting the $\widetilde{d}_R \to \bar{s}\bar{t}$ and $\widetilde{d}_R \to \bar{b}\bar{t}$ scenarios (Rpv2L1bS, Rpv2L1bM, and Rpv2L2bS), only same-sign pairs with negatively charged leptons are considered (indicated by the N^- in the lepton requirement). This selection was chosen as the down squarks decay exclusively to antiquarks in these models. All signal regions allow any number of further signal leptons in addition to the same-sign pair, except Rpv2L0b optimized for the $\widetilde{g} \to q\bar{q}\widetilde{\chi}_1^0$, $\widetilde{\chi}_1^0 \to q\bar{q}\ell$ model, for which a requirement of exactly two leptons was found to be more sensitive. The region Rpc3LSS1b optimized for the $\widetilde{t}_1 \to tW^{\mp}W^*\widetilde{\chi}_1^0$ model is the only SR requiring all three leptons to have the same charge ($\ell^+\ell^+\ell^+$ or $\ell^-\ell^-\ell^-$). Furthermore, requirements on the ratio $E_{\mathrm{T}}^{\mathrm{miss}}/m_{\mathrm{eff}}$ are included for some signal regions, since they were found to be more sensible in many cases than only cuts on $E_{\mathrm{T}}^{\mathrm{miss}}$ or m_{eff}.
Studies on the utilization of additional techniques (W/Z-tagging) or more complex kinematic quantities, such as the m_{T2} variable [216] to enhance the sensitivity in the signal regions have been performed. In general, these did not show any significant improvement with respect to the SRs based on simple event or object properties as they are used here. Details and auxiliary material about these studies is given in Appendix F and G. Also the usage of orthogonal SRs binned in different m_{eff}, $E_{\mathrm{T}}^{\mathrm{miss}}$, or N_{jets} ranges was tested and found to have no sizable effect on the final analysis results.

VIII.2.6. RESULTS FOR 36.1 FB^{-1} OF DATA

The observed and expected event yields for 36.1 fb^{-1} in the 19 signal regions are shown in Figure VIII.9. The detailed numbers of the yields for data and all background sources[12], as well as the associated p-values and significances for each SR are listed in Table VIII.3. No significant deviation between data and the SM prediction is observed in any of the signal regions. In fact, data and SM background largely agree within their uncertainties. The biggest excess is observed in the signal region Rpv2L1bM, corresponding to a significance of 1.5 σ.

The relative uncertainties of the total background estimates for all of the 19 signal regions are presented in Figure VIII.10. The total values (light blue area) can be subdivided into different sources of uncertainties, such as experimental, theoretical, and statistical uncertainties or uncertainties only associated with the data-driven techniques. These components (indicated as colored lines) are shown separately to specify the most important sources of uncertainties for each of the signal regions. The total uncertainties amount to 25–50% of the predicted SM background. Although the most relevant uncertainties are typically either theoretical errors or uncertainties attributed to the data-driven methods, no particular source of uncertainty is dominant in all of the signal regions. A detailed breakdown of the systematic uncertainties in each signal region can also be found in Appendix H.

[12] A detailed breakdown of the "Rare" category to its fractional subcomponents can be found in Appendix H.

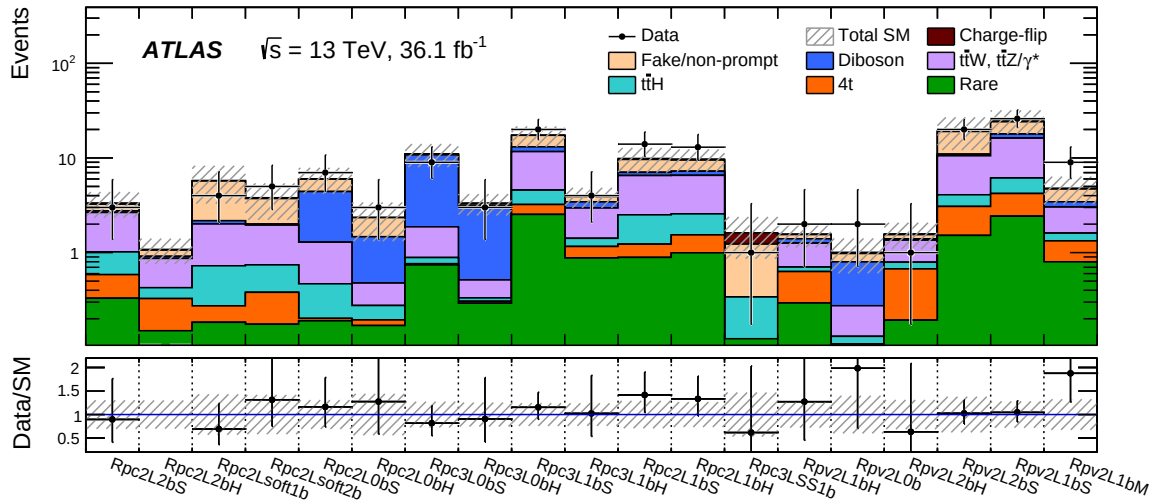

Figure VIII.9.: Observed and expected event yields in the 2016 signal regions for an integrated luminosity of 36.1 fb^{-1}. The bottom panel shows the ratio between data and the SM prediction. The uncertainty bands include all experimental and theoretical systematic uncertainties as well as the statistical errors [8].

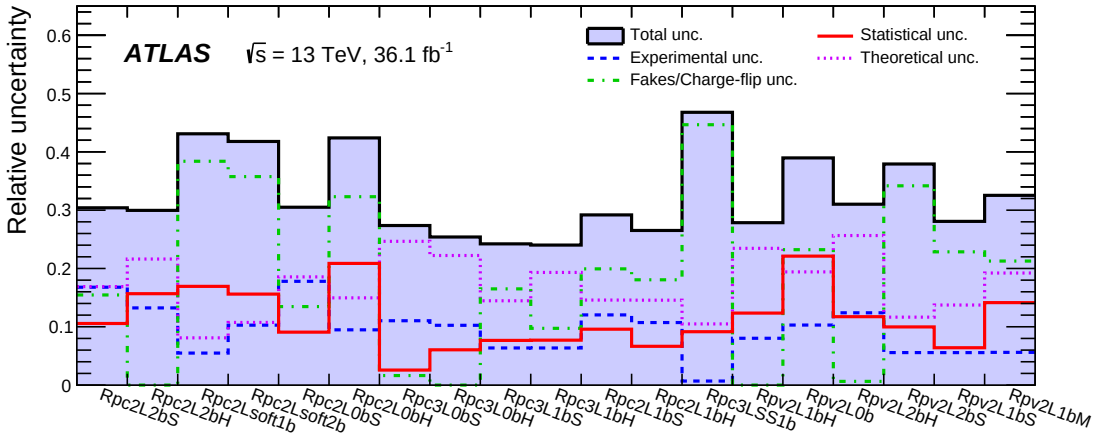

Figure VIII.10.: The relative uncertainties of the total background estimates in the 2016 signal regions. The total uncertainty can be subdivided into different sources (experimental, theoretical, statistical, and data-driven). The fractional uncertainties are superimposed to indicate which error type is the dominant one for the individual SRs [8].

Signal region	Rpc2L2bS	Rpc2L2bH	Rpc2Lsoft1b	Rpc2Lsoft2b	Rpc2L0bS	Rpc2L0bH
Observed events	3	0	4	5	7	3
Total background	3.3 ± 1.0	1.80 ± 0.32	5.8 ± 2.5	3.8 ± 1.6	6.0 ± 1.8	2.4 ± 1.0
Fake/non-prompt leptons	0.5 ± 0.6	0.15 ± 0.15	3.5 ± 2.4	1.7 ± 1.5	1.6 ± 1.0	0.9 ± 0.9
Charge-flip	0.10 ± 0.01	0.02 ± 0.01	0.08 ± 0.02	0.08 ± 0.02	0.05 ± 0.01	0.01 ± 0.01
$t\bar{t}$+W/Z	1.6 ± 0.4	0.44 ± 0.14	1.3 ± 0.4	1.21 ± 0.33	0.82 ± 0.31	0.20 ± 0.10
Diboson	0.10 ± 0.10	0.04 ± 0.02	0.17 ± 0.09	0.05 ± 0.03	3.1 ± 1.4	1.0 ± 0.5
$t\bar{t}$+H	0.43 ± 0.25	0.10 ± 0.06	0.45 ± 0.24	0.36 ± 0.21	0.27 ± 0.15	0.08 ± 0.07
$t\bar{t}t\bar{t}$ (4-top)	0.26 ± 0.13	0.18 ± 0.09	0.09 ± 0.05	0.21 ± 0.11	0.01 ± 0.01	0.02 ± 0.02
Rare	0.33 ± 0.18	0.15 ± 0.09	0.18 ± 0.10	0.17 ± 0.10	0.19 ± 0.11	0.17 ± 0.10
p-value	0.71	0.91	0.69	0.30	0.36	0.35
Significance	–	–	–	0.5σ	0.4σ	0.4σ

Signal region	Rpc3L0bS	Rpc3L0bH	Rpc3L1bS	Rpc3L1bH	Rpc2L1bS	Rpc2L1bH	Rpc3LSS1b
Observed events	9	3	20	4	14	13	1
Total background	11.0 ± 3.0	3.3 ± 0.8	17 ± 4	3.9 ± 0.9	9.8 ± 2.9	9.8 ± 2.6	1.6 ± 0.8
Fake/non-prompt leptons	0.23 ± 0.23	0.15 ± 0.15	4.2 ± 3.1	0.5 ± 0.5	2.5 ± 2.2	2.3 ± 1.9	0.9 ± 0.7
Charge-flip	–	–	–	–	0.25 ± 0.04	0.25 ± 0.05	0.39 ± 0.08
$t\bar{t}$+W/Z	0.98 ± 0.25	0.18 ± 0.08	7.1 ± 1.1	1.54 ± 0.28	4.0 ± 1.0	4.0 ± 0.9	–
Diboson	8.9 ± 2.9	2.6 ± 0.8	1.4 ± 0.5	0.48 ± 0.17	0.5 ± 0.3	0.7 ± 0.3	–
$t\bar{t}$+H	0.12 ± 0.08	0.03 ± 0.02	1.4 ± 0.7	0.25 ± 0.14	1.3 ± 0.7	1.0 ± 0.6	0.22 ± 0.12
$t\bar{t}t\bar{t}$ (4-top)	0.02 ± 0.01	0.01 ± 0.01	0.7 ± 0.4	0.28 ± 0.15	0.34 ± 0.17	0.54 ± 0.28	–
Rare	0.7 ± 0.4	0.29 ± 0.16	2.5 ± 1.3	0.9 ± 0.5	0.9 ± 0.5	1.0 ± 0.6	0.12 ± 0.07
p-value	0.72	0.85	0.32	0.46	0.17	0.21	0.56
Significance	–	–	0.5σ	0.1σ	1.0σ	0.8σ	–

Signal region	Rpv2L1bH	Rpv2L0b	Rpv2L2bH	Rpv2L2bS	Rpv2L1bS	Rpv2L1bM
Observed events	2	2	1	20	26	9
Total background	1.6 ± 0.4	1.0 ± 0.4	1.6 ± 0.5	19 ± 7	25 ± 7	4.8 ± 1.6
Fake/non-prompt leptons	0.15 ± 0.15	0.18 ± 0.31	0.15 ± 0.15	8 ± 7	6 ± 6	1.3 ± 1.2
Charge-flip	0.02 ± 0.01	0.03 ± 0.02	0.03 ± 0.01	0.46 ± 0.08	0.74 ± 0.12	0.10 ± 0.02
$t\bar{t}$+W/Z	0.56 ± 0.14	0.14 ± 0.08	0.56 ± 0.15	6.5 ± 1.3	10.1 ± 1.7	1.4 ± 0.5
Diboson	0.14 ± 0.06	0.52 ± 0.21	0.04 ± 0.02	0.42 ± 0.16	1.7 ± 0.6	0.42 ± 0.15
$t\bar{t}$+H	0.07 ± 0.05	0.02 ± 0.02	0.12 ± 0.07	1.0 ± 0.5	1.9 ± 1.0	0.28 ± 0.15
$t\bar{t}t\bar{t}$ (4-top)	0.34 ± 0.17	0.01 ± 0.01	0.48 ± 0.24	1.6 ± 0.8	1.8 ± 0.9	0.53 ± 0.27
Rare	0.29 ± 0.17	0.10 ± 0.06	0.19 ± 0.13	1.5 ± 0.8	2.4 ± 1.2	0.8 ± 0.4
p-value	0.33	0.19	0.55	0.48	0.44	0.07
Significance	0.4σ	0.9σ	–	0.1σ	0.2σ	1.5σ

Table VIII.3.: Observed and expected numbers of events in the 2016 signal regions for an integrated luminosity of 36.1 fb^{-1}. Background categories shown as "–" do not contribute to a region. The respective p-values and significances are also stated. Significances indicated as "–" correspond to regions with more expected than observed events ($p_0 > 0.5$).

VIII.2.7. STATISTICAL INTERPRETATIONS FOR 36.1 FB^{-1}

In the absence of any significant deviation from the SM prediction, model-independent and model-dependent limits can be computed according to the prescriptions explained in Section VII.8.3 and VII.8.4. Furthermore, the latest results can additionally be interpreted in the context of the new signal scenarios introduced in section VIII.2.1.

MODEL-INDEPENDENT UPPER LIMITS

The model-independent upper limits on the number of BSM events $N_{\text{BSM}}^{\text{obs}}$ ($N_{\text{BSM}}^{\text{exp}}$) are stated in Table VIII.4 for all signal regions. Normalizing by the integrated luminosity translates them into upper limits on the visible signal cross-sections $\sigma_{\text{vis}}^{\text{obs}}$ ($\sigma_{\text{vis}}^{\text{exp}}$). The computation is done analogous to the previous version of this analysis, using a frequentist-based approach with 10^4 pseudo-experiments to derive observed and expected limits at 95% CL_s.

Signal region	$N_{\text{BSM}}^{\text{obs}}$	$N_{\text{BSM}}^{\text{exp}}$	$\sigma_{\text{vis}}^{\text{obs}}$ [fb]	$\sigma_{\text{vis}}^{\text{exp}}$ [fb]
Rpc2L2bS	5.5	$5.6^{+2.2}_{-1.5}$	0.15	$0.16^{+0.06}_{-0.04}$
Rpc2L2bH	3.6	$3.9^{+1.4}_{-0.4}$	0.10	$0.11^{+0.04}_{-0.01}$
Rpc2Lsoft1b	6.3	$7.1^{+2.5}_{-1.5}$	0.17	$0.20^{+0.07}_{-0.04}$
Rpc2Lsoft2b	7.7	$6.2^{+2.6}_{-1.5}$	0.21	$0.17^{+0.07}_{-0.04}$
Rpc2L0bS	8.3	$7.5^{+2.6}_{-1.8}$	0.23	$0.20^{+0.07}_{-0.05}$
Rpc2L0bH	6.1	$5.3^{+2.1}_{-1.3}$	0.17	$0.16^{+0.06}_{-0.04}$
Rpc3L0bS	8.3	$9.3^{+3.1}_{-2.3}$	0.23	$0.26^{+0.09}_{-0.06}$
Rpc3L0bH	5.4	$5.5^{+2.2}_{-1.5}$	0.15	$0.16^{+0.06}_{-0.04}$
Rpc3L1bS	14.7	$12.6^{+5.1}_{-3.4}$	0.41	$0.35^{+0.14}_{-0.10}$
Rpc3L1bH	6.1	$5.9^{+2.2}_{-1.8}$	0.17	$0.16^{+0.06}_{-0.05}$
Rpc2L1bS	13.7	$10.0^{+3.7}_{-1.6}$	0.38	$0.28^{+0.10}_{-0.05}$
Rpc2L1bH	12.4	$9.7^{+3.4}_{-2.6}$	0.34	$0.27^{+0.09}_{-0.07}$
Rpc3LSS1b	3.9	$4.0^{+1.8}_{-0.3}$	0.11	$0.11^{+0.05}_{-0.01}$
Rpv2L1bH	4.8	$4.1^{+1.9}_{-0.4}$	0.13	$0.11^{+0.05}_{-0.01}$
Rpv2L0b	5.2	$4.0^{+1.7}_{-0.3}$	0.14	$0.11^{+0.05}_{-0.01}$
Rpv2L2bH	3.9	$4.1^{+1.8}_{-0.4}$	0.11	$0.11^{+0.05}_{-0.01}$
Rpv2L2bS	17.5	$16.8^{+5.2}_{-4.2}$	0.48	$0.47^{+0.14}_{-0.12}$
Rpv2L1bS	18.1	$17.2^{+5.9}_{-4.2}$	0.50	$0.48^{+0.16}_{-0.12}$
Rpv2L1bM	11.4	$7.3^{+2.5}_{-1.8}$	0.31	$0.20^{+0.07}_{-0.05}$

Table VIII.4.: Observed and expected model-independent upper limits on the number of BSM events (N_{BSM}) and on the visible signal cross-sections (σ_{vis}) for the 2016 signal regions.

EXCLUSION LIMITS ON SIGNAL SCENARIOS

Exclusion limits can be placed for the twelve different supersymmetric benchmark scenarios considered for this analysis. For scenarios where more than one signal region is utilized, the final combined limits are obtained by selecting the SR yielding the best expected sensitivity for each point of the SUSY parameter space individually and setting the limit according to this previously chosen configuration. The detailed

information which SRs are used for which points of the signal grids is given in Appendix H. For the sake of visibility, the 95% CL_s upper limits on the cross-sections for particular mass points (gray numbers) are not shown in these plots. However, tables providing this information for each signal point can be found in Appendix H. The observed and expected limits for the four initial SUSY benchmark models explained in Section VII.1 are presented in Figure VIII.11. Interpretations for these models have also been done in the previous analysis versions with 3.2 fb^{-1} (blue lines) and 13.2 fb^{-1} of data (not shown here). If available, also the observed limits from other ATLAS analyses [209] which released interpretations for the same models are superimposed.

For the $\widetilde{g} \to t\bar{t}\widetilde{\chi}_1^0$ model (Figure VIII.11a), the limit on the gluino mass could be extended to 1.75 TeV for scenarios with light neutralinos below 400 GeV. The limit for neutralinos is extended up to $m_{\widetilde{\chi}_1^0} \lesssim 950$ GeV for gluino masses in a range of 1.2–1.5 TeV. With respect to the 2015 version of the analysis, the limits could be improved by about 550 and 300 GeV for gluino and neutralino masses, respectively. An increased sensitivity could also be achieved in the kinematic region with $m_{\widetilde{g}} \in [2m_W + m_{\widetilde{\chi}_1^0},\ 2m_t + m_{\widetilde{\chi}_1^0}]$, corresponding to $t \to bW^{\pm}$ decays via off-shell top quarks in this model. Scenarios up to $\approx$50 GeV close to the kinematically forbidden region can be excluded. This improvement can certainly be attributed to the new signal regions used for this model, which have been especially designed for the off-shell top region (Rpc2Lsoft1b/2b). A more detailed look at the exclusion limit in the region with off-shell top decays is presented in Appendix H.
For the $\widetilde{b}_1 \to tW^{\pm}\widetilde{\chi}_1^0$ model (Figure VIII.11b), the limit can be improved to around 700 GeV for the bottom squark mass and approximately 270 GeV for the neutralino mass. Also in this case, the analysis is particularly sensitive in the region with a small mass difference between $\widetilde{b}_1$ and $\widetilde{\chi}_1^0$, where basically all scenarios up to $m_{\widetilde{b}_1} \approx 550$ GeV ($m_{\widetilde{\chi}_1^0} \approx 280$ GeV) can be excluded at 95% confidence level. The exclusion limit for the $\widetilde{g} \to q\bar{q}(\ell\bar{\ell}/\nu\nu)\widetilde{\chi}_1^0$ model (Figure VIII.11c) reaches $m_{\widetilde{g}} \approx 1.87$ TeV for very light neutralinos and $m_{\widetilde{\chi}_1^0} \approx 1.2$ TeV for gluino masses around 1.5 TeV, extending the 2015 limit by around 550 GeV for gluino and 400 GeV for neutralino masses. Therefore, it is still the most far-reaching limit among the four initial benchmark models. For the $\widetilde{g} \to q\bar{q}W^{\pm}Z\widetilde{\chi}_1^0$ model (Figure VIII.11d), gluino masses below $\approx$1.6 TeV and neutralino masses below $\approx$920 GeV can be excluded, corresponding to an increase of about 500 GeV for gluinos and 400 GeV for neutralinos, compared to the limits obtained with 3.2 fb^{-1} of data.

The exclusion limits for the additional scenarios introduced in Section VIII.2.1 are presented in the Figures VIII.12 and VIII.13. For models simulated with only one free parameter, the observed and expected upper limit on the production cross-section times branching ratio ($\sigma_{\text{prod}} \times \text{BR}$) is plotted against the independent parameter. For the $\widetilde{g} \to tbd$ and $\widetilde{g} \to tsd$ scenarios with an R-parity violating top squark decay (Figure VIII.12a and VIII.12b), gluino masses up to 1.4 TeV and top squark masses up to 1.1 TeV can be excluded. The exclusion limits for the neutralino mediated processes with decays via RPV couplings in the baryonic (or leptonic) sector, as shown in Figure VIII.12c (VIII.12d) reach around 1.8 TeV for the gluino mass and 1.7 (1.3) TeV for the neutralino mass.
The upper limits on $\sigma_{\text{prod}} \times \text{BR}$ for the models featuring direct production of right-handed down squarks with decays via RPV couplings (Figure VIII.13a and VIII.13b) can be compared to the theoretical predictions for fixed gluino masses. They are superimposed as red and blue lines for $m_{\widetilde{g}} = 1.4$ and 2.0 TeV, respectively[13]. In both scenarios, these cases can be excluded for down squarks masses of around 500 GeV (for $m_{\widetilde{g}} = 2.0$ TeV) and around 600 GeV (for $m_{\widetilde{g}} = 1.4$ TeV)[14]. The upper limit on

[13] The $\pm 1\,\sigma$ variations of the theoretical uncertainties are indicated by the dashed lines in the same color.
[14] Given by $m_{\widetilde{d}_R}$ of the intersection point between the observed limit and the theoretical evolution for a given gluino mass.

the $\widetilde{t}_1 \to t W^{\mp} W^{*} \widetilde{\chi}_1^0$ model with an RPC decay of top squarks to top quarks and a cascade of charginos and neutralinos decaying subsequently to $W^{\pm}$ bosons and the lightest neutralinos is presented in Figure VIII.13c. Top squark masses up to 700 GeV can be excluded at 95% CL_s. Finally, the limit on the NUHM2 model (Figure VIII.13d) allows to exclude values of the $m_{1/2}$ parameter below 650 GeV. Considering the other (fixed) parameters in this model, this corresponds to a gluino mass of around 1.6 TeV [214].

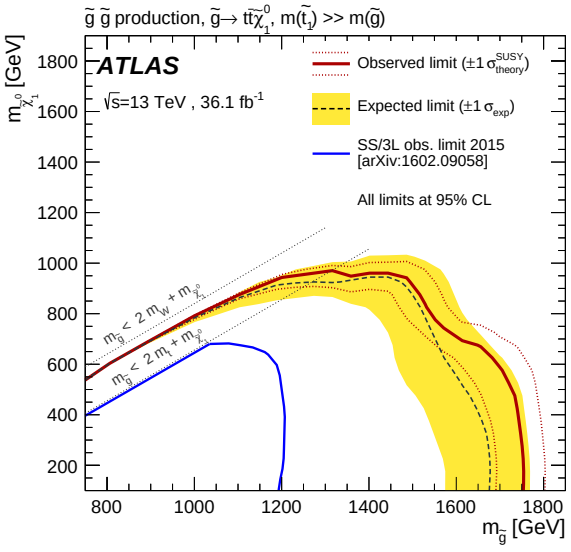

(a) $\widetilde{g} \to t\bar{t}\widetilde{\chi}_1^0$ scenario: Rpc2L2bS(H), Rpc2Lsoft1b(2b)

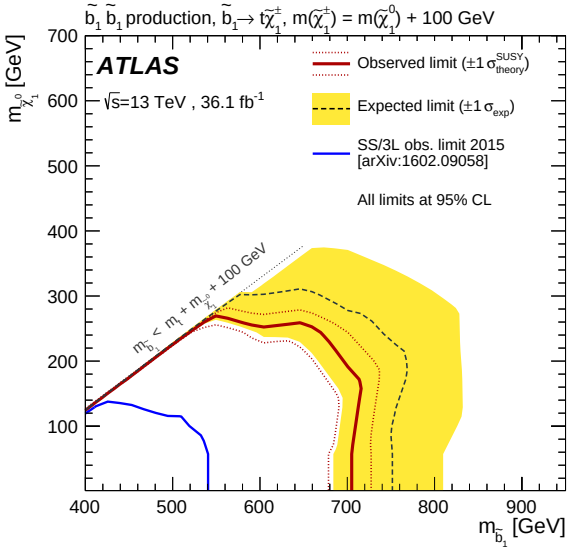

(b) $\widetilde{b}_1 \to t W^{\pm} \widetilde{\chi}_1^0$ scenario: Rpc2L1bS(H)

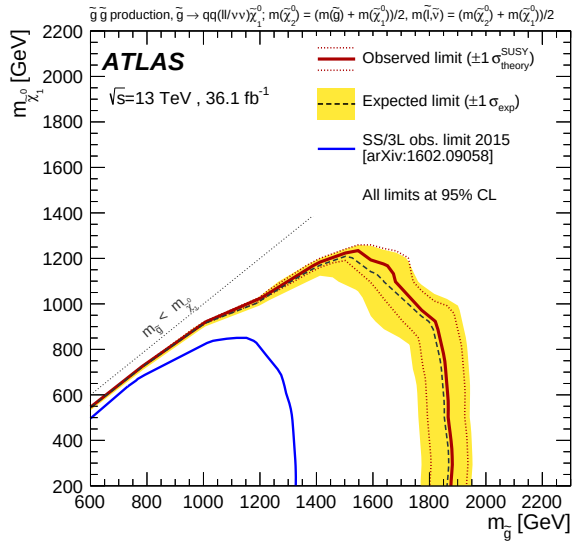

(c) $\widetilde{g} \to q\bar{q}(\ell\bar{\ell}/\nu\nu)\widetilde{\chi}_1^0$ scenario: Rpc3L0bS(H)

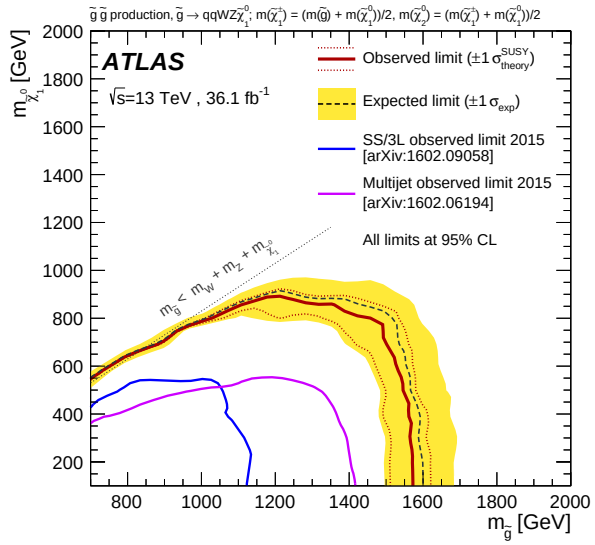

(d) $\widetilde{g} \to q\bar{q}W^{\pm}Z\widetilde{\chi}_1^0$ scenario: Rpc2L0bS(H)

Figure VIII.11.: Observed and expected exclusion limits on superpartner masses in the context of the four initial RPC SUSY scenarios for 36.1 fb^{-1}. The limits are derived for the $\widetilde{g} \to t\bar{t}\widetilde{\chi}_1^0$ (a), $\widetilde{b}_1 \to t W^{\pm} \widetilde{\chi}_1^0$ (b), $\widetilde{g} \to q\bar{q}(\ell\bar{\ell}/\nu\nu)\widetilde{\chi}_1^0$ (c), and $\widetilde{g} \to q\bar{q}W^{\pm}Z\widetilde{\chi}_1^0$ (d) scenario. The SRs used to obtain the combined limit for each scenario are specified in the subtitles [8].

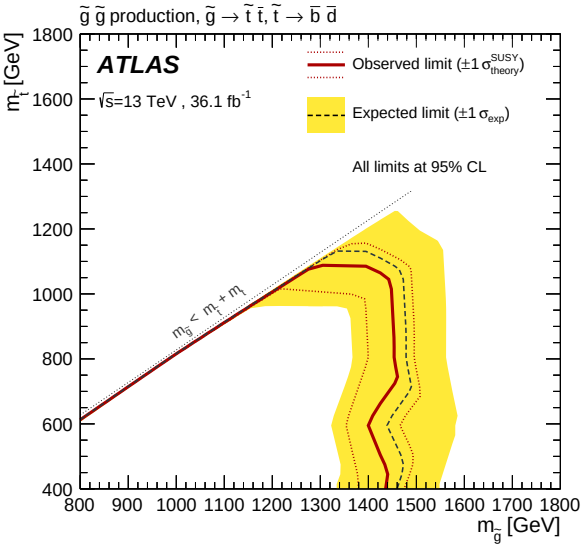

(a) $\widetilde{g} \to tbd$ scenario: Rpv2L1bH

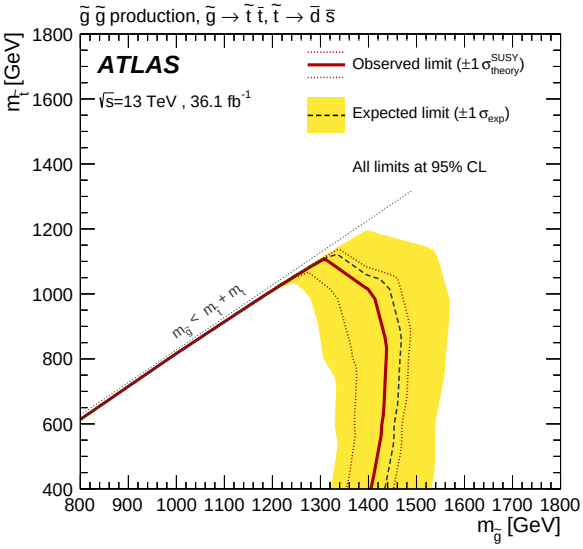

(b) $\widetilde{g} \to tsd$ scenario: Rpv2L1bH

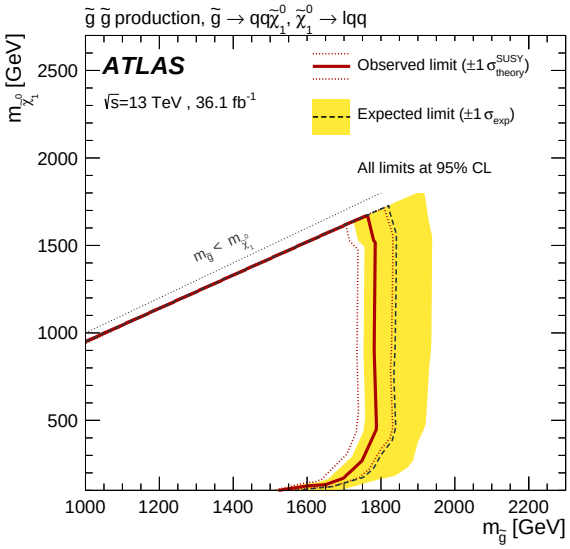

(c) $\widetilde{g} \to q\bar{q}\widetilde{\chi}_1^0$, $\widetilde{\chi}_1^0 \to q\bar{q}\ell$ scenario: Rpv2L0b

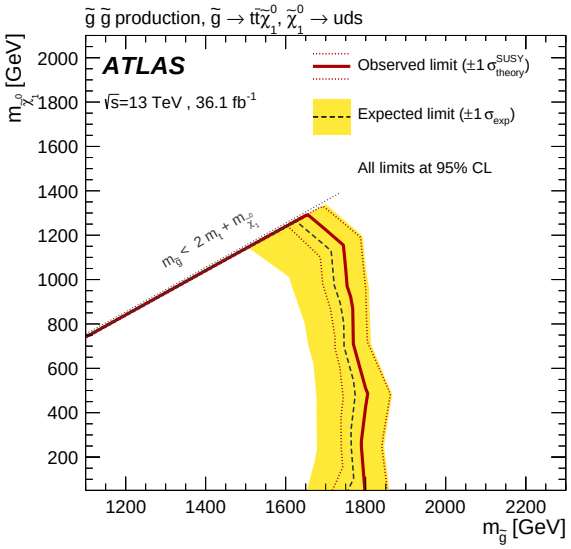

(d) $\widetilde{g} \to t\bar{t}\widetilde{\chi}_1^0$, $\widetilde{\chi}_1^0 \to uds$ scenario: Rpv2L2bH

Figure VIII.12.: Observed and expected exclusion limits on superpartner masses in the context of SUSY models featuring gluino pair production with RPV decay chains for 36.1 fb^{-1}. The limits are derived for the $\widetilde{g} \to tbd$ (a), $\widetilde{g} \to tsd$ (b), $\widetilde{g} \to q\bar{q}\widetilde{\chi}_1^0$, $\widetilde{\chi}_1^0 \to q\bar{q}\ell$ (c), and $\widetilde{g} \to t\bar{t}\widetilde{\chi}_1^0$, $\widetilde{\chi}_1^0 \to uds$ (d) scenario. The SRs used to obtain the limits are specified in the subtitles [8].

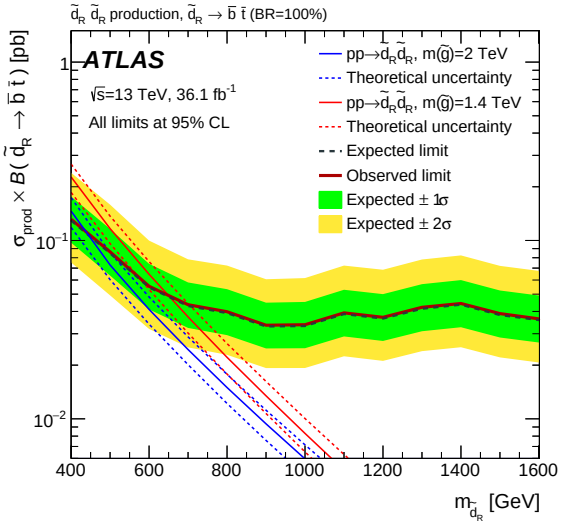

(a) $\widetilde{d_R} \to \bar{b}\bar{t}$ scenario: Rpv2L2bS

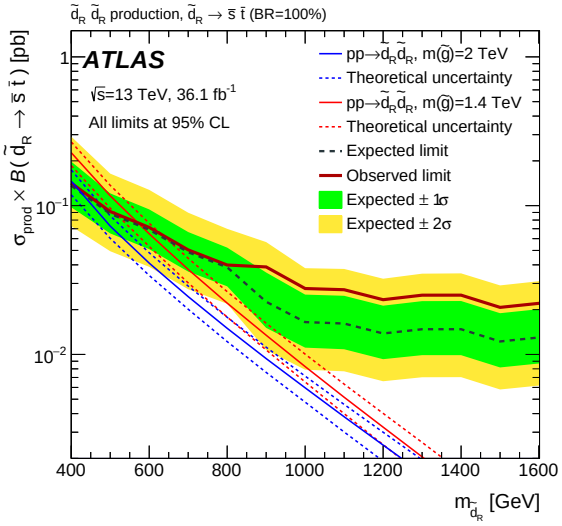

(b) $\widetilde{d_R} \to \bar{s}\bar{t}$ scenario: Rpv2L1bS(M)

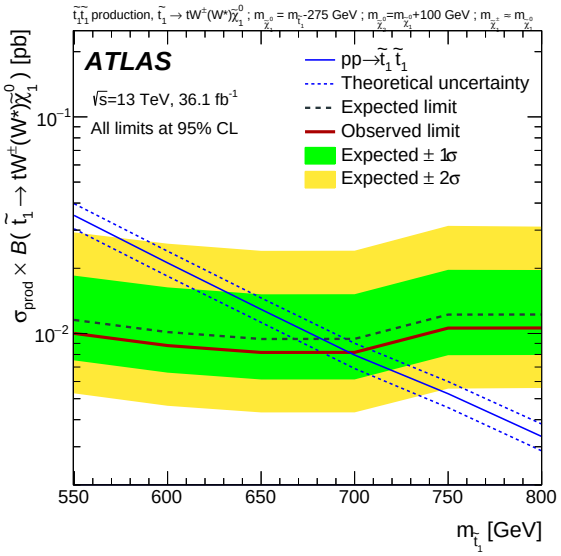

(c) $\widetilde{t}_1 \to t\,W^{\mp}W^{*}\,\widetilde{\chi}_1^0$ scenario: Rpc3LSS1b

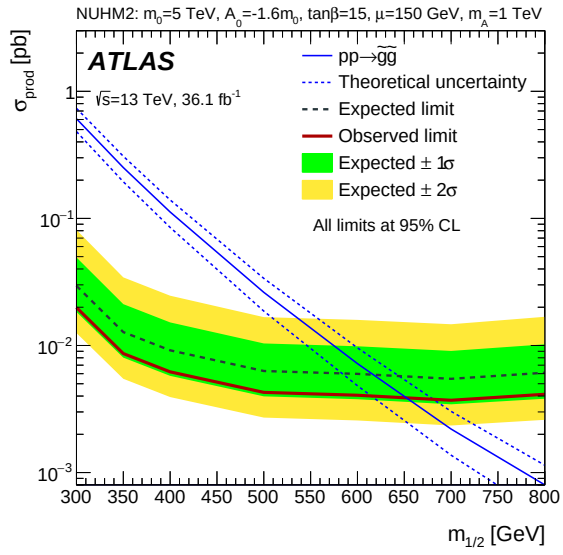

(d) NUHM2: Rpc2L2bH

Figure VIII.13.: Observed and expected upper limits on $\sigma_{\text{prod}} \times \text{BR}$ (in pb) for SUSY models featuring direct production right-handed down squarks with RPV decays, $\widetilde{d_R} \to \bar{b}\bar{t}$ (a) and $\widetilde{d_R} \to \bar{s}\bar{t}$ (b) as well as the $\widetilde{t}_1 \to t\,W^{\mp}W^{*}\,\widetilde{\chi}_1^0$ scenario (c) and the NUHM2 model (d). The uncertainty bands around the expected upper limit show the $\pm 1\,\sigma$ (green) and $\pm 2\,\sigma$ (yellow) variations. The SRs used to obtain the combined limits are specified in the subtitles [8].

IX. Analysis Prospects for the full Run II Data

After discussing the initial version of the same-sign/3L analysis restarted for Run II, as well as the updates and developments during the subsequent year, this chapter is dedicated to potential improvements and prospects of the search for the end of the Run II data taking.
Given the amount of data collected in 2016 and 2017, the most probable total integrated luminosity after the full Run II data taking will be around 120 fb^{-1}, as already outlined in Section IV.5. The perspectives and limitations of the analysis for this amount of data will be presented in the following sections.

IX.1. Evolution and Limitations of the Analysis Sensitivity

The evolution of the expected exclusion limits[1] for different luminosity values in the context of the four SUSY benchmark scenarios which have been utilized throughout all iterations of the analysis during Run II are shown in Figure IX.1 and IX.2. If available, also the according Run I limit is shown. The largest values of excluded gluino, neutralino, or bottom squark masses for each of the models and for the different luminosities are stated in Table IX.1.
In most cases, the best improvement could actually be achieved by updating the 3.2 fb^{-1} results to 13.2 fb^{-1}. Comparing the results obtained with 13.2 fb^{-1} and 36.1 fb^{-1} of data, the exclusion limits did not increase to a significant extent anymore. This is especially true for the $\widetilde{g} \to q\bar{q}(\ell\bar{\ell}/\nu\nu)\widetilde{\chi}_1^0$ and $\widetilde{g} \to q\bar{q}W^{\pm}Z\widetilde{\chi}_1^0$ models, where the expected exclusion limits on gluino and neutralino masses could only be improved by around 100 GeV, although the luminosity is almost three times higher. An exception is the limit evolution for the $\widetilde{b}_1 \to tW^{\pm}\widetilde{\chi}_1^0$ scenario, where the improvement for the full 2015+2016 dataset is still notable (most likely due to the changed SR strategy and the reduction of the uncertainties associated with the fake/non-prompt lepton background).
A possible reason for the apparent saturation of the $\widetilde{g} \to q\bar{q}(\ell\bar{\ell}/\nu\nu)\widetilde{\chi}_1^0$ and $\widetilde{g} \to q\bar{q}W^{\pm}Z\widetilde{\chi}_1^0$ limits is that the signal regions targeting these scenarios are typically dominated by diboson background, which has a large theoretical uncertainty limiting the sensitivity of the signal regions[2]. Obviously, this problem cannot be addressed by simply analyzing a larger amount of data. The uncertainty could potentially be reduced by relying on MC samples with improved simulations and lower inaccuracies of the Monte Carlo modeling. Another strategy is to use data to constrain the diboson background in dedicated regions with a high purity of this process (WZ, ZZ control regions). Implementations of control regions to constrain dominant background sources is a strategy commonly used in SUSY searches and could be beneficial also in the same-sign/3L case in order to rely not completely on Monte Carlo[3]. Similar methods could also be feasible to reduce uncertainties associated with the $t\bar{t}$+W/Z background, which could help to improve the sensitivity in regions with b-jet requirements. However, the definition of control regions with high $t\bar{t}$+W/Z purities is far more complicated, as it became apparent already while optimizing the $\mathrm{t\bar{t}W}$ and $\mathrm{t\bar{t}Z}$ validation regions presented in Section VIII.2.4.

[1] The intention of these plots is to show the limit evolution due to the optimization procedure and the development of the analysis techniques. Accordingly, only the expected limits are compared among each other.
[2] The theoretical diboson uncertainty is the dominant one in the signal regions with a b-jet veto Rpv2L0bS(H) and Rpc3L0bS(H). Its contribution to each of the SRs can be found in Appendix H.
[3] With CRs to constrain the WZ, ZZ background, the prediction in the SR is taken from the normalized MC. Thus, they can reduce normalization uncertainties. However, uncertainties attributed to the MC modeling have still be taken into account.

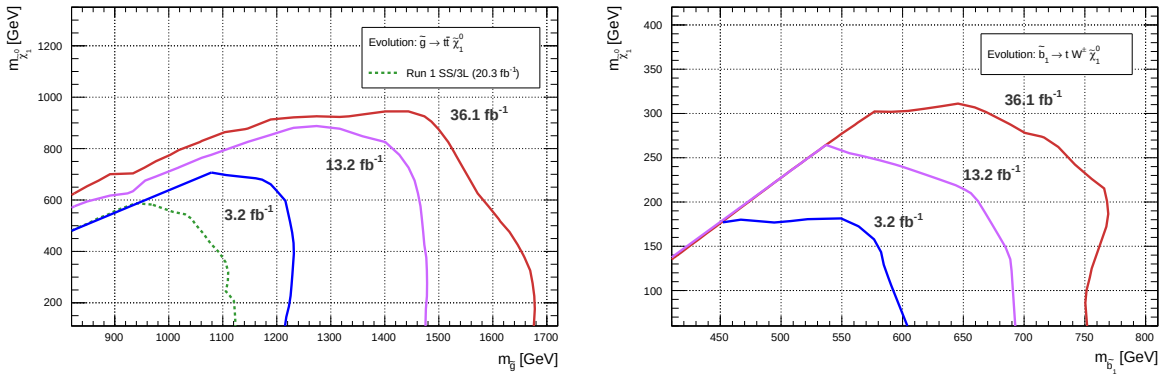

Figure IX.1.: Evolution of the expected exclusion limits for the $\widetilde{g} \to t\bar{t}\widetilde{\chi}_1^0$ (left) and $\widetilde{b}_1 \to tW^{\pm}\widetilde{\chi}_1^0$ (right) scenarios for the different luminosity values the analysis has been performed with. If available, the (expected) limits from the Run I SS/3L analysis are also shown.

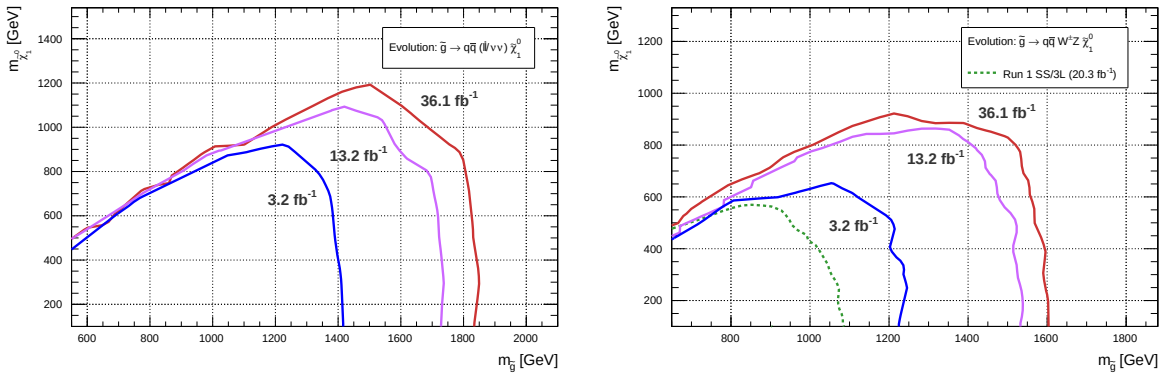

Figure IX.2.: Evolution of the expected exclusion limits for the $\widetilde{g} \to q\bar{q}(\ell\bar{\ell}/\nu\nu)\widetilde{\chi}_1^0$ (left) and $\widetilde{g} \to q\bar{q}W^{\pm}Z\widetilde{\chi}_1^0$ (right) scenarios for the different luminosity values the analysis has been performed with. If available, the (expected) limits from the Run I SS/3L analysis are also shown.

IX.2. EXPECTED RESULTS FOR FULL RUN II LUMINOSITY

IX.2.1. EXPECTED EVENT YIELDS IN SIGNAL AND VALIDATION REGIONS

Taking into account the performances of the LHC and the ATLAS experiment in the recent years 2016 and 2017, the total integrated luminosity after the full Run II data taking will be most likely around 120 fb^{-1} [149]. The expected event yields in the current validation and signal regions for this luminosity can be calculated to get a first impression of the contribution of prompt same-sign and three-lepton sources for this amount of recorded data.

Figure IX.3 and IX.4 show the expected event yields from prompt background processes in the validation and signal regions, as they were defined in Table VIII.1 and VIII.2, respectively. The dashed lines indicate the currently observed yields for 36.1 fb^{-1}. The contributions from reducible background processes (FNP leptons and charge-flip) are not included in these plots, as their evolution cannot properly be predicted for the end of Run II. Simply rescaling the predictions for 36.1 fb^{-1} to 120 fb^{-1} is probably an overestimation, since fake and charge-flip rates can most likely be further reduced with more elaborated object identification methods or enhanced selection tools[4]. The same applies also to the experimental

[4] As it has happened already in case of the electron charge ID tool, which could significantly reduce the charge-flip rates.

Model	3.2 fb^{-1}	13.2 fb^{-1}	36.1 fb^{-1}
	best exp. $m_{\tilde{g}}^{95}$ [GeV]		
$\tilde{g} \to t\bar{t}\tilde{\chi}_1^0$	1220 ± 50	1470 ± 100	1680 ± 100
$\tilde{g} \to q\bar{q}(\ell\bar{\ell}/\nu\nu)\tilde{\chi}_1^0$	1420 ± 50	1740 ± 100	1860 ± 100
$\tilde{g} \to q\bar{q}W^{\pm}Z\tilde{\chi}_1^0$	1250 ± 50	1540 ± 100	1600 ± 100
	best exp. $m_{\tilde{b}_1}^{95}$ [GeV]		
$\tilde{b}_1 \to tW^{\pm}\tilde{\chi}_1^0$	605 ± 60	690 ± 60	770 ± 60
	best exp. $m_{\tilde{\chi}_1^0}^{95}$ [GeV]		
$\tilde{g} \to t\bar{t}\tilde{\chi}_1^0$	700 ± 50	900 ± 50	950 ± 70
$\tilde{g} \to q\bar{q}(\ell\bar{\ell}/\nu\nu)\tilde{\chi}_1^0$	920 ± 70	1100 ± 100	1200 ± 100
$\tilde{g} \to q\bar{q}W^{\pm}Z\tilde{\chi}_1^0$	620 ± 50	870 ± 50	900 ± 100
$\tilde{b}_1 \to tW^{\pm}\tilde{\chi}_1^0$	180 ± 50	260 ± 50	310 ± 60

Table IX.1.: Largest values of excluded gluino, neutralino, or bottom squark masses (computed at 95% CL_s) for each of the four benchmark scenarios and for different luminosities. The uncertainties of the results correspond to the $\pm 1\,\sigma$ variations of the exclusion limit (yellow band) at that point.

systematic uncertainties, where extrapolating the current values to 120 fb^{-1} is probably a too conservative approach. Thus, the predictions made for the full Run II luminosity include only theoretical and statistical uncertainties of the Monte Carlo samples used. Their relative contributions (σ_{SM}/SM) are shown in the bottom panel. Furthermore, it has to be emphasized that most likely a re-optimization of the signal regions for 120 fb^{-1} will be performed for any future release of the analysis. The event yields presented here should rather be regarded as preliminary indicator and benchmark for future optimization studies.

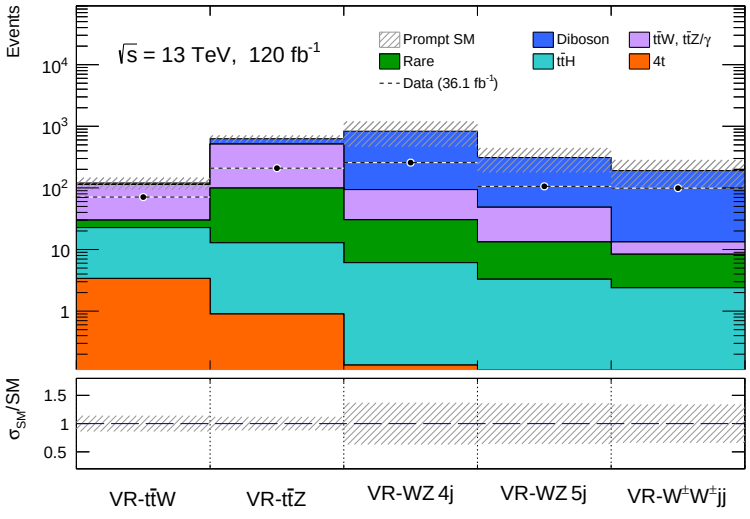

Figure IX.3.: Expected event yields for 120 fb^{-1} in the validation regions, as they were designed in 2016. The reducible background processes are not included since their evolution cannot be predicted for the end of Run II. The dashed lines indicate the currently observed yields for 36.1 fb^{-1}. The bottom panel shows the relative uncertainties (only theoretical and statistical) for each SR.

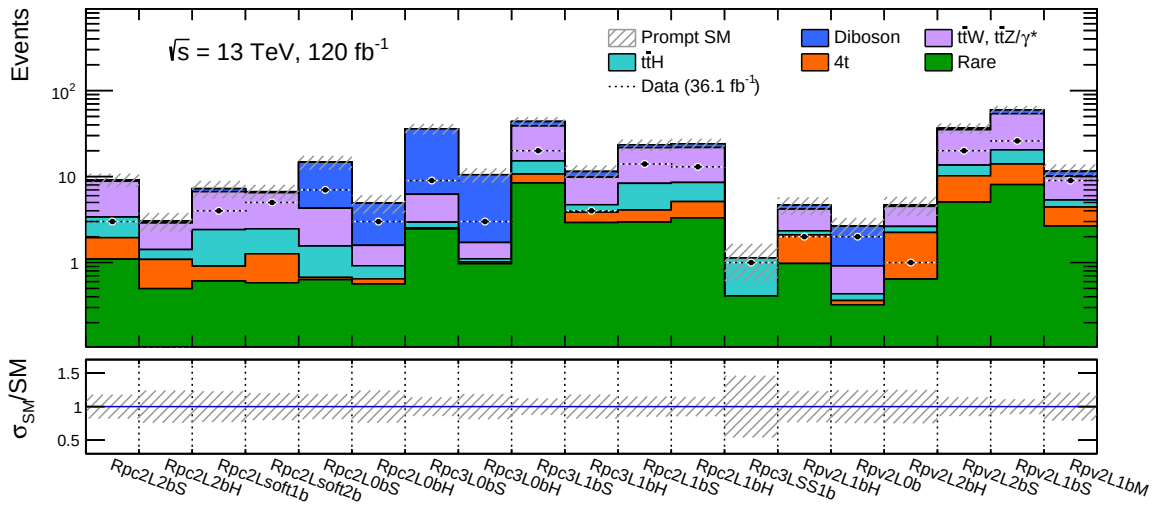

Figure IX.4.: Expected event yields in the 2016 signal regions for 120 fb^{-1}. The reducible background processes are not included since their evolution cannot be predicted for the end of Run II. The dashed lines indicate the currently observed yields for 36.1 fb^{-1}. The bottom panel shows the relative uncertainties (only theoretical and statistical) for each SR.

IX.2.2. EXPECTED EXCLUSION LIMITS FOR RUN II

Besides the predicted event yields, also the expected exclusion limits for an integrated luminosity of 120 fb^{-1} can be computed to evaluate the sensitivity of the current signal regions to the various SUSY scenarios for the full Run II data.

The expected limits are calculated under the same assumptions as the event yields were obtained: considering only prompt SS/3L sources and taking into account only theoretical as well as statistical uncertainties. The interpretations are done in the context of the same twelve signal processes as for the most recent version of the analysis. The SR strategy for these models is also adopted from the previous version. The two-dimensional exclusion limits (at 95% CL$_s$) on neutralino, gluino, and squark masses are presented in Figure IX.5 and IX.6. The expected upper limits on $\sigma_{\text{prod}} \times \text{BR}$ for the signals simulated with only one free parameter are shown in Figure IX.7. Observed limits from previous analysis versions (3.2 fb^{-1} in blue, 36.1 fb^{-1} in violet) are superimposed to get a better impression of the limit evolution.

The results show that the present exclusion limits can still be moderately improved by just taking advantage of the additional data collected until the end of Run II. Also these results can obviously only be considered as a first benchmark for more refined optimization studies. The assumptions made to obtain these limits might lead to too optimistic (no systematic uncertainties) or too pessimistic (using SRs optimized for 36.1 fb^{-1}) results. In particular, the expected limits obtained from SRs which have typically large contributions of reducible background sources[5], as it is the case for the $\widetilde{b}_1 \to t\,W^{\pm}\,\widetilde{\chi}_1^0$ model (Figure IX.5b) or the $\widetilde{d}_R \to \bar{b}\,\bar{t}$ scenario (Figure IX.7a) might be overestimated. On the other hand, limits derived from signal regions dominated by prompt SS/3L sources, like the limit on the $\widetilde{g} \to q\bar{q}\,(\ell\bar{\ell}/\nu\nu)\,\widetilde{\chi}_1^0$ (Figure IX.5c) or the $\widetilde{g} \to t\bar{t}\,\widetilde{\chi}_1^0$, $\widetilde{\chi}_1^0 \to uds$ (Figure IX.6d) model, can provide a more realistic (or even conservative) indication of the analysis potential for the full Run II data.

[5] Considering the background composition for 36.1 fb^{-1} as benchmark.

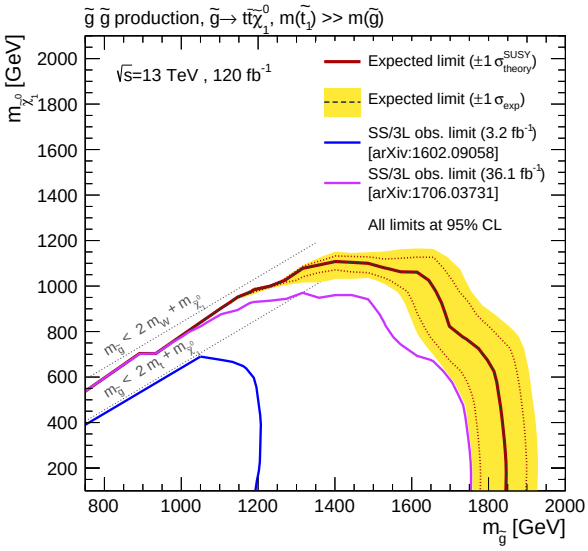

(a) $\widetilde{g} \to t\bar{t}\,\widetilde{\chi}_1^0$ scenario: Rpc2L2bS(H), Rpc2Lsoft1b(2b)

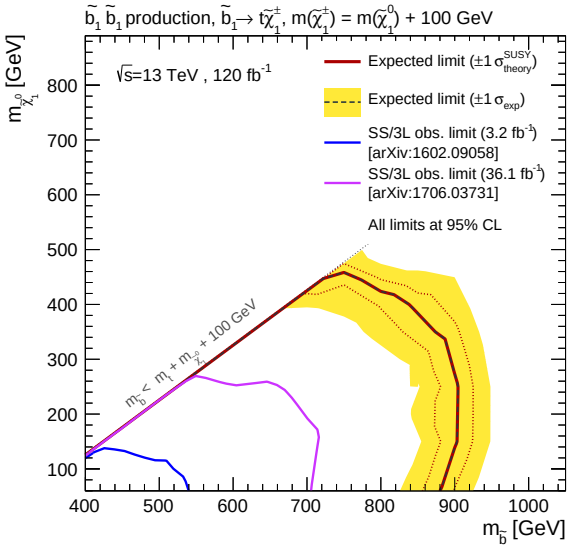

(b) $\widetilde{b}_1 \to t\,W^{\pm}\,\widetilde{\chi}_1^0$ scenario: Rpc2L1bS(H)

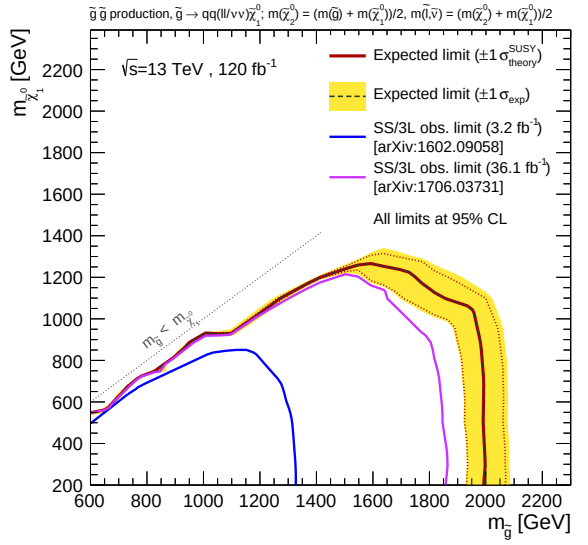

(c) $\widetilde{g} \to q\bar{q}\,(\ell\bar{\ell}/\nu\nu)\,\widetilde{\chi}_1^0$ scenario: Rpc3L0bS(H)

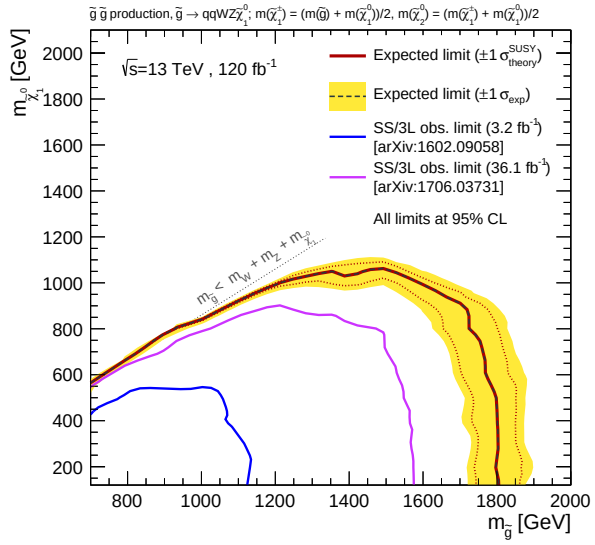

(d) $\widetilde{g} \to q\bar{q}\,W^{\pm}Z\,\widetilde{\chi}_1^0$ scenario: Rpc2L0bS(H)

Figure IX.5.: Expected exclusion limits on the mass of $\widetilde{\chi}_1^0$ as function of the gluino or light bottom squark mass in the context of the four initial RPC SUSY scenarios for a luminosity of 120 fb^{-1}. The limits are derived for the $\widetilde{g} \to t\bar{t}\,\widetilde{\chi}_1^0$ (a), $\widetilde{b}_1 \to t\,W^{\pm}\,\widetilde{\chi}_1^0$ (b), $\widetilde{g} \to q\bar{q}\,(\ell\bar{\ell}/\nu\nu)\,\widetilde{\chi}_1^0$ (c), and $\widetilde{g} \to q\bar{q}\,W^{\pm}Z\,\widetilde{\chi}_1^0$ (d) scenario. The SRs used to obtain the combined limits (specified in the subtitles) are the same as for the 2016 version of the analysis. The violet lines indicate the previously observed limits for 36.1 fb^{-1}.

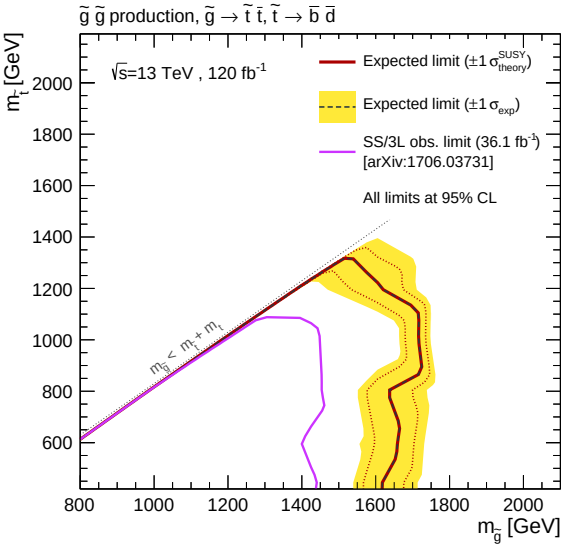

(a) $\widetilde{g} \to tbd$ scenario: Rpv2L1bH

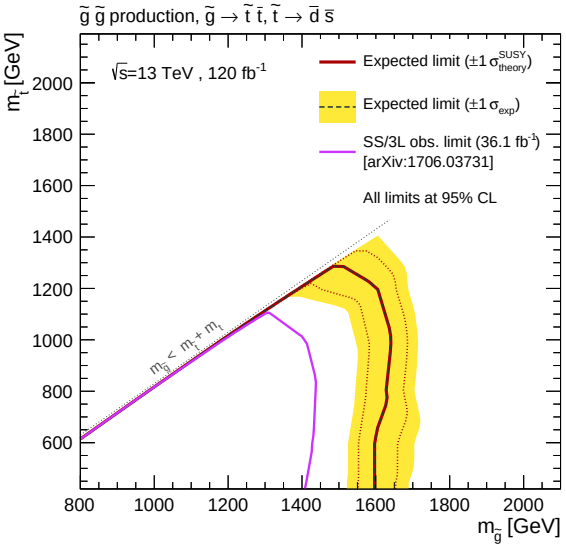

(b) $\widetilde{g} \to tsd$ scenario: Rpv2L1bH

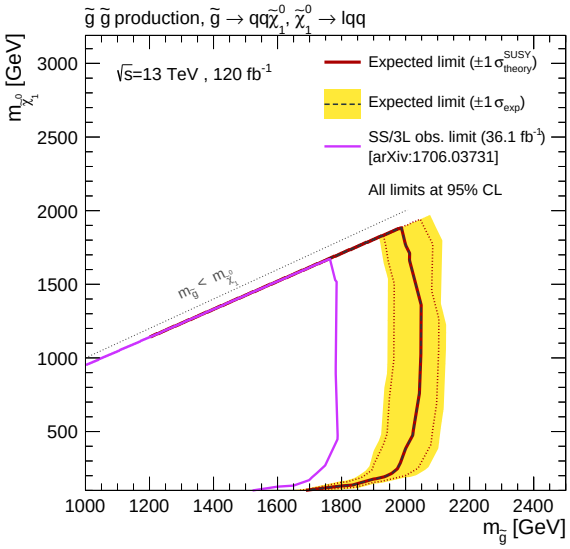

(c) $\widetilde{g} \to q\bar{q}\widetilde{\chi}_1^0$, $\widetilde{\chi}_1^0 \to q\bar{q}\ell$ scenario: Rpv2L0b

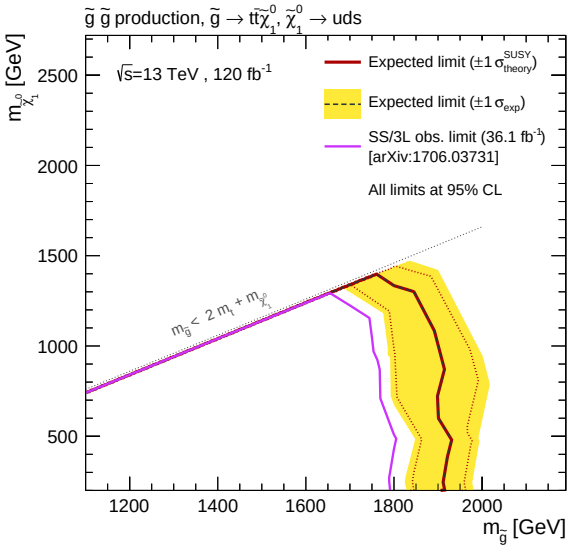

(d) $\widetilde{g} \to t\bar{t}\widetilde{\chi}_1^0$, $\widetilde{\chi}_1^0 \to uds$ scenario: Rpv2L2bH

Figure IX.6.: Expected exclusion limits on superpartner masses in the context of SUSY models featuring gluino pair production with RPV decay chains for a luminosity of 120 fb^{-1}. The limits are derived for the $\widetilde{g} \to tbd$ (a), $\widetilde{g} \to tsd$ (b), $\widetilde{g} \to q\bar{q}\widetilde{\chi}_1^0$, $\widetilde{\chi}_1^0 \to q\bar{q}\ell$ (c), and $\widetilde{g} \to t\bar{t}\widetilde{\chi}_1^0$, $\widetilde{\chi}_1^0 \to uds$ (d) scenario. The SRs used to obtain the limits (specified in the subtitles) are the same as for the 2016 version of the analysis. The violet lines indicate the previously observed limits for 36.1 fb^{-1}.

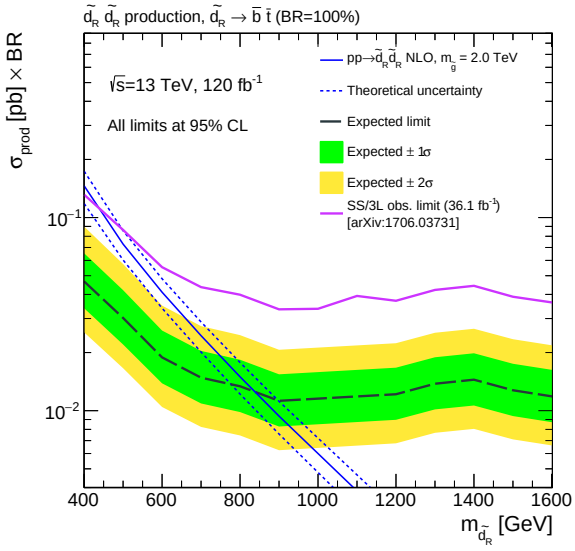

(a) $\widetilde{d}_R \to \bar{b}\bar{t}$ scenario: Rpv2L2bS

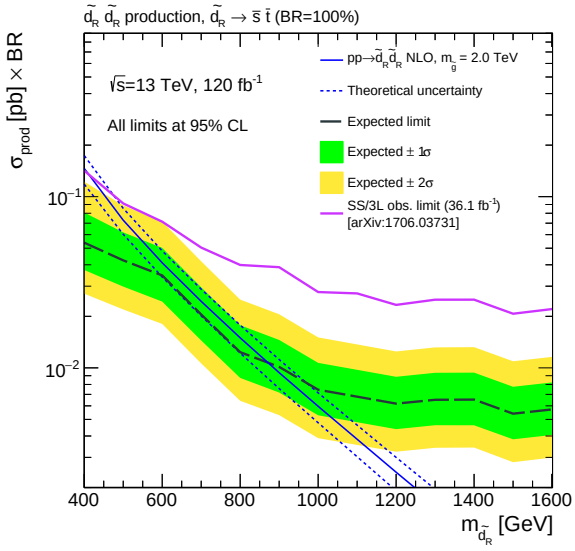

(b) $\widetilde{d}_R \to \bar{s}\bar{t}$ scenario: Rpv2L1bS(M)

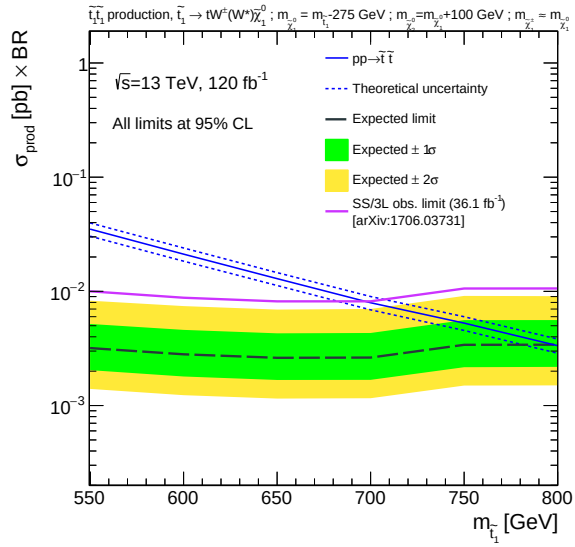

(c) $\widetilde{t}_1 \to t\,W^{\mp}W^{*}\,\widetilde{\chi}_1^0$ scenario: Rpc3LSS1b

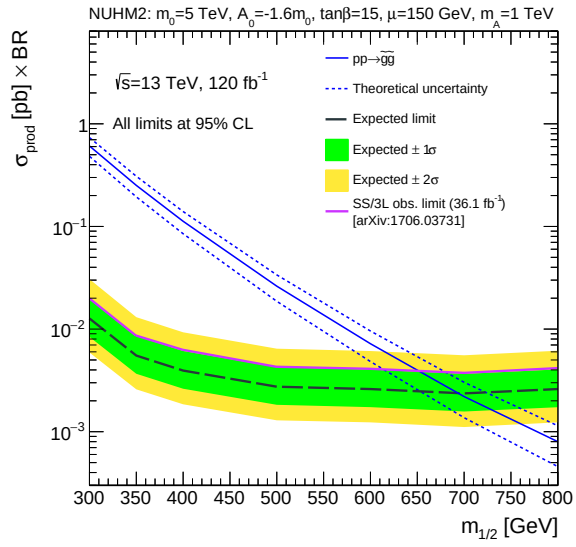

(d) NUHM2: Rpc2L2bH

Figure IX.7.: Expected upper limits on $\sigma_{\text{prod}} \times \text{BR}$ (in pb) for the $\widetilde{d}_R \to \bar{b}\bar{t}$ (a), $\widetilde{d}_R \to \bar{s}\bar{t}$ (b), $\widetilde{t}_1 \to t\,W^{\mp}W^{*}\,\widetilde{\chi}_1^0$ (c), and the NUHM2 (d) model for a luminosity of 120 fb^{-1}. The SRs used to obtain the combined limits (specified in the subtitles) are the same as for the 2016 version of the analysis. The violet lines indicate the previously observed limits for 36.1 fb^{-1}.

IX.3. FURTHER CHALLENGES AND PERSPECTIVES

Some problems limiting the sensitivity of the same-sign/3L search in the past have been raised already in Section IX.1. Many other aspects how future work could improve the analysis are conceivable. Some of them are mentioned here:

- **Background estimation:**

  Besides the implementation of control regions for the dominant prompt SS/3L background sources to constrain their uncertainties, the large uncertainties associated with the data-driven methods have to be reduced to achieve a more precise prediction in the signal regions enriched with fake/non-prompt leptons or the charge-flip background. Especially in the regions with b-jet requirements, the contributions from FNP leptons build typically the largest backgrounds and their relative uncertainties amount to 15–40%, depending on the SR (see Appendix H).

  This problem can either be addressed by trying to mitigate the contribution from the reducible background sources in the SRs (e.g. by an improved object identification) or with a more accurate prediction from the data-driven methods, for instance with better fake rate measurements or by combining independent background estimation methods. An ABCD method[6] as alternative to the matrix and MC template method to estimate the fake/non-prompt lepton contributions in the SRs was tested already in 2016 and provided results consistent with the other approaches. Also, several alternative methods exist to estimate the background coming from charge-flip electrons. Alternative techniques could be utilized not only to validate the nominal methods, but also to provide a more precise combined prediction for the reducible background processes. Furthermore, a more advanced usage of BDT-based techniques for the background reduction can be considered.

- **Signal region strategy:**

  Besides an improved background estimation, the analysis can also be revisited in terms of the signal region strategy. While the Run I SS/3L analysis used signal regions binned in different m_{eff} ranges to derive discovery and exclusion limits on the signal scenarios, in the Run II version discussed in this thesis, inclusive SRs were used to present the final results as well as for setting model-dependent limits. Since the former signal region strategy of the SS/3L analysis was to use very stringent selection requirements in order to keep the expected event yields small, binned signal regions would have led to large statistical uncertainties in each SR attenuating the overall sensitivity of the analysis. Relaxing the total kinematic requirements in each SR selection and binning them in different m_{eff}, $E_{\text{T}}^{\text{miss}}$, or N_{jets} ranges instead, was tried already in 2016 and was found to have no sizable effect on the final analysis result. However, with the increased amount of data collected at the end of Run II, this approach might be helpful, at least to obtain better exclusion limits than it was possible by only using inclusive signal regions.

  Also using additional kinematic or event shape variables could enhance the sensitivity to various models. Thus, they are certainly worth being revisited for any further version of the analysis.

- **Model-dependent interpretations:**

  As it was demonstrated already throughout the previous chapters, the same-sign/3L analysis is sensitive to a large variety of supersymmetric scenarios. In addition to the strong production

[6] The ABDC method relied on control regions defined by inverting the $E_{\text{T}}^{\text{miss}}$ requirement in the SRs. For the FNP lepton prediction in the signal region, a SR/CR transfer factor was applied using data events with the same kinematic requirements as in the CR and SR but only at least one signal lepton (and one proxy object for the FNP lepton).

modes of SUSY particles (via squarks and gluinos) that have been investigated in this analysis, also electroweak production of superpartners can potentially lead to same-sign or three-lepton final states [217]. Although scenarios featuring strong production have in general higher cross-sections at the LHC than electroweak processes, direct production of electroweak SUSY particles might dominate for cases where the masses of gluinos and squarks are significantly larger and therefore inaccessible with the current center-of-mass energy. Besides supersymmetry, this event signature is present in many other BSM scenarios, such as seesaw models (see Section II.2.5), models featuring the production of vector-like quarks, or scenarios with universal extra dimensions [218–220]. Models predicting the occurrence of doubly charged Higgs bosons in the context of different BSM theories can also create final states with same-sign leptons [221]. Obviously, dedicated signal regions have to be designed to obtain a viable sensitivity to these models, but in principle all of them are possible scenarios that can be explored in the context of SS/3L searches. Including some of these scenarios for future releases of the analysis could be helpful to increase the scope of the search and to make it more meaningful, also for a theoretical evaluation of the results.

Another possible way to interpret the analysis results is to use them for a dedicated scan on the full pMSSM parameter space (defined in Section II.1.6), as it has been performed already after Run I [188]. This will probably be done after finalizing the Run II data taking and for the combined results from different SUSY searches, to investigate regions of the pMSSM parameter space that were not explored yet. In this context, the results from the SS/3L analysis represent an important piece to achieve sensitivity for the compressed points of the pMSSM spectrum.

X. Conclusions

The analysis described in this thesis is a search for supersymmetric phenomena in final states with either two leptons of the same electric charge or three leptons, together with jets and missing transverse energy. It was performed with data collected by the ATLAS experiment coming from proton-proton collisions at a center-of-mass energy of $\sqrt{s}$ = 13 TeV. Several updated versions of this analysis were conducted since the beginning of the Run II data taking.

The first resumption of this search after Run I was performed with an integrated luminosity of 3.2 fb^{-1}, utilizing four signal regions optimized for different supersymmetric benchmark scenarios with same-sign or three-lepton signatures in the final states. Besides the common same-sign or three-lepton requirement, the regions were based on cuts on the missing transverse energy, the effective mass, as well as number and p_{T} of the additional jets and b-jets in the events. As no significant deviations from the Standard Model predictions have been observed in any of the signal regions, model-independent limits on potential BSM contributions as well as model-dependent exclusion limits in the context of the four corresponding benchmark models have been derived. This analysis built the template for subsequent updates and improved versions of the search using the data collected during the year 2016. An intermediate update with 13.2 fb^{-1} of data was performed in the middle of 2016 to show the increase of the sensitivity and to introduce improvements regarding the object identification and the signal region strategy.

The most recent version of the analysis was done with the full datasets from 2015 and 2016, corresponding to a total integrated luminosity of 36.1 fb^{-1}. In addition to a full re-optimization of the signal regions to account for the increased amount of data, new supersymmetric signal scenarios leading to final states with same-sign lepton pairs or three leptons have been introduced and new signal regions dedicated to these processes have been added to the search. In particular signal regions and interpretations in the context of models with R-parity violating decays of the superpartners were introduced, since the small Standard Model background for same-sign or three-lepton events allows the analysis to be sensitive also to this class of supersymmetric scenarios. A signal region based on a unique topology of three leptons with the same electric charge, without any additional kinematic requirement, was designed to target top squark pair production. In total, 19 partially overlapping signal regions inspired by twelve different supersymmetric scenarios have been examined. Furthermore, various improvements concerning the object selection, the trigger strategy, and the background estimation have been implemented to enhance the analysis sensitivity. In this regard, one has to emphasize new methods to mitigate reducible background sources, such as the improved electron selection utilizing the charge ID selector tool or the reduction of systematic uncertainties, as it is done with the combination of the matrix and the Monte Carlo template method to provide a more reliable and precise prediction of the fake/non-prompt lepton background. Also in this version of the analysis, no significant deviations from the Standard Model predictions were observed in any of the signal regions. Consequently, model-independent upper limits and model-dependent exclusion limits for the various models have been placed.

For the simplified R-parity conserving SUSY models featuring gluino pair production, gluino masses up to 1.87 TeV and neutralino masses up to 1.2 TeV were excluded at 95% confidence level. For the RPC models featuring direct production of bottom or top squarks, squark masses below 700 GeV were also excluded. In R-parity violating scenarios, the 95% exclusion limits reached gluino masses of about 1.8 TeV, neutralino masses of 1.3 TeV, and top squark masses of 1.1 TeV. In RPV SUSY models featuring direct production of right-handed down squark pairs, squark masses were probed up to 500 GeV. For the two-extra-parameter non-universal Higgs model (NUHM2), the results allowed to exclude values of the $m_{1/2}$ parameter below 650 GeV, corresponding to a gluino mass of around 1.6 TeV.

The progress achieved between the initial Run II version of the search and the current status of the analysis can be especially demonstrated by looking at the evolution of the exclusion limits on the masses of superpartners for the four SUSY benchmarks models, which have gone through all iterations of this analysis during the last two years. For the models featuring gluino pair production, the exclusion limits on gluino and neutralino masses were increased by 400–500 GeV, comparing the results obtained for 3.2 fb^{-1} and 36.1 fb^{-1} of data. For the scenario featuring direct production of bottom squarks, the limit on the squarks masses improved by around 150 GeV. Also in very compressed SUSY mass spectra, important achievements could be rendered, especially in terms of the increased sensitivity to the $\widetilde{g} \to t\bar{t}\widetilde{\chi}_1^0$ scenario with $t \to bW^{\pm}$ decays via off-shell top quarks (a kinematic region which was not accessible by any other analysis doing interpretations in the context of these models before). Considering the fact that even the initial Run II version of the analysis was capable of improving the latest results from Run I significantly, the development of the search within the recent years is remarkable and shows the intense effort applied on many different aspects of the analysis. Comparing the results of the same-sign/three-lepton analysis with other searches for supersymmetric phenomena in distinct final states, the unique potential of exploring this event signature, in particular for supersymmetric scenarios with compressed mass spectra, becomes apparent. Thus, it also complements other searches for squarks and gluinos that are more dedicated to higher kinematic regions targeting large mass splittings between the superpartners, as well as analyses motivated especially by R-parity violating SUSY scenarios.

The prospects and limitations of the analysis for the end of Run II have been evaluated assuming a total integrated luminosity of 120 fb^{-1}, which is the most likely value given the amount of data collected in 2016 and 2017. The studies showed that some of the present exclusion limits can still be moderately improved by simply analyzing a larger amount of data. However, a refined re-optimization of the signal regions is essential to exploit the full potential of the search. Also additional limiting aspects, such as the large theoretical uncertainties of the prompt same-sign/three-lepton background or the large uncertainties associated with the data-driven techniques, need to be reduced in order to obtain significant improvements with respect to the current performance. Some other challenges and projects which could be beneficial for future releases of the analysis have been briefly discussed.

Although it was not possible to find evidence for supersymmetry or to observe any indication for physics beyond the Standard Model, the achievements of this search during the past two years are noteworthy. The analysis could be improved in many crucial aspects and a lot of interesting regions of the supersymmetric parameter space were explored. Accordingly, the same-sign/three-lepton analysis has been established as one of the most sensitive SUSY searches in Run II and represents now an important field among the searches for new physics at the ATLAS experiment.

APPENDIX

Details about various topics related to the analysis which did not have a crucial impact on the main results are briefly presented in this Appendix. Also auxiliary material about the different versions of the analysis can be found here.

A: LIST OF DATA AND MONTE CARLO SAMPLES

A complete list of all data and simulated background samples used in the most recent version of the analysis is presented in the Tables A.1 and A.2. The signal samples are produced with the ATLASFASTII simulation and summarized in Table A.3. The total integrated luminosity for the 2015 data samples amounts to 3.2 fb^{-1}, while for all samples listed in the table (2015+2016), it is 36.1 fb^{-1}.
For the simulated samples also more specific information is given, such as the generator cross-sections (times branching ratios), the k-factors of the processes, the efficiencies ε_{f} of samples with an event filter applied, and the virtual luminosity L_{vir} (corresponding to the number of generated events N_{gen}).

Year	Data sample	Run range	N_{events}
2015	`data15_13TeV.periodD`	276262−276954	138674593
2015	`data15_13TeV.periodE`	278748−279928	211476524
2015	`data15_13TeV.periodF`	279932−280368	128666156
2015	`data15_13TeV.periodG`	280423−281075	268772059
2015	`data15_13TeV.periodH`	281130−281411	189929882
2015	`data15_13TeV.periodJ`	282631−284484	486875844
2016	`data16_13TeV.periodA`	296939−300287	361236098
2016	`data16_13TeV.periodB`	300345−300908	369173081
2016	`data16_13TeV.periodC`	301912−302393	623945258
2016	`data16_13TeV.periodD`	302737−303499	755068142
2016	`data16_13TeV.periodE`	303638−303892	295672990
2016	`data16_13TeV.periodF`	303943−304494	443266046
2016	`data16_13TeV.periodG`	305291−306714	511334552
2016	`data16_13TeV.periodI`	307124−308084	739289024
2016	`data16_13TeV.periodK`	309311−309759	319067464
2016	`data16_13TeV.periodL`	310015−311481	838918533

Table A.1: List of all 2015 and 2016 data samples used in the most recent version of the analysis. The table shows the sample names (data taking periods), the according run ranges and the stored data events. The total integrated luminosity is 3.2 fb^{-1} for the 2015 samples and 36.1 fb^{-1} for all the samples in the table.

Process	Monte Carlo ID	$\sigma \times$ BR [pb]	k-factor	ε_f [%]	N_{gen}	L_{vir} [nb^{-1}]
$t\bar{t}$+W	410155	0.54830	1.10	100	7492900	12423.4
$t\bar{t}$+WW	410081	0.0081	1.22	100	50000	5059.1
$t\bar{t}$+Z ($Z \to ee$)	410218	0.03689	1.12	100	140880	34097.5
$t\bar{t}$+Z ($Z \to \mu\mu$)	410219	0.03689	1.12	100	1409600	34116.9
$t\bar{t}$+Z ($Z \to \tau\tau$)	410220	0.03660	1.12	100	934300	22792.3
$t\bar{t}$+WZ	407321	0.00027	1.34	100	60000	168067.2
tZ	410050	0.25013	1.00	100	997200	4152.8
$tW^{\pm}Z$	410215	0.01558	1.00	100	88000	5656.3
$tt\bar{t}$ (3-top)	304014	0.00164	1.00	100	200000	121951.2
$t\bar{t}t\bar{t}$ (4-top)	410080	0.00916	1.00	100	198800	21703.1
$t\bar{t}$+H ($H \to \ell\ell\ell\ell$)	343365	0.05343	1.00	100	4895000	91615.2
$t\bar{t}$+H ($H \to \ell\ell qq$)	343366	0.22276	1.00	100	4904000	22014.7
$t\bar{t}$+H ($H \to qqqq$)	343367	0.23082	1.00	100	4534000	19643.0
W+H	342284	1.10210	1.25	100	99400	72.2
Z+H	342285	0.60072	1.45	100	99200	113.9
$ZZ \to \ell\ell\ell\ell$	363490	1.25570	1.00	100	17825300	14195.5
	361072	0.03150	0.91	100	60000	2093.1
	361073	0.02095	0.91	100	502000	26331.7
$WZ \to \ell\ell\ell\nu$	363491	4.58770	1.00	100	15772084	3437.9
	361071	0.04229	0.91	100	978000	25413.2
$W^{\pm}W^{\pm} \to \ell^{\pm}\ell^{\pm}\nu\nu jj$	361069	0.02576	0.91	100	492000	20988.3
	361070	0.04337	0.91	100	488000	12364.9
WWW	361620	0.00834	1.00	100	59800	7170.3
WWZ	361621	0.00173	1.00	100	59600	34450.9
	361622	0.00343	1.00	100	59800	17434.4
WZZ	361623	0.00022	1.00	100	49800	226363.6
	361624	0.00192	1.00	44.4	49800	58365.2
ZZW	361625	0.00002	1.00	100	35000	1750000.0
	361626	0.00044	1.00	22.5	34600	348874.4
	361627	0.00045	1.00	44.8	35000	173572.4
$W^{\pm}W^{\pm}$ (DPS)	407309	0.03404	1.00	100	95000	2790.7

Table A.2: List of all simulated Monte Carlo samples used to model the prompt SS/3L background. The table shows the simulated physics processes, the IDs of the according MC samples, the generator cross-sections times branching ratios of the decays ($\sigma \times$ BR), the k-factors and filter efficiencies ε_f, the number of generated events N_{gen}, and the equivalent virtual luminosities L_{vir} (in nb^{-1}).

Signal scenario	Samples	Monte Carlo IDs	N_{gen}
$\widetilde{g} \to t\bar{t}\,\widetilde{\chi}_1^0$	164	370100−370249 373421−373448	100000
$\widetilde{b}_1 \to tW^{\pm}\widetilde{\chi}_1^0$	69	372300−372368	10000
$\widetilde{g} \to q\bar{q}W^{\pm}Z\widetilde{\chi}_1^0$	118	371200−371317	20000
$\widetilde{g} \to q\bar{q}\,(\ell\bar{\ell}/\nu\nu)\,\widetilde{\chi}_1^0$	96	372444−373478	50000
$\widetilde{t}_1 \to tW^{\mp}W^{*}\widetilde{\chi}_1^0$	9	388230−388238	5000
$\widetilde{g} \to t\bar{t}\,\widetilde{\chi}_1^0,\ \widetilde{\chi}_1^0 \to uds$	58	403110−403176	10000
$\widetilde{g} \to q\bar{q}\,\widetilde{\chi}_1^0,\ \widetilde{\chi}_1^0 \to q\bar{q}\ell$	56	403693−404425	10000
$\widetilde{g} \to tsd$	28	403426−403453	20000
$\widetilde{g} \to tbd$	28	403454−403481	20000
$\widetilde{d}_R \to \bar{s}\bar{t}$	15	403380−403394	20000
$\widetilde{d}_R \to \bar{b}\bar{t}$	15	403395−403409	20000
NUHM2	7	370600−370606	50000

Table A.3: List of simulated samples for the SUSY signal model grids. The table shows the signal scenarios, the numbers of available samples for each grid, the ranges of Monte Carlo IDs, and the average number of generated events N_{gen} per signal sample. The cross-sections depend on the mass parameters of the SUSY particles and are obtained from [199].

B: DETAILS ON THE INTERMEDIATE ANALYSIS UPDATE IN 2016

The intermediate update of the analysis with 13.2 fb^{-1} of data included a set of re-optimized and new signal regions, as well as an extended interpretation of the results in the context of additional RPV SUSY models. Since these scenarios are also addressed in the final version with 36.1 fb^{-1} of data, the limits obtained in the intermediate results were not shown in the main part of this thesis.

The signal regions used for this update are summarized in Table B.1. Besides the same-sign or 3L selection, they include requirements on the number of jets N_{jets}, b-jets $N_{b\text{-jets}}$, the transverse momenta of the jets $p_{\text{T}}^{\text{jet}}$, m_{eff}, and $E_{\text{T}}^{\text{miss}}$. The SRs for the RPV scenarios do not have $E_{\text{T}}^{\text{miss}}$ requirements but more stringent cuts on m_{eff} and N_{jets} instead. For the SRs targeting the $\widetilde{d}_R \to \bar{b}\bar{t}$ and $\widetilde{d}_R \to \bar{s}\bar{t}$ models, only negatively charged lepton pairs were selected (indicated as N^-). The numbers of observed and expected events in the signal regions are listed in Table B.2. No significant disagreement between data and the predicted SM background was observed in any of the signal regions.

Signal region	N_ℓ^{signal}	N_{jets}	$p_{\text{T}}^{\text{jet}}$ [GeV]	$N_{b\text{-jets}}^{20}$	$E_{\text{T}}^{\text{miss}}$ [GeV]	m_{eff} [GeV]	Targeted signal
SR1b	≥ 2	≥ 6	> 25	≥ 1	> 200	> 650	$\widetilde{b}_1 \to t W^{\pm} \widetilde{\chi}_1^0$
SR3b	≥ 2	≥ 6	> 25	≥ 3	> 150	> 600	$\widetilde{g} \to t\bar{t} \widetilde{\chi}_1^0$
SR0b1	≥ 2	≥ 6	> 25	$= 0$	> 150	> 500	$\widetilde{g} \to q\bar{q} W^{\pm} Z \widetilde{\chi}_1^0$
SR0b2	≥ 2	≥ 6	> 40	$= 0$	> 150	> 900	$\widetilde{g} \to q\bar{q} W^{\pm} Z \widetilde{\chi}_1^0$
SR3L1	≥ 3	≥ 4	> 40	$= 0$	> 150	–	$\widetilde{g} \to q\bar{q} (\ell\bar{\ell}/\nu\nu) \widetilde{\chi}_1^0$
SR3L2	≥ 3	≥ 4	> 40	$= 0$	> 200	> 1500	$\widetilde{g} \to q\bar{q} (\ell\bar{\ell}/\nu\nu) \widetilde{\chi}_1^0$
SR1b-GG	≥ 2	≥ 6	> 50	≥ 1	–	> 1200	$\widetilde{g} \to tbd$, $\widetilde{g} \to tsd$
SR1b-DD	$\geq 2^-$	≥ 4	> 50	≥ 1	–	> 1000	$\widetilde{d}_R \to \bar{s}\bar{t}$
SR3b-DD	$\geq 2^-$	≥ 4	> 50	≥ 3	–	> 1800	$\widetilde{d}_R \to \bar{b}\bar{t}$

Table B.1: Summary of the signal region definitions and the targeted SUSY processes for the intermediate analysis update using 13.2 fb^{-1} of data. The selections for SR1b-GG, SR1b-DD, and SR3b-DD are optimized for the newly added RPV scenarios.

The observed and expected exclusion limits for the four additional RPV scenarios are presented in Figure B.1, with the SRs used to obtain the limits specified in the subtitles. Note that for this version of the analysis, the limits for the $\widetilde{d}_R \to \bar{b}\bar{t}$ and $\widetilde{d}_R \to \bar{s}\bar{t}$ models are shown as two-dimensional exclusion limits (not as one-dimensional upper limits on $\sigma_{\text{prod}} \times \text{BR}$ as in Section VIII.2.7)[1].
In the $\widetilde{g} \to tsd$ and $\widetilde{g} \to tbd$ scenarios, gluino masses up to 1.3 TeV and neutralino masses up to 1 TeV can be excluded at 95% confidence level. In the $\widetilde{d}_R \to \bar{s}\bar{t}$ and $\widetilde{d}_R \to \bar{b}\bar{t}$ models, down squark masses up to 700 GeV can be excluded for $m_{\widetilde{g}} \approx 700$ GeV.

[1] The $\widetilde{d}_R \to \bar{b}\bar{t}$ and $\widetilde{d}_R \to \bar{s}\bar{t}$ signal samples are simulated with only one free parameter (the down squark mass) and a fixed gluino mass of 2 TeV. A two-dimensional exclusion limit can only be obtained by rescaling the signals to different production cross-sections according to different gluino masses. Since no substantial information can be obtained by deriving exclusion limits for artificially rescaled signal processes, this way to present the limits has been discarded for the 36.1 fb^{-1} results.

Signal region	SR1b	SR0b1	SR0b2	SR3L1	SR3L2
Observed events	12	5	0	6	2
Total background	11.4 ± 2.8	8.8 ± 2.9	1.6 ± 0.8	6.1 ± 2.2	1.2 ± 0.5
Fake/non-prompt leptons	3.3 ± 2.1	2.9 ± 2.0	0.4 ± 0.5	0.29 ± 0.29	0.15 ± 0.15
Charge-flip	1.43 ± 0.19	0.50 ± 0.09	0.08 ± 0.03	–	–
$t\bar{t}$+W	2.0 ± 0.7	0.45 ± 0.17	0.13 ± 0.06	0.09 ± 0.04	0.01 ± 0.01
$t\bar{t}$+Z	1.6 ± 0.6	0.45 ± 0.18	0.10 ± 0.04	0.69 ± 0.25	0.10 ± 0.04
Diboson	0.5 ± 0.4	3.7 ± 1.9	0.5 ± 0.5	4.2 ± 2.0	0.7 ± 0.4
Rare	2.7 ± 0.9	0.8 ± 0.4	0.18 ± 0.12	0.8 ± 0.4	0.21 ± 0.13

Signal region	SR3b	SR1b-GG	SR1b-DD	SR3b-DD
Observed events	2	2	12	4
Total background	1.6 ± 0.6	1.7 ± 0.5	12.0 ± 2.7	1.9 ± 0.8
Fake/non-prompt leptons	0.2 ± 0.5	0.21 ± 0.33	2.5 ± 1.7	0.5 ± 0.6
Charge-flip	0.14 ± 0.03	0.18 ± 0.07	1.74 ± 0.22	0.14 ± 0.03
$t\bar{t}$+W	0.17 ± 0.06	0.33 ± 0.11	1.8 ± 0.6	0.18 ± 0.07
$t\bar{t}$+Z	0.19 ± 0.07	0.26 ± 0.08	2.8 ± 0.9	0.30 ± 0.10
Diboson	< 0.1	0.08 ± 0.19	0.6 ± 0.4	< 0.1
Rare	0.89 ± 0.31	0.64 ± 0.34	2.6 ± 1.3	0.8 ± 0.4

Table B.2: Observed and expected event yields in the signal regions for 13.2 fb^{-1}. The "Rare" category is defined as in the 2015 version of the analysis (including the $t\bar{t}$+H and 4-top background). Background processes shown as "–" do not contribute to the according SR.

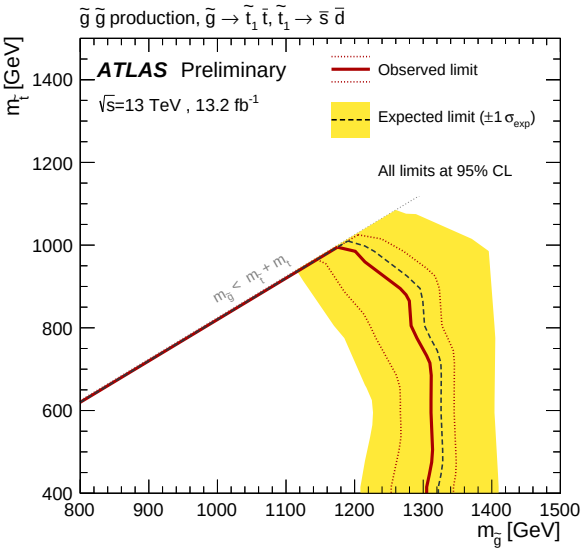

(a) $\widetilde{g} \to tsd$ scenario: SR1b-GG

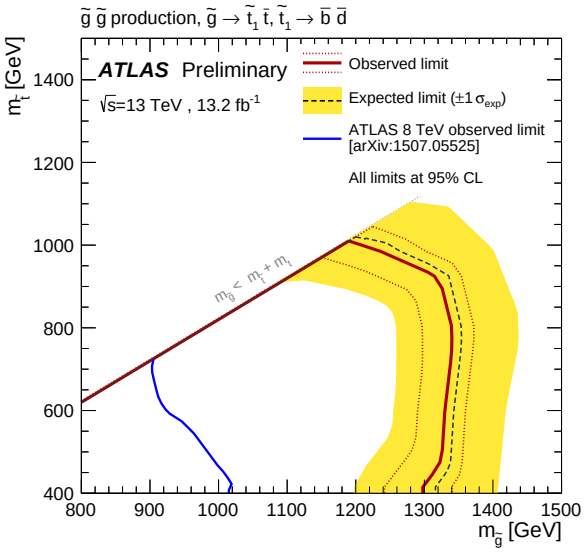

(b) $\widetilde{g} \to tbd$ scenario: SR1b-GG

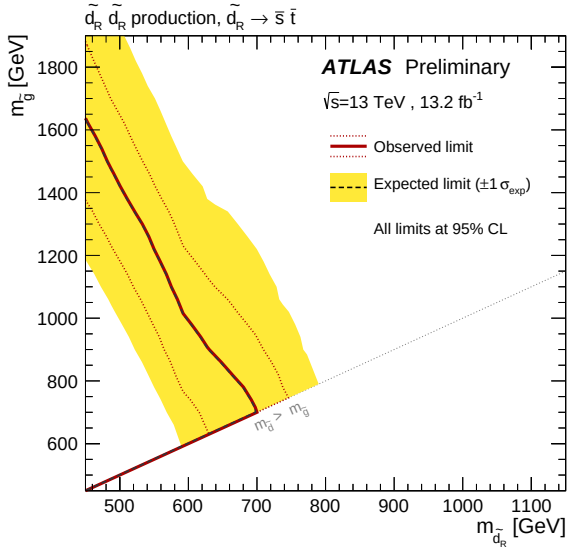

(c) $\widetilde{d}_R \to \bar{s}\bar{t}$ scenario: SR1b-DD

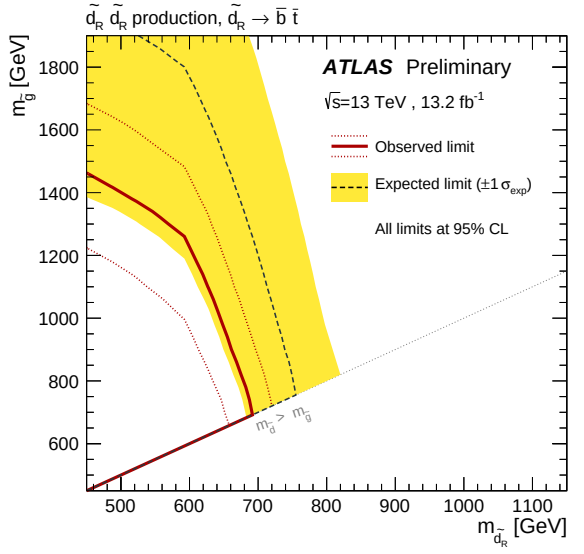

(d) $\widetilde{d}_R \to \bar{b}\bar{t}$ scenario: SR3b-DD

Figure B.1: Observed and expected exclusion limits on the masses of superpartners in the context of the RPV SUSY scenarios, as they were firstly introduced in 2016. The limits are shown for the $\widetilde{g} \to tsd$ (a), $\widetilde{g} \to tbd$ (b), $\widetilde{d}_R \to \bar{s}\bar{t}$ (c), and $\widetilde{d}_R \to \bar{b}\bar{t}$ (d) scenario. The signal regions used to obtain the limits are specified in the subtitles [7].

C: TRIGGER EVALUATION FOR 2016

For the 2016 data taking, the trigger strategy used in 2015 had to be revisited since the ATLAS trigger menu was partially modified. Further details of the efficiency studies described in Section VIII.2.2 are presented in the following.

Figure C.1 shows the efficiency evolution of the new dimuon trigger `HLT_mu22_mu8noL1` (left) and the electron-muon trigger `HLT_e17_lhloose_nod0_mu14` (right) in a simulated $WZ \to \ell\ell\ell\nu$ sample, plotted against the transverse momenta of the second trigger items (complementing the plots from Figure VIII.3, for which the efficiencies for the first trigger items were shown). This confirms that the efficiency plateau is reached for high p_{T} values of both triggered leptons. Also the $E_{\mathrm{T}}^{\mathrm{miss}}$ trigger combination used in the 2016 trigger configuration was tested. Figure C.2 shows the efficiency evolution for the "or" combination between `HLT_xe100_mht_L1XE50` and `HLT_xe110_mht_L1XE50` in a $t\bar{t}$ Monte Carlo sample with a simple preselection applied to be closer to the SR requirements (one lepton with $p_{\mathrm{T}} > 35$ GeV, selected by a single-lepton trigger, $E_{\mathrm{T}}^{\mathrm{miss}} > 25$ GeV, and $m_{\mathrm{T}} > 20$ GeV). The trigger efficiency was probed for different jet multiplicities (left) and different lepton flavors (right). In all cases, the trigger turn-ons behave similar and the triggers are fully efficient at $E_{\mathrm{T}}^{\mathrm{miss}}$ values of around 250 GeV.

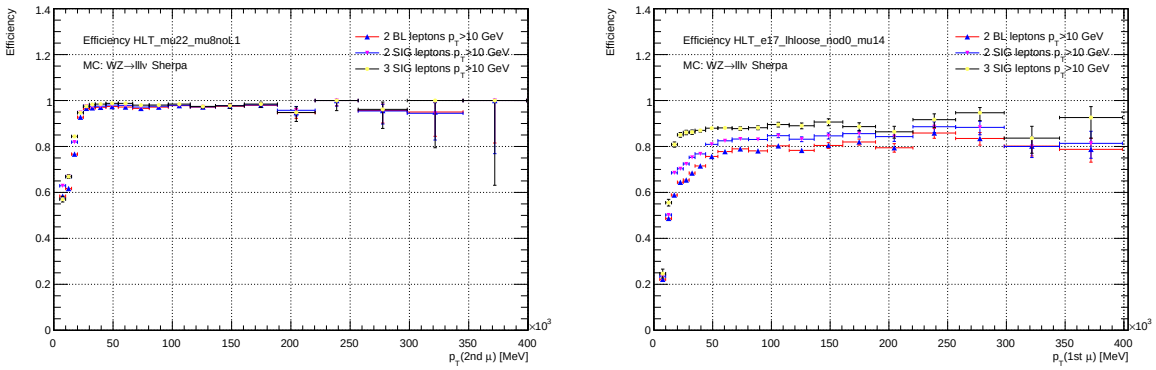

Figure C.1: Left: Efficiency evolution for the dimuon trigger `HLT_mu22_mu8noL1` in a simulated $WZ \to \ell\ell\ell\nu$ sample plotted against the p_{T} of the subleading muon for different lepton flavors. Right: Efficiency of the electron-muon trigger `HLT_e17_lhloose_nod0_mu14` plotted against the p_{T} of the triggered muon.

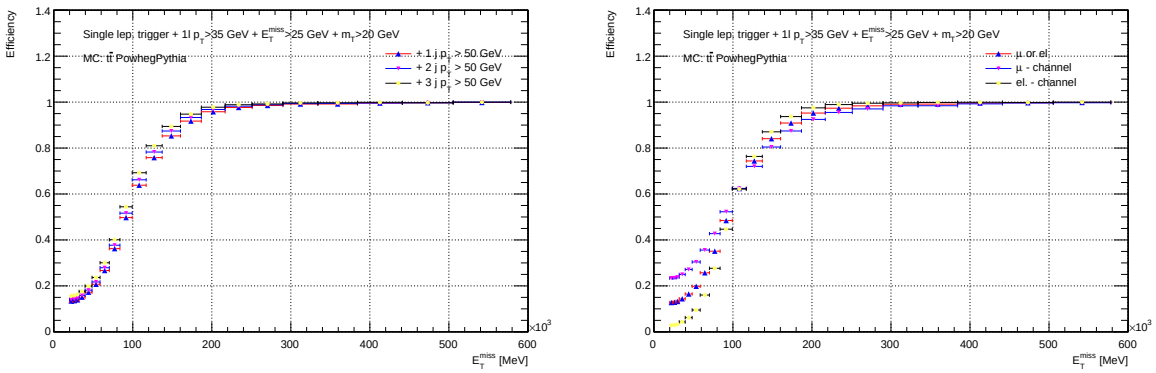

Figure C.2: Efficiency evolution for the "or" combination between `HLT_xe100_mht_L1XE50` and `HLT_xe110_mht_L1XE50` in a simulated $t\bar{t}$ sample for different jet multiplicities (left) and different lepton preselections (right). A simple preselection is applied on the $t\bar{t}$ sample to be closer to the SR requirements.

A comparison of the total event yields for different choices of dilepton or $E_{\mathrm{T}}^{\mathrm{miss}}$ triggers (or their combinations) in a $t\bar{t}$ Monte Carlo sample is shown in Figure C.3. All triggers show the expected performance for this kind of sample. Most events are selected by the various dilepton triggers (in a simulated $t\bar{t}$ sample, significantly more events with two leptons than with large $E_{\mathrm{T}}^{\mathrm{miss}}$ are expected). The number of selected events for the two $E_{\mathrm{T}}^{\mathrm{miss}}$ triggers is comparable.
The performance of the $E_{\mathrm{T}}^{\mathrm{miss}}$ trigger combination was evaluated also in real data events. Figure C.4 shows the efficiency evolution computed for some early 2016 data runs (run no. 297170, 297447, 297730, corresponding to approximately 4.7 pb^{-1}) with a simple preselection applied (two same-sign leptons with $p_{\mathrm{T}} > 20$ GeV). The turn-on in data is similar as expected from the test in Monte Carlo. Also in real data, the $E_{\mathrm{T}}^{\mathrm{miss}}$ triggers are fully efficient at a missing transverse energy of about 250 GeV.

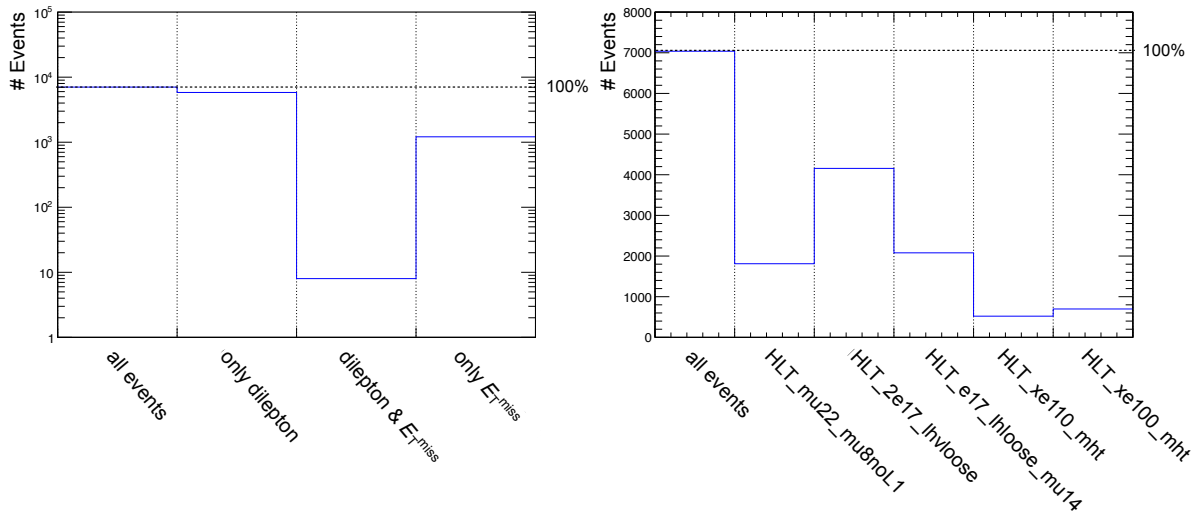

Figure C.3: Total yields of triggered events in a $t\bar{t}$ MC sample for several dilepton triggers, $E_{\mathrm{T}}^{\mathrm{miss}}$ triggers, or trigger combinations applied. The labels dilepton and $E_{\mathrm{T}}^{\mathrm{miss}}$ on the left plot refer to a logical "or" between all dilepton or the $E_{\mathrm{T}}^{\mathrm{miss}}$ triggers specified in the right plot.

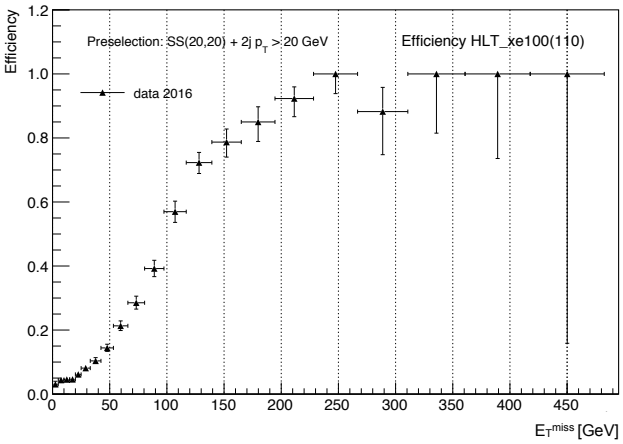

Figure C.4: Efficiency of the "or" combination between `HLT_xe100_mht_L1XE50` and `HLT_xe110_mht_L1XE50` for some early 2016 data runs, corresponding to around 4.7 pb^{-1}. The efficiency evolution in data is similar to the behavior in simulated events.

D: CHANGES OF OBJECT RECOMMENDATIONS BETWEEN 2015 AND 2016

In order to fulfill the latest ATLAS recommendations, the objects definitions for leptons and jets had to be marginally adapted for the 2015+2016 version of the analysis. Among continuous updates of things like calibration files, SF measurements, and updated evaluations of systematic uncertainties, some modifications of the objects definitions were applied:

- The JVT cut for jets was changed from JVT > 0.64 for jets with $p_{\mathrm{T}} < 50$ GeV and $|\eta| < 2.4$ to JVT > 0.59 for jets with $p_{\mathrm{T}} < 60$ GeV and $|\eta| < 2.4$.

  This was done to account for the higher pile-up environment in 2016 data and to maintain the rejection rate for pile-up jets.

- The *MV2c20 b*-tagging algorithm was replaced by *MV2c10*, optimized with another *c*-jet fraction ($\approx 7\%$) in the training sample.

- The *tightLH* identification WP for signal electrons has been replaced by *mediumLH* since the identification efficiency is larger (without significant changes in the fake rate).

  The updated definition for baseline electrons requires an additional hit in the inner B-Layer (denoted as *LooseAndBLayerLH* WP).

- The overlap removal between baseline objects was changed to a more elaborated approach, relying on p_{T} dependent distance parameters between leptons and jets. This prescription has been standardized within the SUSY group.

  While the rejection of jets close to leptons is still done with a fixed cone size of $\Delta R = 0.2$, the jet-lepton matching to reject electrons and muons close to jets is now performed with a p_{T} dependent cone size of $\Delta R_y = \min\{0.4, 0.1 + 9.6\,\mathrm{GeV}/p_{\mathrm{T}}(\ell)\}$. In 2015, also for this step a fixed value of $\Delta R_y = 0.4$ was used. This change yields a significant improvement of the lepton efficiency, in particular for high-p_{T} leptons, where the OR cones become more narrow, allowing closer distances between leptons and jets.

Dedicated studies have been done to confirm that these changes have no significant effect on the overall analysis performance. In fact, the sensitivity of the analysis is in general improved for the updated object recommendations.

E: IMPACT OF $W^{\pm}W^{\pm}$ PRODUCTION VIA DOUBLE PARTON SCATTERING

Double parton scattering (DPS) $W^{\pm}W^{\pm}$ production occurs when two partons interact simultaneously in a proton-proton collision and two single $W^{\pm}$ production processes overlap in an event. As this process can be a potentially relevant source of same-sign leptons, the sensitivity of the search to this background type was revisited using simulated events. A Monte Carlo sample produced at LO with the PYTHIA8 generator was used to probe the expected impact of DPS $W^{\pm}W^{\pm} \to \ell^{\pm}\ell^{\pm}\nu\nu$ production in regions close to the analysis signal regions.

The production cross-section of a DPS $W^{\pm}W^{\pm}$ process can be derived from the cross-sections of the single $W^{\pm}$ production modes $\sigma_{W^{\pm}}$ and an effective area parameter σ_{eff}, which has to be obtained from measurements:

$$\sigma^{\text{DPS}}_{W^{\pm}W^{\pm}} = \frac{\sigma_{W^+}\sigma_{W^+} + \sigma_{W^-}\sigma_{W^-} + 2\,\sigma_{W^+}\sigma_{W^-}}{\sigma_{\text{eff}}} = 0.19 - 0.38\,\text{pb}.$$

Since the PYTHIA8 Monte Carlo generator is known to have a deficient prediction for events with high jet multiplicities, a W+jets (single parton scattering) sample was produced with the same simulation framework and compared to the prediction from a SHERPA sample for large numbers of jets. Correction factors for each jet multiplicity were derived from the difference between the PYTHIA8 and SHERPA predictions and applied to the DPS $W^{\pm}W^{\pm}$ sample, depending on the number of additional jets ($p_{\text{T}} > 20$ GeV) in the simulated events.

The comparison between the PYTHIA8 and SHERPA sample, normalized to an integrated luminosity of 36.5 fb^{-1} is shown on the left of Figure E.1. Since the PYTHIA8 W+jets sample does not contain events anymore for $N^{20}_{\text{jets}} > 7$, the ratio between the prediction of the samples was fitted with an exponential function to extrapolate the correction factors towards higher jet multiplicities. On the right of Figure E.1, the direct comparison between the original and the corrected DPS sample is shown. The large correction factors for events with high jet multiplicities affect only a small fraction of events in the DPS sample.

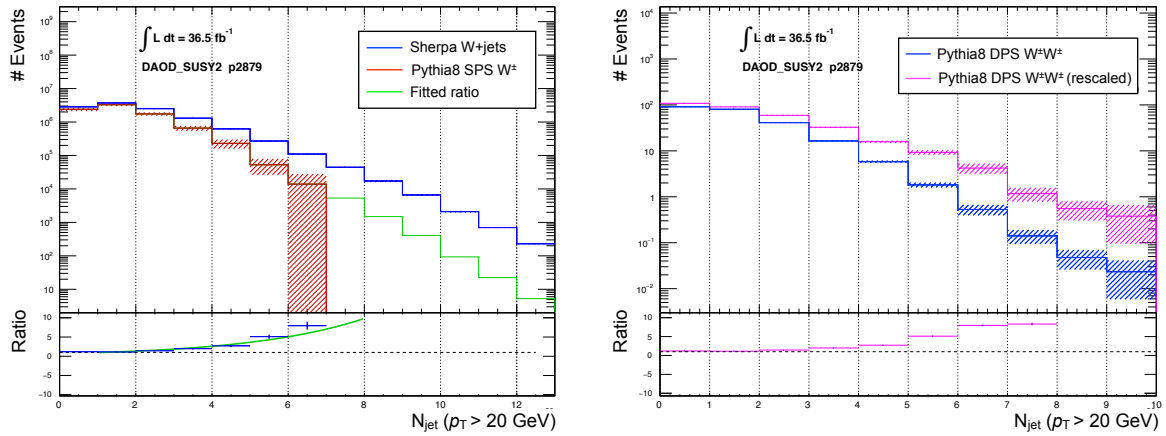

Figure E.1: Left: Direct comparison of W+jets production simulated with SHERPA (blue) and PYTHIA8 (red), plotted against the number of jets with $p_{\text{T}} > 20$ GeV. The green line shows the extrapolation of the PYTHIA8 prediction for high jet multiplicities ($N^{20}_{\text{jets}} > 7$). Right: Comparison of the original (blue) and the rescaled (purple) DPS $W^{\pm}W^{\pm}$ sample. All event yields are normalized to a integrated luminosity of 36.5 fb^{-1}.

The predictions from the uncorrected and corrected DPS $W^{\pm}W^{\pm}$ sample was probed in two partially overlapping control regions where this process could have a relevant impact, denoted as CR0b1 and

CR0b2. The contributions of double parton scattering in the CRs was compared to data and the various other background constituents.

- CR0b1: 2 SS lep. ($p_{\mathrm{T}}^{\ell} > 20$ GeV), $N_{\mathrm{jets}}^{20} > 2$, $N_{b\text{-jets}} = 0$, $E_{\mathrm{T}}^{\mathrm{miss}} > 20$ GeV, SR veto
- CR0b2: 2 SS lep. ($p_{\mathrm{T}}^{\ell} > 20$ GeV), $N_{\mathrm{jets}}^{20} > 3$, $N_{b\text{-jets}} = 0$, $E_{\mathrm{T}}^{\mathrm{miss}} > 50$ GeV, SR veto

The results for these control regions with the original and the corrected[2] DPS background included are shown in Figure E.2. Since the reducible background processes were estimated with $t\bar{t}$ Monte Carlo for this test, there is no perfect agreement between data and the predicted background in the CRs. The impact of the (corrected) DPS process in CR0b1 and CR0b2 amounts only to 0.2–0.3% relative to the other background constituents. Accordingly, the impact of DPS $W^{\pm}W^{\pm}$ production on the signal regions was neglected for this analysis.

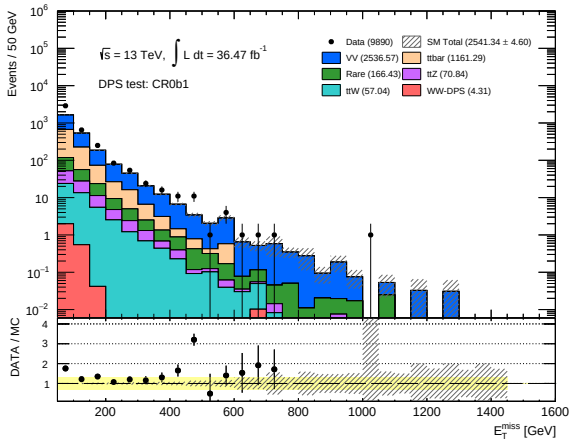

(a) CR0b1

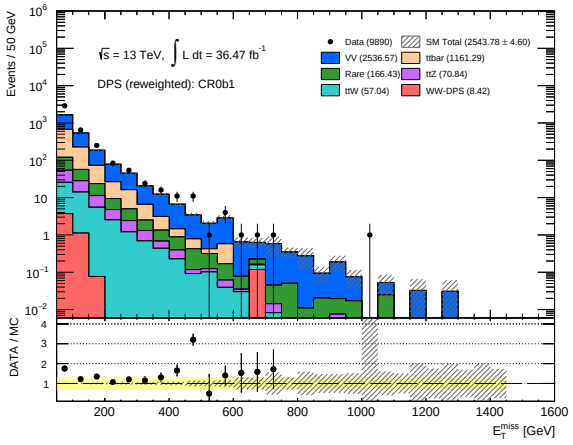

(b) CR0b1, corrected DPS

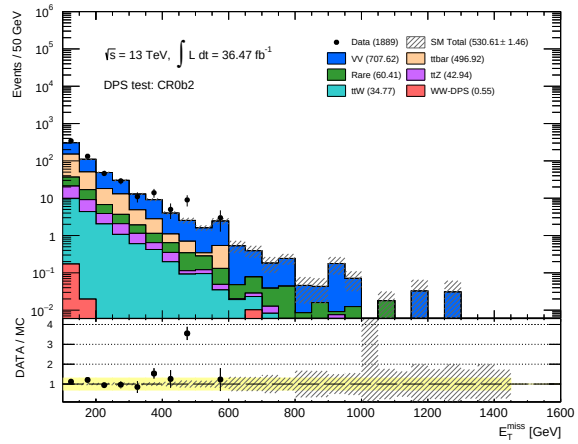

(c) CR0b2

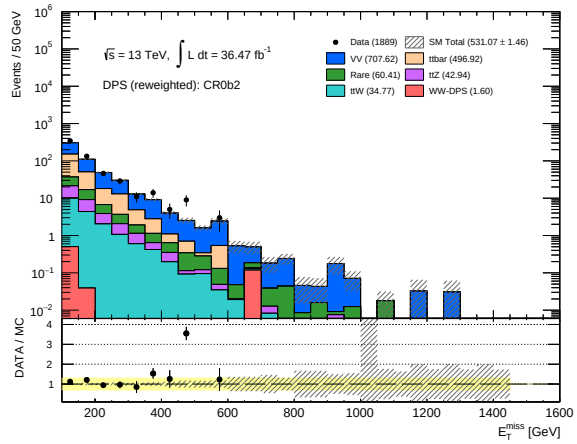

(d) CR0b2, corrected DPS

Figure E.2: The $E_{\mathrm{T}}^{\mathrm{miss}}$ distributions in CR0b1 (a,b) and CR0b2 (c,d) including the original PYTHIA8 DPS $W^{\pm}W^{\pm}$ sample (left) and the corrected sample (right). The bottom panels show the data-MC ratios. The DPS contribution (red) is in all cases negligible with respect to the other background components.

[2]The difference between the uncorrected and corrected DPS prediction can be regarded as a benchmark for the uncertainty of the PYTHIA8 sample.

F: POTENTIAL OF W/Z-TAGGING IN SIGNAL REGIONS

For some of the supersymmetric models explored in this analysis, several associated heavy gauge bosons are produced that might decay also to light-flavor quark pairs instead of leptons and neutrinos. In fact, the branching ratios for $W \to qq$ ($Z \to qq$) decays are 67.6% (69.9%) [11] and, therefore, larger as for leptonic decays. The potential to identify such a hadronic decay (W/Z-tagging) and to use it for the signal region optimization has been investigated. Especially for the scenario featuring gluino pair production with a two-step decay to four light-flavor quarks, two Z^0, two $W^\pm$ bosons, and two neutralinos ($\widetilde{g} \to q\bar{q}W^\pm Z\widetilde{\chi}_1^0$ model), this approach could be promising, since even with a hadronic decay of one of the heavy gauge bosons, leptonic decays of the other bosons can lead to SS/3L final states.
The identification of hadronic decays of heavy gauge bosons is mainly based on the invariant mass reconstruction. Although many newer W or Z-taggers rely on additional jet-substructure quantities to obtain higher purities of $W/Z \to qq$ events, the most effective selection is to build the invariant mass of a jet m_j and to check whether it is in a specific range around the nominal Z^0 or $W^\pm$ boson mass. If a heavy gauge boson decays to a pair of quarks, the decay products can be reconstructed either as one or as two jets, depending on the angular separation $\Delta R(q, q)$ between the initial quarks. These two scenarios, referred to as "unresolved" (one jet) or "resolved" (two jets) cases, are depicted in Figure F.1 and have to be treated with different selection approaches.

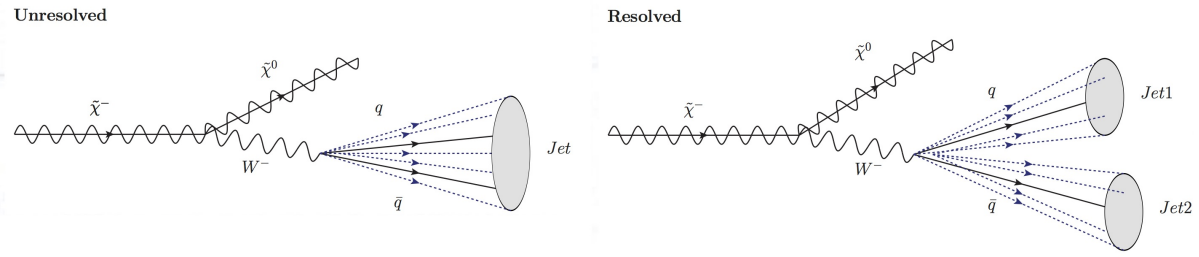

Figure F.1: Illustration of the two distinct reconstruction cases for hadronic $W^\pm$ decays: unresolved as one jet (left) or resolved as two jets (right). It depends on the p_T of the $W^\pm$ boson which case is more likely to happen.

For the studies presented here, only the unresolved case was considered, since the larger background contamination and a more complex reconstruction in the resolved case would have required a more refined revision of the signal regions. However, it was found that the default AntiKt4EMTopo jet algorithm with a distance parameter of $R = 0.4$ is not suitable for W or Z-tagging, as the jet cones are typically too narrow to for an efficient identification. Figure F.2 shows the angular separation $\Delta R(q, q)$ between the two initial quarks from a hadronic $W^\pm$ decay plotted against the reconstructed transverse momentum of the $W^\pm$ boson p_T^W for two simulated signal points from the $\widetilde{b}_1 \to tW^\pm\widetilde{\chi}_1^0$ (left) and $\widetilde{g} \to q\bar{q}W^\pm Z\widetilde{\chi}_1^0$ (right) grid. For the majority of events, the angular separation is larger than 0.4, which does not allow them to be reconstructed as a single jet. Only for $W^\pm$ bosons with large transverse momenta, corresponding to signal scenarios with large mass differences between charginos and neutralinos, an unresolved reconstruction is possible.
To address this issue, the default jets were "reclustered" to jets with a distance parameter of $R = 1.0$, utilizing a dedicated software framework, denoted as *jet-reclustering tool*. This creates large-R jets starting from calibrated jets with smaller radii. Calibrations factors and uncertainties from the small-R jets are propagated directly to the reclustered jets. For the W-tagging, a simple approach was used relying just

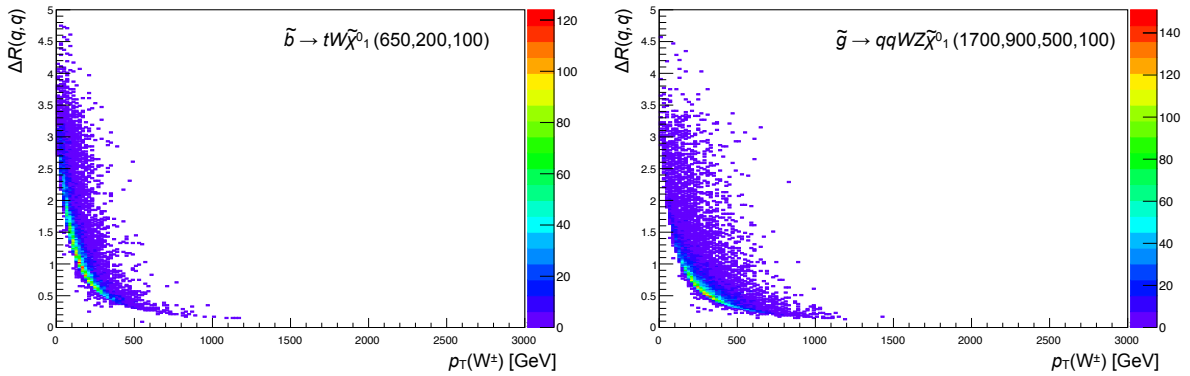

Figure F.2: Angular separation $\Delta R(q, q)$ between the two quarks from a hadronic $W^{\pm}$ decay plotted against the reconstructed p_{T} of the $W^{\pm}$ boson. The plots show the distributions for a specific point of the $\widetilde{b}_1 \to t\,W^{\pm}\,\widetilde{\chi}^0_1$ (left) and the $\widetilde{g} \to q\bar{q}W^{\pm}Z\,\widetilde{\chi}^0_1$ (right) signal grids. The signal parameters (superpartner masses) are indicated on the plots.

on an invariant mass requirement for the large-R jets ($m_W - 15\,\mathrm{GeV} < m_j^{R=1} < m_W + 15\,\mathrm{GeV}$). Any of the reclustered large-R jets fulfilling this requirement was considered as originating from a hadronic $W^{\pm}$ decay[3]. In the context of the re-optimization procedure for SR0b5j targeting the $\widetilde{g} \to q\bar{q}W^{\pm}Z\,\widetilde{\chi}^0_1$ model, a W-tag requirement was added to be sensitive to possible hadronic decays of the $W^{\pm}$ bosons in the final states produced in this scenario. As the re-optimization was done for the intermediate analysis update after the 2015 release, these studies were performed for an expected luminosity of 10 fb^{-1}. The SM background was modeled purely with simulated samples, using $t\bar{t}$ MC for the reducible background processes.

The plots in Figure F.3 show the m_{eff} distribution of the original SR0b5j (top), as it was defined for the 3.2 fb^{-1} version of the analysis (see Table VII.4) and the distributions by requiring one (bottom left) or two (bottom right) W-tags in addition to the standard selection[4]. Several signal points from the $\widetilde{g} \to q\bar{q}W^{\pm}Z\,\widetilde{\chi}^0_1$ grid are superimposed (dashed lines) to illustrate the signal contributions to these regions. It is clearly visible that a large amount of SM background in the SR can be removed by demanding at least one tagged W in addition to the original SR selection cuts. However, also the signal contribution is reduced significantly. The background and signal efficiencies (computed separately for each individual signal point) of the one (left-hand side) and two (right-hand side) W-tag requirements are presented in Figure F.4. Although, requiring one W-tag in SR0b5j reduces the SM background by around 76%, also for most of the signal points, the efficiency is reduced to a similar extent. Accordingly, W-tagging seems not to provide any additional discrimination between background and signal events for this type of model. The same applies also for requiring two W-tags in the SR, which removes basically the entire SM background but reduces the signal contribution by more than 90% in most cases.

Similar studies have been performed also for the SRs targeting the $\widetilde{b}_1 \to t\,W^{\pm}\,\widetilde{\chi}^0_1$ scenario, yielding similar results. Furthermore, it was tried to relax cuts on $E_{\mathrm{T}}^{\mathrm{miss}}$, m_{eff}, or N_{jets} in the SRs and to replace them by W-tag requirements, which gave even worse sensitivities than the results presented here (it was found that the optimal configuration of $E_{\mathrm{T}}^{\mathrm{miss}}$, m_{eff}, and N_{jets} cuts seems to be almost independent from the W-tag requirement for the signal processes investigated). Since it was not possible in the context of these studies

[3] This invariant mass range covers obviously also the nominal Z^0 mass. Since no further specific identification requirements are applied for this study, this approach can be also considered as a common W/Z-tagging.

[4] Note that the W-tag is applied only for the reclustered $R = 1.0$ jets in the events. The former selections cuts on number and p_{T} of the jets are still applied to the default $R = 0.4$ jet collection.

to design a W-tag based SR with a significant background rejection, but maintaining a signal acceptance comparable to the standard signal regions, this approach was discarded for future versions of the analysis.

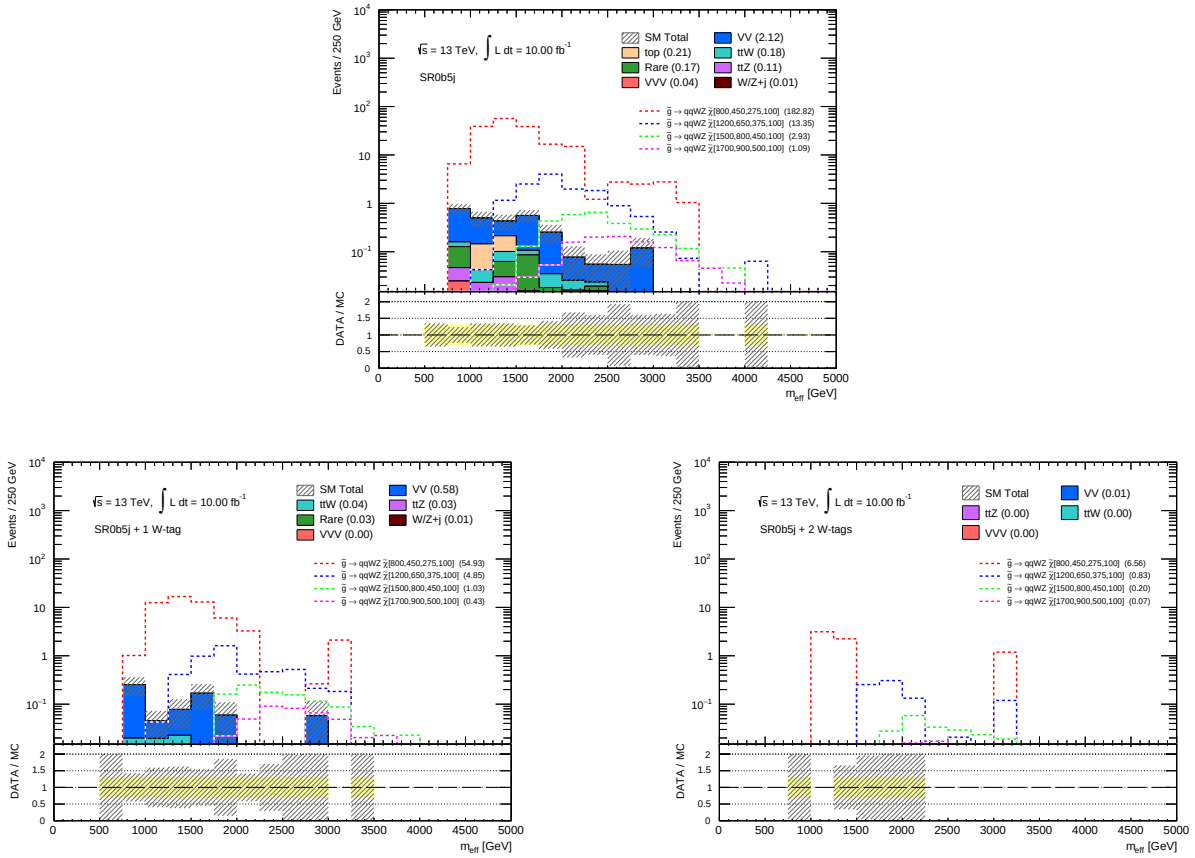

Figure F.3: Effective mass distributions in the signal region SR0b5j (top) and requiring one (bottom left) or two (bottom right) W-tags in addition to the baseline definition. Several points from the $\widetilde{g} \to q\bar{q}W^{\pm}Z\widetilde{\chi}_1^0$ grid are superimposed (dashed lines) to show their contributions to the SRs. The event yields are normalized to a luminosity of 10 fb^{-1}.

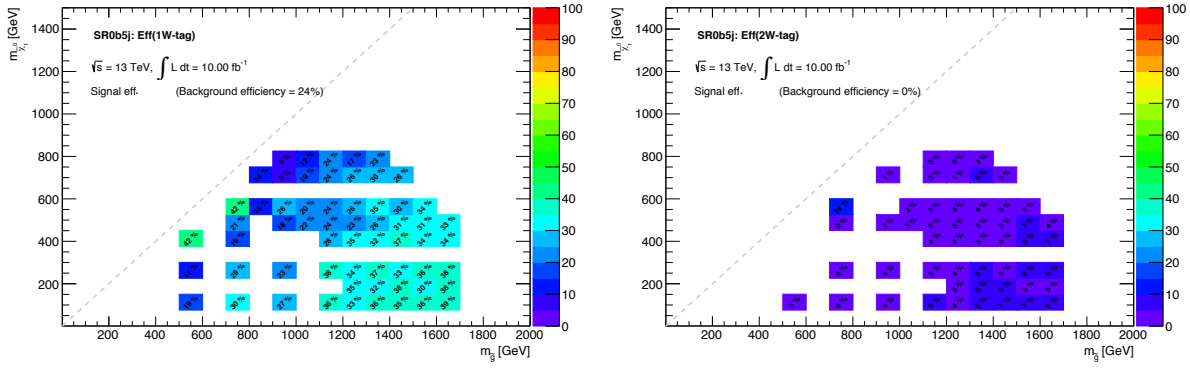

Figure F.4: Background and signal efficiencies of the W-tag requirement in SR0b5j. The efficiencies are computed for background and each signal point separately by building the ratio between the SR yields with one (left) or two (right) additional W-tags and the event yields in the original SR. There is no substantial difference between the effects of the W-tag for signal and background.

G: STUDIES OF m_{T2} BASED SIGNAL REGIONS

In all recent version of the same-sign/3L analysis, the signal regions were defined in terms of requirements on simple variables, such as the number of jets (b-jets), E_T^{miss}, m_{eff}, or the transverse momenta of particles. The utilization of a more complex variable, denoted as m_{T2} [216], was tested.

The m_{T2} variable has been introduced especially for SUSY searches exploring decays to invisible particles. It assumes a final state with E_T^{miss} and two detected particles from two semi-invisible decays of an initially produced particle pair. It relies on the balance between the transverse masses m_T of the two decay legs originating from the particle pair. Therefore, m_{T2} can be written as a function of the total missing transverse momentum and the momenta of two visible particles in an event. It is defined as:

$$m_{T2}^2 = \min_{\vec{p}_{T,1}+\vec{p}_{T,2}=\vec{p}_T} \left\{ \max\left(m_T^2(\vec{p}_T^{\,\ell_1}, \vec{p}_{T,1}),\, m_T^2(\vec{p}_T^{\,\ell_2}, \vec{p}_{T,2}) \right) \right\},$$

where $\vec{p}_{T,1} + \vec{p}_{T,2} = \vec{p}_T$ are all possible combinations of two-momenta that add up to the observed missing transverse momentum. The vectors $\vec{p}_T^{\,\ell_{1(2)}}$ are the transverse momenta of the leading and subleading lepton, respectively. Typically, the shapes of m_{T2} distributions are significantly different for SM background and RPC SUSY scenarios featuring pair production of squarks or gluinos with subsequent decays to neutralinos and SM particles. In the context of the SR re-optimization for the full 2015+2016 dataset, the sensitivity of this variable in the SS/3L analysis was tested by defining signal regions with m_{T2} requirements and compare their sensibility to the SRs based on standard variables.

Two signal regions, denoted as SR0b[m_{T2}] and SR3L[m_{T2}] were defined targeting the $\widetilde{g} \to q\bar{q}W^{\pm}Z\widetilde{\chi}_1^0$ and the $\widetilde{g} \to q\bar{q}(\ell\bar{\ell}/\nu\nu)\widetilde{\chi}_1^0$ model, respectively. They were compared to the performance of SR0b2 and SR3L2 targeting the same models but relying only on standard variables. The definitions of all SRs are summarized in Table G.1. In order to have no significant reduction of the event yields in the m_{T2}-based selections with respect to the standard SRs, some other requirements were relaxed in the former. The additional condition chosen for both SR0b[m_{T2}] and SR3L[m_{T2}] is $m_{T2} > 100$ GeV to remove the largest fraction of the diboson background[5]. The studies were done for an expected luminosity of 35 fb^{-1}. The SM background was modeled purely with simulated Monte Carlo samples, using $t\bar{t}$ MC for the reducible background sources.

Signal region	N_ℓ^{signal}	N_{jets}	p_T^{jet} [GeV]	$N_{b\text{-jets}}^{20}$	E_T^{miss} [GeV]	m_{eff} [GeV]	m_{T2} [GeV]
SR0b[m_{T2}]	≥ 2	≥ 5	40	$= 0$	150	1300	100
SR0b2	≥ 2	≥ 6	40	$= 0$	175	1500	–
SR3L[m_{T2}]	≥ 3	≥ 3	40	$= 0$	200	1400	100
SR3L2	≥ 3	≥ 4	40	$= 0$	200	1800	–

Table G.1: Summary of the definitions for the m_{T2}-based signal regions SR0b[m_{T2}], SR3L[m_{T2}] and the corresponding SR0b2, SR3L2, targeting the same models but relying on standard variables.

The m_{T2} and the E_T^{miss} distributions for SR0b[m_{T2}] and the corresponding SR0b2 are shown in Figure G.1. Several signal points from the $\widetilde{g} \to q\bar{q}W^{\pm}Z\widetilde{\chi}_1^0$ grid are superimposed (dashed lines) demonstrating the obvious shape difference between m_{T2} distributions for the signal and the SM background. The m_{T2} distributions show also that the $m_{T2} > 100$ GeV requirement removes the largest fraction of diboson and

[5] The m_{T2} distribution for $WW \to \ell\ell\nu\nu$ processes has its maximum typically at the nominal $W^{\pm}$ mass: $m_W \approx 80.4$ GeV.

$t\bar{t}$+W/Z backgrounds in the signal regions. However, also a major fraction of the signal is rejected by applying a m_{T2} requirement. The same set of plots for SR3L2 and SR3L[m_{T2}] is shown in Figure G.2 with some points from the $\widetilde{g} \to q\bar{q}(\ell\bar{\ell}/\nu\nu)\widetilde{\chi}_1^0$ grid superimposed. In both cases, the ratio between signal and background yields can be improved compared to the standard SRs.
Figure G.3 shows the relative changes of the event yields for background and the various signal points, comparing the regions based on m_{T2} and their respective standard SRs. In both of the evaluated cases, more than 50% of the total SM background can be removed, whereas the signal efficiencies are in general not affected that strongly ($\approx 70\%$). For many points, the signal efficiency can even be increased ($> 100\%$) with the m_{T2}-based approach.

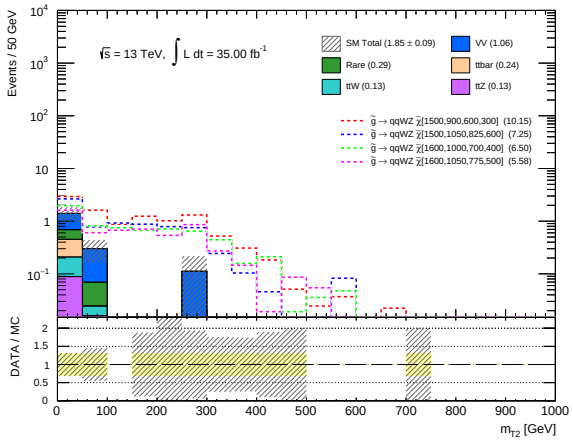

(a) m_{T2} distribution in SR0b2

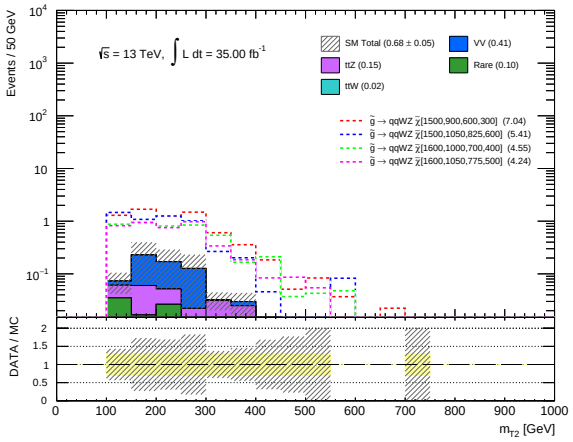

(b) m_{T2} distribution in SR0b[m_{T2}]

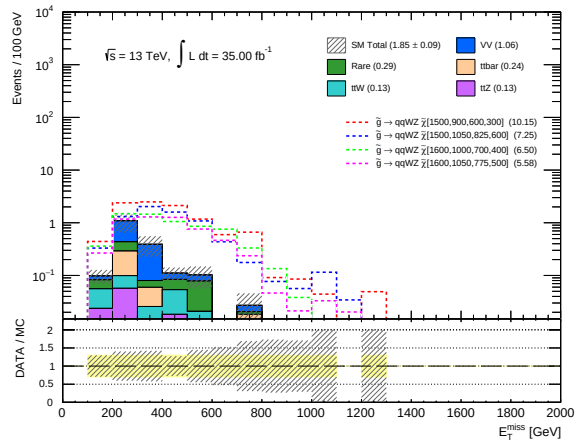

(c) $E_{\mathrm{T}}^{\mathrm{miss}}$ distribution in SR0b2

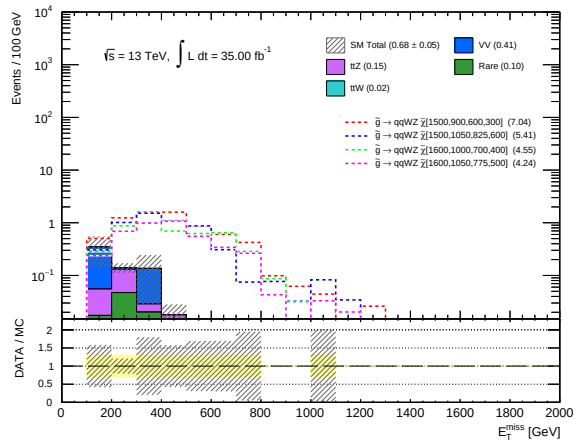

(d) $E_{\mathrm{T}}^{\mathrm{miss}}$ distribution in SR0b[m_{T2}]

Figure G.1: The m_{T2} (top) and $E_{\mathrm{T}}^{\mathrm{miss}}$ (bottom) distributions in SR0b2 (left) and the modified SR0b[m_{T2}] (right), which is similar to SR0b2 but includes also a m_{T2} requirement. The event yields are normalized to a luminosity of 35 fb^{-1}. Several points from the $\widetilde{g} \to q\bar{q}W^{\pm}Z\widetilde{\chi}_1^0$ grid are superimposed (dashed lines) to show their contributions to the SRs.

A more elaborated evaluation of the SR sensitivities can be obtained by comparing the expected exclusion limits computed with the HISTFITTER framework [207], which is shown in Figure G.4. This considers all theoretical and experimental systematic uncertainties, as well as the statistical errors in the signal regions. The limits were calculated for the $\widetilde{g} \to q\bar{q}W^{\pm}Z\widetilde{\chi}_1^0$ (left) and $\widetilde{g} \to q\bar{q}(\ell\bar{\ell}/\nu\nu)\widetilde{\chi}_1^0$ (right) scenario.

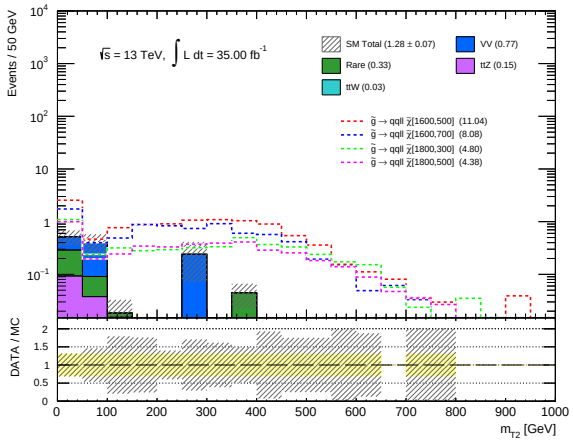

(a) m_{T2} distribution in SR3L2

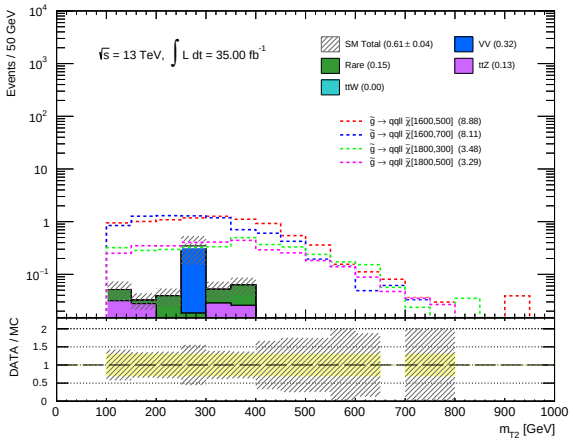

(b) m_{T2} distribution in SR3L[m_{T2}]

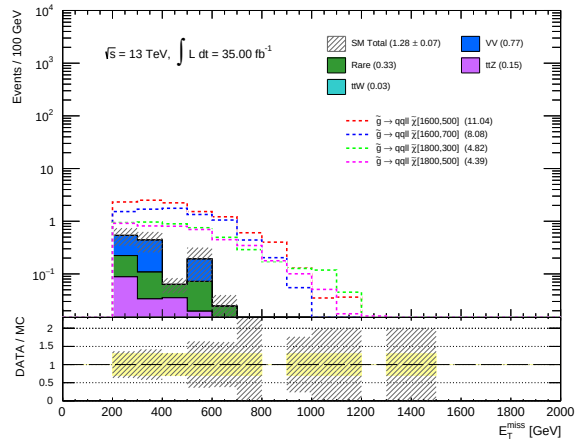

(c) $E_{\mathrm{T}}^{\mathrm{miss}}$ distribution in SR3L2

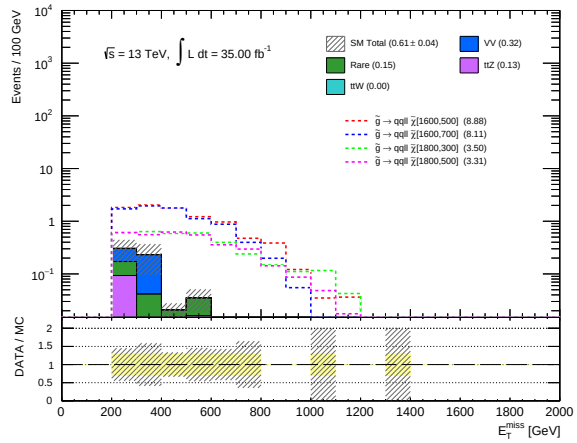

(d) $E_{\mathrm{T}}^{\mathrm{miss}}$ distribution in SR3L[m_{T2}]

Figure G.2: The m_{T2} (top) and $E_{\mathrm{T}}^{\mathrm{miss}}$ (bottom) distributions in SR3L2 (left) and the modified SR3L[m_{T2}] (right), which is similar to SR3L2 but includes also a m_{T2} requirement. The event yields are normalized to a luminosity of 35 fb^{-1}. Several points from the $\widetilde{g} \to q\bar{q}\,(\ell\bar{\ell}/\nu\nu)\,\widetilde{\chi}_1^0$ grid are superimposed (dashed lines) to show their contributions to the SRs.

Comparing the expected exclusion reach for SR0b2 and SR3L2 (red solid lines) to the performance of SR0b[m_{T2}] and SR3L[m_{T2}] (blue dashed lines), no significant improvement of the m_{T2}-based SRs with respect to the regions using standard variables could be achieved. The biggest improvement is around 100 GeV of additionally excluded neutralino masses in the region $(m_{\widetilde{g}}, m_{\widetilde{\chi}_1^0}) = (1.7\,\mathrm{TeV},\ 1.1\,\mathrm{TeV})$ of the $\widetilde{g} \to q\bar{q}\,(\ell\bar{\ell}/\nu\nu)\,\widetilde{\chi}_1^0$ grid. Although the pure signal-to-background ratio increases for the regions based on m_{T2}, this improvement is apparently not clearly present for the final exclusion limits. The reason for this can most likely be attributed to the increased statistical uncertainty of the background estimation which attenuates the expected exclusion power.

Other cut configurations including requirements on m_{T2} were tested, but none of them was found to provide a significant improvement compared to equivalent SRs based on standard variables. It should be noted that the m_{T2} variable is especially designed for scenarios with high $E_{\mathrm{T}}^{\mathrm{miss}}$ values. Accordingly, the signal acceptance is lower for compressed scenarios with small mass differences between $\widetilde{\chi}_1^0$ and $\widetilde{\chi}_1^{\pm}$, which reduces the sensitivity to these cases. The signal efficiency in that region of the $\widetilde{g} \to q\bar{q}\,(\ell\bar{\ell}/\nu\nu)\,\widetilde{\chi}_1^0$

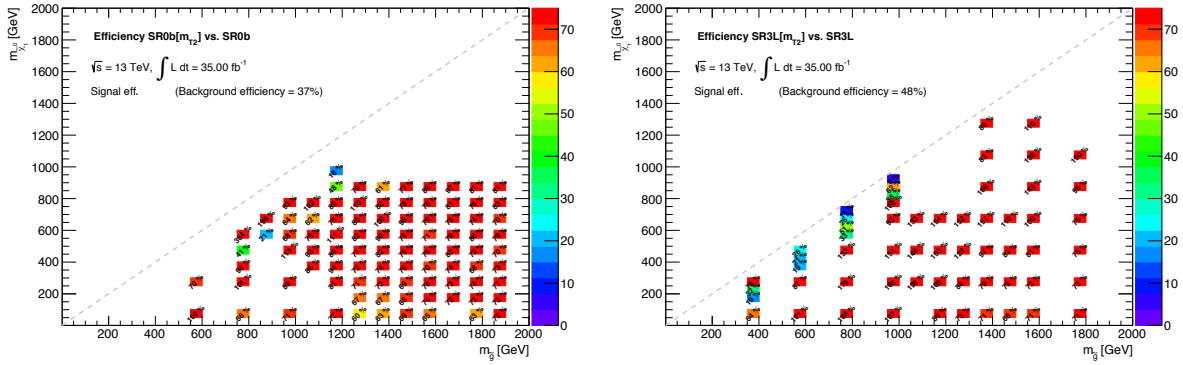

Figure G.3: The efficiencies of SR0b[m_{T2}] (left) and SR3L[m_{T2}] (right) with respect to SR0b2 and SR3L2. The numbers are computed for background and each signal point separately by building the ratio between the event yields in the SRs with the m_{T2} requirement and its respective SR using standard variables.

grid amounts only to 20–60%, as indicated in Figure G.3 (left). Since the same-sign/3L analysis is particularly designed to have its main focus on the regions with small mass splittings between SUSY particles (and no serious improvements with respect to the standard SR could be achieved also in other kinematics regions), it has been decided not to use m_{T2} in the signal regions and to rely on a higher number of standard variables instead.

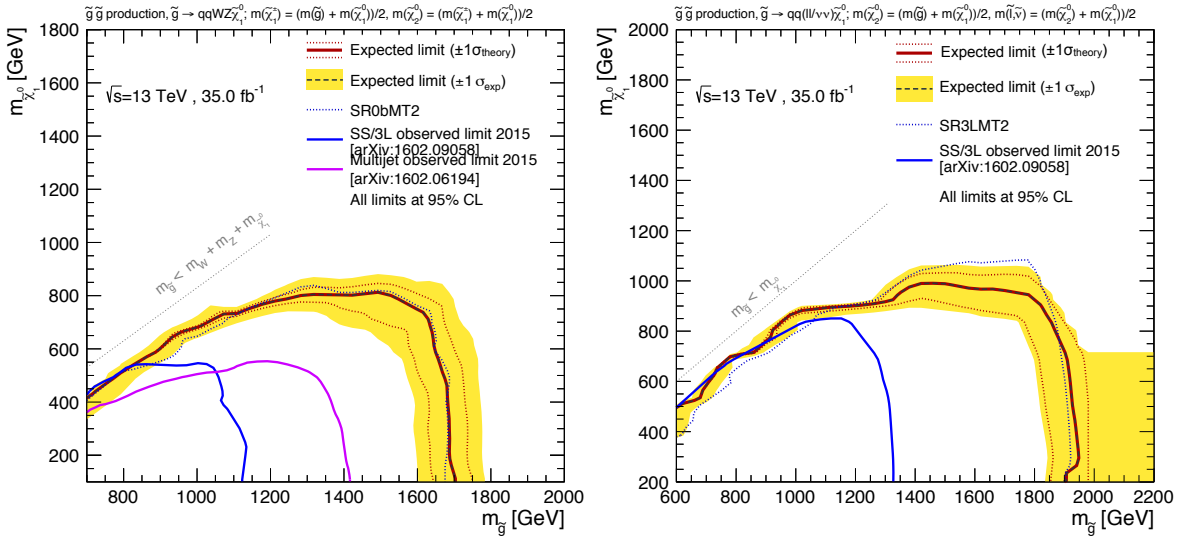

Figure G.4: Expected exclusion limits on neutralino and gluino masses in the context of the $\widetilde{g} \to q\bar{q}W^{\pm}Z\widetilde{\chi}_1^0$ (left) and $\widetilde{g} \to q\bar{q}(\ell\bar{\ell}/\nu\nu)\widetilde{\chi}_1^0$ (right) scenario. The limits obtained from SR0b2 and SR3L2 (red solid lines) are compared to the limits obtained from the m_{T2}-based regions SR0b[m_{T2}] and SR3L[m_{T2}] (blue dashed lines). The study is performed for a luminosity of 35 fb^{-1}.

H: DETAILS ON THE SIGNAL REGIONS AND STATISTICAL INTERPRETATIONS FOR 36.1 FB^{-1}

More details about the background composition, the uncertainties in the signal regions, as well as the statistical interpretations for the 36.1 fb^{-1} version of the analysis are given in this section.

The fractional subcomponents of the background category denoted as "Rare" in the signal and validation regions are given in Figure H.1. It includes tZ, $tW^{\pm}Z$, $t\bar{t}$+WW, $t\bar{t}$+WZ, $tt\bar{t}$ and triboson production, which are too small to be listed separately in the results. In the signal regions with b-jet requirements, $tW^{\pm}Z$ and $t\bar{t}$+WW are the dominant subcomponents, whereas for the regions with a b-jet veto also triboson production has a significant contribution. Only for the region Rpc3LSS1b, the "Rare" background is dominated by $t\bar{t}$+WZ.

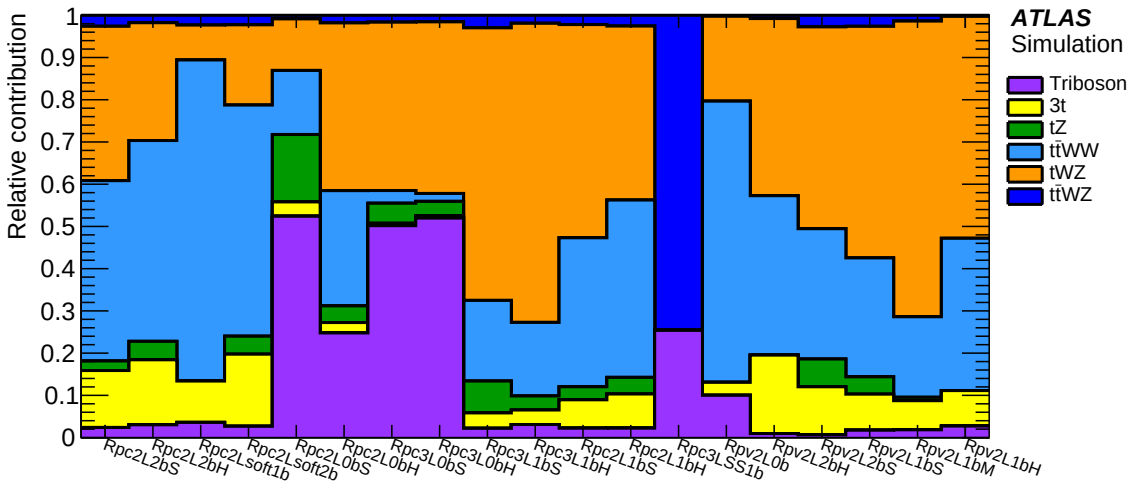

Figure H.1: Breakdown of the "Rare" category to its fractional subcomponents for each of the 2016 signal regions. It includes tZ, $tW^{\pm}Z$, $t\bar{t}$+WW, $t\bar{t}$+WZ, $tt\bar{t}$ and triboson production [8].

For SUSY scenarios where more than one signal region is used to derive the final exclusion limits, the SR with the best expected sensitivity is chosen for each point of the signal grid individually and the combined limits are placed according to this decision.
Maps showing the best expected signal region per grid point for the $\widetilde{g} \to t\bar{t}\widetilde{\chi}_1^0$ (a), $\widetilde{b}_1 \to tW^{\pm}\widetilde{\chi}_1^0$ (b), $\widetilde{g} \to q\bar{q}(\ell\bar{\ell}/\nu\nu)\widetilde{\chi}_1^0$ (c), and $\widetilde{g} \to q\bar{q}W^{\pm}Z\widetilde{\chi}_1^0$ (d) model are provided in Figure H.2. The plots confirm the intended behavior of the SRs, with the separated selections optimized for compressed SUSY spectra (suffix "S", red) and the large mass splittings (suffix "H", blue) being in most cases indeed the best choice for these kinematic regions. The map for the $\widetilde{g} \to t\bar{t}\widetilde{\chi}_1^0$ grid (Figure H.2 a) contains four different SRs, with Rpc2Lsoft1b(2b) considered only in the scenarios with off-shell top quarks between $m_{\widetilde{g}} > 2m_t + m_{\widetilde{\chi}_1^0}$ and $m_{\widetilde{g}} > 2m_W + m_{\widetilde{\chi}_1^0}$.

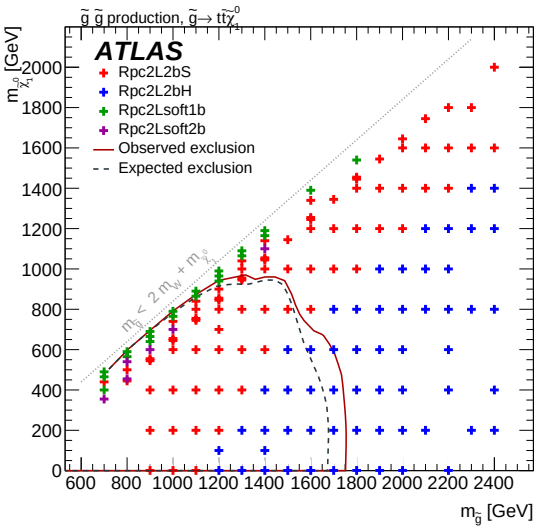

(a) $\widetilde{g} \to t\bar{t}\widetilde{\chi}_1^0$ scenario: Rpc2L2bS(H), Rpc2Lsoft1b(2b)

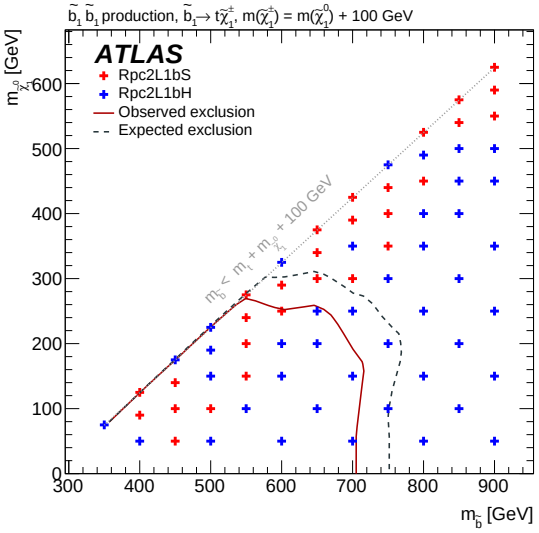

(b) $\widetilde{b}_1 \to tW^{\pm}\widetilde{\chi}_1^0$ scenario: Rpc2L1bS(H)

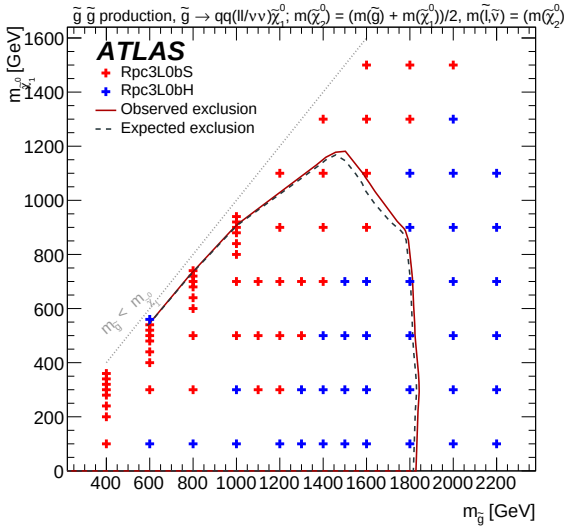

(c) $\widetilde{g} \to q\bar{q}(\ell\bar{\ell}/\nu\nu)\widetilde{\chi}_1^0$ scenario: Rpc3L0bS(H)

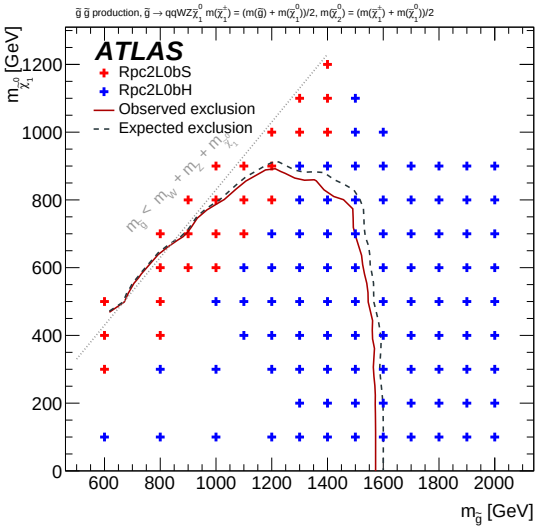

(d) $\widetilde{g} \to q\bar{q}W^{\pm}Z\widetilde{\chi}_1^0$ scenario: Rpc2L0bS(H)

Figure H.2: The best expected signal region per signal grid point, shown for the $\widetilde{g} \to t\bar{t}\widetilde{\chi}_1^0$ (a), $\widetilde{b}_1 \to tW^{\pm}\widetilde{\chi}_1^0$ (b), $\widetilde{g} \to q\bar{q}(\ell\bar{\ell}/\nu\nu)\widetilde{\chi}_1^0$ (c), and $\widetilde{g} \to q\bar{q}W^{\pm}Z\widetilde{\chi}_1^0$ (d) scenario. The SRs chosen for the individual signal points are indicated in different colors. These configurations are then used to set the final combined exclusion limits [8].

To get a better impression of the sensitivity in the very compressed region of the $\widetilde{g} \to t\bar{t}\widetilde{\chi}_1^0$ scenario, Figure H.3 shows the observed and expected exclusion limit only in the region with off-shell top decays. While the x-axis shows the gluino mass, the y-axis is parametrized as $m_{\widetilde{\chi}_1^0} + 2m_t - m_{\widetilde{g}}$ (left-hand side) and $m_{\widetilde{g}} - m_{\widetilde{\chi}_1^0}$ (right-hand side), respectively. For gluino masses below 800 GeV, scenarios up to $m_{\widetilde{g}} - m_{\widetilde{\chi}_1^0} \approx$ 200 GeV can be excluded at 95% confidence level.

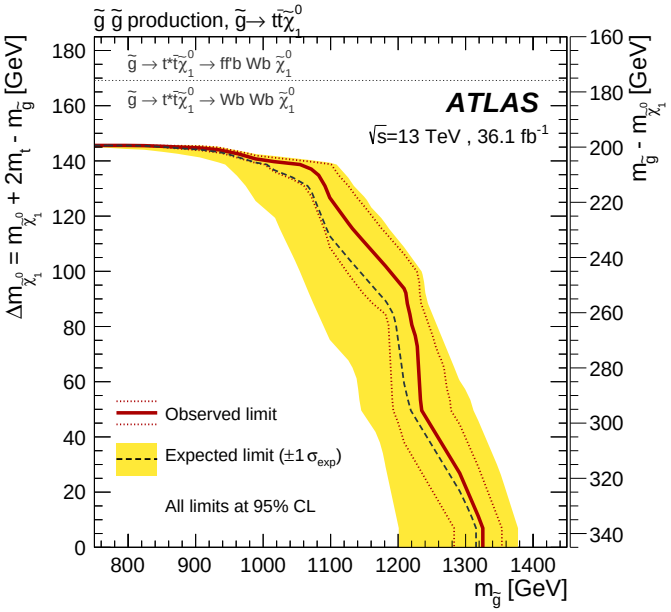

Figure H.3: Observed and expected exclusion limit for the $\widetilde{g} \to t\bar{t}\widetilde{\chi}_1^0$ scenario in the off-shell top region. The y-axis is parametrized as $m_{\widetilde{\chi}_1^0} + 2m_t - m_{\widetilde{g}}$ (left) and $m_{\widetilde{g}} - m_{\widetilde{\chi}_1^0}$ (right). For $m_{\widetilde{g}} < 800$ GeV, scenarios up to $m_{\widetilde{g}} - m_{\widetilde{\chi}_1^0} \approx 200$ GeV can be excluded at 95% CL [8].

A detailed breakdown of the dominant systematic uncertainties on the background estimation in each of the 2016 signal regions is provided in the Tables H.1–H.19. The individual components of the uncertainties can be correlated and do not necessarily add up quadratically to the total uncertainty. The percentages show the size of the uncertainties relative to the total expected background. The largest components are usually theoretical uncertainties or uncertainties associated with the data-driven methods.

The 95% CL model-independent upper limits on the signal production cross-sections $\mathrm{UL}^{95}(\sigma_{\mathrm{prod}})$ (in fb) for each signal point of the $\widetilde{g} \to t\bar{t}\widetilde{\chi}_1^0$, $\widetilde{b}_1 \to tW^{\pm}\widetilde{\chi}_1^0$, $\widetilde{g} \to q\bar{q}(\ell\bar{\ell}/\nu\nu)\widetilde{\chi}_1^0$, and $\widetilde{g} \to q\bar{q}W^{\pm}Z\widetilde{\chi}_1^0$ model are stated in the Tables H.20–H.23. The upper limits for the R-parity violating $\widetilde{g} \to q\bar{q}\widetilde{\chi}_1^0$, $\widetilde{\chi}_1^0 \to q\bar{q}\ell$, $\widetilde{g} \to t\bar{t}\widetilde{\chi}_1^0$, $\widetilde{\chi}_1^0 \to uds$, $\widetilde{g} \to tbd$, and $\widetilde{g} \to tsd$ models are summarized in the Tables H.24–H.26. These values are calculated with the same prescription as the gray numbers indicated on the plots in Figure VII.13 but computed for the 36.1 fb^{-1} version of the analysis. The difference to the upper limits listed Table VIII.4 is that the efficiency and acceptance specific to each individual signal point is considered in the computation. For the sake of visibility the numbers could not be shown directly on the plots. Instead, they are provided in these tables.

Uncertainty of signal region	Rpc2L2bS
Total background expectation	3.35
Statistical error ($\sqrt{N_{\text{exp}}}$)	$\pm$1.83
Total background systematic	$\pm$1.02 [30.4%]
Fake lepton systematics	$\pm$0.52 [15.5%]
Theory uncertainty: Rare	$\pm$0.51 [15.2%]
Jet energy scale (NP-1)	$\pm$0.50 [14.9%]
MC statistics	$\pm$0.35 [10.4%]
Theory uncertainty: ttW/Z	$\pm$0.25 [7.5%]
b-jets SF	$\pm$0.19 [5.7%]
Luminosity	$\pm$0.09 [2.7%]
c-jets SF	$\pm$0.08 [2.4%]
Jet energy scale (NP-3)	$\pm$0.08 [2.4%]
Jet energy scale (NP-2)	$\pm$0.06 [1.8%]
Jet energy resolution	$\pm$0.06 [1.8%]
MET soft-term resolution 1	$\pm$0.06 [1.8%]
MET soft-term resolution 2	$\pm$0.04 [1.2%]
Jet vertex tagger	$\pm$0.04 [1.2%]
Theory uncertainty: diboson	$\pm$0.04 [1.2%]
MET soft-term scale	$\pm$0.03 [0.9%]
Muon SF (sys.)	$\pm$0.03 [0.9%]
EGamma resolution	$\pm$0.03 [0.9%]
Electron identification SF	$\pm$0.03 [0.9%]
EGamma scale	$\pm$0.01 [0.3%]
Electron isolation SF	$\pm$0.01 [0.3%]
Muon (ID reconstruction)	$\pm$0.01 [0.3%]
Flavor tagging 1	$\pm$0.01 [0.3%]
Light-jets SF	$\pm$0.01 [0.3%]
Electron reconstruction SF	$\pm$0.01 [0.3%]
Muon SF (stat.)	$\pm$0.01 [0.3%]
Muon (MS reconstruction)	$\pm$0.01 [0.3%]
Flavor tagging 2	$\pm$0.01 [0.3%]

Table H.1: Breakdown of the dominant systematic uncertainties on the background estimation in signal region Rpc2L2bS for an integrated luminosity of 36.1 fb^{-1}. The individual uncertainties can be correlated and do not necessarily add up quadratically to the total uncertainty. The percentages show the size of the uncertainties relative to the total expected background.

Uncertainty of signal region	Rpc2L2bH
Total background expectation	1.08
Statistical error ($\sqrt{N_{\text{exp}}}$)	$\pm$1.04
Total background systematic	$\pm$0.32 [29.6%]
Theory uncertainty: Rare	$\pm$0.21 [19.4%]
MC statistics	$\pm$0.17 [15.7%]
Jet energy scale (NP-1)	$\pm$0.11 [10.2%]
Theory uncertainty: ttW/Z	$\pm$0.10 [9.3%]
b-jets SF	$\pm$0.06 [5.6%]
Jet energy scale (NP-2)	$\pm$0.04 [3.7%]
Jet energy scale (NP-3)	$\pm$0.04 [3.7%]
Luminosity	$\pm$0.03 [2.8%]
Jet energy resolution	$\pm$0.03 [2.8%]
c-jets SF	$\pm$0.02 [1.9%]
Jet η-intercalibration	$\pm$0.02 [1.9%]
Electron identification SF	$\pm$0.02 [1.9%]
Theory uncertainty: diboson	$\pm$0.01 [0.9%]
Muon SF (sys.)	$\pm$0.01 [0.9%]
MET soft-term resolution 1	$\pm$0.01 [0.9%]
MET soft-term resolution 2	$\pm$0.01 [0.9%]
Jet vertex tagger	$\pm$0.01 [0.9%]
Flavor tagging 1	$\pm$0.01 [0.9%]
Electron isolation SF	$\pm$0.01 [0.9%]

Table H.2: Breakdown of the dominant systematic uncertainties on the background estimation in signal region Rpc2L2bH for an integrated luminosity of 36.1 fb^{-1}. The individual uncertainties can be correlated and do not necessarily add up quadratically to the total uncertainty. The percentages show the size of the uncertainties relative to the total expected background.

Uncertainty of signal region	Rpc2Lsoft1b
Total background expectation	5.78
Statistical error ($\sqrt{N_{\text{exp}}}$)	±2.40
Total background systematic	±2.49 [43.1%]
Fake lepton systematics	±2.22 [38.4%]
MC statistics	±0.98 [17.0%]
Theory uncertainty: Rare	±0.36 [6.2%]
Jet energy scale (NP-1)	±0.30 [5.2%]
Theory uncertainty: ttW/Z	±0.29 [5.0%]
Luminosity	±0.07 [1.2%]
Theory uncertainty: diboson	±0.06 [1.0%]
Jet energy scale (NP-3)	±0.06 [1.0%]
MET soft-term resolution 1	±0.04 [0.7%]
Jet energy scale (NP-2)	±0.04 [0.7%]
Jet energy resolution	±0.03 [0.5%]
b-jets SF	±0.03 [0.5%]
Jet vertex tagger	±0.03 [0.5%]
Electron identification SF	±0.03 [0.5%]
c-jets SF	±0.03 [0.5%]
MET soft-term scale	±0.02 [0.3%]
Light-jets SF	±0.02 [0.3%]
Charge-flip systematics	±0.02 [0.3%]
Muon SF (sys.)	±0.02 [0.3%]
Electron reconstruction SF	±0.01 [0.2%]
Jet η-intercalibration	±0.01 [0.2%]
MET soft-term resolution 2	±0.01 [0.2%]
Muon (ID reconstruction)	±0.01 [0.2%]
Muon SF (stat.)	±0.01 [0.2%]

Table H.3: Breakdown of the dominant systematic uncertainties on the background estimation in signal region Rpc2Lsoft1b for an integrated luminosity of 36.1 fb^{-1}. The individual uncertainties can be correlated and do not necessarily add up quadratically to the total uncertainty. The percentages show the size of the uncertainties relative to the total expected background.

Uncertainty of signal region	Rpc2Lsoft2b
Total background expectation	3.80
Statistical error ($\sqrt{N_{\text{exp}}}$)	±1.95
Total background systematic	±1.59 [41.8%]
Fake lepton systematics	±1.36 [35.8%]
MC statistics	±0.59 [15.5%]
Theory uncertainty: Rare	±0.37 [9.7%]
Jet energy scale (NP-1)	±0.35 [9.2%]
Theory uncertainty: ttW/Z	±0.17 [4.5%]
b-jets SF	±0.13 [3.4%]
c-jets SF	±0.07 [1.8%]
Luminosity	±0.06 [1.6%]
Jet energy scale (NP-3)	±0.06 [1.6%]
MET soft-term resolution 2	±0.04 [1.1%]
Jet energy scale (NP-2)	±0.04 [1.1%]
MET soft-term scale	±0.03 [0.8%]
Jet energy resolution	±0.03 [0.8%]
Jet vertex tagger	±0.03 [0.8%]
MET soft-term resolution 1	±0.02 [0.5%]
Charge-flip systematics	±0.02 [0.5%]
Theory uncertainty: diboson	±0.02 [0.5%]
Muon SF (sys.)	±0.02 [0.5%]
Electron identification SF	±0.01 [0.3%]
Muon (MS reconstruction)	±0.01 [0.3%]
EGamma scale	±0.01 [0.3%]
EGamma resolution	±0.01 [0.3%]
Jet η-intercalibration	±0.01 [0.3%]
Electron reconstruction SF	±0.01 [0.3%]
Light-jets SF	±0.01 [0.3%]

Table H.4: Breakdown of the dominant systematic uncertainties on the background estimation in signal region Rpc2Lsoft2b for an integrated luminosity of 36.1 fb^{-1}. The individual uncertainties can be correlated and do not necessarily add up quadratically to the total uncertainty. The percentages show the size of the uncertainties relative to the total expected background.

Uncertainty of signal region	Rpc2L0bS
Total background expectation	6.02
Statistical error ($\sqrt{N_{\text{exp}}}$)	±2.45
Total background systematic	±1.84 [30.6%]
Theory uncertainty: diboson	±1.06 [17.6%]
Jet energy scale (NP-1)	±1.01 [16.8%]
Fake lepton systematics	±0.81 [13.5%]
MC statistics	±0.55 [9.1%]
Theory uncertainty: ttW/Z	±0.24 [4.0%]
Theory uncertainty: Rare	±0.23 [3.8%]
Jet energy scale (NP-3)	±0.19 [3.2%]
b-jets SF	±0.18 [3.0%]
Jet energy scale (NP-2)	±0.15 [2.5%]
Luminosity	±0.14 [2.3%]
Jet energy resolution	±0.13 [2.2%]
c-jets SF	±0.09 [1.5%]
Jet vertex tagger	±0.06 [1.0%]
Muon SF (sys.)	±0.05 [0.8%]
Light-jets SF	±0.04 [0.7%]
Electron identification SF	±0.04 [0.7%]
Jet η-intercalibration	±0.04 [0.7%]
MET soft-term scale	±0.03 [0.5%]
MET soft-term resolution 1	±0.02 [0.3%]
Electron isolation SF	±0.02 [0.3%]
Electron reconstruction SF	±0.01 [0.2%]
Muon SF (stat.)	±0.01 [0.2%]
MET soft-term resolution 2	±0.01 [0.2%]
Charge-flip systematics	±0.01 [0.2%]
EGamma resolution	±0.01 [0.2%]
Electron charge-ID SF	±0.01 [0.2%]
Muon isolation SF (sys.)	±0.01 [0.2%]
Muon TTVA (stat.)	±0.01 [0.2%]
Muon scale	±0.01 [0.2%]
Flavor tagging 1	±0.01 [0.2%]
Pile-up reweighting	±0.01 [0.2%]
Muon (MS reconstruction)	±0.01 [0.2%]

Table H.5: Breakdown of the dominant systematic uncertainties on the background estimation in signal region Rpc2L0bS for an integrated luminosity of 36.1 fb^{-1}. The individual uncertainties can be correlated and do not necessarily add up quadratically to the total uncertainty. The percentages show the size of the uncertainties relative to the total expected background.

Uncertainty of signal region	Rpc2L0bH
Total background expectation	2.35
Statistical error ($\sqrt{N_{\text{exp}}}$)	$\pm$1.53
Total background systematic	$\pm$1.00 [42.6%]
Fake lepton systematics	$\pm$0.76 [32.3%]
MC statistics	$\pm$0.49 [20.9%]
Theory uncertainty: diboson	$\pm$0.32 [13.6%]
Jet energy scale (NP-1)	$\pm$0.19 [8.1%]
Theory uncertainty: Rare	$\pm$0.14 [6.0%]
Jet energy resolution	$\pm$0.08 [3.4%]
b-jets SF	$\pm$0.06 [2.6%]
Theory uncertainty: ttW/Z	$\pm$0.06 [2.6%]
Luminosity	$\pm$0.05 [2.1%]
c-jets SF	$\pm$0.04 [1.7%]
Jet energy scale (NP-3)	$\pm$0.03 [1.3%]
Jet energy scale (NP-2)	$\pm$0.03 [1.3%]
Muon SF (sys.)	$\pm$0.02 [0.9%]
Jet vertex tagger	$\pm$0.01 [0.4%]
Light-jets SF	$\pm$0.01 [0.4%]
Electron identification SF	$\pm$0.01 [0.4%]
MET soft-term resolution 1	$\pm$0.01 [0.4%]
Electron isolation SF	$\pm$0.01 [0.4%]
Jet η-intercalibration	$\pm$0.01 [0.4%]
Flavor tagging 1	$\pm$0.01 [0.4%]

Table H.6: Breakdown of the dominant systematic uncertainties on the background estimation in signal region Rpc2L0bH for an integrated luminosity of 36.1 fb^{-1}. The individual uncertainties can be correlated and do not necessarily add up quadratically to the total uncertainty. The percentages show the size of the uncertainties relative to the total expected background.

Uncertainty of signal region	Rpc3L0bS
Total background expectation	11.02
Statistical error ($\sqrt{N_{\text{exp}}}$)	±3.32
Total background systematic	±3.02 [27.4%]
Theory uncertainty: diboson	±2.68 [24.3%]
Jet energy scale (NP-1)	±1.04 [9.4%]
Theory uncertainty: Rare	±0.44 [4.0%]
Jet energy resolution	±0.37 [3.4%]
Luminosity	±0.35 [3.2%]
MC statistics	±0.28 [2.5%]
b-jets SF	±0.21 [1.9%]
c-jets SF	±0.20 [1.8%]
Jet energy scale (NP-3)	±0.20 [1.8%]
Jet energy scale (NP-2)	±0.20 [1.8%]
Muon SF (sys.)	±0.18 [1.6%]
Fake lepton systematics	±0.18 [1.6%]
Electron identification SF	±0.17 [1.5%]
Theory uncertainty: ttW/Z	±0.16 [1.5%]
Jet vertex tagger	±0.09 [0.8%]
Electron isolation SF	±0.09 [0.8%]
MET soft-term resolution 2	±0.08 [0.7%]
Light-jets SF	±0.08 [0.7%]
Jet η-intercalibration	±0.05 [0.5%]
Electron reconstruction SF	±0.04 [0.4%]
Flavor tagging 1	±0.04 [0.4%]
Muon SF (stat.)	±0.04 [0.4%]
Muon isolation SF (sys.)	±0.03 [0.3%]
Electron charge-ID SF	±0.03 [0.3%]
MET soft-term resolution 1	±0.03 [0.3%]
Pile-up reweighting	±0.03 [0.3%]
Muon (MS reconstruction)	±0.02 [0.2%]
Muon TTVA (stat.)	±0.02 [0.2%]
EGamma scale	±0.02 [0.2%]
Muon TTVA (sys.)	±0.02 [0.2%]
Muon isolation SF (stat.)	±0.02 [0.2%]
MET soft-term scale	±0.01 [0.1%]

Table H.7: Breakdown of the dominant systematic uncertainties on the background estimation in signal region Rpc3L0bS for an integrated luminosity of 36.1 fb^{-1}. The individual uncertainties can be correlated and do not necessarily add up quadratically to the total uncertainty. The percentages show the size of the uncertainties relative to the total expected background.

Uncertainty of signal region	Rpc3L0bH
Total background expectation	3.31
Statistical error ($\sqrt{N_{\text{exp}}}$)	$\pm$1.82
Total background systematic	$\pm$0.84 [25.4%]
Theory uncertainty: diboson	$\pm$0.71 [21.5%]
Jet energy scale (NP-1)	$\pm$0.27 [8.2%]
MC statistics	$\pm$0.20 [6.0%]
Theory uncertainty: Rare	$\pm$0.17 [5.1%]
Jet energy scale (NP-2)	$\pm$0.10 [3.0%]
Luminosity	$\pm$0.10 [3.0%]
Jet energy resolution	$\pm$0.08 [2.4%]
c-jets SF	$\pm$0.07 [2.1%]
Jet energy scale (NP-3)	$\pm$0.07 [2.1%]
Muon SF (sys.)	$\pm$0.07 [2.1%]
Theory uncertainty: ttW/Z	$\pm$0.06 [1.8%]
Electron identification SF	$\pm$0.06 [1.8%]
b-jets SF	$\pm$0.06 [1.8%]
Electron isolation SF	$\pm$0.04 [1.2%]
Jet vertex tagger	$\pm$0.03 [0.9%]
Light-jets SF	$\pm$0.03 [0.9%]
Flavor tagging 1	$\pm$0.02 [0.6%]
MET soft-term resolution 1	$\pm$0.01 [0.3%]
MET soft-term resolution 2	$\pm$0.01 [0.3%]
Muon isolation SF (sys.)	$\pm$0.01 [0.3%]
Muon SF (stat.)	$\pm$0.01 [0.3%]
Electron reconstruction SF	$\pm$0.01 [0.3%]
Electron charge-ID SF	$\pm$0.01 [0.3%]
Pile-up reweighting	$\pm$0.01 [0.3%]
Muon (ID reconstruction)	$\pm$0.01 [0.3%]
Muon (MS reconstruction)	$\pm$0.01 [0.3%]
MET soft-term scale	$\pm$0.01 [0.3%]
Muon TTVA (stat.)	$\pm$0.01 [0.3%]
Jet η-intercalibration	$\pm$0.01 [0.3%]
Muon TTVA (sys.)	$\pm$0.01 [0.3%]

Table H.8: Breakdown of the dominant systematic uncertainties on the background estimation in signal region Rpc3L0bH for an integrated luminosity of 36.1 fb^{-1}. The individual uncertainties can be correlated and do not necessarily add up quadratically to the total uncertainty. The percentages show the size of the uncertainties relative to the total expected background.

Uncertainty of signal region	Rpc3L1bS
Total background expectation	17.33
Statistical error ($\sqrt{N_{\text{exp}}}$)	±4.16
Total background systematic	±4.20 [24.2%]
Fake lepton systematics	±2.86 [16.5%]
Theory uncertainty: Rare	±2.29 [13.2%]
MC statistics	±1.33 [7.7%]
Jet energy scale (NP-1)	±0.93 [5.4%]
Theory uncertainty: ttW/Z	±0.92 [5.3%]
Theory uncertainty: diboson	±0.45 [2.6%]
Luminosity	±0.42 [2.4%]
c-jets SF	±0.29 [1.7%]
Electron identification SF	±0.26 [1.5%]
b-jets SF	±0.25 [1.4%]
Muon SF (sys.)	±0.21 [1.2%]
Jet energy scale (NP-3)	±0.17 [1.0%]
Jet energy scale (NP-2)	±0.14 [0.8%]
Jet vertex tagger	±0.12 [0.7%]
Electron isolation SF	±0.11 [0.6%]
Jet η-intercalibration	±0.08 [0.5%]
MET soft-term resolution 2	±0.06 [0.3%]
Light-jets SF	±0.05 [0.3%]
Electron reconstruction SF	±0.05 [0.3%]
Muon SF (stat.)	±0.04 [0.2%]
Jet energy resolution	±0.04 [0.2%]
EGamma scale	±0.03 [0.2%]
Muon isolation SF (sys.)	±0.03 [0.2%]
MET soft-term scale	±0.03 [0.2%]
Electron charge-ID SF	±0.03 [0.2%]
Pile-up reweighting	±0.03 [0.2%]
Muon TTVA (stat.)	±0.03 [0.2%]
Muon TTVA (sys.)	±0.02 [0.1%]
Muon isolation SF (stat.)	±0.02 [0.1%]
EGamma resolution	±0.01 [0.1%]
Muon (MS reconstruction)	±0.01 [0.1%]
Flavor tagging 2	±0.01 [0.1%]
Muon low-p_{T} (sys.)	±0.01 [0.1%]

Table H.9: Breakdown of the dominant systematic uncertainties on the background estimation in signal region Rpc3L1bS for an integrated luminosity of 36.1 fb^{-1}. The individual uncertainties can be correlated and do not necessarily add up quadratically to the total uncertainty. The percentages show the size of the uncertainties relative to the total expected background.

Uncertainty of signal region	Rpc3L1bH
Total background expectation	3.90
Statistical error ($\sqrt{N_{\text{exp}}}$)	±1.97
Total background systematic	±0.94 [24.1%]
Theory uncertainty: Rare	±0.71 [18.2%]
Fake lepton systematics	±0.38 [9.7%]
MC statistics	±0.30 [7.7%]
Theory uncertainty: ttW/Z	±0.22 [5.6%]
Jet energy scale (NP-1)	±0.16 [4.1%]
Theory uncertainty: diboson	±0.15 [3.8%]
Luminosity	±0.11 [2.8%]
c-jets SF	±0.09 [2.3%]
Jet energy resolution	±0.08 [2.1%]
Electron identification SF	±0.08 [2.1%]
Muon SF (sys.)	±0.07 [1.8%]
b-jets SF	±0.05 [1.3%]
Electron isolation SF	±0.04 [1.0%]
Jet energy scale (NP-3)	±0.04 [1.0%]
Jet η-intercalibration	±0.04 [1.0%]
Light-jets SF	±0.03 [0.8%]
Jet vertex tagger	±0.03 [0.8%]
MET soft-term resolution 2	±0.02 [0.5%]
Electron reconstruction SF	±0.01 [0.3%]
MET soft-term resolution 1	±0.01 [0.3%]
MET soft-term scale	±0.01 [0.3%]
Muon SF (stat.)	±0.01 [0.3%]
Muon isolation SF (sys.)	±0.01 [0.3%]
Pile-up reweighting	±0.01 [0.3%]
Electron charge-ID SF	±0.01 [0.3%]
Jet energy scale (NP-2)	±0.01 [0.3%]
Flavor tagging 1	±0.01 [0.3%]
EGamma scale	±0.01 [0.3%]
Muon TTVA (stat.)	±0.01 [0.3%]
Muon TTVA (sys.)	±0.01 [0.3%]

Table H.10: Breakdown of the dominant systematic uncertainties on the background estimation in signal region Rpc3L1bH for an integrated luminosity of 36.1 fb^{-1}. The individual uncertainties can be correlated and do not necessarily add up quadratically to the total uncertainty. The percentages show the size of the uncertainties relative to the total expected background.

Uncertainty of signal region	Rpc2L1bS
Total background expectation	9.88
Statistical error ($\sqrt{N_{\text{exp}}}$)	±3.14
Total background systematic	±2.89 [29.3%]
Fake lepton systematics	±1.97 [19.9%]
Theory uncertainty: Rare	±1.25 [12.7%]
Jet energy scale (NP-1)	±1.14 [11.5%]
MC statistics	±0.95 [9.6%]
Theory uncertainty: ttW/Z	±0.69 [7.0%]
Luminosity	±0.23 [2.3%]
Theory uncertainty: diboson	±0.18 [1.8%]
Jet energy scale (NP-3)	±0.15 [1.5%]
Jet energy scale (NP-2)	±0.14 [1.4%]
MET soft-term resolution 2	±0.12 [1.2%]
b-jets SF	±0.11 [1.1%]
Jet energy resolution	±0.10 [1.0%]
Jet vertex tagger	±0.10 [1.0%]
MET soft-term scale	±0.09 [0.9%]
MET soft-term resolution 1	±0.08 [0.8%]
c-jets SF	±0.07 [0.7%]
Muon SF (sys.)	±0.07 [0.7%]
Electron identification SF	±0.05 [0.5%]
Charge-flip systematics	±0.04 [0.4%]
Muon (ID reconstruction)	±0.03 [0.3%]
EGamma scale	±0.02 [0.2%]
Electron isolation SF	±0.02 [0.2%]
Electron reconstruction SF	±0.02 [0.2%]
Muon SF (stat.)	±0.02 [0.2%]
Jet η-intercalibration	±0.02 [0.2%]
EGamma resolution	±0.02 [0.2%]
Flavor tagging 2	±0.01 [0.1%]
Electron charge-ID SF	±0.01 [0.1%]
Light-jets SF	±0.01 [0.1%]
Muon scale	±0.01 [0.1%]
Muon isolation SF (sys.)	±0.01 [0.1%]
Muon TTVA (stat.)	±0.01 [0.1%]
Pile-up reweighting	±0.01 [0.1%]

Table H.11: Breakdown of the dominant systematic uncertainties on the background estimation in signal region Rpc2L1bS for an integrated luminosity of 36.1 fb^{-1}. The individual uncertainties can be correlated and do not necessarily add up quadratically to the total uncertainty. The percentages show the size of the uncertainties relative to the total expected background.

Uncertainty of signal region	Rpc2L1bH
Total background expectation	9.75
Statistical error ($\sqrt{N_{\text{exp}}}$)	±3.12
Total background systematic	±2.59 [26.6%]
Fake lepton systematics	±1.76 [18.1%]
Theory uncertainty: Rare	±1.28 [13.1%]
Jet energy scale (NP-1)	±0.98 [10.1%]
MC statistics	±0.65 [6.7%]
Theory uncertainty: ttW/Z	±0.56 [5.7%]
Theory uncertainty: diboson	±0.24 [2.5%]
Luminosity	±0.23 [2.4%]
Jet energy scale (NP-2)	±0.19 [1.9%]
Jet energy scale (NP-3)	±0.19 [1.9%]
b-jets SF	±0.11 [1.1%]
Jet energy resolution	±0.11 [1.1%]
Jet vertex tagger	±0.09 [0.9%]
Muon SF (sys.)	±0.08 [0.8%]
Electron identification SF	±0.08 [0.8%]
c-jets SF	±0.07 [0.7%]
MET soft-term scale	±0.07 [0.7%]
MET soft-term resolution 2	±0.06 [0.6%]
MET soft-term resolution 1	±0.05 [0.5%]
Jet η-intercalibration	±0.05 [0.5%]
Charge-flip systematics	±0.04 [0.4%]
Electron isolation SF	±0.03 [0.3%]
Light-jets SF	±0.03 [0.3%]
Muon SF (stat.)	±0.02 [0.2%]
Muon (ID reconstruction)	±0.02 [0.2%]
Electron reconstruction SF	±0.02 [0.2%]
Electron charge-ID SF	±0.01 [0.1%]
Flavor tagging 2	±0.01 [0.1%]
Muon isolation SF (sys.)	±0.01 [0.1%]
Pile-up reweighting	±0.01 [0.1%]
EGamma resolution	±0.01 [0.1%]
Muon TTVA (stat.)	±0.01 [0.1%]
Muon (MS reconstruction)	±0.01 [0.1%]
Muon TTVA (sys.)	±0.01 [0.1%]

Table H.12: Breakdown of the dominant systematic uncertainties on the background estimation in signal region Rpc2L1bH for an integrated luminosity of 36.1 fb^{-1}. The individual uncertainties can be correlated and do not necessarily add up quadratically to the total uncertainty. The percentages show the size of the uncertainties relative to the total expected background.

Uncertainty of signal region	Rpc3LSS1b
Total background expectation	1.62
Statistical error ($\sqrt{N_{\text{exp}}}$)	$\pm$1.27
Total background systematic	$\pm$0.76 [46.9%]
Fake lepton systematics	$\pm$0.72 [44.4%]
Theory uncertainty: Rare	$\pm$0.17 [10.5%]
MC statistics	$\pm$0.15 [9.3%]
Charge-flip systematics	$\pm$0.07 [4.3%]
Luminosity	$\pm$0.01 [0.6%]
Muon SF (sys.)	$\pm$0.01 [0.6%]
Electron identification SF	$\pm$0.01 [0.6%]

Table H.13: Breakdown of the dominant systematic uncertainties on the background estimation in signal region Rpc3LSS1b for an integrated luminosity of 36.1 fb^{-1}. The individual uncertainties can be correlated and do not necessarily add up quadratically to the total uncertainty. The percentages show the size of the uncertainties relative to the total expected background.

Uncertainty of signal region	Rpv2L1bH
Total background expectation	1.57
Statistical error ($\sqrt{N_{\text{exp}}}$)	$\pm$1.25
Total background systematic	$\pm$0.44 [28.0%]
Theory uncertainty: Rare	$\pm$0.35 [22.3%]
MC statistics	$\pm$0.19 [12.1%]
Jet energy scale (NP-1)	$\pm$0.10 [6.4%]
Theory uncertainty: ttW/Z	$\pm$0.10 [6.4%]
Theory uncertainty: diboson	$\pm$0.05 [3.2%]
Luminosity	$\pm$0.04 [2.5%]
c-jets SF	$\pm$0.04 [2.5%]
Electron identification SF	$\pm$0.04 [2.5%]
Jet energy scale (NP-2)	$\pm$0.03 [1.9%]
Jet energy scale (NP-3)	$\pm$0.02 [1.3%]
Muon SF (sys.)	$\pm$0.02 [1.3%]
Electron isolation SF	$\pm$0.02 [1.3%]
MET soft-term resolution 1	$\pm$0.02 [1.3%]
Jet η-intercalibration	$\pm$0.01 [0.6%]
Jet vertex tagger	$\pm$0.01 [0.6%]
Jet energy resolution	$\pm$0.01 [0.6%]
b-jets SF	$\pm$0.01 [0.6%]
MET soft-term resolution 2	$\pm$0.01 [0.6%]
EGamma scale	$\pm$0.01 [0.6%]
Light-jets SF	$\pm$0.01 [0.6%]

Table H.14: Breakdown of the dominant systematic uncertainties on the background estimation in signal region Rpv2L1bH for an integrated luminosity of 36.1 fb^{-1}. The individual uncertainties can be correlated and do not necessarily add up quadratically to the total uncertainty. The percentages show the size of the uncertainties relative to the total expected background.

Uncertainty of signal region	Rpv2L0b
Total background expectation	1.01
Statistical error ($\sqrt{N_{\text{exp}}}$)	$\pm$1.00
Total background systematic	$\pm$0.39 [38.6%]
Fake lepton systematics	$\pm$0.23 [22.8%]
MC statistics	$\pm$0.22 [21.8%]
Theory uncertainty: diboson	$\pm$0.18 [17.8%]
Jet energy scale (NP-1)	$\pm$0.08 [7.9%]
Theory uncertainty: Rare	$\pm$0.07 [6.9%]
Theory uncertainty: ttW/Z	$\pm$0.05 [5.0%]
b-jets SF	$\pm$0.04 [4.0%]
Luminosity	$\pm$0.03 [3.0%]
Jet energy scale (NP-2)	$\pm$0.02 [2.0%]
Jet energy scale (NP-3)	$\pm$0.02 [2.0%]
c-jets SF	$\pm$0.02 [2.0%]
Jet energy resolution	$\pm$0.02 [2.0%]
Muon SF (sys.)	$\pm$0.01 [1.0%]
Flavor tagging 1	$\pm$0.01 [1.0%]
Light-jets SF	$\pm$0.01 [1.0%]
Jet vertex tagger	$\pm$0.01 [1.0%]
Jet η-intercalibration	$\pm$0.01 [1.0%]
Electron isolation SF	$\pm$0.01 [1.0%]
Electron identification SF	$\pm$0.01 [1.0%]

Table H.15: Breakdown of the dominant systematic uncertainties on the background estimation in signal region Rpv2L0b for an integrated luminosity of 36.1 fb^{-1}. The individual uncertainties can be correlated and do not necessarily add up quadratically to the total uncertainty. The percentages show the size of the uncertainties relative to the total expected background.

Uncertainty of signal region	Rpv2L2bH
Total background expectation	1.58
Statistical error ($\sqrt{N_{\text{exp}}}$)	±1.26
Total background systematic	±0.49 [31.0%]
Theory uncertainty: Rare	±0.40 [25.3%]
MC statistics	±0.19 [12.0%]
Jet energy scale (NP-1)	±0.13 [8.2%]
c-jets SF	±0.10 [6.3%]
Theory uncertainty: ttW/Z	±0.09 [5.7%]
b-jets SF	±0.06 [3.8%]
Jet energy resolution	±0.05 [3.2%]
Jet energy scale (NP-3)	±0.05 [3.2%]
Luminosity	±0.04 [2.5%]
Jet energy scale (NP-2)	±0.04 [2.5%]
Jet η-intercalibration	±0.03 [1.9%]
Electron identification SF	±0.03 [1.9%]
Flavor tagging 1	±0.02 [1.3%]
Muon SF (sys.)	±0.02 [1.3%]
Theory uncertainty: diboson	±0.02 [1.3%]
Jet vertex tagger	±0.02 [1.3%]
Electron isolation SF	±0.01 [0.6%]
Charge-flip systematics	±0.01 [0.6%]
Flavor tagging 2	±0.01 [0.6%]
Light-jets SF	±0.01 [0.6%]
EGamma resolution	±0.01 [0.6%]

Table H.16: Breakdown of the dominant systematic uncertainties on the background estimation in signal region Rpv2L2bH for an integrated luminosity of 36.1 fb^{-1}. The individual uncertainties can be correlated and do not necessarily add up quadratically to the total uncertainty. The percentages show the size of the uncertainties relative to the total expected background.

Uncertainty of signal region	Rpv2L2bS
Total background expectation	19.49
Statistical error ($\sqrt{N_{\text{exp}}}$)	±4.41
Total background systematic	±7.39 [37.9%]
Fake lepton systematics	±6.66 [34.2%]
Theory uncertainty: Rare	±2.04 [10.5%]
MC statistics	±1.94 [10.0%]
Theory uncertainty: ttW/Z	±0.98 [5.0%]
b-jets SF	±0.70 [3.6%]
Jet energy scale (NP-1)	±0.60 [3.1%]
c-jets SF	±0.37 [1.9%]
Luminosity	±0.35 [1.8%]
Electron identification SF	±0.25 [1.3%]
Jet energy scale (NP-2)	±0.18 [0.9%]
Muon SF (sys.)	±0.16 [0.8%]
Theory uncertainty: diboson	±0.13 [0.7%]
Flavor tagging 1	±0.13 [0.7%]
Jet energy scale (NP-3)	±0.12 [0.6%]
Electron isolation SF	±0.11 [0.6%]
Jet energy resolution	±0.11 [0.6%]
Jet vertex tagger	±0.10 [0.5%]
Light-jets SF	±0.07 [0.4%]
Charge-flip systematics	±0.07 [0.4%]
Jet η-intercalibration	±0.06 [0.3%]
MET soft-term resolution 1	±0.05 [0.3%]
MET soft-term resolution 2	±0.04 [0.2%]
MET soft-term scale	±0.03 [0.2%]
EGamma scale	±0.03 [0.2%]
Electron reconstruction SF	±0.03 [0.2%]
Muon SF (stat.)	±0.03 [0.2%]
Electron charge-ID SF	±0.03 [0.2%]
Muon isolation SF (sys.)	±0.02 [0.1%]
Pile-up reweighting	±0.02 [0.1%]
Muon (MS reconstruction)	±0.02 [0.1%]
Muon TTVA (stat.)	±0.02 [0.1%]
Muon TTVA (sys.)	±0.01 [0.1%]
Trigger SF	±0.01 [0.1%]
Muon isolation SF (stat.)	±0.01 [0.1%]

Table H.17: Breakdown of the dominant systematic uncertainties on the background estimation in signal region Rpv2L2bS for an integrated luminosity of 36.1 fb^{-1}. The individual uncertainties can be correlated and do not necessarily add up quadratically to the total uncertainty. The percentages show the size of the uncertainties relative to the total expected background.

Uncertainty of signal region	Rpv2L1bS
Total background expectation	24.86
Statistical error ($\sqrt{N_{\text{exp}}}$)	±4.99
Total background systematic	±6.98 [28.1%]
Fake lepton systematics	±5.68 [22.8%]
Theory uncertainty: Rare	±3.07 [12.3%]
MC statistics	±1.59 [6.4%]
Theory uncertainty: ttW/Z	±1.41 [5.7%]
Jet energy scale (NP-1)	±1.14 [4.6%]
Luminosity	±0.57 [2.3%]
Theory uncertainty: diboson	±0.50 [2.0%]
c-jets SF	±0.38 [1.5%]
Electron identification SF	±0.37 [1.5%]
Muon SF (sys.)	±0.27 [1.1%]
b-jets SF	±0.26 [1.0%]
Jet energy scale (NP-2)	±0.25 [1.0%]
Jet energy scale (NP-3)	±0.20 [0.8%]
Electron isolation SF	±0.17 [0.7%]
Jet vertex tagger	±0.15 [0.6%]
Charge-flip systematics	±0.11 [0.4%]
Jet η-intercalibration	±0.11 [0.4%]
Light-jets SF	±0.11 [0.4%]
MET soft-term resolution 2	±0.08 [0.3%]
MET soft-term resolution 1	±0.05 [0.2%]
Electron reconstruction SF	±0.05 [0.2%]
Muon SF (stat.)	±0.05 [0.2%]
Electron charge-ID SF	±0.04 [0.2%]
EGamma scale	±0.04 [0.2%]
Flavor tagging 1	±0.04 [0.2%]
Muon isolation SF (sys.)	±0.04 [0.2%]
Pile-up reweighting	±0.04 [0.2%]
MET soft-term scale	±0.03 [0.1%]
Muon TTVA (stat.)	±0.03 [0.1%]
Muon TTVA (sys.)	±0.02 [0.1%]
Jet energy resolution	±0.02 [0.1%]
Trigger SF	±0.02 [0.1%]
Muon (ID reconstruction)	±0.02 [0.1%]
Muon (MS reconstruction)	±0.02 [0.1%]

Table H.18: Breakdown of the dominant systematic uncertainties on the background estimation in signal region Rpv2L1bS for an integrated luminosity of 36.1 fb^{-1}. The individual uncertainties can be correlated and do not necessarily add up quadratically to the total uncertainty. The percentages show the size of the uncertainties relative to the total expected background.

Uncertainty of signal region	Rpv2L1bM
Total background expectation	4.80
Statistical error ($\sqrt{N_{\text{exp}}}$)	±2.19
Total background systematic	±1.56 [32.5%]
Fake lepton systematics	±1.02 [21.3%]
Theory uncertainty: Rare	±0.80 [16.7%]
MC statistics	±0.68 [14.2%]
Theory uncertainty: ttW/Z	±0.43 [9.0%]
Jet energy scale (NP-1)	±0.19 [4.0%]
Theory uncertainty: diboson	±0.13 [2.7%]
Luminosity	±0.11 [2.3%]
Electron identification SF	±0.11 [2.3%]
Jet energy scale (NP-2)	±0.08 [1.7%]
c-jets SF	±0.07 [1.5%]
Muon SF (sys.)	±0.06 [1.3%]
b-jets SF	±0.05 [1.0%]
Electron isolation SF	±0.04 [0.8%]
Jet energy scale (NP-3)	±0.04 [0.8%]
Jet energy resolution	±0.03 [0.6%]
Jet vertex tagger	±0.03 [0.6%]
Jet η-intercalibration	±0.02 [0.4%]
Charge-flip systematics	±0.02 [0.4%]
MET soft-term resolution 1	±0.01 [0.2%]
EGamma scale	±0.01 [0.2%]
Light-jets SF	±0.01 [0.2%]
Muon (MS reconstruction)	±0.01 [0.2%]
Muon SF (stat.)	±0.01 [0.2%]
MET soft-term resolution 2	±0.01 [0.2%]
Electron reconstruction SF	±0.01 [0.2%]
MET soft-term scale	±0.01 [0.2%]
Muon isolation SF (sys.)	±0.01 [0.2%]
Electron charge-ID SF	±0.01 [0.2%]
Pile-up reweighting	±0.01 [0.2%]
Muon scale	±0.01 [0.2%]

Table H.19: Breakdown of the dominant systematic uncertainties on the background estimation in signal region Rpv2L1bM for an integrated luminosity of 36.1 fb^{-1}. The individual uncertainties can be correlated and do not necessarily add up quadratically to the total uncertainty. The percentages show the size of the uncertainties relative to the total expected background.

Model $\widetilde{g} \to t\bar{t}\widetilde{\chi}_1^0$

$(m_{\widetilde{g}}, m_{\widetilde{\chi}_1^0})$ [GeV]	$\mathrm{UL}^{95}(\sigma_{\mathrm{prod}})$ [fb]	$(m_{\widetilde{g}}, m_{\widetilde{\chi}_1^0})$ [GeV]	$\mathrm{UL}^{95}(\sigma_{\mathrm{prod}})$ [fb]
(700, 490)	449.2	(1600, 1245)	38.7
(1600, 1390)	365.4	(1300, 955)	38.6
(800, 590)	349.5	(1900, 1545)	38.5
(1000, 790)	289.6	(1000, 600)	38.1
(1200, 990)	268.5	(2000, 1645)	33.7
(700, 440)	237.7	(1200, 800)	31.9
(1300, 1090)	229.1	(1400, 1000)	29.8
(1400, 1190)	220.7	(2200, 1800)	28.7
(800, 540)	217.6	(1600, 1200)	27.7
(800, 565)	217.3	(2400, 2000)	27.5
(1100, 890)	194.9	(2000, 1600)	26.9
(1100, 865)	143.6	(900, 400)	26.9
(900, 665)	139.9	(1800, 1400)	25.9
(1600, 1340)	136.2	(1100, 600)	20.1
(700, 355)	125.3	(900, 1)	20.0
(1000, 700)	124.8	(1200, 700)	19.3
(900, 640)	123.3	(900, 200)	18.6
(800, 455)	120.7	(1000, 1)	17.4
(1100, 840)	117.1	(1300, 800)	17.3
(1300, 1040)	117.0	(1000, 400)	16.8
(1000, 740)	112.3	(1900, 1400)	16.7
(1200, 965)	111.3	(1500, 1000)	16.7
(1400, 1140)	110.4	(1700, 1200)	16.4
(900, 600)	109.8	(1100, 1)	16.3
(1300, 1065)	107.9	(2100, 1600)	15.9
(1400, 1165)	107.7	(1100, 400)	15.8
(800, 500)	100.6	(1000, 200)	15.7
(1800, 1540)	97.3	(2300, 1800)	15.0
(1400, 1100)	85.3	(1200, 600)	14.9
(800, 445)	85.2	(1400, 800)	14.5
(1200, 940)	78.6	(1100, 200)	14.5
(1200, 900)	75.3	(1600, 1000)	13.7
(900, 545)	74.2	(2200, 1600)	13.1
(1100, 800)	73.2	(1200, 200)	13.1
(1300, 1000)	60.6	(2000, 1400)	13.1
(900, 555)	55.3	(1800, 1200)	13.0
(1200, 855)	50.7	(1200, 400)	12.6
(1300, 945)	48.6	(1300, 600)	12.5
(1000, 645)	48.3	(1300, 400)	12.3
(1000, 655)	48.0	(1500, 800)	12.1
(1100, 745)	48.0	(1700, 1000)	11.5
(1600, 1255)	46.7	(1400, 600)	11.3
(1200, 845)	46.5	(2100, 1400)	11.3
(1400, 1055)	41.7	(1800, 1000)	10.9
(1800, 1445)	41.1	(1600, 800)	10.9
(1500, 1145)	41.0	(1900, 1200)	10.9
(2100, 1745)	40.7	(2300, 1600)	10.6
(1100, 755)	39.5	(2200, 1400)	10.6
(1400, 1045)	39.2	(2000, 1200)	10.4
(1700, 1345)	39.1	(2400, 1600)	10.2
(1800, 1455)	38.8	(2300, 1400)	7.2

Table H.20: The 95% $\mathrm{CL_s}$ upper limits on production cross-sections (in fb) obtained using the signal efficiency and acceptance specific to each point of the $\widetilde{g} \to t\bar{t}\widetilde{\chi}_1^0$ signal grid.

Model $\widetilde{b}_1 \to t W^{\pm} \widetilde{\chi}_1^0$

$(m_{\widetilde{b}_1}, m_{\widetilde{\chi}_1^0})$ [GeV]	$\mathrm{UL}^{95}(\sigma_{\mathrm{prod}})$ [fb]	$(m_{\widetilde{b}_1}, m_{\widetilde{\chi}_1^0})$ [GeV]	$\mathrm{UL}^{95}(\sigma_{\mathrm{prod}})$ [fb]
(350, 75)	1661.1	(750, 300)	70.4
(400, 125)	787.2	(900, 500)	66.0
(400, 50)	597.7	(700, 50)	65.4
(450, 175)	584.6	(800, 350)	64.8
(400, 90)	576.8	(700, 150)	61.0
(500, 225)	385.6	(850, 400)	58.2
(450, 50)	382.0	(750, 100)	57.0
(450, 100)	350.7	(900, 450)	53.1
(450, 140)	331.2	(750, 200)	52.6
(550, 275)	314.9	(800, 50)	52.5
(500, 190)	303.9	(800, 250)	45.0
(500, 150)	290.0	(900, 50)	44.8
(600, 325)	285.0	(850, 300)	43.0
(500, 100)	229.9	(800, 150)	42.9
(550, 240)	222.7	(850, 200)	42.5
(600, 290)	222.1	(850, 100)	41.6
(650, 375)	216.0	(900, 350)	41.4
(500, 50)	204.3	(900, 150)	36.6
(700, 425)	197.6	(900, 250)	36.6
(650, 340)	187.8		
(550, 200)	177.0		
(600, 250)	172.4		
(800, 525)	164.9		
(550, 150)	160.9		
(900, 625)	152.3		
(550, 100)	151.9		
(750, 475)	150.8		
(700, 390)	150.0		
(850, 575)	145.3		
(650, 300)	138.0		
(800, 490)	134.6		
(600, 200)	132.0		
(750, 440)	122.9		
(700, 350)	118.5		
(750, 400)	112.5		
(850, 540)	111.4		
(600, 150)	109.4		
(800, 450)	108.6		
(600, 50)	108.0		
(900, 590)	107.3		
(700, 300)	106.1		
(650, 250)	101.0		
(900, 550)	93.9		
(850, 500)	93.3		
(750, 350)	91.7		
(650, 200)	89.1		
(700, 250)	76.9		
(850, 450)	75.0		
(650, 100)	74.4		
(800, 400)	72.6		

Table H.21: The 95% $\mathrm{CL_s}$ upper limits on production cross-sections (in fb) obtained using the signal efficiency and acceptance specific to each point of the $\widetilde{b}_1 \to t W^{\pm} \widetilde{\chi}_1^0$ signal grid.

Model $\widetilde{g} \to q\bar{q}(\ell\bar{\ell}/\nu\nu)\widetilde{\chi}_1^0$

$(m_{\widetilde{g}}, m_{\widetilde{\chi}_1^0})$ [GeV]	$\mathrm{UL}^{95}(\sigma_{\mathrm{prod}})$ [fb]	$(m_{\widetilde{g}}, m_{\widetilde{\chi}_1^0})$ [GeV]	$\mathrm{UL}^{95}(\sigma_{\mathrm{prod}})$ [fb]
(800, 740)	2110.4	(1400, 300)	2.4
(800, 720)	516.3	(1400, 100)	2.4
(800, 700)	217.9	(2000, 1100)	2.4
(1400, 1300)	213.1	(2000, 1100)	2.4
(1200, 1100)	212.7	(1600, 500)	2.3
(400, 240)	161.8	(1600, 100)	2.3
(600, 480)	157.5	(1800, 700)	2.2
(1000, 880)	125.2	(1600, 300)	2.2
(400, 200)	121.0	(1800, 500)	2.1
(800, 680)	113.8	(1800, 100)	2.1
(600, 440)	65.0	(2000, 900)	2.0
(600, 400)	54.9	(2200, 1100)	2.0
(800, 640)	49.7	(1800, 300)	2.0
(1000, 840)	47.5	(2000, 100)	1.9
(600, 100)	43.4	(2000, 500)	1.9
(1000, 800)	31.7	(2000, 700)	1.9
(800, 600)	31.0	(2200, 700)	1.8
(600, 300)	23.7	(2200, 900)	1.8
(800, 500)	19.2	(2000, 300)	1.8
(1000, 700)	15.1	(2200, 300)	1.8
(1200, 900)	14.4	(2200, 500)	1.8
(1400, 1100)	12.4	(2200, 100)	1.7
(1600, 1300)	11.9		
(800, 100)	11.1		
(1800, 1500)	10.6		
(1100, 700)	9.0		
(800, 300)	8.5		
(1000, 500)	7.4		
(1200, 700)	6.8		
(1600, 1100)	6.3		
(1000, 300)	6.2		
(1400, 900)	6.1		
(1100, 500)	5.9		
(2000, 1500)	5.3		
(1300, 700)	5.1		
(1800, 1300)	5.1		
(1100, 300)	5.1		
(1200, 500)	4.7		
(1800, 1100)	4.6		
(1600, 900)	4.6		
(1400, 700)	4.5		
(1200, 300)	4.4		
(1300, 500)	4.4		
(2000, 1300)	4.2		
(1000, 100)	4.1		
(1400, 500)	3.1		
(1600, 700)	2.8		
(1200, 100)	2.7		
(1300, 300)	2.7		
(1300, 100)	2.6		

Table H.22: The 95% $\mathrm{CL_s}$ upper limits on production cross-sections (in fb) obtained using the signal efficiency and acceptance specific to each point of the $\widetilde{g} \to q\bar{q}(\ell\bar{\ell}/\nu\nu)\widetilde{\chi}_1^0$ signal grid.

Model $\widetilde{g} \to q\bar{q}W^{\pm}Z\widetilde{\chi}_1^0$

$(m_{\widetilde{g}}, m_{\widetilde{\chi}_1^0})$ [GeV]	$\mathrm{UL}^{95}(\sigma_{\mathrm{prod}})$ [fb]	$(m_{\widetilde{g}}, m_{\widetilde{\chi}_1^0})$ [GeV]	$\mathrm{UL}^{95}(\sigma_{\mathrm{prod}})$ [fb]
(1000, 900)	6645.4	(1300, 400)	13.5
(600, 400)	920.0	(1400, 300)	13.1
(1000, 800)	403.5	(1800, 900)	13.0
(600, 300)	253.4	(1400, 500)	12.9
(600, 100)	252.1	(1900, 800)	12.6
(1100, 900)	249.4	(1500, 600)	12.5
(1300, 1100)	241.8	(1300, 300)	12.0
(1400, 1200)	215.6	(1400, 400)	11.9
(1200, 1000)	205.3	(1300, 100)	11.9
(1100, 800)	106.8	(1600, 700)	11.6
(1300, 1000)	84.7	(1500, 400)	11.5
(1200, 900)	83.2	(1600, 600)	11.5
(1400, 1100)	82.2	(1700, 700)	11.5
(1000, 600)	82.2	(1600, 500)	11.4
(1000, 700)	74.5	(1300, 200)	11.4
(1200, 800)	69.0	(1900, 900)	11.1
(800, 300)	68.6	(1800, 800)	11.0
(1500, 1100)	57.7	(1400, 100)	10.9
(1400, 1000)	57.7	(1400, 200)	10.9
(1300, 900)	57.6	(1500, 500)	10.9
(1100, 600)	42.3	(1700, 600)	10.6
(800, 100)	37.1	(1500, 200)	10.5
(1000, 500)	35.5	(2000, 600)	10.5
(1300, 800)	34.1	(1500, 100)	10.4
(1200, 700)	33.4	(1800, 700)	10.3
(1400, 900)	31.1	(1800, 600)	10.3
(1500, 1000)	30.6	(1500, 300)	10.2
(1100, 500)	29.9	(1900, 700)	10.1
(1200, 600)	28.2	(1600, 300)	9.8
(1600, 1000)	26.5	(2000, 400)	9.8
(1400, 800)	24.1	(2000, 800)	9.6
(1000, 300)	22.9	(1700, 400)	9.6
(1300, 700)	21.9	(1900, 100)	9.6
(1100, 400)	21.6	(1600, 400)	9.4
(1500, 900)	21.6	(2000, 900)	9.2
(1400, 700)	19.5	(1900, 400)	9.2
(1000, 100)	19.0	(1900, 300)	9.1
(1200, 500)	19.0	(1700, 500)	9.1
(1200, 400)	17.4	(2000, 700)	9.1
(1300, 600)	17.4	(1600, 100)	9.1
(1600, 900)	17.4	(1800, 200)	9.1
(1600, 800)	14.9	(2000, 100)	8.9
(1200, 300)	14.6	(1800, 500)	8.8
(1300, 500)	14.6	(1700, 200)	8.8
(1500, 800)	14.4	(1700, 100)	8.8
(1500, 700)	14.3	(1900, 500)	8.8
(1200, 100)	14.2	(1800, 400)	8.7
(1400, 600)	14.1	(2000, 500)	8.7
(1700, 900)	13.7	(1800, 300)	8.7
(1700, 800)	13.7	(2000, 300)	8.5

Table H.23: The 95% $\mathrm{CL_s}$ upper limits on production cross-sections (in fb) obtained using the signal efficiency and acceptance specific to each point of the $\widetilde{g} \to q\bar{q}W^{\pm}Z\widetilde{\chi}_1^0$ signal grid.

Model $\widetilde{g} \to q\bar{q}\widetilde{\chi}_1^0, \widetilde{\chi}_1^0 \to q\bar{q}\ell$	
$(m_{\widetilde{g}}, m_{\widetilde{\chi}_1^0})$ [GeV]	$\mathrm{UL}^{95}(\sigma_{\mathrm{prod}})$ [fb]
(2000, 50)	79.6
(1900, 50)	58.0
(1800, 50)	54.9
(1600, 50)	37.2
(1400, 50)	33.8
(1200, 50)	28.5
(1000, 50)	26.8
(1000, 100)	9.9
(1000, 125)	7.7
(1200, 120)	6.6
(1000, 950)	6.3
(1400, 140)	6.2
(1200, 150)	5.4
(1600, 160)	5.1
(1800, 180)	5.0
(1000, 250)	4.9
(1900, 190)	4.8
(1600, 200)	4.7
(1400, 175)	4.6
(1200, 1140)	4.6
(2000, 200)	4.5
(1000, 500)	4.4
(2200, 220)	4.4
(1800, 225)	4.2
(1000, 850)	4.1
(1900, 237)	4.0
(2000, 250)	3.8
(1600, 1520)	3.8
(1200, 300)	3.8
(1400, 1330)	3.6
(2200, 275)	3.6
(2200, 2090)	3.6
(1800, 1710)	3.4
(1400, 700)	3.3
(1400, 350)	3.3
(1900, 475)	3.2
(2200, 550)	3.2
(1900, 1805)	3.2
(1200, 1020)	3.2
(1600, 400)	3.2
(1800, 900)	3.1
(1200, 600)	3.1
(1800, 1530)	3.1
(1900, 950)	3.0
(2000, 500)	3.0
(1900, 1615)	3.0
(2200, 1100)	3.0
(1800, 450)	3.0
(1600, 800)	3.0
(1600, 1360)	2.9
(1400, 1190)	2.9

Table H.24: The 95% $\mathrm{CL_s}$ upper limits on production cross-sections (in fb) obtained using the signal efficiency and acceptance specific to each point of the RPV $\widetilde{g} \to q\bar{q}\widetilde{\chi}_1^0, \widetilde{\chi}_1^0 \to q\bar{q}\ell$ signal grid

Model $\widetilde{g} \to t\bar{t}\widetilde{\chi}_1^0, \widetilde{\chi}_1^0 \to uds$	
$(m_{\widetilde{g}}, m_{\widetilde{\chi}_1^0})$ [GeV]	$\mathrm{UL}^{95}(\sigma_{\mathrm{prod}})$ [fb]
(1100, 740)	13.9
(1200, 840)	10.3
(1300, 940)	8.5
(1100, 375)	7.5
(1500, 1140)	7.3
(1400, 1040)	7.0
(1800, 1440)	6.3
(1700, 1340)	6.2
(1100, 10)	6.1
(1100, 50)	6.1
(1600, 1240)	6.1
(1200, 563)	5.8
(1200, 287)	5.0
(1200, 50)	5.0
(1300, 630)	4.8
(1400, 783)	4.7
(1200, 10)	4.4
(1300, 320)	4.2
(1600, 994)	4.1
(1500, 858)	4.1
(1300, 50)	3.9
(1800, 1202)	3.8
(1700, 1118)	3.7
(1300, 10)	3.7
(1800, 963)	3.6
(1800, 725)	3.5
(1400, 525)	3.5
(1500, 575)	3.5
(1600, 748)	3.4
(1700, 50)	3.3
(1400, 10)	3.3
(1500, 293)	3.3
(1600, 50)	3.2
(1400, 50)	3.1
(1400, 268)	3.1
(2000, 243)	3.0
(1500, 10)	3.0
(1800, 10)	3.0
(1700, 10)	3.0
(1700, 675)	3.0
(1800, 248)	3.0
(1600, 256)	2.9
(1600, 502)	2.9
(2000, 10)	2.9
(1600, 10)	2.9
(2000, 50)	2.8
(1800, 50)	2.8
(1700, 453)	2.8
(1700, 232)	2.8
(2000, 476)	2.7
(1800, 487)	2.7

Table H.25: The 95% $\mathrm{CL_s}$ upper limits on production cross-sections (in fb) obtained using the signal efficiency and acceptance specific to each point of the RPV $\widetilde{g} \to t\bar{t}\widetilde{\chi}_1^0, \widetilde{\chi}_1^0 \to uds$ signal grid.

Model $\widetilde{g} \to tbd$	
$(m_{\widetilde{g}}, m_{\widetilde{\chi}_1^0})$ [GeV]	$\mathrm{UL}^{95}(\sigma_{\mathrm{prod}})$ [fb]
(800, 400)	344.8
(800, 600)	303.3
(1000, 800)	111.6
(1000, 600)	110.9
(1000, 400)	88.4
(1200, 1000)	66.5
(1200, 400)	41.1
(1200, 600)	34.6
(1400, 1200)	34.5
(1200, 800)	32.7
(1800, 1600)	31.0
(1600, 1400)	29.2
(1400, 600)	25.7
(1400, 400)	21.7
(1400, 1000)	20.6
(1400, 800)	20.0
(1600, 400)	19.7
(1600, 1200)	18.6
(1600, 800)	17.8
(1800, 400)	16.7
(1800, 1000)	16.6
(1800, 1200)	16.1
(1800, 1400)	15.5
(1800, 600)	15.5
(1600, 600)	15.1
(1800, 800)	13.4
(1600, 1000)	8.8
Model $\widetilde{g} \to tsd$	
(800, 600)	326.0
(1000, 800)	96.5
(1000, 600)	70.5
(1200, 1000)	48.5
(1200, 800)	47.0
(1400, 1200)	45.6
(1800, 1600)	41.0
(1200, 600)	39.4
(1600, 1400)	28.3
(1400, 1000)	24.3
(1400, 600)	22.4
(1400, 800)	21.8
(1800, 1400)	21.4
(1800, 400)	20.7
(1600, 600)	20.4
(1600, 400)	20.3
(1800, 1200)	19.6
(1600, 1200)	19.4
(1800, 800)	18.3
(1600, 800)	17.4
(1800, 1000)	17.3
(1600, 1000)	16.4
(1800, 600)	14.8

Table H.26: The 95% $\mathrm{CL_s}$ upper limits on production cross-sections (in fb) obtained using the signal efficiency and acceptance specific to each point of the RPV $\widetilde{g} \to tbd$ (top) and $\widetilde{g} \to tsd$ (bottom) signal grid.

BIBLIOGRAPHY

[1] *First beam in the LHC - Accelerating science (press release)* CERN Press Office. 10 September 2008. Retrieved 2008-10-09. URL: https://press.cern/press-releases/2008/09.

[2] ATLAS Collaboration, *The ATLAS Experiment at the CERN Large Hadron Collider*, 2008, JINST **3** (2008) S08003.

[3] CMS Collaboration, *The CMS Experiment at the CERN LHC*, 2008, JINST **3** (2008) S08004.

[4] ATLAS Collaboration, *Search for supersymmetry at $\sqrt{s}$ = 8 TeV in final states with jets and two same-sign leptons or three leptons with he ATLAS detector*, 2014, JHEP **1406** (2014) 035, arXiv:1404.2500 [hep-ex].

[5] Borschensky et al., *Squark and gluino production cross sections in pp collisions at $\sqrt{s}$ = 13, 14, 33 and 100 TeV*, 2014, Eur. Phys. J. **C74** (2014) 3174, arXiv:1407.5066 [hep-ph].

[6] ATLAS Collaboration, *Search for supersymmetry at $\sqrt{s}$ = 13 TeV in final states with jets and two same-sign leptons or three leptons with the ATLAS detector*, 2016, Eur. Phys. J. **C76** (2016) 259, arXiv:1602.09058 [hep-ex].

[7] ATLAS Collaboration, *Search for supersymmetry with two same-sign leptons or three leptons using 13.2 fb^{-1} of $\sqrt{s}$ = 13 TeV pp collision data collected by the ATLAS detector*, ATLAS-CONF-2016-037, 2016, URL: http://inspirehep.net/record/1479668.

[8] ATLAS Collaboration, *Search for supersymmetry in final states with two same-sign or three leptons and jets using 36 fb^{-1} of $\sqrt{s}$=13 TeV pp collision data with the ATLAS detector*, 2017, JHEP **09** (2017) 084, arXiv:1706.03731 [hep-ex].

[9] P. W. Higgs, *Broken Symmetry and the Mass of Gauge Vector Mesons*, 1964, Phys. Rev. Lett. **13** (1964) 508.

[10] F. Englert and R. Brout, *Broken Symmetry and the Mass of Gauge Vector Mesons*, 1964, Phys. Rev. Lett. **13** (1964) 321.

[11] Particle Data Group, Patrignani et al., *Review of Particle Physics*, 2016, Chin. Phys. **C40** (2016) 100001.

[12] Super-Kamiokande Collaboration (super-K), *Evidence for oscillation of atmospheric neutrinos*, 1998, Phys. Rev. Lett. **81** (1998) 1562, arXiv:hep-ex/9807003 [hep-ex].

[13] H. D. Politzer, *Reliable Perturbative Results for Strong Interactions?*, 1973, Phys. Rev. Lett. **30** (1973) 1346.

[14] ATLAS Collaboration, *Observation of a new particle in the search for the Standard Model Higgs boson with the ATLAS detector at the LHC*, 2012, Phys. Lett. **B716** (2012) 1, arXiv:1207.7214 [hep-ex].

[15] CMS Collaboration, *Observation of a new boson at a mass of 125 GeV with the CMS experiment at the LHC*, 2012, Phys. Lett. **B716** (2012) 30, arXiv:1207.7235 [hep-ex].

[16] ATLAS and CMS Collaboration, *Combined Measurement of the Higgs Boson Mass in pp Collisions at $\sqrt{s}$ = 7 and 8 TeV with the ATLAS and CMS Experiments*, 2015, Phys. Rev. Lett. **114** (2015) 191803, arXiv:1503.07589 [hep-ex].

[17] CMS Collaboration, *Measurement of the top quark mass using proton-proton data at $\sqrt{s}$ = 7 and 8 TeV*, 2016, Phys. Rev. **D93** (2016) 072004, arXiv:1509.04044 [hep-ex].

[18] CERN, Science and Technology Facilities Council, *The Standard Model of Particle Physics* URL: http://www.stfc.ac.uk/research.

[19] E. Fermi, *Tentativo di una teoria dei raggi β*, 1934, Nuovo Cimento **11** (1934) 1.

[20] T. D. Lee and C. N. Yang, *Question of Parity Conservation in Weak Interactions*, 1956, Phys. Rev. **104** (1956) 254.

[21] Wu et al., *Experimental Test of Parity Conservation in Beta Decay*, 1957, Phys. Rev. **105** (1957) 1413.

[22] C. N. Yang and R. L. Mills, *Conservation of Isotopic Spin and Isotopic Gauge Invariance*, 1954, Phys. Rev. **96** (1954) 191.

[23] S. L. Glashow, *Partial Symmetries of Weak Interactions*, 1961, Nulc. Phys. **22** (1961) 579.

[24] A. Salam, *Weak and Electromagnetic Interactions*, 1968, Conf. Proc. **C680519** (1968) 367, URL: http://inspirehep.net/record/53083.

[25] S. Weinberg, *A model of leptons*, 1967, Phys. Rev. Lett. **19** (1967) 1264.

[26] T. Nakano and K. Nishijima, *Charge Independence for V-particles*, 1953, Progress of Theoretical Physics **10** (1953) 581.

[27] N. Cabibbo, *Unitary Symmetry and Leptonic Decays*, 1963, Phys. Rev. Lett. **10** (1963) 531.

[28] M. Kobayashi and T. Maskawa, *CP-Violation in the Renormalizable Theory of Weak Interaction*, 1973, Progress of Theoretical Physics **49** (1973) 652.

[29] A. J. Macfarlane and A. Sudbery and P. H. Weisz, *On Gell-Mann's λ-matrices, d- and f-tensors, octets, and parametrizations of SU(3)*, 1968, Comm. in Mathematical Physics **11** (1968) 77.

[30] D. J. Gross and F. Wilczek, *Ultraviolet Behavior of Non-Abelian Gauge Theories*, 1973, Phys. Rev. Lett. **30** (1973) 1343.

[31] H. D. Politzer, *Reliable Perturbative Results for Strong Interactions?*, 1973, Phys. Rev. Lett. **30** (1973) 1346.

[32] G. t'Hooft and M. Veltman, *Regularization and renormalization of gauge fields*, 1972, Nucl. Phys. **B44** (1972) 189.

[33] CMS Collaboration, W. de Boer, *The Discovery of the Higgs Boson with the CMS Detector and its Implications for Supersymmetry and Cosmology*, 2013, arXiv:1309.0721 [hep-ph].

[34] J. Goldstone and A. Salam and S. Weinberg, *Broken Symmetries*, 1962, Phys. Rev. **127** (1962) 965.

[35] J. Glimm, *The Yukawa coupling of quantum fields in two dimensions. II*, 1967, Comm. Math. Phys. **6** (1967) 61, URL: http://projecteuclid.org/euclid.cmp/1103840171.

[36] H. Georgi and S. L. Glashow, *Unity of All Elementary-Particle Forces*, 1974, Phys. Rev. Lett. **32** (1974) 438.

[37] LIGO Scientific Collaboration and Virgo Collaboration, *Observation of Gravitational Waves from a Binary Black Hole Merger*, 2016, Phys. Rev. Lett. **116** (2016) 061102.

[38] Z. Maki and M. Nakagawa and S. Sakata, *Remarks on the Unified Model of Elementary Particles*, 1962, Progress of Theoretical Physics **28** (1962) 870.

[39] J. H. Christenson and J. W. Cronin and V. L. Fitch and R. Turlay, *Evidence for the* 2π *Decay of the* K_2^0 *Meson*, 1964, Phys. Rev. Lett. **13** (1964) 138.

[40] BABAR Collaboration, *Measurement of CP-Violating Asymmetries in* B^0 *Decays to CP Eigenstates*, 2001, Phys. Rev. Lett. **86** (2001) 2515.

[41] Belle Collaboration, *Observation of Large CP Violation in the Neutral B Meson System*, 2001, Phys. Rev. Lett. **87** (2001) 091802.

[42] R. D. Peccei and H. R. Quinn, *CP Conservation in the Presence of Pseudoparticles*, 1977, Phys. Rev. Lett. **38** (1977) 1440.

[43] V. Trimble, *Existence and Nature of Dark Matter in the Universe*, 1987, Annual Review of Astronomy and Astrophysics **25** (1987) 425.

[44] G. Goldhaber, *The Acceleration of the Expansion of the Universe: A Brief Early History of the Supernova Cosmology Project (SCP)*, 2009, AIP Conference Proceedings **1166** (2009) 53.

[45] *Dark Energy, Dark Matter* NASA Science: Astrophysics. June 5, 2015. URL: https://science.nasa.gov/astrophysics/focus-areas/what-is-dark-energy.

[46] Clowe et al., *A direct empirical proof of the existence of dark matter*, 2006, Astrophys. J. **648** (2006) L109–L113, arXiv:astro-ph/0608407 [astro-ph].

[47] J. A. Golfand and A. Yu and E. P. Likhtman, *Extension of the algebra of Poincaré group generators and violation of P invariance*, 1971, JETP Lett. **13** (1971) 323.

[48] D. V. Volkov and P. Akulov, *Is the neutrino a Goldstone particle?*, 1973, Phys. Lett. **B46** (1973) 109.

[49] J. Wess and B. Zumino, *Supergauge transformations in four dimensions*, 1974, Nucl. Phys. **B70** (1974) 39.

[50] A. Salam and J. Strathdee, *Super-symmetry and non-Abelian gauges*, 1974, Phys. Lett. **B51** (1974) 353.

[51] J. Wess and B. Zumino, *Supergauge invariant extension of quantum electrodynamics*, 1974, Nucl. Phys. **B78** (1974) 1.

[52] S. Ferrara and B. Zumino, *Supergauge invariant Yang-Mills theories*, 1974, Nucl. Phys. **B79** (1974) 413.

[53] S. Coleman and J. Mandula, *All Possible Symmetries of the S Matrix*, 1967, Phys. Rev. **159** (1967) 1251.

[54] R. Haag and J. T. Lopuszanski and M. Sohnius, *All possible generators of supersymmetries of the S matrix*, 1975, Nucl. Phys. **B88** (1975) 257.

[55] S. Dimopoulos and H. Georgi, *Softly broken supersymmetry and SU(5)*, 1981, Nucl. Phys. **B193** (1981) 150.

[56] S. Dimopoulos and S. Raby and F. Wilczek, *Supersymmetry and the scale of unification*, 1981, Phys. Rev. **D24** (1981) 1681.

[57] The Nobel Prize in Physics 2004, *Can the forces of Nature be unified?* URL: https://www.nobelprize.org/nobel_prizes/physics/laureates/2004/phypub4highen.jpg.

[58] S. P. Martin, *A Supersymmetry primer*, 1997, Adv. Ser. Direct. High Energy Phys. **18** (1997) 1, arXiv:hep-ph/9709356 [hep-ph].

[59] R. Barbieri and S. Ferrara and C. A. Savoy, *Gauge models with spontaneously broken local supersymmetry*, 1982, Phys. Lett. **B119** (1982) 343.

[60] M. Dine and A. E. Nelson, *Dynamical supersymmetry breaking at low-energies*, 1993, Phys. Rev. **D48** (1993) 1277, arXiv:hep-ph/9303230 [hep-ph].

[61] P. Binetruy and E. Dudas, *Gaugino condensation and the anomalous U(1)*, 1996, Phys. Lett. **B389** (1996) 503, arXiv:hep-th/9607172 [hep-th].

[62] L. J. Hall and D. Pinner and J. T. Ruderman, *A Natural SUSY Higgs Near 126 GeV*, 2012, JHEP **04** (2012) 131, arXiv:1112.2703 [hep-ph].

[63] N. Craig, *The State of Supersymmetry after Run I of the LHC*, 2013, arXiv:1309.0528 [hep-ph].

[64] M. Maniatis, *The Next-to-Minimal Supersymmetric extension of the Standard Model reviewed*, 2010, Int. J. Mod. Phys. **A25** (2010) 3505, arXiv:0906.0777 [hep-ph].

[65] M. Cahill-Rowley and J. L. Hewett and A. Ismail and T. G. Rizzo, *pMSSM Studies at the 7, 8 and 14 TeV LHC*, 2013, arXiv:1307.8444 [hep-ph].

[66] G. L. Kane and C. Kolda and L. Roszkowski and J. D. Wells, *Study of constrained minimal supersymmetry*, 1994, Phys. Rev. **D49** (1994) 6173.

[67] T. Kaluza, *Zum Unitätsproblem in der Physik*, 1921, Sitzungsber. Preuss. Aka. der Wissenschaften (1921) 966, URL: https://archive.org/details/sitzungsberichte1921preussi.

[68] O. Klein, *Quantentheorie und fünfdimensionale Relativitätstheorie*, 1926, Zeitschrift für Physik **37** (1926) 895.

[69] A. Djouadi and G. Moreau and R. K. Singh, *Kaluza-Klein excitations of gauge bosons at the LHC*, 2008, Nucl. Phys. **B797** (2008) 1, arXiv:0706.4191 [hep-ph].

[70] L. Randall and R. Sundrum, *Large Mass Hierarchy from a Small Extra Dimension*, 1999, Phys. Rev. Lett. **83** (1999) 3370.

[71] C. Lovelace, *Pomeron form factors and dual Regge cuts*, 1971, Phys. Lett. **B34** (1971) 500.

[72] J. Scherk and J. H. Schwarz, *Dual models for non-hadrons*, 1974, Nucl. Phys. **B81** (1974) 118.

[73] M. B. Green and J. H. Schwarz, *Superstring field theory*, 1984, Nucl. Phys. **B243** (1984) 475.

[74] E. Farhi and L. Susskind, *Technicolour*, 1981, Physics Reports **74** (1981) 277.

[75] S. Dimopoulos and L. Susskind, *Mass without scalars*, 1979, Nucl. Phys. **B155** (1979) 237.

[76] CAST Collaboration, Aune et al., *Solar axion search with the CAST experiment*, 2008, arXiv:0810.1874 [hep-ex].

[77] ADMX Collaboration, D. Lyapustin, *The Axion Dark Matter eXperiment*, 2011, arXiv:1112.1167 [astro-ph].

[78] D. Borah, *Abelian Extension of Standard Model with Four Generations*, 2012, Phys. Rev. **D85** (2012) 015006, arXiv:1109.3363 [hep-ph].

[79] A. Lenz, *Constraints on a Fourth Generation of Fermions from Higgs Boson Searches*, 2013, Advances in High Energy Physics **2013** (2013) 13.

[80] P. Langacker, *The Physics of Heavy Z' Gauge Bosons*, 2009, Rev. Mod. Phys. **81** (2009) 1199, arXiv:0801.1345 [hep-ph].

[81] F. Villatoro, *Standard Model 4 generations* URL: http://francis.naukas.com/?attachment_id=26695.

[82] M. Lindner and T. Ohlsson and G. Seidl, *Seesaw mechanisms for Dirac and Majorana neutrino masses*, 2002, Phys. Rev. **D65** (2002) 053014, arXiv:hep-ph/0109264 [hep-ph].

[83] E. Majorana, *Teoria simetrica dell'elettrone e del positrone*, 1937, Nuovo Cimento **14** (1937) 171.

[84] P. H. Gu and H. Zhang and S. Zhou, *A Minimal Type II Seesaw Model*, 2006, Phys. Rev. **D74** (2006) 076002, arXiv:hep-ph/0606302 [hep-ph].

[85] E. D. Courant and H. S. Snyder, *Theory of the alternating-gradient synchrotron*, 1958, Annals of Physics **3** (1958) 1.

[86] LHC Machine Outreach, *Relative beam sizes around IP1 (Atlas) in collision* URL: https://lhc-machine-outreach.web.cern.ch/lhc-machine-outreach.

[87] V. N. Gribov and L. N. Lipatov, *Deep inelastic ep scattering in perturbation theory*, 1972, Sov. J. Nucl. Phys. **15** (1972) 438, Yad. Fiz.15,781(1972).

[88] Y. L. Dokshitzer, *Calculation of the Structure Functions for Deep Inelastic Scattering and e^+e^- Annihilation by Perturbation Theory in Quantum Chromodynamics*, 1977, Sov. Phys. JETP **46** (1977) 641, Zh. Eksp. Teor. Fiz.73,1216(1977).

[89] G. Altarelli and G. Parisi, *Asymptotic freedom in parton language*, 1977, Nucl. Phys. **B126** (1977) 298.

[90] S. Forte and G. Watt, *Progress in the Determination of the Partonic Structure of the Proton*, 2013, Ann. Rev. Nucl. Part. Sci. **63** (2013) 291, arXiv:1301.6754 [hep-ph].

[91] Dulat et al., *New parton distribution functions from a global analysis of quantum chromodynamics*, 2016, Phys. Rev. **D93** (2016) 033006, arXiv:1506.07443 [hep-ph].

[92] A. D. Martin and W. J. Stirling and R. S. Thorne and G. Watt, *Parton distributions for the LHC*, 2009, Eur. Phys. J. **C63** (2009) 189, arXiv:0901.0002 [hep-ph].

[93] NNPDF Collaboration, Ball et al., *Parton distributions for the LHC Run II*, 2015, JHEP **04** (2015) 040, arXiv:1410.8849 [hep-ph].

[94] M. R. Whalley and D. Bourilkov and R. C. Group, *The Les Houches accord PDFs (LHAPDF) and LHAGLUE*, 2005, arXiv:hep-ph/0508110 [hep-ph].

[95] M. H. Seymour and M. Marx, *Monte Carlo Event Generators*, 2013, Proc. SUSSP **69** (2013) 287, arXiv:1304.6677 [hep-ph].

[96] S. Hoeche, *Introduction to parton-shower event generators* URL: http://inspirehep.net/record/1328513.

[97] S. Hoeche and Y. Li and S. Prestel, *Combining parton showers and NNLO matrix elements*, 2015, Moriond QCD Conf. Proc. **50** (2015) 135, arXiv:1507.05325 [hep-ph].

[98] J. C. Collins, *Sudakov form-factors*, 1989, Adv. Ser. Direct. High Energy Phys. **5** (1989) 573, arXiv:hep-ph/0312336 [hep-ph].

[99] T. Sjöstrand, *A model for initial state parton showers*, 1985, Phys. Lett. **B157** (1985) 321.

[100] T. Sjöstrand and S. Mrenna and P. Z. Skands, *A Brief Introduction to PYTHIA 8.1*, 2008, Comput. Phys. Commun. **178** (2008) 852, arXiv:0710.3820 [hep-ph].

[101] Gleisberg et al., *Event generation with SHERPA 1.1*, 2009, JHEP **02** (2009) 007, arXiv:0811.4622 [hep-ph].

[102] S. Platzer and S. Gieseke, *Dipole Showers and Automated NLO Matching in Herwig++*, 2012, Eur. Phys. J. **C72** (2012) 2187, arXiv:1109.6256 [hep-ph].

[103] K. G. Wilson, *Confinement of quarks*, 1974, Phys. Rev. **D10** (1974) 2445.

[104] W. Bietenholz, *Hadron Physics from Lattice QCD*, 2016, Int. J. Mod. Phys. **E25** (2016) 1642008, arXiv:1605.08103 [hep-ph].

[105] D. Amati and G. Veneziano, *Preconfinement as a property of perturbative QCD*, 1979, Phys. Lett **B83** (1979) 87.

[106] B. Andersson and G. Gustafson and G. Ingelman and T. Sjöstrand, *Parton fragmentation and string dynamics*, 1983, Physics Reports **97** (1983) 31.

[107] D. J. Lange, *The EvtGen particle decay simulation package*, 2001, Nucl. Instrum. Meth. **A462** (2001) 152.

[108] R. Field, *Underlying event in hadronic collisions*, 2012, Ann. Rev. Nucl. Part. Sci. **62** (2012) 453.

[109] ATLAS Collaboration, *Luminosity Public Results for Run-2* URL: https://twiki.cern.ch/twiki/bin/view/AtlasPublic/LuminosityPublicResultsRun2.

[110] Agostinelli et al., *Geant4 - a simulation toolkit*, 2003, Nucl. Instrum. Meth. **A506** (2003) 250.

[111] Allison et al., *Recent developments in Geant4*, 2016, Nucl. Instrum. Meth. **A835** (2016) 186.

[112] ATLAS Collaboration, *The ATLAS Simulation Infrastructure*, 2010, Eur. Phys. J. **C70** (2010) 823.

[113] *CERN Annual Personnel Statistics 2015* CERN-HR-STAFF-STAT-2015. URL: https://cds.cern.ch/record/2154389.

[114] UA1 Collaboration, *Experimental Observation of Lepton Pairs of Invariant Mass Around 95 GeV/c^2 at the CERN SPS Collider*, 1983, Phys. Lett. **B126** (1983) 398.

[115] UA1 Collaboration, *Experimental observation of isolated large transverse energy electrons with associated missing energy at $\sqrt{s}$=540 GeV*, 1983, Phys. Lett. **B122** (1983) 103.

[116] UA2 Collaboration, *Evidence for $Z^0 \to e^+e^-$ at the CERN pp collider*, 1983, Phys. Lett. **B129** (1983) 130.

[117] UA2 Collaboration, *Observation of Single Isolated Electrons of High Transverse Momentum in Events with Missing Transverse Energy at the CERN anti-pp Collider*, 1983, Phys. Lett. **B122** (1983) 476.

[118] NA48 Collaboration, *A New measurement of direct CP violation in two pion decays of the neutral kaon*, 1999, Phys. Lett. **B465** (1999) 335, arXiv:hep-ex/9909022 [hep-ex].

[119] Brüning et al., *LHC Design Report*, CERN, Geneva, 2004, URL: https://cds.cern.ch/record/782076.

[120] LEP Study Group, *LEP design report*, CERN, Geneva, 1984, URL: https://cds.cern.ch/record/102083.

[121] Educational Observatory Resources, *CERN Accelerators* URL: http://edu-observatory.org/RaySociety/CosmicRays/iu.png.

[122] J. L. Caron, *LHC quadrupole cross section.* 1998, . URL: http://cds.cern.ch/record/841485.

[123] ALICE Collaboration, *The ALICE experiment at the CERN LHC*, 2008, JINST **3** (2008) S08002.

[124] LHCb Collaboration, *The LHCb Detector at the LHC*, 2008, JINST **3** (2008) S08005.

[125] LHCf Collaboration, *The LHCf detector at the CERN Large Hadron Collider*, 2008, Journal of Instrumentation **3** (2008) S08006.

[126] TOTEM Collaboration, *The TOTEM Experiment at the CERN Large Hadron Collider*, 2008, Journal of Instrumentation **3** (2008) S08007.

[127] MoEDAL Collaboration, *Technical Design Report of the MoEDAL Experiment*, 2009, URL: http://inspirehep.net/record/1299494.

[128] ATLAS Collaboration, K. Sliwa, *ATLAS Overview and Main Results*, 2013, arXiv:1305.4551 [hep-ex].

[129] ATLAS Collaboration, *ATLAS inner detector: Technical Design Report, 1*, CERN, Geneva, 1997, URL: https://cds.cern.ch/record/331063.

[130] ATLAS Collaboration, *ATLAS inner detector: Technical Design Report, 2*, CERN, Geneva, 1997, URL: https://cds.cern.ch/record/331064.

[131] ATLAS Collaboration, *ATLAS Insertable B-Layer Technical Design Report*, ATLAS-TDR-19, 2010, URL: http://inspirehep.net/record/1609508.

[132] ATLAS Collaboration, K. Potamianos, *The upgraded Pixel detector and the commissioning of the Inner Detector tracking of the ATLAS experiment for Run-2 at the Large Hadron Collider*, 2015, arXiv:1608.07850 [physics.ins-det].

[133] ATLAS Collaboration, *ATLAS liquid-argon calorimeter: Technical Design Report*, CERN, Geneva, 1996, URL: https://cds.cern.ch/record/331061.

[134] ATLAS Collaboration, *ATLAS tile calorimeter: Technical Design Report*, CERN, Geneva, 1996, URL: https://cds.cern.ch/record/331062.

[135] A. Artamonov et al., *The ATLAS Forward Calorimeter*, 2008, Journal of Instrumentation **3** (2008) P02010.

[136] ATLAS Collaboration, *ATLAS muon spectrometer: Technical design report*, CERN, Geneva, 1997, URL: https://cds.cern.ch/record/331068.

[137] ATLAS Collaboration, *ATLAS high-level trigger, data-acquisition and controls: Technical Design Report*, CERN, Geneva, 2003, URL: https://cds.cern.ch/record/616089.

[138] ATLAS Collaboration, A. Ruiz Martinez, *The Run-2 ATLAS Trigger System*, 2015, J. Phys. Conf. Ser. **762** (2015) 012003.

[139] ATLAS Collaboration, *Performance of the ATLAS Trigger System in 2015*, 2017, Eur. Phys. J. **C77** (2017) 317, arXiv:1611.09661 [hep-ex].

[140] ATLAS Collaboration, E. Simioni, *The Topological Processor for the future ATLAS Level-1 Trigger: from design to commissioning*, 2014, arXiv:1406.4316 [physics.ins-det].

[141] Annovi et al., *Fast TracKer (FTK) Technical Design Report*, CERN, Geneva, 2013, URL: http://inspirehep.net/record/1614084.

[142] Eck et al., *LHC computing Grid : Technical Design Report*, CERN, Geneva, 2005, URL: http://inspirehep.net/record/692916.

[143] Abdel Khalek et al., *The ALFA Roman Pot detectors of ATLAS*, 2016, Journal of Instrumentation **11** (2016) P11013.

[144] F. Lasagni Manghi et al., *The LUCID detector ATLAS luminosity monitor and its electronic system*, 2016, Nucl. Instrum. Meth. **824** (2016) 311.

[145] ATLAS Collaboration, O. Viazlo, *ATLAS LUCID detector upgrade for LHC Run 2*, ATL-FWD-PROC-2015-004, 2015, URL: https://cds.cern.ch/record/2062038.

[146] S. Abdel Khalek et al., *The ALFA Roman Pot detectors of ATLAS*, 2016, Journal of Instrumentation **11** (2016) P11013.

[147] S. van der Meer, *Calibration of the effective beam height in the ISR*, CERN, Geneva, 1968, URL: https://cds.cern.ch/record/296752, CERN-ISR-PO-68-31. ISR-PO-68-31.

[148] ATLAS Collaboration, *Luminosity determination in pp collisions at $\sqrt{s}$=8 TeV using the ATLAS detector at the LHC*, 2016, Eur. Phys. J. **C76** (2016) 653, arXiv:1608.03953 [hep-ex].

[149] ATLAS Collaboration, F. Pastore, *ATLAS Run-2 status and performance*, 2016, Nucl. Part. Phys. Proc. **270** (2016) 3.

[150] ATLAS Collaboration, *Muon reconstruction performance of the ATLAS detector in proton-proton collision data at $\sqrt{s}$=13 TeV*, 2016, Eur. Phys. J. **C76** (2016) 292, arXiv:1603.05598 [hep-ex].

[151] Cornelissen et al., *Concepts, Design and Implementation of the ATLAS New Tracking (NEWT)*, ATL-SOFT-PUB-2007-007, 2007, URL: http://inspirehep.net/record/1197243.

[152] ATLAS Collaboration, *Track Reconstruction Performance of the ATLAS Inner Detector at $\sqrt{s}$=13 TeV*, ATLAS-PHYS-PUB-2015-018, 2015, URL: http://cds.cern.ch/record/2037683.

[153] ATLAS Collaboration, *Measurement of the muon reconstruction performance of the ATLAS detector using 2011 and 2012 LHC proton-proton collision data*, 2014, Eur. Phys. J. **C74** (2014) 3130, arXiv:1407.3935 [hep-ex].

[154] Alioli et al., *A general framework for implementing NLO calculations in shower Monte Carlo programs: the POWHEG BOX*, 2010, JHEP **06** (2010) 043, arXiv:1002.2581 [hep-ph].

[155] J. W. Fowler, *Maximum-likelihood fits to histograms for improved parameter estimation*, 2014, J. Low Temp. Physics **176** (2014) 414, arXiv:1312.5622 [physics.data-an].

[156] M. Oreglia, *A Study of the Reactions $\psi' \to \gamma\gamma\psi$*, SLAC-R-0236, 1980, URL: http://www.slac.stanford.edu/pubs/slacreports/slac-r-236.html.

[157] ATLAS Collaboration, *Electron efficiency measurements with the ATLAS detector using the 2015 LHC proton-proton collision data*, ATLAS-CONF-2016-024, 2016, URL: http://inspirehep.net/record/1467063.

[158] W. Lampl et al., *Calorimeter Clustering Algorithms: Description and Performance*, ATL-LARG-PUB-2008-002, 2008, URL: http://inspirehep.net/record/807147.

[159] ATLAS Collaboration, *Improved electron reconstruction in ATLAS using the Gaussian Sum Filter-based model for bremsstrahlung*, ATLAS-CONF-2012-047, 2012, URL: http://inspirehep.net/record/1204271.

[160] ATLAS Collaboration, *Electron and photon energy calibration with the ATLAS detector using LHC Run 1 data*, 2014, Eur. Phys. J. **C74** (2014) 3071, arXiv:1407.5063 [hep-ex].

[161] ATLAS Collaboration, *Electron and photon energy calibration with the ATLAS detector using data collected in 2015 at $\sqrt{s}$=13 TeV*, ATL-PHYS-PUB-2016-015, 2016, URL: http://cds.cern.ch/record/2203514.

[162] R. Atkin, *Review of jet reconstruction algorithms*, 2015, J. Phys. Conf. Ser. **645** (2015) 012008.

[163] ATLAS Collaboration, *Topological cell clustering in the ATLAS calorimeters and its performance in LHC Run 1*, 2017, Eur. Phys. J. **C77** (2017) 490, arXiv:1603.02934 [hep-ex].

[164] Catani et al., *Longitudinally invariant K_t clustering algorithms for hadron hadron collisions*, 1993, Nucl. Phys. **B406** (1993) 187.

[165] M. Cacciari and G. P. Salam and G. Soyez, *The anti-k_t jet clustering algorithm*, 2008, JHEP **2008** (2008) 063, arXiv:0802.1189 [hep-ph].

[166] CMS Collaboration, *A Cambridge-Aachen (C-A) based Jet Algorithm for boosted top-jet tagging*, 2009, URL: https://inspirehep.net/record/925377.

[167] M. Cacciari and G. P. Salam and G. Soyez, *FastJet User Manual*, 2012, Eur. Phys. J. **C72** (2012) 1896, arXiv:1111.6097 [hep-ph].

[168] ATLAS Collaboration, *Jet energy scale measurements and their systematic uncertainties in proton-proton collisions at $\sqrt{s} = 13$ TeV with the ATLAS detector*, 2017, arXiv:1703.09665 [hep-ex].

[169] M. Cacciari and G. P. Salam, *Pileup subtraction using jet areas*, 2008, Phys. Lett. **B659** (2008) 119, arXiv:0707.1378 [hep-ph].

[170] ATLAS Collaboration, *In situ jet pseudorapidity intercalibration of the ATLAS detector using dijet events in $\sqrt{s} = 7$ TeV proton-proton 2011 data*, ATLAS-CONF-2012-124, 2012, URL: http://inspirehep.net/record/1204293.

[171] ATLAS Collaboration, *Performance of b-Jet Identification in the ATLAS Experiment*, 2016, JINST **11** (2016) P04008, arXiv:1512.01094 [hep-ex].

[172] ATLAS Collaboration, M. Lehmacher, *b-Tagging Algorithms and their Performance at ATLAS*, 2008, arXiv:0809.4896 [hep-ex].

[173] G. Piacquadio and C. Weiser, *A new inclusive secondary vertex algorithm for b-jet tagging in ATLAS*, 2008, J. Phys. Conf. Ser. **119** (2008) 032032.

[174] ATLAS Collaboration, *Calibration of the performance of b-tagging for c and light-flavour jets in the 2012 ATLAS data*, ATLAS-CONF-2014-046, 2014, URL: http://inspirehep.net/record/1304981.

[175] Breiman et al., *Classification and Regression Trees*, Taylor & Francis, 1984, URL: https://books.google.de/books?id=JwQx-WOmSyQC.

[176] ATLAS Collaboration, *Optimisation of the ATLAS b-tagging performance for the 2016 LHC Run*, ATL-PHYS-PUB-2016-012, 2016, URL: https://cds.cern.ch/record/2160731.

[177] D0 Collaboration, *b-Jet Identification in the D0 Experiment*, 2010, Nucl. Instrum. Meth. **A620** (2010) 490, arXiv:1002.4224 [hep-ex].

[178] ATLAS Collaboration, *b-tagging efficiency calibration from 2015+2016 data on $t\bar{t}$ events* URL: http://atlas.web.cern.ch/Atlas/GROUPS/PHYSICS/PLOTS/FTAG-2017-003.

[179] ATLAS Collaboration, *Identification and energy calibration of hadronically decaying tau leptons with the ATLAS experiment in pp collisions at $\sqrt{s}$=8 TeV*, 2015, Eur. Phys. J. **C75** (2015) 303.

[180] ATLAS Collaboration, *Measurement of the tau lepton reconstruction and identification performance in the ATLAS experiment using pp collisions at $\sqrt{s}$=13 TeV*, ATLAS-CONF-2017-029, 2017, URL: http://inspirehep.net/record/1597609.

[181] ATLAS Collaboration, *Photon identification in 2015 ATLAS data*, ATL-PHYS-PUB-2016-014, 2016, URL: http://cds.cern.ch/record/2203125.

[182] ATLAS Collaboration, *Performance of algorithms that reconstruct missing transverse momentum in $\sqrt{s} = 8$ TeV proton-proton collisions in the ATLAS detector*, 2017, Eur. Phys. J. **C77** (2017) 241, arXiv:1609.09324 [hep-ex].

[183] ATLAS Collaboration, *Performance of missing transverse momentum reconstruction for the ATLAS detector in the first proton-proton collisions at $\sqrt{s}$= 13 TeV*, 2015, URL: https://cds.cern.ch/record/2037904.

[184] ATLAS Collaboration, *Expected performance of missing transverse momentum reconstruction for the ATLAS detector at $\sqrt{s}$= 13 TeV*, ATL-PHYS-PUB-2015-023, 2015, URL: https://cds.cern.ch/record/2037700.

[185] ATLAS Collaboration, *Search for squarks and gluinos with the ATLAS detector in final states with jets and missing transverse momentum using $\sqrt{s} = 8$ TeV proton-proton collision data*, 2014, JHEP **09** (2014) 176, arXiv:1405.7875 [hep-ex].

[186] ATLAS Collaboration, *Search for squarks and gluinos in events with isolated leptons, jets and missing transverse momentum at $\sqrt{s} = 8$ TeV with the ATLAS detector*, 2015, JHEP **04** (2015) 116, arXiv:1501.03555 [hep-ex].

[187] ATLAS Collaboration, *Summary of the searches for squarks and gluinos using $\sqrt{s} = 8$ TeV pp collisions with the ATLAS experiment at the LHC*, 2015, JHEP **10** (2015) 054, arXiv:1507.05525 [hep-ex].

[188] ATLAS Collaboration, *Summary of the ATLAS experiments sensitivity to supersymmetry after LHC Run 1 - interpreted in the phenomenological MSSM*, 2015, JHEP **10** (2015) 134, arXiv:1508.06608 [hep-ex].

[189] ATLAS Collaboration, *Summary plots from the ATLAS Supersymmetry physics group* URL: https://atlas.web.cern.ch/Atlas/GROUPS/PHYSICS/CombinedSummaryPlots/SUSY.

[190] ATLAS Collaboration, *ATLAS Run 1 searches for direct pair production of third-generation squarks at the Large Hadron Collider*, 2015, Eur. Phys. J. **C75** (2015) 510, arXiv:1506.08616 [hep-ex].

[191] S. Roy and B. Mukhopadhyaya, *Some implications of a supersymmetric model with R-parity breaking bilinear interactions*, 1997, Phys. Rev. **D55** (1997) 7020, arXiv:hep-ph/9612447 [hep-ph].

[192] T. Appelquist and H.C. Cheng and B. A. Dobrescu, *Bounds on universal extra dimensions*, 2001, Phys. Rev. **D64** (2001) 035002, arXiv:hep-ph/0012100 [hep-ph].

[193] Alwall et al., *The automated computation of tree-level and next-to-leading order differential cross sections, and their matching to parton shower simulations*, 2014, JHEP **07** (2014) 079, arXiv:1405.0301 [hep-ph].

[194] A. Kulesza and L. Motyka, *Threshold resummation for squark-antisquark and gluino-pair production at the LHC*, 2009, Phys. Rev. Lett. **102** (2009) 111802, arXiv:0807.2405 [hep-ph].

[195] Alwall et al., *MadGraph 5: Going Beyond*, 2011, JHEP **06** (2011) 128, arXiv:1106.0522 [hep-ph].

[196] ATLAS Collaboration, *ATLAS Run 1 Pythia8 tunes*, ATL-PHYS-PUB-2014-021, 2014, URL: https://cds.cern.ch/record/1966419.

[197] P. Z. Skands, *Tuning Monte Carlo Generators: The Perugia Tunes*, 2010, Phys. Rev. **D82** (2010) 074018, arXiv:1005.3457 [hep-ph].

[198] S. Gieseke and C. Rohr and A. Siodmok, *Colour reconnections in Herwig++*, 2012, Eur. Phys. J. **C72** (2012) 2225, arXiv:1206.0041 [hep-ph].

[199] ATLAS Collaboration, *LHC SUSY Cross Section Working Group* URL: https://twiki.cern.ch/twiki/bin/view/LHCPhysics/SUSYCrossSections.

[200] ATLAS Collaboration, *Tagging and suppression of pileup jets*, ATLAS-CONF-2014-018, 2014, URL: http://inspirehep.net/record/1295764.

[201] ATLAS Collaboration, *ATLAS Data Quality Operations in 2012*, ATL-DAPR-INT-2015-001, 2015, URL: https://cds.cern.ch/record/1982821.

[202] Schott et al., *RooStats for Searches*, 2011, arXiv:1203.1547 [physics.data-an].

[203] Buckley et al., *LHAPDF6: parton density access in the LHC precision era*, 2015, Eur. Phys. J. **C75** (2015) 132, arXiv:1412.7420 [hep-ph].

[204] Cowan et al., *Asymptotic formulae for likelihood-based tests of new physics*, 2011, Eur. Phys. J. **C71** (2011) 1554, arXiv:1007.1727 [physics.data-an].

[205] J. Neyman and E. S. Pearson, *On the Problem of the Most Efficient Tests of Statistical Hypotheses*, 1933, JSTOR **231** (1933) 289.

[206] A. L. Read, *Presentation of search results: the CL_s technique*, 2002, J. Phys. **G28** (2002) 2693.

[207] Baak et al., *HistFitter software framework for statistical data analysis*, 2015, Eur. Phys. J. **C75** (2015) 153, arXiv:1410.1280 [hep-ex].

[208] ATLAS Collaboration, *Search for pair production of gluinos decaying via stop and sbottom in events with b-jets and large missing transverse momentum in pp collisions at $\sqrt{s} = 13$ TeV with the ATLAS detector*, 2016, Phys. Rev. **D94** (2016) 032003, arXiv:1605.09318 [hep-ex].

[209] ATLAS Collaboration, *Search for new phenomena in final states with large jet multiplicities and missing transverse momentum with ATLAS using $\sqrt{s} = 13$ TeV proton-proton collisions*, 2016, Phys. Lett. **B757** (2016) 334–355, arXiv:1602.06194 [hep-ex].

[210] C. Csaki and Y. Grossman and B. Heidenreich, *MFV SUSY: A Natural Theory for R-Parity Violation*, 2012, Phys. Rev. **D85** (2012) 095009, arXiv:1111.1239 [hep-ph].

[211] E. Nikolidakis and C. Smith, *Minimal Flavor Violation, Seesaw, and R-parity*, 2008, Phys. Rev. **D77** (2008) 015021, arXiv:0710.3129 [hep-ph].

[212] Huang et al., *Same-Sign Dilepton Excesses and Light Top Squarks*, 2015, Phys. Rev. **D92** (2015) 075035, arXiv:1507.01601 [hep-ph].

[213] J. R. Ellis and T. Falk and K. A. Olive and Y. Santoso, *Exploration of the MSSM with nonuniversal Higgs masses*, 2003, Nucl. Phys. **B652** (2003) 259–347, arXiv:hep-ph/0210205 [hep-ph].

[214] J. R. Ellis and K. A. Olive and Y. Santoso, *The MSSM parameter space with nonuniversal Higgs masses*, 2002, Phys. Lett. **B539** (2002) 107–118, arXiv:hep-ph/0204192 [hep-ph].

[215] Alwall et al., *A Standard format for Les Houches event files*, 2007, Comput. Phys. Commun. **176** (2007) 300, arXiv:hep-ph/0609017 [hep-ph].

[216] C. G. Lester and D. Summers, *Measuring masses of semi-invisibly decaying particles pair produced at hadron colliders*, 1999, Phys. Lett. **B463** (1999) 99, arXiv:hep-ph/9906349 [hep-ph].

[217] ATLAS Collaboration, *Search for direct pair production of a chargino and a neutralino decaying to the 125 GeV Higgs boson in $\sqrt{s} = 8$ TeV pp collisions with the ATLAS detector*, 2015, Eur. Phys. J. **C75** (2015) 208, arXiv:1501.07110 [hep-ex].

[218] M. Muhlleitner and M. Spira, *A Note on doubly charged Higgs pair production at hadron colliders*, 2003, Phys. Rev. **D68** (2003) 117701, arXiv:hep-ph/0305288 [hep-ph].

[219] Chivukula et al., *Top Quark Seesaw Theory of Electroweak Symmetry Breaking*, 1999, Phys. Rev. **D59** (1999) 075003, arXiv:hep-ph/9809470 [hep-ph].

[220] J. Alwall and P. Schuster and N. Toro, *Simplified Models for a First Characterization of New Physics at the LHC*, 2009, Phys. Rev. **D79** (2009) 075020, arXiv:0810.3921 [hep-ph].

[221] ATLAS Collaboration, *Search for doubly charged Higgs boson production in multi-lepton final states with the ATLAS detector using proton-proton collisions at $\sqrt{s}$ = 13 TeV*, 2017, arXiv:1710.09748 [hep-ex].

List of Figures

List of Tables

PUBLICATIONS AND AUTHOR'S CONTRIBUTIONS

Most of the material presented in this thesis is based on work performed within the ATLAS Collaboration. Thus, it is typically created from the contributions of many people and cannot be attributed to a single person.
The figures and plots containing an *ATLAS* or *ATLAS Preliminary* label were created in the context of ATLAS papers or conference notes. The publications with a significant contribution from the author of this thesis and the details about these contributions are indicated in this section. All plots without dedicated *ATLAS* or *ATLAS Preliminary* labels are private work done by the author of this thesis.

- *Search for supersymmetry at $\sqrt{s}$ = 13 TeV in final states with jets and two same-sign leptons or three leptons with the ATLAS detector* [6]:

  Studies about trigger strategy and event selection (single-lepton, dilepton, and $E_{\mathrm{T}}^{\mathrm{miss}}$ triggers). Optimization of signal regions (especially in terms of lepton p_{T} requirements and flavor selection). Production of input trees with experimental systematic uncertainties. Implementation of the analysis in the HISTFITTER framework. Statistical interpretations of the results and production of SUSY exclusion plots.

- *Search for supersymmetry with two same-sign leptons or three leptons using 13.2 fb^{-1} of $\sqrt{s}$ = 13 TeV pp collision data collected by the ATLAS detector* [7]:

  Validation of trigger strategy for 2016 data (including tests of new triggers). Production of input trees with experimental systematic uncertainties. Studies on potential of hadronic W/Z-tagging in signal regions. Statistical interpretations of the results and production of SUSY exclusion plots with HISTFITTER.

- *Search for supersymmetry in final states with two same-sign or three leptons and jets using 36 fb^{-1} of $\sqrt{s}$ = 13 TeV pp collision data with the ATLAS detector* [8]:

  Review and validation of trigger strategy for 2016 data. Studies of m_{T2} variable and feasibility tests for m_{T2}-based signal regions. Investigation of potential impact of double parton scattering $W^{\pm}W^{\pm}$ production in signal regions. Evaluation of systematic uncertainties in signal regions (including validation of analysis robustness against choice of JES NP and Egamma NP set). Production of signal region summary plots and tables. Statistical interpretations of the results and production of SUSY exclusion plots with HISTFITTER.

- *Muon reconstruction performance of the ATLAS detector in proton-proton collision data at $\sqrt{s}$ = 13 TeV* [150]:

  Validation of muon momentum calibration (scale and resolution) in $Z^0 \to \mu\mu$ events for early 2015 Monte Carlo productions.

ACKNOWLEDGEMENTS

I would like to express my gratitude to all my colleagues and friends who supported me in many different ways during the recent years.

First of all, I would like to thank my advisors *Prof. Gregor Herten* and *Prof. Ulrich Landgraf*, who invited me to join their research group for my Diploma and Ph.D. thesis, for their constant support, as well as their supervision and dedication to my analysis.

Furthermore, I have to thank our awesome group here at the University of Freiburg: *Zuzana Rurikova*, *Andrea Knue*, *Martin Nagel*, *Kim Heidegger*, *Martina Pagacova*, *Manfredi Ronzani*, *Veronika Magerl*, *Simone Curcio*, *Thorwald Klapdor-Kleingrothaus*, *Manuel Guth*, *Giulia Gonella*, *Simona Gargiulo*, *Riccardo Mori*, *Patrick Scholer*, *Niklas Scheidtmann*, *Bernhard Pfeifer*, *Jürgen Tobias*, and *Ulrich Holland*, including also the former group members *Andrea di Simone*, *Simone Amoroso*, *Jan Erik Sundermann*, *Tomas Javurek*, and *Valerio Consorti* (sorry if I forgot someone). Thanks to you I could really enjoy my working hours (in fact, it didn't feel like work at all) and I had always a reason to look forward to a relaxing coffee break in the late morning or the afternoon. It's no exaggeration to say that you are the best colleagues one could imagine. A special thanks goes to my office and analysis mate *Peter Tornambé*, who had to endure me in the last three years: your thesis will definitely surpass this one!

A special gratitude and recognition deserves also the same-sign/3L analysis team I had the pleasure to work with for the last years. Especially the people I directly worked with: *Julien Maurer*, *Ximo Poveda*, *Otilia Ducu*, *Othmane Rifki*, and *Simon Berlendis*, but also all the other team members (unfortunately, some of them I never met personally). All of you did an outstanding job during the last years and without your help this thesis would probably not be worth the paper it's printed on.

Also thanks to *Dilip Jana* for the fruitful and efficient discussions about the HISTFITTER framework and his help with the NUHM2 model.

During my time as Ph.D. student I met a lot of nice and intelligent people at various summer schools, workshops, conferences, and other events. Thanks a lot for all the interesting and profound discussions about particle physics and other topics. Also these experiences made my years as Ph.D. student a fantastic and unique time I will never forget.

I would also like to thank all the other people outside physics with whom I shared my time in Freiburg: *Pascal*, *Tom*, *Bernd*, *Domi*, *René*, *Lena*, *Johannes*, *Christoph*, *Manu*, *Notheisenzinho*, *Morti*, *Felix*, *Meike*, *Robert*, and *Ingo*. I'm really grateful for all the nice activities we went through together, like SC Freiburg football matches, funny evenings at O'Kellys, or our exiting Pub-Quiz nights. Freiburg is a lively city, but you guys made it truly livable.

Probably there are still a lot of people who I have to thank and I forgot to mention at this point. Sorry for that! If I'll ever write another Ph.D. thesis, I will mention you there.

And last but not least, a very, very special thanks to my parents *Sonja & Ersilio Cardillo* and my brother *Dino Cardillo*. I will keep on doing my best. . . means usually around 95%. Well, 100% is not possible for a lazy guy like me ;-)